TÜRKİYE DEPREM MÜHENDİSLİĞİ DERNEĞİ

EARTHQUAKE ENGINEERING ASSOCIATION OF TURKEY

5.ICEES ANKARA 2019

5th International Conference on Earthquake Engineering and Seismology

8-11 OCTOBER 2019

ANKARA, TURKEY

METU Cultural and Convention Center

POSTER PROCEEDING BOOK

For more information about the event, please check the website at
http://www.5icees.com

For further informations please do not hesitate to contact us at
5icees@tdmd.org.tr

ODTÜ METU

/ 5icees

İZMİR VE ÇEVRESİNİN SİSMOLOJİK VE SİSMOTEKTONİK AÇIDAN İNCELENMESİ

Ahi L.E[1], Kalkar B.[2], Gök E.[3] ve Polat O.[4]

[1] *Yüksek Jeofizik Mühendisi/ İzmir, Türkiye*
[2] *Lisansüstü Öğrencisi/Jeofizik Mühendisliği, Dokuz Eylül Üniversitesi/İzmir, Türkiye*
[3] *Dr. Öğr. Üyesi/Jeofizik Mühendisliği, Dokuz Eylül Üniversitesi/İzmir, Türkiye*
[4] *Prof. Dr./Jeofizik Mühendisliği, Dokuz Eylül Üniversitesi/İzmir, Türkiye*
Email: livaneezgi@gmail.com

ÖZET:

Bu çalışmada, İzmir ve çevresinde yer alan İzmirNET ve AFAD kuvvetli yer hareketi istasyon ağları kullanılarak çalışma alanına ait sismik aktivite gözlenmiştir. İzmirNET istasyon ağı İzmir'de bulunan ilk kuvvetli yer hareketi istasyon ağıdır (Gök ve Polat, 2011). Batı Anadolu'da yer alan bu istasyon ağı deprem tehlikesi konusuna işaret eden önemli bir istasyon ağıdır. İzmirNET istasyon ağı İzmir'de bulunan ilk kuvvetli yer hareketi istasyon ağıdır (Gök ve Polat, 2011). Batı Anadolu'da yer alan bu istasyon ağı deprem tehlikesi konusuna işaret eden önemli bir istasyon ağıdır. Bilindiği üzere, İzmir ekonomi, endüstri, populasyon vb. konularında Türkiye'de İstanbul ve Ankara'dan sonra yer alan üçüncü büyük şehirdir. Ayrıca şehir, geçmişte yıkıcı depremlere tanıklık etmiştir. Bu sebeplerden dolayı, İzmir önemli bir şehirdir ve çalışma kapsamında sismolojik ve sismotektonik açıdan çalışılmak üzere tercih edilmiştir. Çalışma alanı 36.0°-40.5° enlemleri ile 25.5°-30.0° boylamlarıyla sınırlıdır. Veri setini $1.0 \leq M \leq 6.5$ büyüklüğünde 2426 adet, $3.0 \leq M \leq 6.5$ büyüklüğünde 1004 adet deprem oluşturmaktadır. İstasyon ağları tarafından 2008-2018 yılları arasında kaydedilen deprem verileri, SEISAN programında incelenmiştir (Havskov v.d., 2016). Bu çalışma kapsamında, program ile P - S fazları, büyüklük, derinlik, deprem episantrları gibi deprem parametreleri elde edilmiştir. $1.0 \leq M \leq 6.5$ büyüklüğündeki depremlere Tamlık Analizi fonksiyonu uygulanmış, ardından $3.0 \leq M \leq 6.5$ büyüklüğündeki depremlerin yıllara göre değişimi ile bu depremlerin kümülatif momentlerinin yıllara göre değişimi incelenmiştir. Maksimum kümülatif moment değeri 15×10^{25} erg olarak hesaplanmıştır. Bölgenin sismisitesini gözlemleyebilmek için sismisite haritası, Boylam-Derinlik ve Enlem-Derinlik haritaları elde edilmiştir. Sismisite haritası incelendiğinde depremlerin KD-GB ile KB-GD yönlü kümelendiği, özellikle İzmir Körfezi ve çevresinde yoğun bir sismik aktivite gözlenmiştir. İzmir ve çevresinde baskın olarak normal faylanma ve doğrultu atımlı faylanma karakterine sahip depremler gözlenmiştir.

ANAHTAR KELİMELER: İzmirNET, sismoloji, deprem, sismik aktivite, kuvvetli yer hareketi.

SEISMOLOGICAL AND SEISMOTECTONICS OBSERVATION OF IZMIR AND SURROUNDINGS

ABSTRACT:

In this study, IzmirNET and AFAD strong ground motion station network was used, which is located in Izmir and its surrounding area, to define the seismic activity of Izmir and its surrounding area. IzmirNET is the first strong ground motion station network in Izmir (Gok and Polat, 2011). That network is critically important in western Turkey because of the network to pointing earthquake hazard issues. As is known, after Istanbul and Ankara, Izmir is the third largest city in Turkey at economy, industry, population, etc. issues. Also, that city was

a witness to historically damaging earthquakes. For these reasons, Izmir is fundamental city and was preferred for performing to study seismological and seismotectonics. The study area was selected between 36.0°-40.5° latitudes and 25.5°-30.0° longitudes. Our database consists of 2426 events of magnitude between 1.0≤M≤6.5 and 1004 events of magnitude between 3.0≤M≤6.5. The earthquake data recorded by the IzmirNET station network between 2008-2018 years, has been analyzed with SEISAN Earthquake Analysis Software (Havskov v.d., 2014). In this study, earthquake parameters such as P phase, S phase, magnitude, depth, etc. have been obtained with that software. After Completeness Check function was applied to events of magnitude between 1.0≤M≤6.5, variances of events of magnitude between 3.0≤M≤6.5 by years and the cumulative moments of these events were examined. The maximum cumulative moment value was calculated by 15x1025 erg. In order to observe to the study area, seismicity map, longitude-depth map, and latitude-depth map were obtained. When that seismicity map is analysed, it is observed that events are clustered in NE-SW and NW-SE directions, especially intense seismic activity in Izmir and around Izmir Bay. Dominantly earthquakes with normal component faulting and strike-slip component faulting characteristics were observed in Izmir and its surrounding area.

KEYWORDS: IzmirNET, seismology, earthquake, seismic activity, strong ground motion.

1. GİRİŞ

Bu çalışma kapsamında, İzmir ve çevresinin sismolojik ve sismotektonik açılardan incelenmesi ve yorumlanması açısından İzmirNET istasyonları ile AFAD'ın kuvvetli yer hareketi istasyonları kullanılmıştır. Bu istasyonlar tarafından, 2008-2018 yılları arasında kaydedilen deprem verileri, çalışmanın veri setini oluşturmaktadır. 10 yıllık veri setiyle, çalışma alanına ait sismik aktivitenin gözlenmesi, deprem verileriyle ilgili parametrelerinin elde edilmesi, bölgenin sismolojik ve sismotektonik açıdan gözlenmesi ve incelenmesi, çalışmanın amacını oluşturmaktadır.

2. ÇALIŞMA ALANININ SİSMOLOJİK AÇIDAN İNCELENMESİ

Çalışma alanı, İzmir ve çevresi olup, 36.0°-40.5° enlemleri ile 25.5°-30.0° boylamları arasında kalan bölgeyi kapsamaktadır. 2008-2018 yıllarını kapsayan, 1.0≤M≤6.5 büyüklüğünde 2426 adet, 3.0≤M≤6.5 büyüklüğünde 1004 adet deprem, çalışmanın veri setini oluşturmaktadır (Şekil 1). Depremler, SEISAN deprem analiz programıyla incelenmiştir. Programla, depremlerin P-S fazları, büyüklük, derinlik, gibi deprem parametreleri elde edilmiştir. Böylelikle, çalışmaya ait deprem kataloğu oluşturulmuştur.

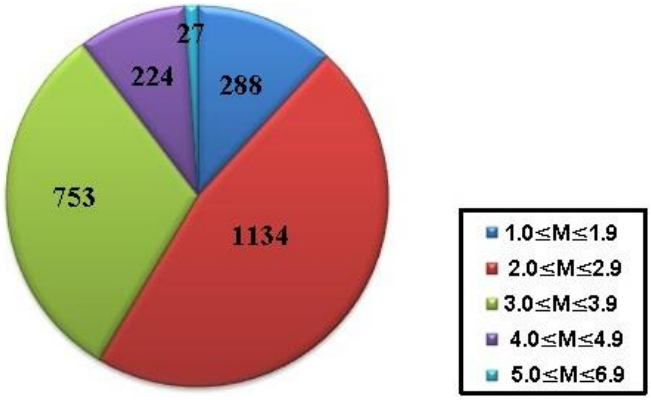

Şekil 1. 2008-2018 yılları arasında ve 1.0≤M≤6.5 büyüklüğündeki depremlerin dağılımı

Deprem kataloğunun oluşturulmasının ardından, yıllara göre değişken deprem büyüklüğü ve artan istasyon sayısı gibi bazı parametrelerin veriler üzerindeki negatif etkisini gözlemlemek amacı ile okunan tüm deprem verilerine (1.0≤M≤6.5) Tamlık Analizi fonksiyonu uygulanmıştır (Şekil 2). Araştırmacılar özellikle deprem olasılık analizleri, veriler ile istatistiksel yaklaşımlar yapılmadan önce tamlık analizi yapılmasını önerilmektedir (Stepp, 1972; Polat v.d., 2008).

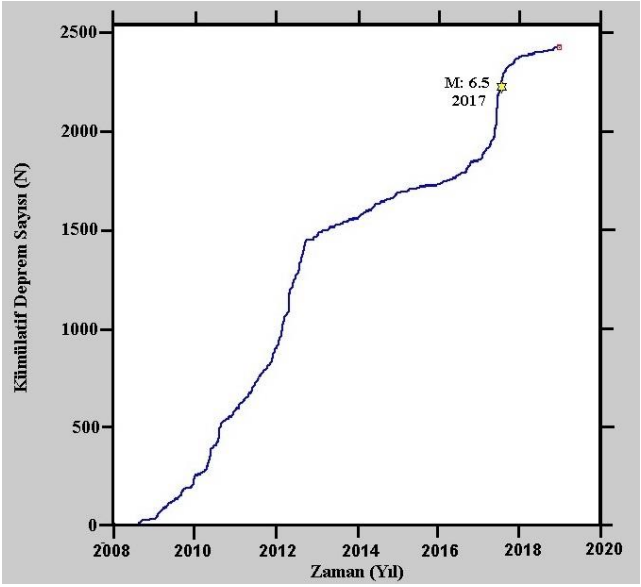

Şekil 2. Tamlık analizi

Tamlık analizi sonucunda, Şekil 3'deki 2008-2018 yıllarını kapsayan grafikten hareketle deprem sayısında artış görülmektedir. Özellikle 2008-2012 ve 2016-2018 yılları arasında yoğun bir sismik aktivite gözlemlenirken, 2013-2015 yılları arasında belirtilen bu yıl aralıklarına göre yoğunluk olarak daha az sismik aktivite gözlemlenmiştir. Tamlık analizinin ardından, istasyonlar tarafından kaydedilen, büyüklükleri 3.0≤M≤6.5 olan depremlerin ve bu depremlerin kümülatif momentlerinin yıllara göre değişimi incelenmiştir. Deprem sayısının ve açığa çıkan sismik enerjinin yıllara göre değişimi Şekil 3'de görülmektedir.

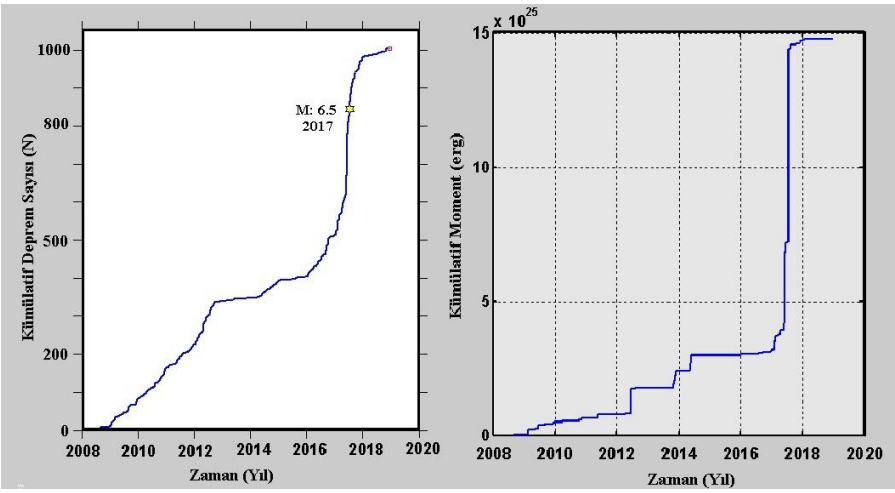

Şekil 3. Deprem sayısının ve açığa çıkan sismik enerjinin yıllara göre değişimi.

Şekil 3'de istasyonların kuruluş yılı olan 2008 yılından 2018 yılına kadar olan süreçte deprem sayısında artış görülmektedir. Yine sismik enerjinin, deprem sayısıyla doğru orantılı bir şekilde artış gösterdiği gözlenmektedir. Hesaplanan maksimum kümülatif moment değeri $15x10^{25}$ erg olarak hesaplanmıştır.

Çalışma alanında meydana gelen 10 yıllık deprem aktivitesi Enlem-Derinlik Boylam-Derinlik kesitleriyle Şekil 4'de görülmektedir.

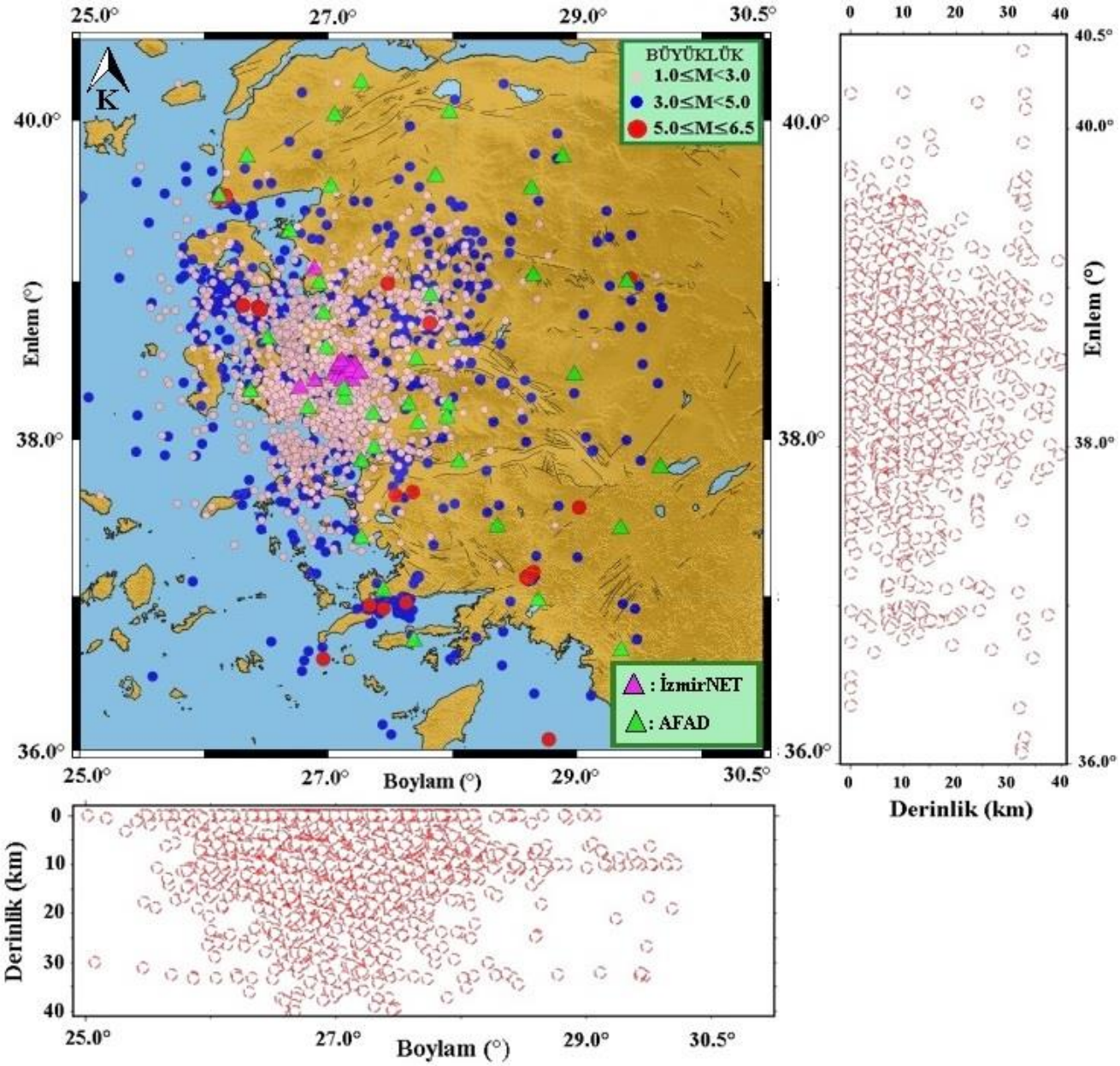

Şekil 4. Çalışma alanında 2008-2018 yılları arasında meydana gelen depremlerin lokasyon haritası.

Şekil 4 incelendiğinde depremlerin, KD-GB ile KB-GD yönlü kümelendiği görülmektedir. Özellikle İzmir Körfezi ve çevresinde yoğun bir sismik aktivite gözlenmektedir. Ege Denizi'nde ve İzmir'in doğusunda ise

depremlerin saçıldığı, yukarda bahsedilen diğer bölgelere nazaran daha az sismik aktivite gözlenmektedir. Boylam-Derinlik ve Enlem-Derinlik kesitlerine bakıldığında deprem aktivitesi en yoğun, 26.0°-28.0° boylamları ile 37.0°-39.5° enlemleri arasında olduğu gözlemlenmiştir.

Çalışma alanına ait deprem verileri okunup, deprem kataloğu oluşturulduktan sonra, M ≥ 4.0 büyüklüğündeki depremlerin odak mekanizma çözümleri yapılmıştır. Depremlerin odak mekanizma çözümleri için SEISAN programının altında çalışan FOCMEC programı kullanılmıştır (Snoke, 2017). FOCMEC programı aracılığıyla depremlere ait dalım, eğim ve kayma açıları elde edilmiştir. Depremlere ait dalım, eğim ve kayma açılarıyla bir dat dosyası oluşturulmuş, bu dat dosyası GMT programına okutulmuştur (Wessel v.d., 2013). GMT programıyla, çalışma alanında meydana gelen M≥4.0 büyüklüğündeki depremlerin odak mekanizma çözümlerini gösteren bir harita elde edilmiştir (Şekil 5).

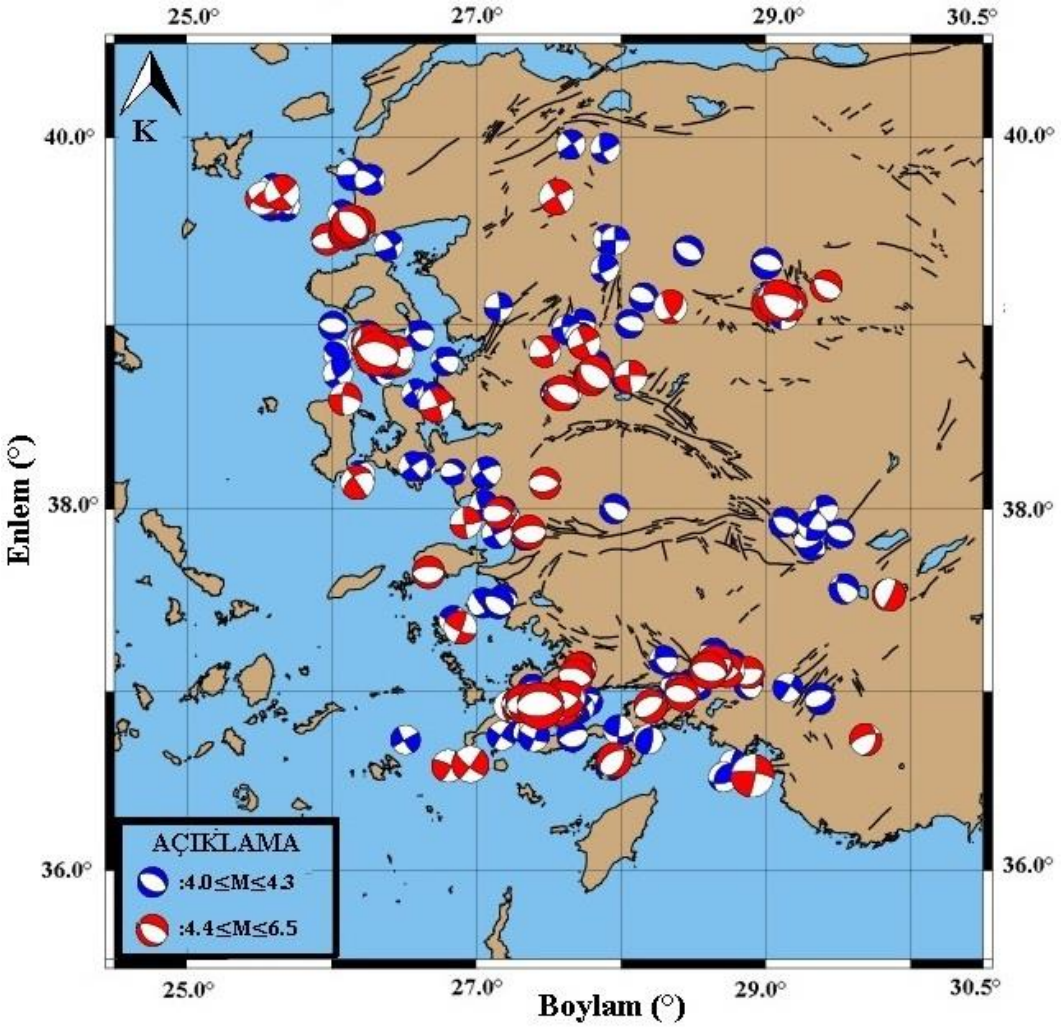

Şekil 5. Çalışma alanında meydana gelen M ≥ 4.0 büyüklüğündeki depremlerin odak mekanizma çözümleri.

Şekil 5'de gösterilen odak mekanizma çözümlerinden hareketle bölgede baskın olarak normal faylanma ve doğrultu atımlı faylanma karakterine sahip depremler gözlenmiştir.

3. SONUÇLAR

Çalışma kapsamında 36.0°-40.5° enlemleri ile 25.5°-30.0° boylamları arasında kalan bölgede 2008-2018 yıllarını kapsayan, 1.0≤M≤6.5 büyüklüğünde 2426 adet, 3.0≤M≤6.5 büyüklüğünde 1004 adet deprem çalışmanın veri setini oluşturmuş ve kullanılmıştır. Bu veri setini oluşturan depremlerin deprem parametreleri (P-S fazları, büyüklük, derinlik vb.) elde edilmiş ve deprem kataloğu oluşturulmuştur. Deprem kataloğunda yer alan 1.0≤M≤6.5 büyüklüğündeki depremlere Tamlık Analizi fonksiyonu uygulanmış, buradan hareketle 2008-2018 yılları arasında deprem sayısındaki artış gözlenmiştir. Tamlık Analizi fonksiyonunda yoğun sismik aktiviteye sahip yıllar 2008-2012 ve 2016-2018 yılları arası olarak, 2013-2015 yılları arası ise bu yıl aralıklarına göre daha az sismik aktiviteye sahip yıl aralığı olarak belirlenmiştir. 3.0≤M≤6.5 büyüklüğündeki depremlerin yıllara göre değişimi, bu depremlerin kümülatif momentlerinin yıllara göre değişimi ile birlikte incelenmiş, açığa çıkan sismik enerjinin deprem sayısıyla doğru orantılı olarak artış gösterdiği gözlenmiştir. Depremlere ait maksimum kümülatif moment değeri hesaplanmış ve maksimum kümülatif moment değeri $15x10^{25}$ erg olarak hesaplanmıştır. Deprem aktivitesinin gözlemlenebilmesi için çalışma alanında meydana gelen depremlerin sismisite haritası, aynı zamanda Enlem-Derinlik Boylam-Derinlik kesitleri elde edilmiştir. Depremlerin, KD-GB ile KB-GD yönlü kümelendiği, özellikle İzmir Körfezi ve çevresinde yoğun bir sismik aktivite gözlenmiştir. Ege Denizi'nde ve İzmir'in doğusunda ise depremlerin saçıldığı, diğer bölgelere nazaran daha az sismik aktivite gözlenmiştir. Elde edilen Boylam-Derinlik ve Enlem-Derinlik kesitlerinde 26.0°-28.0° boylamları ile 37.0°-39.5° enlemleri arasında deprem aktivitesinin en yoğun olduğu aralıklar olarak belirlenmiştir. Çalışma alanına ait sismotektonik çalışmalar kapsamında M ≥ 4.0 büyüklüğündeki depremlerin odak mekanizma çözümleri yapılmış, depremlere ait dalım, eğim ve kayma açıları elde edilmiştir. Ardından depremlerin odak mekanizma çözümlerini gösteren bir harita elde edilmiştir. Odak mekanizma çözümleri bölgede normal ve doğrultu atımlı fayların baskın olduğunu göstermiştir.

KAYNAKLAR

Gök E, Polat O (2011). İzmir kuvvetli yer hareketi deprem istasyon ağı: İzmirNET. Süleyman Demirel Üniversitesi, Fen Bilimleri Enstitüsü Dergisi, **15(3):** 233-243.

Ottomöller L, Voss P, Havskov J (2016). Seisan earthquake analysis software for Windows, Solaris, Linux and Macosx, version 10.5 (İngilizce).

Polat O, Gök E, Yılmaz D (2008). Earthquake hazard of the Aegean extension region (West Turkey), Turkish Journal of Earth Sciences, **17(3):** 593–614 (İngilizce).

Snoke, A. S (2017). FOCMEC: FOCal MEChanism determinations, Virginia Tech, Blaksburg, VA, USA (İngilizce).

Stepp, J. C (1972). Analysis of completeness of the earthquake sample in the Puget Sound area and its effects on statistical estimates of earthquake hazard, Proceedings of the First Microzonation Conference, Seattle, WA (İngilizce).

Wessel, P, Smith, WHF (2013). The generic mapping tools version 4.5.9, Technical Reference and Cookbook Laboratory for Satelitte Altimetry NOAA/NEDDIS (İngilizce).

CONSIDERATION OF SITE RESPONSE ANALYSIS IN SEISMIC PERFORMANCE ANALYSIS OF A ONE-BAY STRUCTURE

Guzel Y.[1], Elia G.[2], Guzel F.[3] and Rouainia M.[4]

[1] *Res. Assist candidate, Necmettin Erbakan University, Konya, Turkey*
[2]*Tenure-track Associate Professor in Geotechnical Engineering (PhD), DICATECh, Technical University of Bari, Bari, Italy,*
[3]*Res. Assist., Igdir University, Igdir, Turkey*
[4] *Reader in Computational Geomechanics (PhD), School of Engineering, Newcastle University, Newcastle, UK,*
Email: y.guzel@newcastle.ac.uk

ABSTRACT:

Propagation of seismic waves through soil deposits may considerably alter their characteristics at surface. This ultimately influences the seismic performance of structures. The influences of soil deposits are included in seismic codes (e.g. EC8) by means of proposed design spectra for different soil classes used in design or retrofitting of structures. Nevertheless, a smooth design spectrum cannot always represent spectral response of an actual input motion over an engineering period of interest due to its irregular spectral shape. Although design spectrum is only used for reference to modify the real input motions, it can still be insufficient in consideration of influences of soil deposits. This study aims to demonstrate the impact of the soil deposits with soil classes D, C and B on the seismic behaviour of one-bay, one-storey structure modelled in OpenSEES. For this purpose, two different approaches are chosen; (i) seven input motions recorded on ground surface are modified and applied to the model, (ii) seven outcrop motions are scaled according to EC8 and processed through the ideal soil deposits by conducting nonlinear site response analysis, then applied to the model. The results indicate that the model is exposed to more drift response when it is on softer soil deposit. In addition, imposing input motions obtained at surface from nonlinear site response analysis causes higher drift responses and less standard deviations than directly imposing input motions, implying the efficiency of the method applied.

KEYWORDS: soil classes, design response spectrum, outcrop motion, site response analysis, seismic performance of structures.

1. INTRODUCTION

Earthquake events are the inevitable fact of the earth planet sitting over the tectonic plates. This natural event is happening in numerous times at different level of magnitudes and, more importantly at different impact levels to the urban areas. In order to minimize the impact of an earthquake event to a site of interest it is necessary to consider input motions, representing the main characteristics of the earthquake events at that site, e.g. magnitudes and distances, in the design of new buildings or retrofitting of existing ones (CEN, 2005).
The design of a building in seismically active regions requires nonlinear analyses under earthquake input motions. From this perspective, the selection and modification of input motions are regarded as critical as the modelling of the buildings (Iervolino and Manfredi, 2008). While different scaling methods have been developed to modify the input motions, their selections are made based on the magnitude and distance hazard distributions of the site under consideration. Different input motion selection and scaling methods, such as peak ground acceleration (PGA) scaling, spectral matching and the mean squared error (MSE) approach, have been proposed mainly for the benefit of structural engineering practitioners (Shome *et al.*, 1998; CEN, 2005; Hancock *et al.*, 2006; Ancheta *et al.*, 2013).

Generally, the building models with single or multi-degree of freedoms are modelled as fixed base and modified input motions are directly applied at the base of the model. The building model is assessed based on the engineering demand parameters (e.g. inter-storey drift response, roof drift response, etc.) (Iervolino and

Manfredi, 2008). Since the nonlinear dynamic analysis of buildings are time and cost consuming, the determination of the adequate number of analyses or input motions is vital. The number of input motions to be considered as adequate depends on the efficiency of the scaling method adapted (Shome *et al.*, 1998). The number of input motions should be such that the mean response of an EDP does not change significantly with the increase in the input motions and does not reduce the scatter anymore in the response. In this regard, EC8 recommends considering seven input motions in order to account the mean response in the building designs.

General practise in selecting input motions for the nonlinear dynamic analysis of buildings is firstly to determine a target response spectrum representing the seismic intensity level of the site under consideration. Secondly, the input motions are selected based on the hazard distributions of the site and modified, accordingly. The target spectrum will either be constructed in compliance with the seismic design codes (e.g. EC8) or will be obtained from the site response analysis. When the design codes consider the influence of soil characteristics on the response spectrum, such influence can be represented better through the site-specific site response analysis. The later application is suggested when the safety of a structure is crucially important (e.g. nuclear power plant) or when the soil deposits consist of soft soil materials. In EC8 soil classes B and C are regarded as stiff soils (stiffness levels are reducing from B to C) and soil class D is regarded as soft soil. However, the suitability of design response spectra for not only soil class D but also soil classes C and B are in question (Pitilakis *et.al.*, 2012). This will favour the use of site response analysis in the nonlinear dynamic analysis of buildings.

The site response analyses can be conducted via frequency domain equivalent linear (EQL) or time domain nonlinear (NL) methods with total or effective stress approaches. The EQL method makes use of the exact continuum solution of wave propagation in horizontally layered visco-elastic materials subjected to vertically propagating transient motions (Roesset, 1977). It models the nonlinear variation of soil shear modulus (G) and damping (D) with shear strain through a sequence of linear analyses with iterative update of stiffness and damping parameters (Kramer, 2014). The analysis is performed adopting a total stress approach. In contrast, NL approaches used in conjunction with a numerical time integration scheme and an effective stress approach are capable of fully capturing soil nonlinearity, pore water pressure build-up and consolidation settlements induced by the earthquake. Although the EQL approximation is simpler and time effective, the NL approach may yield more accurate results. In particular, the benefit of time domain NL schemes can be fully appreciated when the site is shaken by a strong seismic motion (e.g. Elia (2014)).
This paper studies the influence of three different ideal soil deposits (with soil types B, C and D) on the response of the nonlinear one-bay building. By complying with the EC8 prescription, seven outcrop input motions and surface input motions are scaled. Outcrop input motions are firstly processed through the soil deposits conducting nonlinear site response analysis then applied to the fixed base structural model while the surface input motions are directly applied to the model. This paper proceeds by briefly describing the soil and building models. Subsequently, the scaled input motions are described. This is followed by the results and discussions. Finally, the summary of the study is presented with the outcomes.

2. FE SOIL MODELS

An ideal soft clay soil deposit with 50 m depth and 5 m width is modelled in the fully-coupled finite element code SWANDYNE II (Chan, 1995). The soil column is discretised by 250, 1×1 m isoparametric quadrilateral finite elements with 8 solid nodes and 4 fluid nodes (Figure 5.1). This mesh generation ensures that the seismic wave transmission is represented accurately through the FE soil model (Bathe and Saunders, 1984). During the dynamic analyses, the bottom of the mesh is assumed rigid at the bedrock, while the nodes along the vertical sides are characterized by the same displacements (i.e. tied-nodes lateral boundary conditions). The modified input motions are directly applied to the solid nodes at the base of the mesh as prescribed horizontal displacement time histories. The dynamic simulations are carried out with a time step corresponding to that of the earthquake input signals.
The advanced soil model *RMW* (Rouainia and Muir Wood, 2000) is employed to simulate the dynamic soil behaviour during the nonlinear site response analyses. *RMW* has been successfully employed to predict the dynamic performance of different earth structures (Elia and Rouainia, 2012; Elia and Rouainia, 2014) as it can

capture early irreversibility, accumulation of pore pressure, stiffness degradation and damping ratio curves and the destructuration of soil under undrained conditions. In this work, the soil material parameters are determined by conducting a series of undrained cyclic simple shear test simulations under controlled strain levels in order to produce normalised shear modulus (Vucetic and Dobry, 1991). In the dynamic simulations performed with SWANDYNE II, only 2%, 3% and 5% of Rayleigh damping for soil class D, C and B are introduced. This is to ensure that the propagation of spurious high frequencies are avoided and the model underestimation of damping in the small-strain range is compensated (Kwok *et. al.*, 2008).

The initial stiffness profiles of the soil deposit are obtained using the equation proposed by (Viggiani and Atkinson, 1995) for the dependency of the small-strain shear modulus, G_0, on the mean effective stress and overconsolidation ratio. In particular, the dimensionless stiffness parameter *A* is changed in a way that the shear wave velocity at the top 30 m is consistent with the soil classes D, C and B for which A equals to 1050, 6500 and 16000, respectively. Additionally, *m* and *n* in the equation, which depend on the plasticity index, are set equal to 0.27 and 0.84, respectively. In the initialisation phases of the FE models, an overconsolidation ratio of 1.5 is assumed constant with depth. The resulting shear wave velocity profiles have an average value at the top 30 m of the soil column equal to 140, 345 and 540 m/s, thus classifying the deposit as a soil class of D, C and B according to EC8. Accordingly, the first natural periods (T_1) of the deposits are equal to 1.17, 0.47 and 0.3 s, respectively.

Table 1. *RMW* model parameters calibrated against the nonlinear curves given by Vucetic and Dobry (1991).

The model parameter	**λ***	**κ***	**M**	**N**	**R**	**A**	**B**	**H**	**k**	**Ψ**	**r_o**
	0.252	0.0297	1.35	0.22	0.1	0.494	8	0.0	0.5	1	1.75

3. BUILDING MODEL

One-bay frame building model given as an OpenSees example (PEER, 2006) with 11 m height and 12.8 m width is used. The model base nodes are fixed for the displacements and are freed for the rotation. The frame nodes are free to displace and rotate. Beam and column elements are allowed to accommodate nonlinear behaviours while concrete and steel units of the reinforced concrete sections are defined as one single material. From the eigenvalue analysis, the fundamental period of the model is found to be 1.17 s. Two additional periods are considered by changing the mass of the building. This is to observe the influence of the value of fundamental period on the drift response.

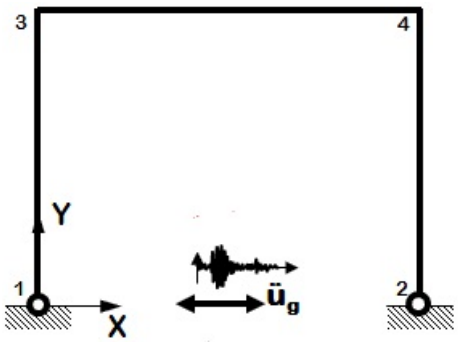

Figure 1. One-bay, one-storey structural model adapted in this study.

4. MODIFICATION OF INPUT MOTIONS

The seven surface input motions recorded on soil classes D, C and B and those at outcrops are modified to the associated EC8 design response spectra at 0.15g and 0.35g seismic intensity levels by using a computer program REXEL (Iervolino *et.al.*, 2010). Since this study is considering ideal soil sites, magnitude and distance

hazard contributions are selected to cover most of the earthquake recordings in the European Strong-motion Database (ESM). The input motions are scaled in such a way that the mean of seven input motions is within the 10% lower limits and 30% upper limits of the target response spectra (shown in Figure 1 and Figure 2). The modified surface input motions are directly applied to the building model while the modified outcrop input motions are firstly propagated through the soil models, then, applied to the building model. It should be noted in here that processing the outcrop input motions through the soil deposits causes the spectral values to be underpredicted at periods less than 0.3 s (seen in Figure 2). This is more apparent at the higher seismic intensity level (i.e. 0.35g) attributing probably to the induced higher strains. Nevertheless, the nonlinear ground response analyses lead to better spectral predictions above the period of 0.3 s. These results are in line with the literature (Kaklamonus, 2013) and cannot bias the research as the periods of the building model are well above the underpredicted region in the spectral response curves.

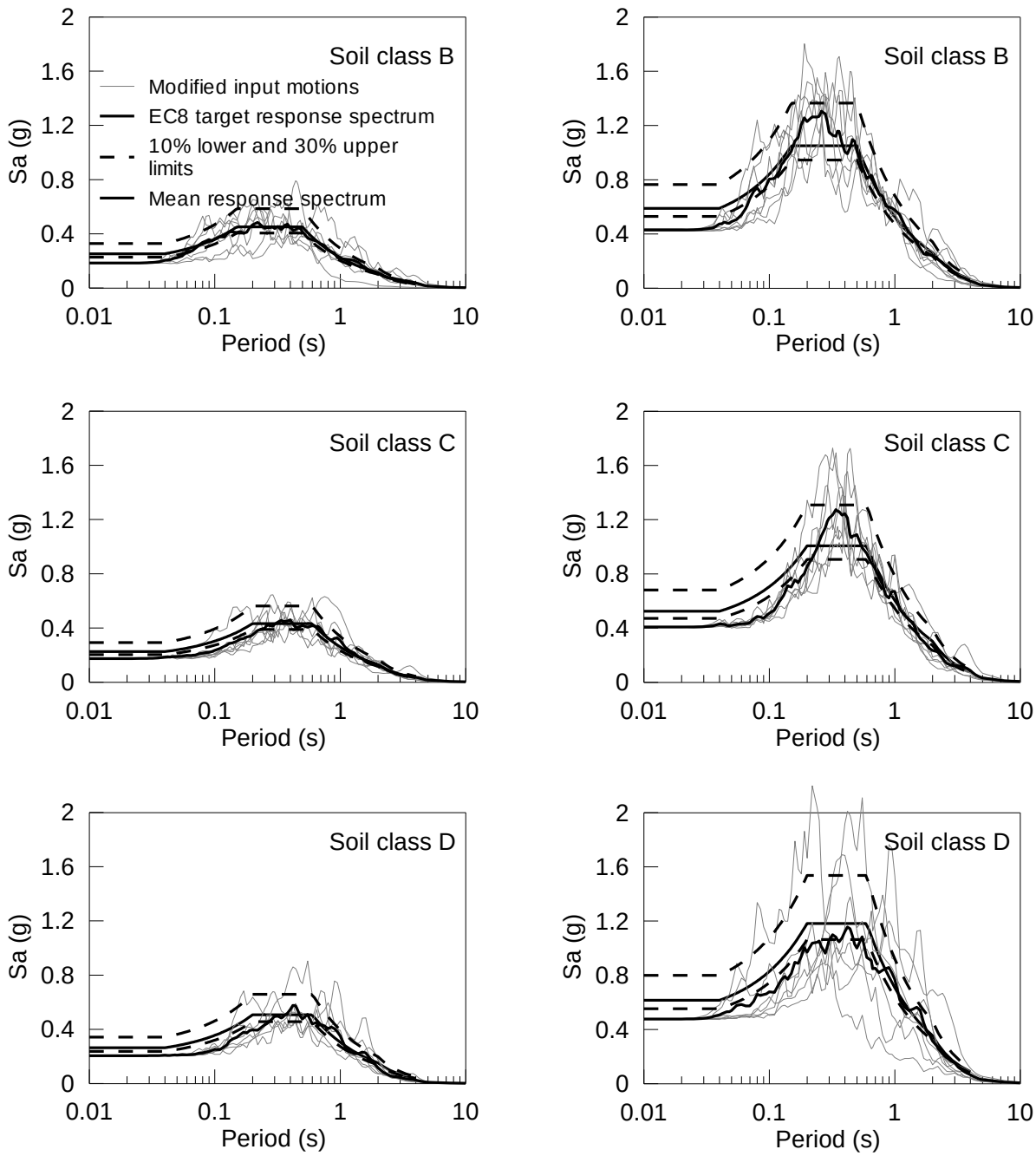

Figure 1. Spectral responses of seven modified surface input motions to the EC8 target response spectra for soil classes B, C and D at 0.15g (left figures) and 0.35g (right figures) seismic intensity levels.

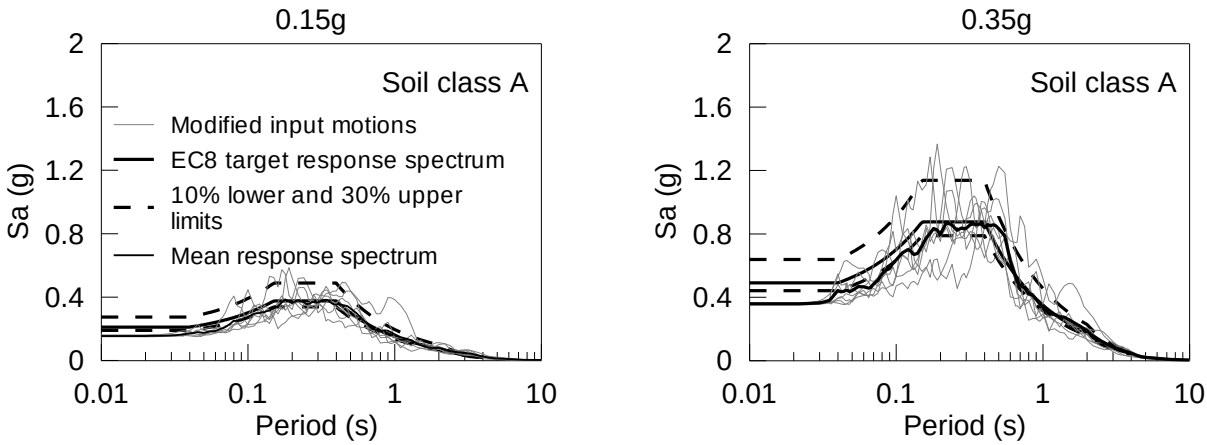

Figure 2. Spectral responses of seven modified outcrop input motions to the EC8 target response spectra of soil class A at 0.15g and 0.35g seismic intensity levels.

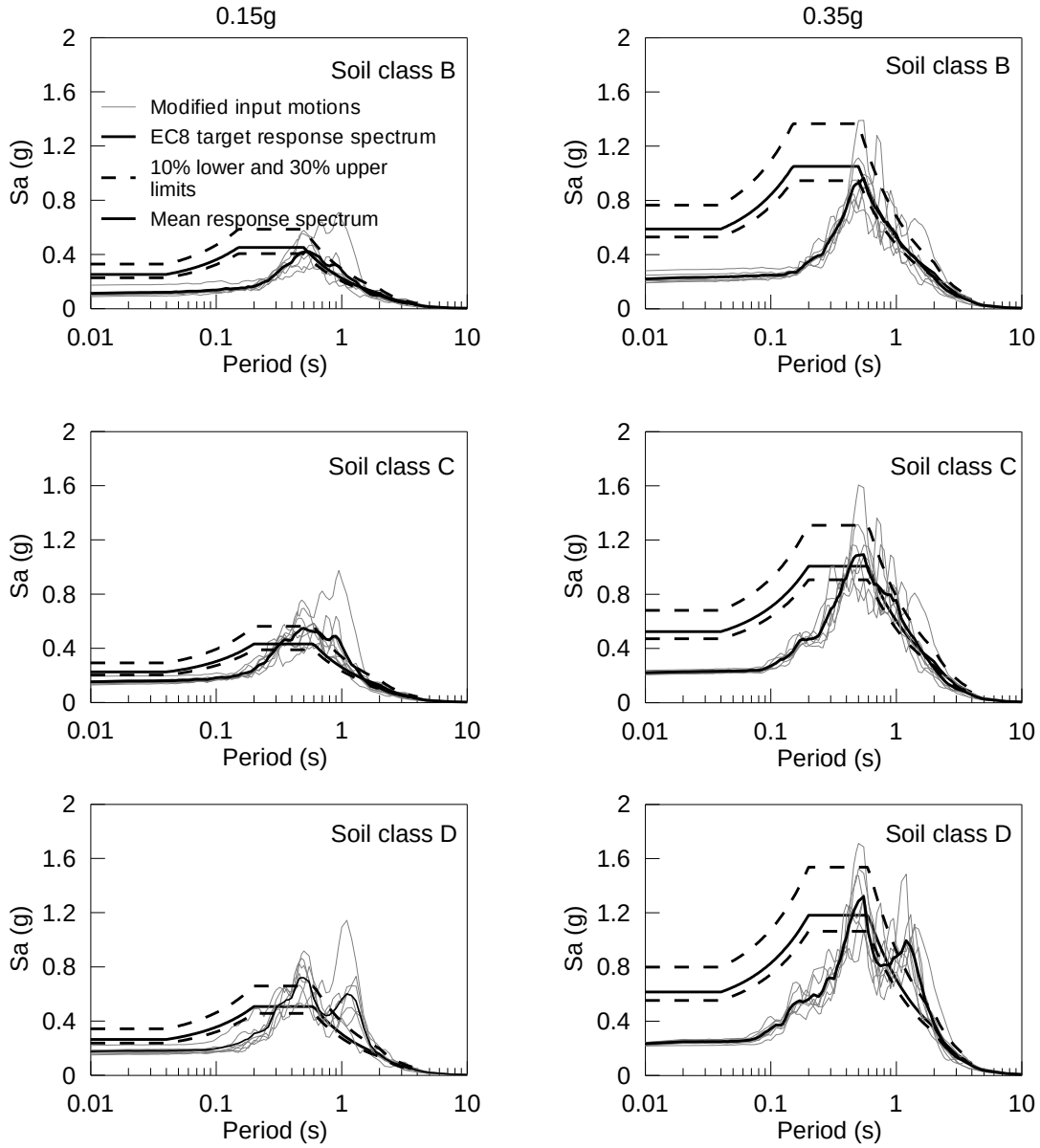

Figure 3. Spectral responses of processed input motions at 0.15g (left figures) and 0.35g (right figures) seismic intensity levels through the soil deposits classified with class B, C and D according to EC8 criterion.

5. RESULTS

The response of nonlinear one-storey one-bay structure model with first mode period of 1.17 s under modified input motions is represented in terms of drift response. Figure 4a and Figure 4b show the drift responses under processed outcrop input motions (Case 1) based on EC8 target response spectra of soil classes B, C and D. Figure 4c and Figure 4d indicate the responses of the model under modified surface input motions recorded on soil classes B, C and D (Case 2). Additionally, Figure 5a and Figure 5b compares the medians of drift responses in Case 1 and Case 2 followed by the standard deviation comparisons in Figure 5c and Figure 5d.
The drift responses in both Case 1 and Case 2 show increases from stiffer soil (i.e. soil type B) to relatively softer soil (i.e., soil type D) with different levels of scatter. This is due to the fact that EC8 considers the influence of soil deposits on the spectral responses by introducing soil factor for each soil type. Since the softer soils has more impact on the spectral responses at the surface than the stiffer soils, given soil factor by EC8 for softer soils is greater than stiffer soils. This means that the EC8 target response spectrum for soil class D has the greatest spectral values followed by the spectrum for soil type C and B, respectively. Hence, selected input motions for soil class D cause, overall, larger drift responses, after that soil class C and soil class B. It is also obvious that the responses are higher at 0.35g seismic intensity level than at 0.15g seismic intensity level, as can be depicted from Figure 4a and Figure 4b or from Figure 4c and Figure 4d.

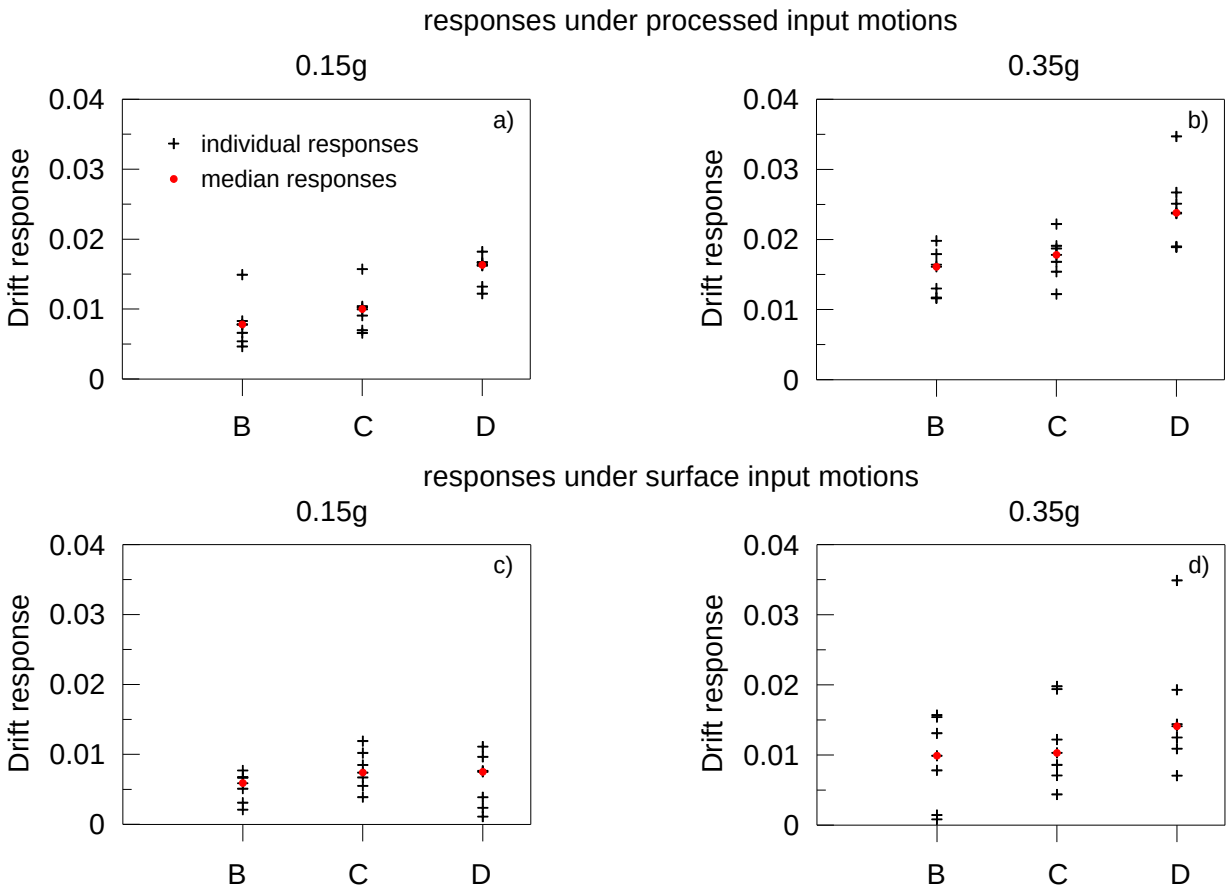

Figure 4. Drift responses of the building model with 1.17 s of first mode period on top of the ideal sites with soil classes B, C and D under; processed input motions (a, b) and surface input motions (c, d) at 0.15g and 0.35g seismic intensity levels.

Figure 4 also indicates that the median responses in Case 1 are greater than those obtained in Case 2. This is shown apparently in Figure 5a and in Figure 5b for the three types of soils. In terms of standard deviations (std), modified surface input motions always lead to drift responses whose std is higher than those obtained

under processed input motions at the higher seismic intensity level and at all soil types. However, this is not quite valid in case of the lower seismic intensity level, especially at soil types B and C.

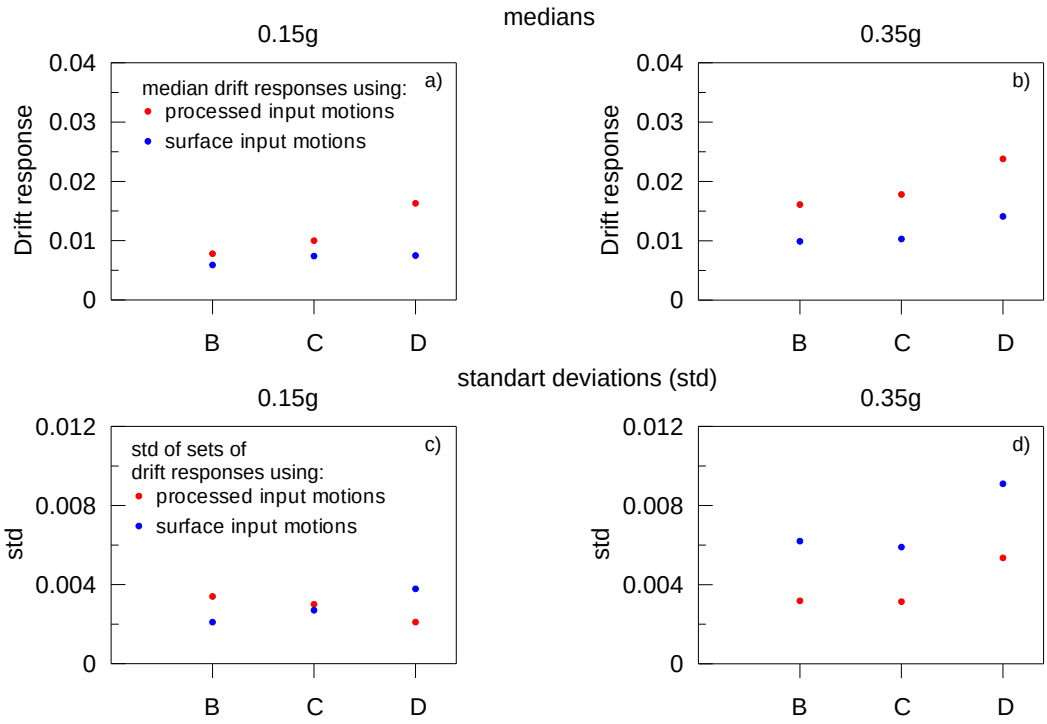

Figure 5. Comparisons of medians (a, b) and standard deviations (c, d) of the sets of drift responses shown in Figure 4 for three different soil types at 0.15g and 0.35g seismic intensity levels.

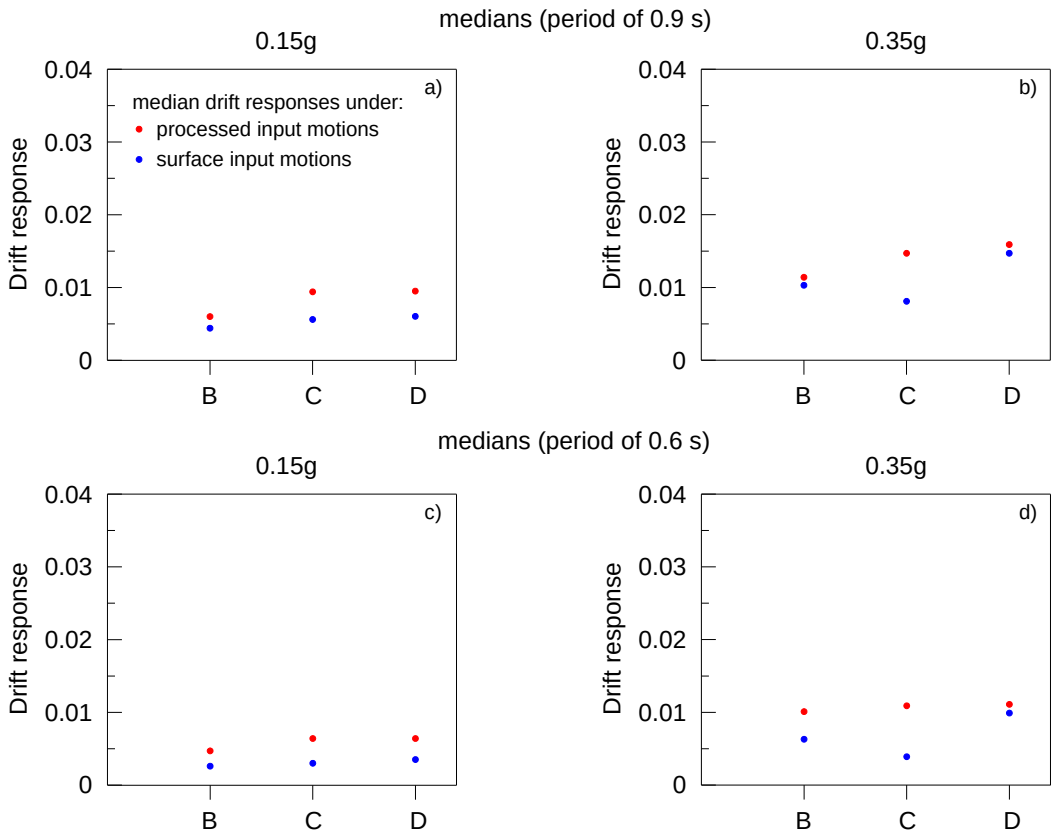

Figure 6. Comparisons of median drift responses of building models with first mode periods of 0.9 s (a, b) and 0.6 s (c, d) under processed input motions and surface input motions.

Additionally, building models with first mode periods of 0.9 s and 0.6 s are analysed under the processed and surface input motions, as seen in Figure 6 (a, b) and Figure 6 (c, d), respectively. It is, again, clear that the median drift responses under processed input motions are larger than those attained from the surface input motions for all three types of soils at both seismic intensity levels. The trend of drift responses getting greater towards the softer soil type is also observed in both building models, attributing to the soil factor given in EC8 being higher for softer soils.

Figure 7 indicates median drift responses of the building models with three different first mode periods, 1.17 s, 0.9 s and 0.6 s under processed (a, b) and modified surface (c, d) input motions. The higher the building period, the larger the median drift response is experienced by the model for each soil class and at both seismic intensity levels.

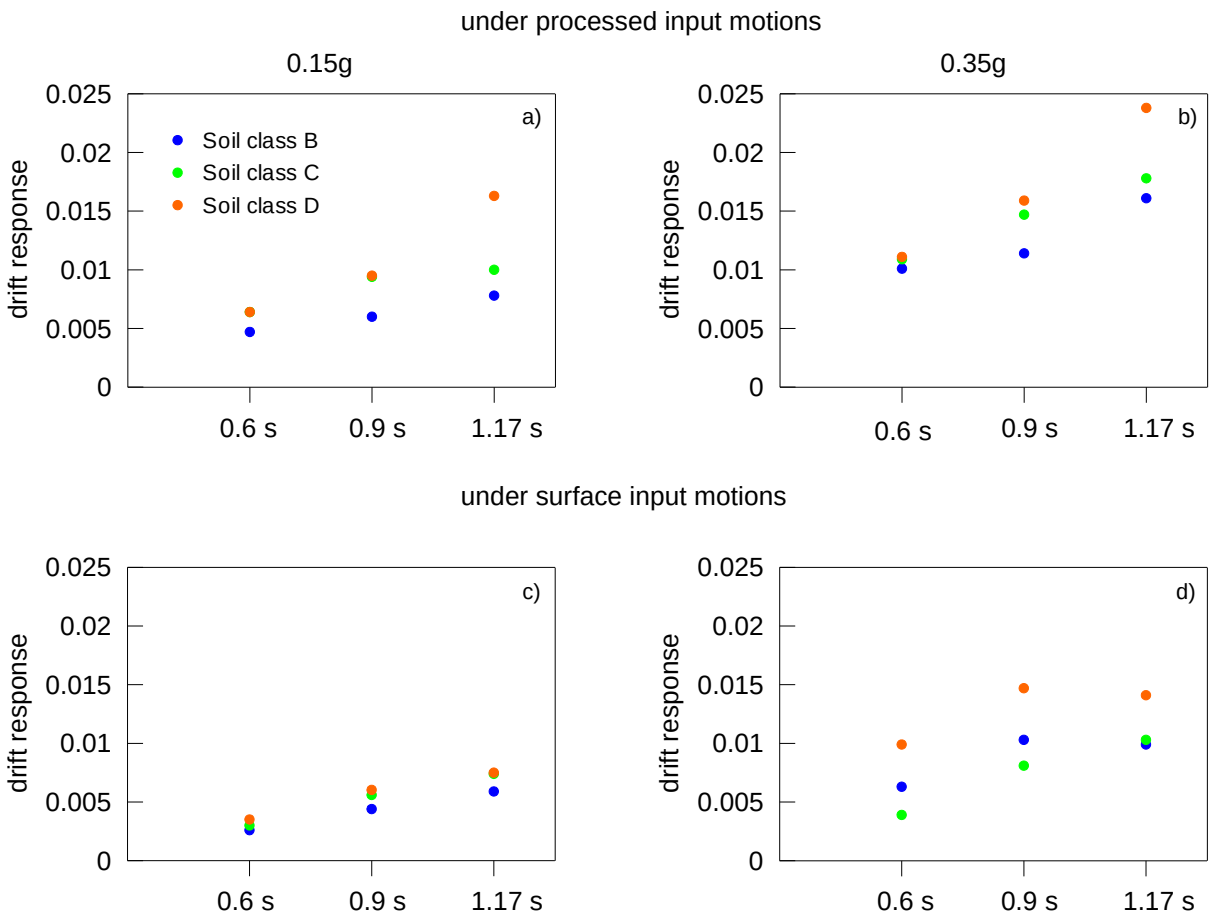

Figure 7. Median drift responses of building models with 0.6 s, 0.9 s and 1,17 s periods on top of the soil types of B, C and D under processed and surface input motions at 0.15g and 0.35g seismic intensity levels.

6. CONCLUSIONS

Selection and modification of input motions has crucial role in seismic design or retrofitting of buildings. This work focuses on the performance of one-bay one storey structure on three different soil classes (soil classes, B, C and D, according to EC8) and under input motions categorized into two groups. While the first group of input motions are directly selected and modified, second group includes input motions processed through the ideal soil deposits by conducting nonlinear site response analyses. The results can be briefly summarised as follows;

1. Processed input motions always leads to higher drift response at both seismic intensity levels than those from surface input motions.
2. Building models on softer soil deposits are exposed to higher drift responses

3. Processed input motions causing less level of standard deviation of drift responses implies this method is more efficient than the use of directly selected and modified input motions

While the results of this study shows good indication for the implementation of input motions and the involvement of the site response analysis, it can be more comprehensive and complement with modelling proper building models with different periods. In addition, sensitivity analysis can be operated in terms of the number of input motions to be considered in seismic performance analysis of buildings with the inclusion of the response analysis.

REFERENCES

Ancheta, T.D., Darragh, R.B., Stewart, J.P., Seyhan, E., Silva, W.J., Chiou, B.S.J., Wooddell, K.E., Graves, R.W., Kottke, A.R. and Boore, D.M. (2013) 'PEER NGA-West2 Database, PEER Report 2013/03, Pacific Earthquake Engineering Research Center', *University of California, Berkeley*.

A. Chan (1995). *User Manual for DIANA-SWANDYNE II*. University of Birmingham.

Ancheta, T.D., Darragh, R.B., Stewart, J.P., Seyhan, E., Silva, W.J., Chiou, B.S.J., Wooddell, K.E., Graves, R.W., Kottke, A.R. and Boore, D.M. (2014) 'NGA-West2 database', *Earthquake Spectra*, 30(3), pp. 989-1005.

Bathe, K.J. and Saunders, H. (1984). 'Finite element procedures in engineering analysis'. American Society of Mechanical Engineers.

CEN (2005). 'Eurocode 8: Design of structures for earthquake resistance–Part 1: General rules, seismic actions and rules for buildings'. CEN Brussels.

Elia, G. and Rouainia, M. (2012). 'Seismic performance of earth embankment using simple and advanced numerical approaches', *Journal of Geotechnical and Geoenvironmental Engineering*, 139(7), pp. 1115-1129.

Elia, G. and Rouainia, M. (2014). 'Performance evaluation of a shallow foundation built on structured clays under seismic loading', *Bulletin of earthquake engineering*, 12(4), pp. 1537-1561.

Hancock, J., Watson-Lamprey, J., Abrahamson, N.A., Bommer, J.J., Markatis, A., McCoy, E. and Mendis, R. (2006). 'An improved method of matching response spectra of recorded earthquake ground motion using wavelets', *Journal of earthquake engineering*, 10(spec01), pp. 67-89.

Iervolino, I. and Cornell, C.A. (2005). 'Record selection for nonlinear seismic analysis of structures', *Earthquake Spectra*, 21(3), pp. 685-713.

Iervolino, I. and Manfredi, G. (2008). 'A Review of Ground Motion Record Selection Strategies for Dynamic Structural Analysis', in Bursi, O.S. and Wagg, D. (eds.) *Modern Testing Techniques for Structural Systems*. Springer Science & Business Media, pp. 131-163.

Iervolino, I., Galasso, C. and Cosenza, E. (2010). 'Rexel: computer aided record selection for code-based seismic structural analysis', *bulletin of earthquake engineering*, 8, pp. 339-392.

Kaklamanos, J., Baise, L.G., Thompson, E.M. and Dorfmann, L. (2015). 'Comparison of 1D linear, equivalent-linear, and nonlinear site response models at six KiK-net validation sites', *Soil Dynamics and Earthquake Engineering*, 69, pp. 207-219.

Kottke, A. and Rathje, E.M. (2008). 'A semi-automated procedure for selecting and scaling recorded earthquake motions for dynamic analysis', *Earthquake Spectra*, 24(4), pp. 911-932.

Kramer, S.L. (1996). Geotechnical Earthquake Engineering. Prentice Hall, Upper Saddle River, N.J.

Kwok, A.O., Stewart, J.P., Hashash, Y.M., Matasovic, N., Pyke, R., Wang, Z. and Yang, Z. (2007). 'Use of exact solutions of wave propagation problems to guide implementation of nonlinear seismic ground response analysis procedures', *Journal of Geotechnical and Geoenvironmental Engineering*, 133(11), pp. 1385-1398.

Mazzoni, S., McKenna, F., Scott, M.H. and Fenves, G.L. (2006). The open system for earthquake engineering simulation (OpenSEES) user command-language manual.

Mazzoni, S., Hachem, M. and Sinclair, M. (2012) *Conference Proceedings, 15th World Conference on Earthquake Engineering*.

PEER (2006). OpenSees: Open system for earthquake engineering simulation, Pacific Earth-quake Engineering Research Center, University of California, Berkeley, CA.

Pitilakis, K., Riga, E. and Anastasiadis, A. (2012) 'Design spectra and amplification factors for Eurocode 8', *Bulletin of Earthquake Engineering*, 10(5), pp. 1377-1400.

Rathje, E.M., Kottke, A.R. and Trent, W.L. (2010) 'Influence of input motion and site property variabilities on seismic site response analysis', *Journal of geotechnical and geoenvironmental engineering*, 136(4), pp. 607-619.
Rey, J., Faccioli, E. and Bommer, J.J. (2002) 'Derivation of design soil coefficients (S) and response spectral shapes for Eurocode 8 using the European Strong-Motion Database', *Journal of seismology*, 6(4), pp. 547-555.

Rouainia, M. and Muir Wood, D. (2000) 'A kinematic hardening constitutive model for natural clays with loss of structure', *Géotechnique*, 50(2), pp. 153-164.

Roesset, J.M. (1977) 'Soil amplification of earthquakes', *Numerical methods in geotechnical engineering*, pp. 639-682.

Seismosoft (2016) *"SeismoMatch 2016 – A computer program for spectrum matching of earthquake records," available from http://www.seismosoft.com*.

Shome, N., Cornell, C.A., Bazzurro, P. and Carballo, J.E. (1998) 'Earthquakes, records, and nonlinear responses', *Earthquake Spectra*, 14(3), pp. 469-500.

Stewart, J.P. and Kwok, A.O. (2008) 'Nonlinear seismic ground response analysis: code usage protocols and verification against vertical array data', *Geotechnical Engineering and Soil Dynamics IV, ASCE Geotechnical Special Publication No. 181*, 181.

Tönük, G., Ansal, A., Kurtuluş, A. and Çetiner, B. (2014) 'Site specific response analysis for performance based design earthquake characteristics', *Bulletin of Earthquake Engineering*, 12(3), pp. 1091-1105.

Viggiani, G. and Atkinson, J.H. (1995) 'Stiffness of fine-grained soil at very small strains', *Géotechnique*, 45(2), pp. 249-265.

ESTIMATION OF CODA WAVE ATTENUATION IN THE ALGIERS AREA

Benkaci N.[1], Airouche A.[1] and Abbes K. [1]

[1] *Centre National de Recherche Appliquée en Génie Parasismique (CGS), Rue Kaddour Rahim Prolongée Hussein Dey, BP 252, Alger 16040, Algérie*
Email: nbenkaci@cgs-dz.org ; benkaci.nassima@gmail.com

ABSTRACT:

The single backscattering model was used to estimate attenuation of coda waves (Q_c) of local earthquakes recorded on three seismic stations in the north of Algeria surrounding Algiers the capital city. We estimated Q_0 and n parameters of the frequency dependent coda-Q using the relation $Q_c = Q_0 f^n$. The used earthquakes were recorded during the 21st May 2003 Boumerdes earthquake (M_w=6.9) by three permanent accelerometric stations located respectively in Keddara, Boumerdes and Dar El Beida. This work is the first of its kind in Algeria and is considered as a preliminary study, which will be extended to other stations in the future. The database was composed of local earthquakes with local magnitude from 2.3 to 4.1. The average frequency dependence of Q_c for the whole area has been estimated by using the $Q_0 f^n$ relation as $57.2f^{0.90}$ for the North-South direction, $56.7f^{0.92}$ for the East-West direction and $70.7f^{0.81}$ for the Vertical direction. The average Q_c values estimated and their frequency dependent relationships correlate well with a highly heterogeneous and highly tectonically active region. The results show also that the attenuation is smaller in the vertical direction compared to the horizontal one in Boumerdes station ($Qc_{EW}(f) = 53.32f^{0.96}$, $Qc_{NS}(f) = 55.44f^{0.94}$, $Qc_Z(f) = 49.95f^{0.98}$), whereas the opposite is observed in Dar El Beida ($Qc_{EW}(f) = 53.24f^{0.92}$, $Qc_{NS}(f) = 56.37f^{0.92}$, $Qc_Z(f) = 67.56f^{0.82}$) and Keddara sites ($Qc_{EW}(f) = 55.64f^{0.88}$, $Qc_{NS}(f) = 48.83f^{0.88}$, $Qc_Z(f) = 87.75f^{0.64}$).

KEYWORDS: Coda waves, attenuation, Boumerdes earthquake, Algeria

1. INTRODUCTION

The evaluation and prediction of strong ground motions by studying the seismic hazard deal with two physical processes, seismic sources and wave propagation. Wave attenuation is one of the properties, which are essentials for seismic hazard mapping.

Generally, seismic attenuation expresses the decrease in the amplitude of seismic waves with increasing distance from the source. Attenuation due to scattering (Q^{-1}) is an elastic process in which the energy is distributed by reflection, refractions and conversion of the incident wave to other waves.

The continuous wave trains following the incident P and S waves are known as coda waves, due to seismic wave scattering in the inhomogeneities existing in the propagation media (Aki, 1969; Sato and Fehler, 2008; Sato et al., 2012). Coda waves of local earthquakes can be considered as back-scattered S-waves (Aki, 1980), their decay Q_c is the quality factor which expresses absorption and scattering attenuation effects following the single scattering theory.

The attenuation function Q_c is very useful in Earth structure modeling, it is applicable to the assessment of seismic hazard studies, add to this the attenuation is one of the basic physical parameters that are related to the seismicity and the regional tectonic activity of an area. In engineering seismology field, attenuation can be used also for strong ground motion prediction. Many studies are carried out worldwide that contribute in an important Q_c database which describes tectonically active zones around the world. The quality factor of the coda wave, has been estimated for different parts of the world (Aki and Chouet, 1975; Sato, 1977; Tselentis, 1998; Bianco et al., 2002; Ugalde et al., 2002; Tripathi and Ugalde, 2004; Ma'hood, M., & Hamzehloo, H, 2009, Pezzo et al., 2011, Morsy et al., 2014, Rajabi Baniani et al., 2014, Farrokhi et al., 2015, Kumar et al., 2016, Singh et al., 2017).

Our study is considered as a first in this field carried for the context of Algeria, the coda attenuation properties are estimated in the North of Algeria using local earthquakes and aftershocks from the 21st May 2003 Boumerdes earthquake.

2. METHODOLOGY

The single backscattering model, proposed by Aki and Chouet (1975), is often used for describing the behavior of the coda waves from local earthquakes. According to this model, the coda waves are interpreted as backscattered body waves generated by randomly distributed heterogeneities in the earth's crust and upper mantle. The coda amplitudes, *A(f,t)*, in a seismogram can be expressed for a central frequency (*f*) over a narrow band width signal, as a function of the lapse time (*t*), measured from the origin time of the seismic event, as:

$$A(f,t) = S(f)t^{-\alpha}\exp\left[-\frac{\pi f t}{Q_c(f)}\right] \quad (1)$$

Where *S(f)* is the source function at frequency *f*. It has been stated that the coda spectrum of small earthquakes at local distances is independent of earthquake size, epicentral distance, and the path between station and epicenter, but it depends on lapse time from the origin time of the earthquake (Aki and Chouet1975; Sato1977; Phillips and Aki1986). This suggests that the coda part of the seismogram is due to an average scattering effect of the medium in the region near the source and station (Kumar et al.2005).α is the geometrical spreading factor, and it is considered as 1 for body waves, and *Qc* represents the quality factor of coda waves. Equation1 becomes

$$ln[A(f,t)t] = c - bt,\ c = \ln\,[S(f)],\ \text{and}\ b = \frac{\pi f}{Q_c(f)} \quad (2)$$

The source factor is considered as a constant for a single frequency, according to Eq.2, the slope of the straight line fitting the measured $ln[A(f,t)t]$ versus *t* gives a *Qc* value for a considered frequency. Equation 2 is obtained for $t > 2t_S$, where t_S is the S-wave travel time (Rautian and Khalturin1978).
Qc is dependent on frequency and follows the law:

$$Q_c(f) = Q_0\left[\frac{f}{f_0}\right]^n \text{and}\ Q_c = Q_0 f^n \quad (3)$$

Where Q_0 is the value of *Qc* at $f_0 = 1$ Hz and *n* is a numerical constant (Singh and Herrmann1983).
The data used in this study are accelerograms, that are bandpass-filtered for 7 frequency bands centered at 1.5, 3, 6, 8, 12, 18, and 24 Hz. A ratio signal to noise (SNR) is calculated by taking a minimum window of 1 second before the onset of *p* waves in order to determine the end of coda window from the signal, in our study we have delimited the end of coda window by SNR>2. We used a window of 20 to 30 second length depending on each signal, it were shifted by one second at a time, simultaneously for each direction of the accelogram. To every estimated *Qc* we associated the lapse time of the middle of the time window T_L. The envelope of the amplitudes $A(f,t)$ was computed for each coda window, from the Hilbert transformed accelerogram, and then smoothed for each central frequency. The envelope was computed for the three directions (East-West, North-South, and Vertical). The logarithm of Eq.(3) allows us to estimate *n* and Q_0 using linear regression on relation

$$log[Q_c(f)] = \log(Q_0)\, nlog(f) \quad (4)$$

Q_c is calculated from the slope β of the fitted line of the regression:

$$Qc = -\frac{\pi f}{\beta} \quad (5)$$

Q_c is rejected in case the error > 0.75.

3. DATA

data used are collected from the 21 may 2003 Boumerdes earthquake recorded from several stations. In our study three sites are chosen (Dar El Beida, Boumerdes and Keddara). These stations are located in the epicentral area, within a perimeter < 100 kilometers, and the signals are selected with a ratio signal to noise SNR > 2. All the events have been located and the obtained parameters are : time, latitude, longitude, depth, magnitude and epicentral distance. A total of 29 events are used in this study.

4. RESULTS AND DISCUSSION

The analysis results of North Algeria coda wave attenuation characteristics is described and discussed in this section. A regression analysis is carried out for the three sites concerning this study. All the coda wave parameters are shown in the figures 1 to 3 for all sites and for the three directions, given with a standard deviation and the correlation factor *R*.
A mean of Q_c values is calculated for the studied region, the characteristics of the coda attenuation are summarized in table 1 for three directions. The Q_c mean values of the studied region are shown in figure 4 represented in three directions, given with a standard deviation and the correlation factor *R*.
In this study, we have used events from CGS (national research center applied on aerthquake engieering, Algiers, Algeria) accelerometric array, with good signal to noise ratio. The selected data are recorded during the 21 May 2003 Boumerdes earthquake (Mw 6.9). The study site is located in East part of the Mitidja basin, known as seismically active zone due to presence of many active faults from Holocene age.

Table 1. Characteristics of the coda mean attenuation for Dar El Beida, Boumerdes and Keddara sites in the three directions EW, NS et Z.

	Dar El Beida		**Boumerdes**		**Keddara**	
	Q_0	**n**	**Q_0**	**n**	**Q_0**	**n**
EW	53,24	0,92	53,32	0,96	55,64	0,88
NS	56,37	0,92	55,44	0,94	48,83	0,88
Z	67,56	0,82	49,95	0,98	87,75	0,64

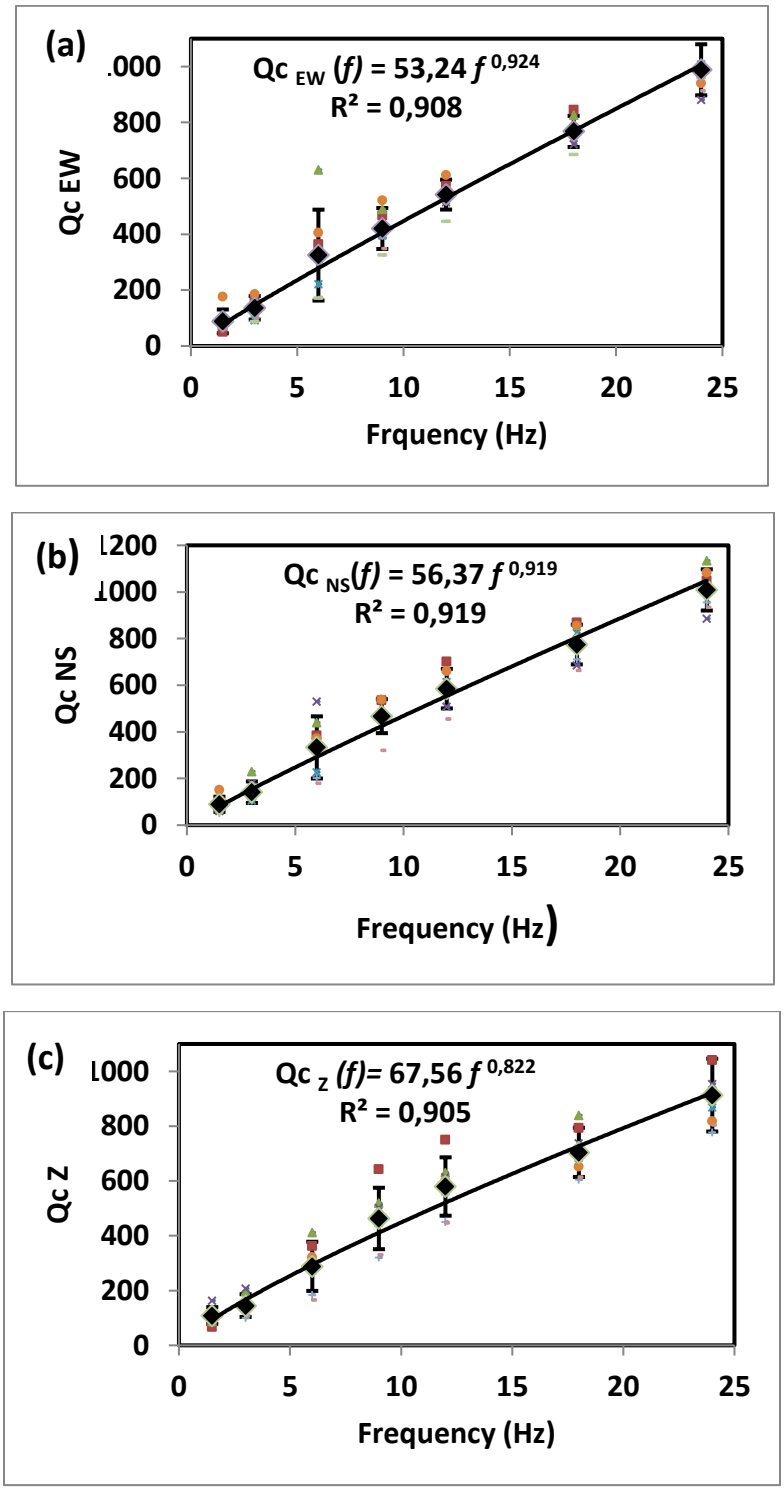

Figure 1. The frequency distribution of measured *Qc* (diamonds) of Dar El Beida site calculated for all events (colored symbols) in (a)EW (b) NS (c) Z directions. The black solid line represents the regression after Eq.(4), given with its equation above the graph and the correlation factor *R* The vertical bars represent the standard deviation.

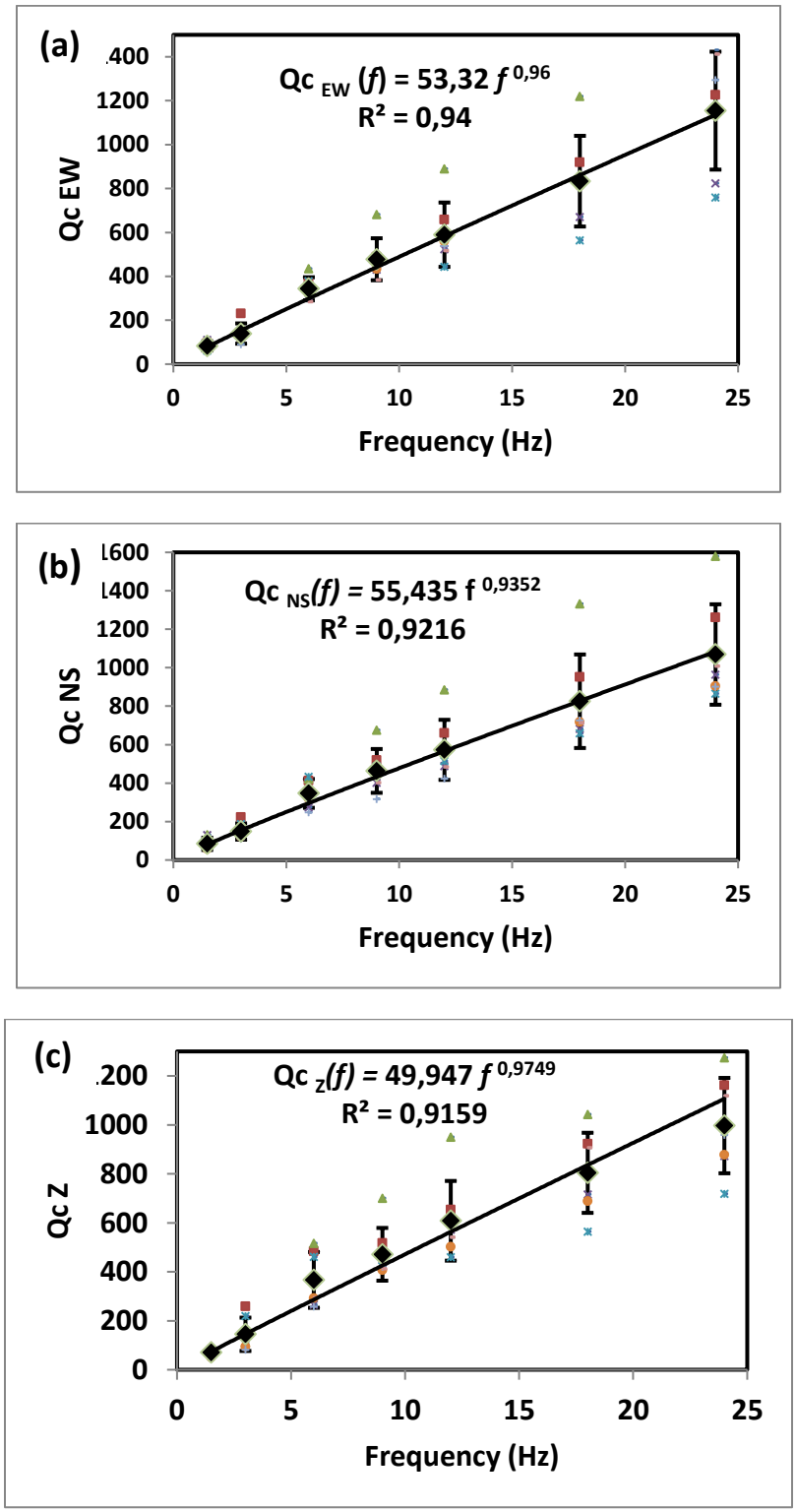

Figure 2. The frequency distribution of measured *Qc* (diamonds) of Boumerdes site calculated for all events (colored symbols) in (a)EW (b) NS (c) Z directions. The black solid line represents the regression after Eq.(4), given with its equation above the graph and the correlation factor *R* The vertical bars represent the standard deviation.

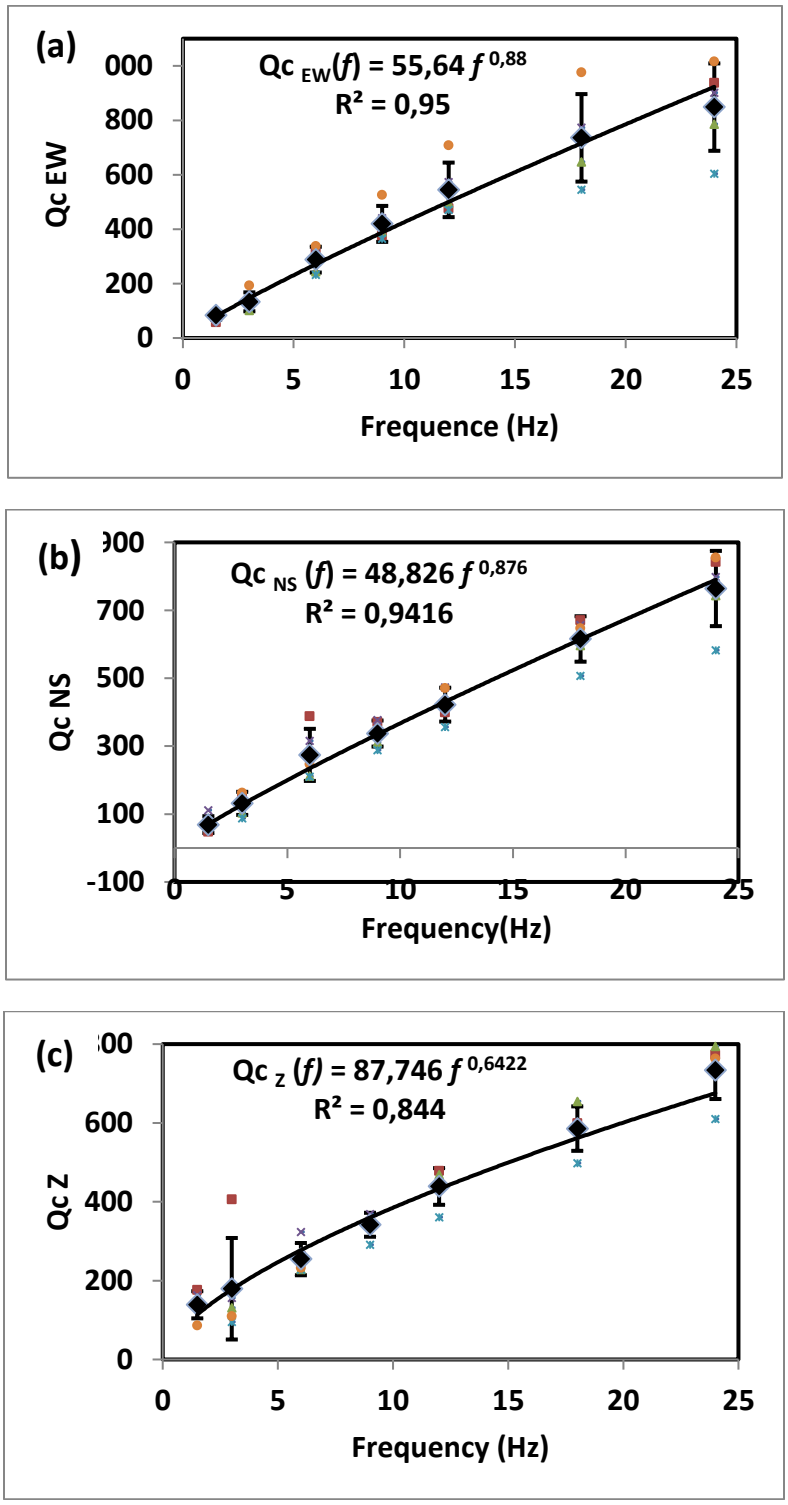

Figure 3. The frequency distribution of measured Qc (diamonds) of Keddara site calculated for all events (colored symbols) in (a)EW (b) NS (c) Z directions. The black solid line represents the regression after Eq.(4), given with its equation above the graph and the correlation factor R The vertical bars represent the standard deviation.

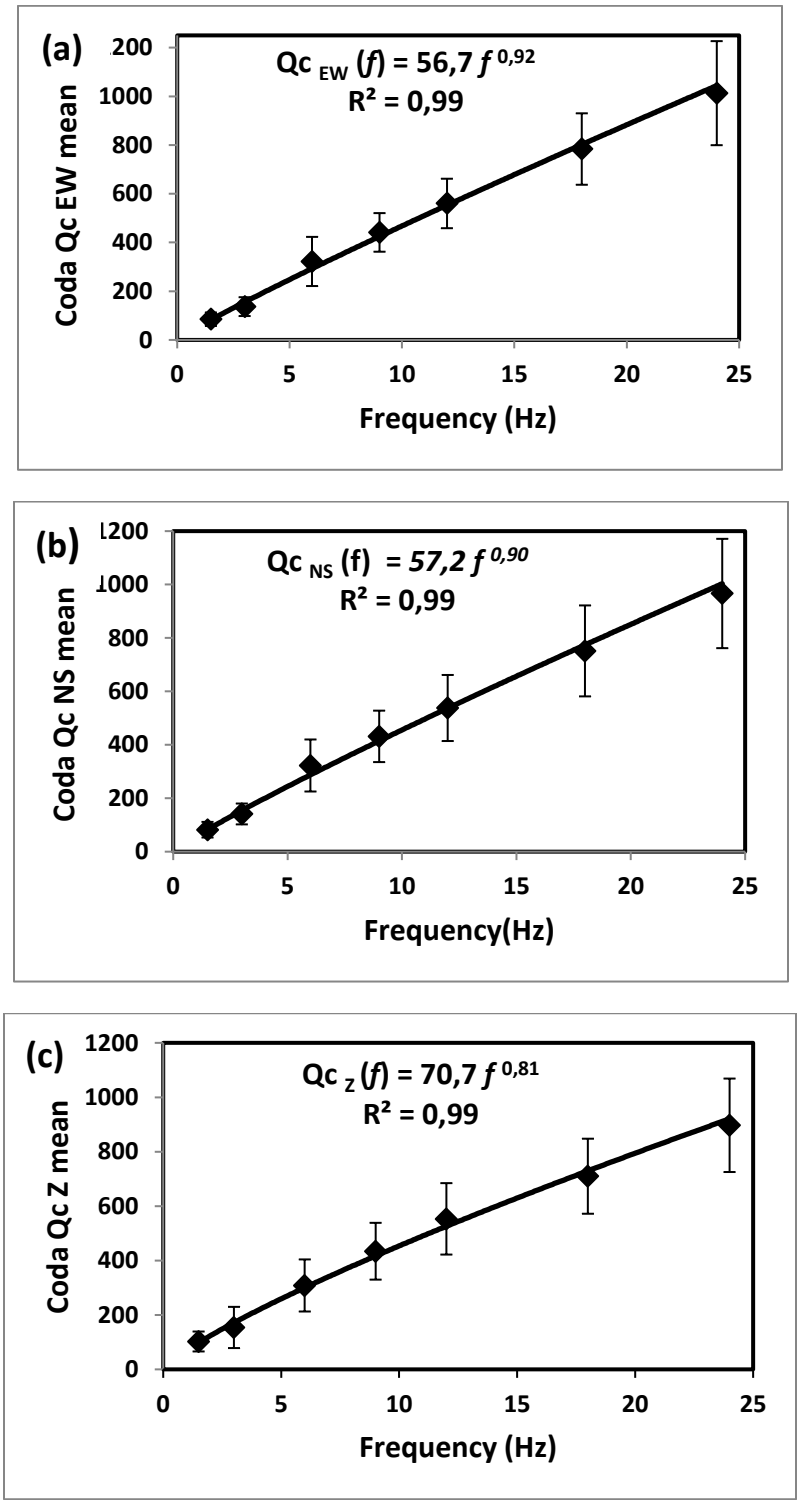

Figure 4. The frequency distribution of measured *Qc* (diamonds) of the epicentral zone in) in (a)EW (b) NS (c) Z directions. The black solid line represents the regression after Eq.(4), given with its equation above the graph and the correlation factor *R* The vertical bars represent the standard deviation.

The 21 May 2003 Boumerdes earthquake (Mw 6.9) is considered as the most destructive due to its superficial focal depth. The results of this study are considered as a first in this field and could be very useful in civil engineering design. Seismic hazard studies show that the attenuation variation depends on the frequency *f* and the geological structures.

On Dar El Beida site the attenuation parameters are equivalent in the horizontal directions and differ from those on the vertical direction ($Qc_{EW}(f) = 53{,}24\, f^{0{,}92}$, $Qc_{NS}(f) = 56{,}37\, f^{0{,}92}$ and $Qc_{Z}(f) = 67{,}56\, f^{0{,}82}$). The same trend is observed on Boumerdes site ($Qc_{EW}(f) = 53{,}32\, f^{0{,}96}$, $Qc_{NS}(f) = 55{,}435\, f^{0{,}9352}$ and $Qc_{Z}(f) = 49{,}947\, f^{0{,}9749}$) and Keddara site ($Qc_{EW}(f) = 55{,}64\, f^{0{,}88}$, $Qc_{NS}(f) = 48{,}826\, f^{0{,}876}$ and $Qc_{Z}(f) = 87{,}746\, f^{0{,}6422}$).

In comparing the attenuation in the three site we notice that the results are similar for Dar El Beida and Boumerdes in three directions (around 50 et 0.92<n<0.98) but differs from Keddaras' site especially in the vertical direction. In Keddara site, the correlation factor is smaller and the results do not correlate well, this is due to the use of short events and consequently the use of short windows for Q_0 calculation. In fact, the window length for Keddara was 10 seconds and 20 seconds for Dar El Beida and Boumerdes. Thus, the results depend on the coda window length.

The coda wave attenuation estimation in the epicentral zone for three directions NS, EW and Z are respectively $57{,}2\, f^{0{,}9}$, $56{,}7\, f^{0{,}92}$ and $70{,}7\, f^{0{,}81}$ respectively. From figures 1 to 4 we notice that the attenuation increases with frequency.

5. CONCLUSION

In this study, the quality factor Q_c and frequency dependent exponent *n* was estimated for the epicentral zone of the 21 may 2003 Boumerdes (Mw 6.9) earthquake, situated in the North-East part of the Mitidja Basin located in North of Algeria, using the single backscattering model of Aki and Chouet (1975) of coda waves envelope. Based on this study and other studies worldwide we can conclude that the studied medium is very heterogeneous. If we look at attenuation values from other regions from the world, ranged from less tectonically and seismic active to the higher, we can cite for example: Yunnan, China (Q_c=49$f^{0.95}$, Li et al.2004), Washington State (Q_c =63 $f^{0.97}$, Havskov et al. 1989), Parkfield (Q_c =79 $f^{0.74}$, Hellweg et al.1995), Zagros Iran (Q_c =99 $f^{0.84}$, Rahimi and Hamzehloo2008), S. Iberia (Q_c=100$f^{0.7}$, Pujades et al. 1991), Garhwal Himalaya (Q_c =126 $f^{0.9}$, Gupta et al. 1995), S. Central Alaska (Q_c =158 $f^{0.79}$, Dutta et al. 2004), NW Himalayan region (Q_c =158 $f^{1.05}$, Kumar et al. 2005), Koyna (Q_c =169 $f^{0.77}$, Gupta et al. 1998), and Aleutian (Q_c =200 $f^{1.05}$, Scherbaum and Kisslinger1985). The larger values ofQ_0 of more than 200 have been observed for inactive or stable regions such as New England (Q_c =460$f^{0.4}$, Pulli 1984), South India (Q_c =460 $f^{0.83}$, Ramakrishna et al.2007), North Iberia (Q_c=600$f^{0.45}$, Pujades et al. 1991), NE USA (Q_c =900$f^{0.35}$, Singh and Herrmann1983), Canadian Shield (Q_c =900 $f^{0.35}$, Hasegawa 1985), and Central USA (Q_c=1000$f^{0.2}$, Singh and Herrmann1983).

REFERENCES

Aki, K. (1969). Analysis of the seismic coda of local earthquakes as scattered waves, J. Geophys. Res.74,no. 2, 615–631.

Aki, K., Chouet, B. (1975). Origin of the coda waves: source, attenuation and scattering effects. J. Geophys. Res. 80, 3322–3342.

Aki, K. (1980). Scattering and attenuation of shear waves in the lithosphere. J. Geophys. Res. 85, 6496–6504 (View Record in Scopus|Cited By in Scopus (80)).

Bianco, F., Pezzo, D.E., Castellano, M., Ibanez, J., Luccio, F.D. (2002). Separation of intrinsic and scattering seismic attenuation in the Southern Apennine Zone, Italy. Geophys. J. Int. 150, 10–22.

Dutta U, Biswas NN, Adams DA, Papageorgiou A (2004) Analysis of S-wave attenuation in southcentral Alaska. Bull Seismol Soc Am 4:16–28. doi:10.1785/0120030072

Farrokhi, M., Hamzehloo, H., Rahimi, H., & Allamehzadeh, M. (2015). Estimation of coda-wave attenuation in the central and eastern Alborz, Iran. *Bulletin of the Seismological Society of America*, *105*(3), 1756-1767.

Gupta SC, Singh VN, Kumar A (1995) Attenuation of coda waves in the Garhwal Himalaya, India. Phys Earth Planet Inter 87:247–253. doi:10.1016/0031-9201(94)02968-H

Gupta SC, Teotia SS, Gautam N (1998) Coda Q estimates in the Koyna region, India. Pure Appl Geophys 153:713–731. doi:10.1007/s000240050216

Hasegawa HS (1985) Attenuation of Lg waves in the Canadian shield. Bull Seismol Soc Am 75:1569–1582

Havskov J, Malone S, Mc Clury D, Crosson R (1989) CodaQ for the state of Washington. Bull Seismol Soc Am 79:1024–1038

Hellweg M, Spandich P, Fletcher JB, Baker LM (1995) Stability of coda Q in the region of Parkfield, California: view from the U.S. geological survey Parkfield dense seismograph array. J Geophys Res 100:2089–2102. doi:10.1029/94JB02888

Kumar N, Parvez IA, Virk HS (2005) Estimation of coda wave attenuation for NW Himalayan region using local earthquakes. Phys Earth Planet Inter 151:243–258. doi:10.1016/j.pepi.2005.03.010

Kumar, S., Singh, P., Singh, P., Biswal, S., & Parija, M. P. (2016). Frequency dependent attenuation characteristics of coda waves in the Northwestern Himalayan (India) region. *Journal of Asian Earth Sciences*, *117*, 337-345.

Li B-J, Qin J-Z, Qian X-D, Ye J-Q (2004) The coda attenuation of the Yao'an area in Yunnan Province. Acta Seismol Sin 17(1):47–53

Ma'hood, M., & Hamzehloo, H. (2009). Estimation of coda wave attenuation in East Central Iran. *Journal of Seismology*, *13*(1), 125-139.

Morsy, M. A., & Abed, A. M. (2013). Attenuation of seismic waves in Central Egypt. *NRIAG Journal of Astronomy and Geophysics*, *2*(1), 8-17.

Sato, H. (1977). Energy Propagation including scattering effects single isotropic scattering approximation. J. Phys. Earth 25, 27–41.

Pezzo, E.D., Bianco, F., Marzorati, S., Aguliera, P., Alema, D.E., Massa, M. (2011). Depth dependent intrinsic and scattering seismic attenuation in the North central Italy. Geophys. J. Int. 186, 373–381.

Phillips S, Aki A (1986) Site amplification of coda waves from local earthquakes in central California. Bull Seismol Soc Am 73:627–648

Pujades L, Canas JA, Egozcue JJ, Puigvi MA, Pous J, Gallart J (1991) Coda Q distribution in the Iberian Peninsula. Geophys J Int 100:285–301. doi:10.1111/j.1365-246X.1990.tb02486.x

Pulli JJ (1984) Attenuation of coda waves in New England. Bull Seismol Soc Am 74:1149–1166

Rahimi H, Hamzehloo H (2008) Lapse time and frequencydependent attenuation of coda waves in the Zagros continental collision zone in Southwestern Iran. J Geophys Eng 5:173–185. doi:10.1088/1742-2132/5/2/004

Rajabi baniani, s., & yokoi, t. (2014). Site effect and q-factor estimation of arasbaran (ahar- arzaghan) earthquake, iran by spectral inversion method. *Bulletin of the International Institute of Seismology and Earthquake Engineering*, *48*, 25-30.

Ramakrishna Rao CV, Seshamma NV, Mandal P (2007) Attenuation studies based on local earthquake coda waves in the southern Indian peninsular shield. Nat Hazards 40(3):527–536. doi:10.1007/s11069-006-9017-x

Rautian TG, Khalturin VI (1978) The use of the coda for determination of the earthquake source spectrum. Bull Seismol Soc Am 68:923–948

Sato H (1977) Energy propagation including scattering effects, single isotropic approximation. J Phys Earth 25:27–41

Sato, H., and M. C. Fehler (2008).Earth Heterogeneity and Scattering Effects on Seismic Waves, Springer-Verlag, New York, New York.

Sato, H., M. C. Fehler, and T. Maeda (2012).Seismic Wave Propagation and Scattering in the Heterogeneous Earth, Second Ed., Springer, New York, New York, 1–496.

Scherbaum F, Kisslinger C (1985) Coda Q in the Adak seismic zone. Bull Seismol Soc Am 75:615–620

Singh SK, Herrmann RB (1983) Regionalization of crustal coda Q in the continental United States. J Geophys Res 88:527–538. doi:10.1029/JB088iB01p00527

Singh, S., Singh, C., Biswas, R., & Singh, A. (2017). Frequency and lapse time dependent seismic attenuation in eastern Himalaya and southern Tibet. Natural Hazards, 85(3), 1709-1722.

Tripathi, J.N., Ugalde, A. (2004). Regional estimation of Qfrom seismic coda observation by the Gauribidanur seismic array (southern India). Phys. Earth Planet. In. 145, 115–126.

Tselentis, G. (1998). Intrinsic and scattering seismic attenuation W. Greece. Pure Appl. Geophys. 153, 703–712.

Ugalde, A., Vargas, C.A., Pujades, L.G., Canas, J.A., 2002. Seismic coda attenuation alter the Mw= 6.2 Armenia (Colombia) earthquake of 25 January, 1999. J. Geophys. Res. 107 (B6), 1–12.

LOCAL MAGNITUDE M_L AND MOMENT MAGNITUDE M_W SCALING RELATIONSHIP FOR BENI HAOUA (APRIL, 25TH 2012) AFTERSHOCKS

Abbes K.[1], Dorbath L.[2], Mehiaoui M.Y.[3], Airouche A.[1], Benkaci N.[1] and Bouhadad Y.[1]

[1]*Dr. Geophysics. National Center of Applied Research in Earthquake Engineering (CGS),Algiers, Algeria*
[2]*Prof., Seismology. EOST- Strasbourg, France*
[3]*Dr., Civil Eng.National School of Public Works, Algiers, Algeria*
Email: kabbes@cgs-dz.org

ABSTRACT:

In order to determine the seismic moment as well as the moment magnitude, we modeled the spectrum displacement of P and S waves in the frequency domain, using cost function method. A set of 35 aftershocks of the BeniHaoua earthquake in the range of magnitudes 0.6 to 4.3 recorded by three component short period stations of our temporary network (CGS). The local magnitude, calculated in the previous published study (Abbes et al., 2015), was compared to the moment magnitude. The obtained results show a linear relation between the local magnitude and the moment magnitude. The scaling relationships for P and S waves are almost identical and defined as follow:
$Mw(p) = 0.62M_L + 0.86$ and $Mw(s) = 0.63M_L + 0.81$.

KEYWORDS: BeniHaoua, spectrum, cost function, seismic moment, scaling relationship.

1. INTRODUCTION

From the theoretical models of sources, we propose to explain, at best, the data recorded during an earthquake. Waveforms or seismograms are easier to analyze in the frequency domain than in the temporal Madariaga (1976). The amplitude of the displacement spectra of the body wave , gives a good idea about the seismic source and their relating parameters. The spectra envelope of a seismic event is composed commonly, in particular, a low frequency plateau proportional to the seismic moment M_0, and a decreasing slope in high frequency which corresponds to the attenuation.
The ω-square model was first introduced by Aki (1967) and then taken up by Brune (1970), is based on the observation of the spectral content resulting from the Fourier transform. Several studies have shown that P and S phases are an effective means (Aki & Richards, 1980 and 2002, Ben-Menahem & Singh, 1981, Das & Kostrov, 1988, Scholz, 1990, Lay & Wallace, 1995, Udias , 1999) to estimate the source parameters, such as the seismic moment M_0p/s, the quality factor Qp/s, the stress drop σp/s and, the source radius Rp/s.
Therefore, the amplitude of the displacement spectra (Fig. 1) was used to determine these parameters. The amplitude spectra (Ω, f: Equation 1) is the representation in the frequency domain of an seismogram (Ω, t) in time.

$$\Omega(f) = \frac{\Omega_0 e^{-(\pi f t/Q)}}{\left[1+(f/f_c)^{\gamma n}\right]^{1/\gamma}} \quad (1)$$

In order to improve seismic hazard assessment methods at the regional scale, it is necessary to define realistic seismic movements adapted to the context of each study. Abercrombie (1995) shows that the slope n varies significantly, but the average slope n = 2 called "ω-square model" gives good results when we study low magnitudes.
The seismic moment M_0 (Equation 2), which characterizes the elastic energy radiated by an earthquake, is defined classically as follows:

$$M_0 = \mu \bar{D} A \tag{2}$$

μ is the shear modulus, **A** is the size of the circular rupture plane (area), $\bar{D}$ is the average source dislocation on the rupture area $A = \pi R^2$.

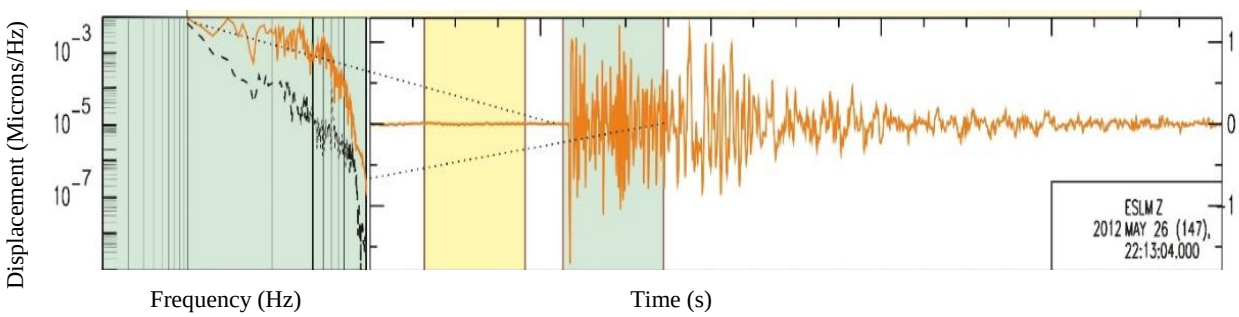

Figure 1. Right: The Z component seismogram of an aftershock (ESLM station). The green window shows the P wave and the yellow one shows the noise. Left: the spectra for the selected windows.

2. DATA

In this part, a fine determination of the source parameters is carried out on aftershocks sequence of the Beni Haoua earthquake. The methodology is based on spectral analysis of the P and S waves (Fig. 1). A set consists 35 well recorded events with local magnitude ranging from ($0.6 \leq M_L \leq 4.3$). This dataset was selected on the basis of the 46 events relocated with HypoDD (Fig. 2). The seismograms recorded by each station (3 components) are processed in the frequency domain via the function of Fourier transform (fft). The P and S waves spectra was modeled. Thus, we obtained, for each event and for the same station, an average (Zp/s, Np/s and Ep/s) of the seismic moment M_0p/s and the moment magnitude M_wp/s.

The pickev code(Fréchet et Thouvenot, 2004) for seismogram picking and processing allows to automatically compute the local magnitude M_L according to the Richter formula (1935). This calculation consists of the following steps: signal integration, high-pass filtering, determination of the peak-to-peak maximum amplitude, reading of the gain of each station, computation of the event-station distance, and, finally, the local magnitude calculation.

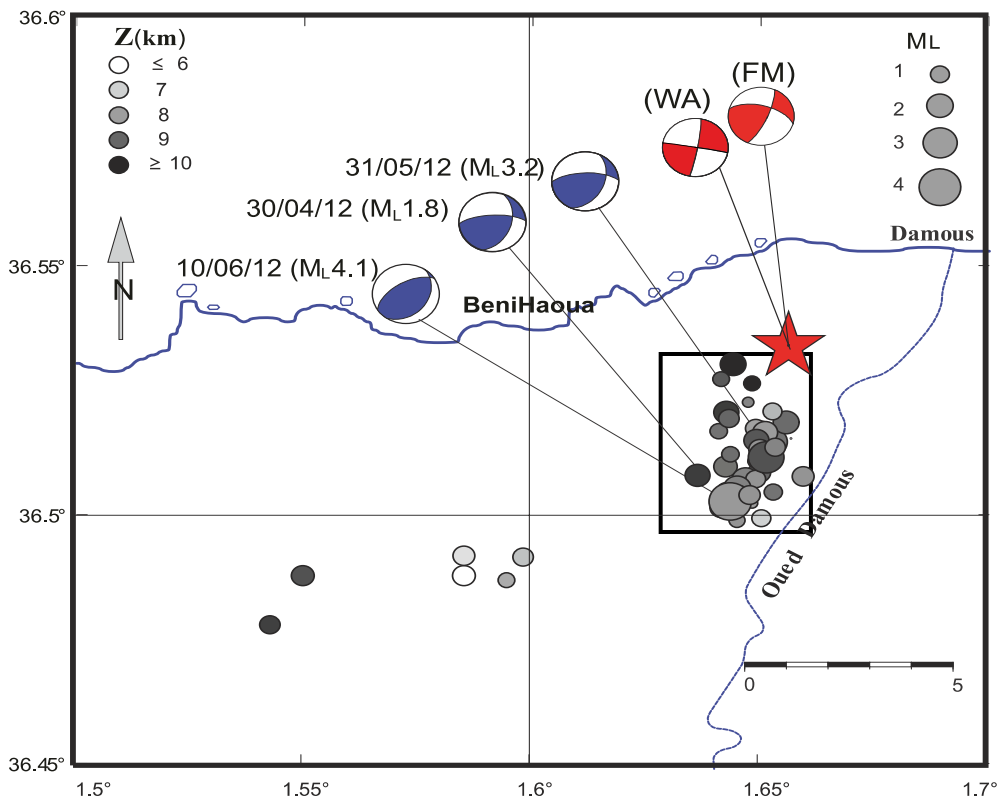

Figure 2. Aftershocks sequence (black rectangular) used to determine the scaling law relating local magnitude M_L to moment magnitude M_w.(Abbes et al., 2015).

3. MOMENT MAGNITUDE ESTIMATION

We used the SAC (Seismic Analysis Code) code to process the chosen P and S windows. the signal was corrected from the instrumental response, remove the mean, apply the taper and finally use the FFT function to obtain the P and S spectra. The obtained curve was modeled using ω-square model. We, therefore, developed a Matlab code based on the coast function algorithm to find iteratively the best fitting for maximum displacement Ω_0p/s, corner frequency fcp/s and the quality factor Qp/s (Fig. 3).

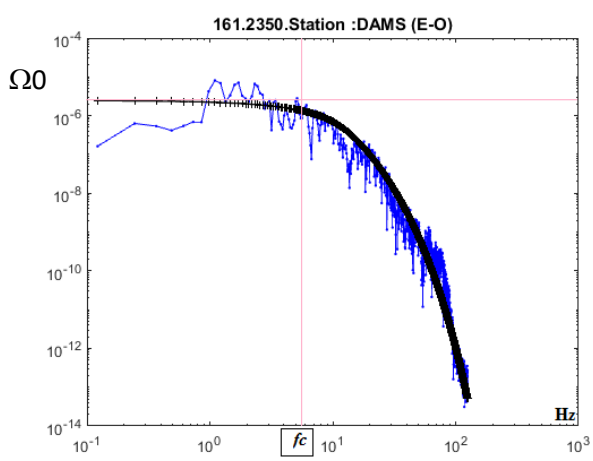

Figure 3. Black: Modeled displacement spectra. Blue: Observed displacement spectra. of an S wave.

The moment magnitude was calculated from the seismic moment M_0 (Equation 3). The latter was estimated from the Madariaga model (1976) for a circular fault plane, using the following parameters: the velocity Vp is equal to 4.5 km/s, the density 2.4 kg/cm3 and the average radiation pattern Θ = 0.52.

$$Mw = \frac{2}{3} log_{10} M_0 - 9.1 \tag{3}$$

4. RESULTS AND CONCLUSION

More than 300 waveform were used to compute the spectra and modeled to obtain moment magnitude M_wp/s. The local magnitudes M_L of the 35 aftershocks ($0.6 \leq M_L \leq 4.3$) estimated by Abbes et al., 2015 was compared to the M_wp/s calculated in this study, in order to define a scaling law following a linear regression.
We define a relationship between moment magnitude and local magnitude $M_w p = 0.62M_L + 0.86$ and $M_w s = 0.63M_L + 0.81$ for P and S waves respectively (Fig.4).

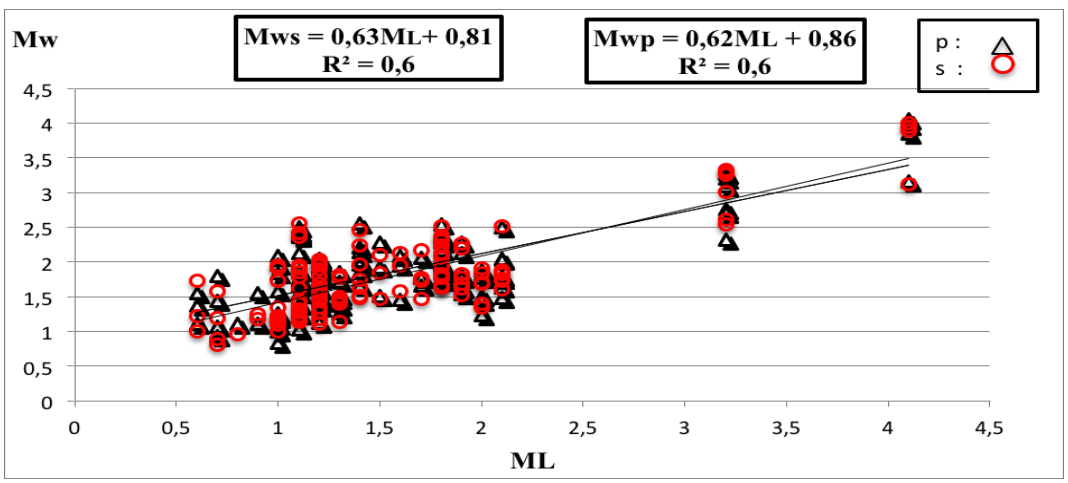

Figure 4. Local Magnitude as a function of moment magnitude

REFERENCES

Abbes, K., Dorbath, L., Dorbath, C., Djeddi, M., Ousadou, F., Maouche, S., et al. (2015). The Beni Haoua, Algeria, Mw 4.9 earthquake: source parameters, engineering, and seismotectonic implications. Journal of Seismology, vol. 20, no 2, p. 655-667.

Abercrombie, R. E. (1995). Earthquake source scaling relationships from 1 to 5 ML using seismograms recorded at 2.5km depth. Journal of Geophysical Research: Solid Earth100.B12 24015-24036.

Aki, K. (1967). Scaling law of seismic spectrum. J. Geophys. Res., 73, 5359– 5376.

Aki, K. and Richards, P.G. (1980). Quantitative seismology. Freeman, San Francisco, Vol. I and II, 932 pp.

Aki, K. et Richards, P.G. (2002). Quantitative seismology (2nd ed.). University Science Books. ISBN 0-935702- 96-2.

Ben-Menahem, A., and Singh, S. J. (1981). Seismic waves and sources. Springer-Verlag, New York, Heidelberg, Berlin, p1108.

Brune, J.N. (1970). Tectonic stress and the spectra of shear waves from earthquakes. J. Geophy. Res., 75, 4997-5009.

Das, S., et Kostrov, B.V. (1988). Principles of earthquake source mechanics. Cambridge University Press.
Fréchet, J. et Thouvenot, F. (2004). Pickev 2000: Software for seismogram picking and processing, earthquake location, and mapping. http://sismalp.obs.ujf-grenoble.fr/ftp-sismalp/msdos

Lay, T. et Wallace, T. C. (1995). Modern Global Seismology. Academic Press.

Madariaga, R. (1976). Dynamics of an expanding circular fault. Bull. Seism. Soc. Am., 66, 639-666.

Richter, C.F. (1935). An instrumental earthquake magnitude scale. Bull. Seismol. Soc. Am. 25:1–31.

Scholz, C. H. (1990). The mechanic of earthquakes and faulting, Cambridge: Cambridge University Press.

Udias, A. (1999). Principles of Seismology. Cambridge: Cambridge University Press.

DEVELOPMENT OF TOOLS FOR ANALYSIS OF SEISMIC WAVES CORELATED WITH OTHER GEOPHYSICAL PARAMETERS

Asimopolos L. [1], Asimopolos A.A. [2], Asimopolos N.S. [3]

[1] *Dr., Geomagnetic Observatory Department, Geological Institute of Romania, Bucharest*
[2] *PhD Student. Assist., Faculty of Transportation, Polytechnic University, Bucharest, Romania*
[3] *Dr., Regional Geology Department, Geological Institute of Romania, Bucharest*
Email: asimopolos@gmail.com, laurentiu.asimopolos@igr.ro

ABSTRACT:

In this paper we present filtration procedures, correlation between several signals and other types of statistical and spectral analyses for which we have developed few procedures that can be used in seismic waves correlated with other geophysical parameters. The filters used provide us with information about the varying degree of regionality of the anomalies and the different depths of the sources, which of course cannot be quantified until all the information has been corroborated. These filters can bring both information about local and surface effects (through residual maps, through "high pass" filters), mid-depth structures (through "band pass" filters) and deep structure down"). The results of methods of analysing trends with polynomial surfaces are similar to those of mobile media methods representing filtration systems. In mobile averages, a portion equal to half of the mobile window used is lost on each side of the studied surface. Unlike mobile averages, the use of trend surfaces keeps the resulting surface size. Moreover, with the analytical expression of the trending surface we can extrapolate the tendency to a larger surface than the initial one. The variance of the correlation factor is calculated in a moving window that packs the entire matrix grid of values for two or more sets of parameters. This type of analysis is relevant for evaluating the correlation of parameters on certain segments of depth, given that each window used reflects the information with a certain degree of regionality and a certain depth range for the source of the studied anomalies. When the correlation factor is closer to the unit value, we can admit that the two sets of parameters studied are predominantly a common cause. Fourier analyses allow the data to be analysed by means of harmonics whose amplitudes and periods can be identified in two or more directions. The disadvantage of the Fourier transform is that with this transformation we lose the time-related information. Since many sequences in a signal are transient and non-stationary, being lost by the classical Fourier transform, we can use the short-term Fourier transform that can analyse small signal sequences associated with time. This connects the both domains (time and frequency), while making the connection with current wavelet and multi-resolution techniques.

KEYWORDS: polynomial surfaces, mobile averages, algorithms for filtering, geophysical data, wavelet

1. INTRODUCTION

Among the filtering methods of geological, geophysical, seismological data (data that is located on a 2D surface or in a 3D space), the moving average method, although very old, is particularly useful.
Many authors have used this technique in various fields.
The analysis of polynomial trends is another old method, based on the smallest squares method used for the smoothing of geological or geophysical data, which many authors have dealt [Asimopolos N.S. – 2017a,b; Asimopolos L. – 2017a,b; Farhang-Boroujeny B. – 2013; Karakus D-2011; Harbaugh J. 1972; Unwin D – 1978]. Combined use of these methods in iterative programs and compared to spectral filtering can bring quantitative information about the parameters analyzed.

At the same time, Matlab currently facilitates data processing in a very fast time [Matlab-2015a; Poularikas D.-2006].

2. METHODOLOGIES

2.1. Tendency polynomial surfaces analysis

A surface occupying a three-dimensional space is a mathematical function with a dependent variable and two independent variables. We can operate mathematically and with functions of four or more variables (hyperspace) that have great importance in some applications.

In the most general case of space $\mathbf{R^n}$, we choose **(n-1)** independent variables and **1** dependent variable that can be expressed by the function $\mathbf{x_n = f(x_1, x_2, ..., x_{n-1})}$, representing the expression of a hyperspace . From **n** dimensions of space Rn, we can choose up to **3** spatial dimensions (latitude, longitude and altitude) and the other **n-4** independent variables can be represented by parameters that have a causal connection with the dependent variable that we analyze by the hyperspace tendency method .

The criterion of the smallest squares, in its general form, can be expressed succinctly by:

$\sum(X_{obs} - X_{tend})^2 = minimum$, where $\mathbf{X_{obs}}$ (respectiv $\mathbf{X_{tend}}$) represent the set of observed values (respectively calculated by trend analysis). The broad description of the algorithms used, the equations of the trend surfaces and the programs developed for calculating the coefficients are in [Asimopolos N.S. – 2017a,b; Asimopolos L. – 2017a,b;]. The simplest example of a trend function is the equation of a straight line:

y = A + Bx, where x is an independent variable, y is dependent variable and constants A and B are calculated so that the sum of deviations is as small as possible.

The simplest example of a trend surface is the equation of a plane:

ztend = A + Bx + Cy, where x and y are independent variables, z is dependent variable and constants A, B and C are calculated so that the sum of the deviations is minimal.

Deviation at a given point is the difference between the observed value and the calculated value and can be expressed by:

deviation = zobs - ztend. It follows that: deviation = zobs - A - Bx - Cy

Expressing the sum of the squares of the deviations with the function Φ (A, B, C) we obtain: $\Phi(A,B,C) = \sum_{i=1}^{n}\left(z_i - A - Bx_i - Cy_i\right)^2$ where z_i are the values observed at each coordinate point (x_i, y_i) and n is the total number of observation points.

If Φ (A, B, C) must be minimized then it is necessary to: $\frac{\delta\Phi}{\delta A} = \frac{\delta\Phi}{\delta B} = \frac{\delta\Phi}{\delta C} = 0$

Result:

$$\frac{\delta F}{\delta A} = \sum_{i=1}^{n} 2\left(z_i - A - Bx_i - Cy_i\right)(-1) = 0 \qquad -\sum_{i=1}^{n} z_i + A\cdot n + B\sum_{i=1}^{n} x_i + C\sum_{i=1}^{n} y_i = 0$$

$$\frac{\delta F}{\delta B} = \sum_{i=1}^{n} 2\left(z_i - A - Bx_i - Cy_i\right)(-x) = 0 \quad , \quad -\sum_{i=1}^{n} z_i x_i + A\sum_{i=1}^{n} x_i + B\sum_{i=1}^{n} x_i^2 + C\sum_{i=1}^{n} x_i y_i = 0$$

$$\frac{\delta F}{\delta C} = \sum_{i=1}^{n} 2\left(z_i - A - Bx_i - Cy_i\right)(-y) = 0 \qquad -\sum_{i=1}^{n} z_i y_i + A\sum_{i=1}^{n} y_i + B\sum_{i=1}^{n} x_i y_i + C\sum_{i=1}^{n} y_i^2 = 0$$

This system of three equations with three unknowns (A, B and C) can be solved by the matrix equation:

$$\begin{bmatrix} A \\ B \\ C \end{bmatrix} = \begin{bmatrix} n & \sum x & \sum y \\ \sum x & \sum x^2 & \sum xy \\ \sum y & \sum xy & \sum y^2 \end{bmatrix}^{-1} \times \begin{bmatrix} \sum z \\ \sum zx \\ \sum zy \end{bmatrix}$$

Trend areas of the second degree or higher are calculated similarly.

Following the same procedure, we have developed programs for the following types of surfaces: The equation of third-degree surfaces:

$Z=A+BX+CY+DX^2+EXY+FY^2+GX^3+HX^2Y+IXY^2+JY^3$

The equation of six-degree surfaces:

$Z=A+BX+CX^2+DX^3+EY+FXY+GX^2Y+HX^3Y+IY^2+JXY^2+KX^2Y^2+LX^3Y^2+MY^3+NXY^3+OX^2Y^3+PX^3Y^3$

For space R4 we can calculate the hyper-surfaces z = f (x, y, w) representing a rectangular region having the nodes of the grid (xi, yl, wk), which has the equation:

$$z(x,y,w) = \sum_{i=0}^{m}\sum_{j=0}^{n}\sum_{k=0}^{p} a_{ijk}x^i y^j w^k$$

The equation of second degree of hyper-surfaces, from space R^4 (X, Y, W, Z), where X, Y, W are the independent variables and Z is dependent variable:

$Z=A+BW+CX+DY+EX^2+FWY+GXY+HWX+IW^2+JY^2$

And so on, the equation of third degree of hyper-surfaces:

$Z=A+BW+CX+DY+EX^2+FWY+GXY+HWX+IW^2+JY^2+KX^3+LW^3+MY^3+NX^2Y+OXY^2+$

$PY^2W+QYW^2+RW^2X+SWX^2+TWXY$

For mobile average method in surface we have developed programs based on the different square windows.

For moving average with different dimensions windows, we have developed programs based on the following algorithms:

We note with a_{ij} the values of the z parameter we are studying in the node of the network (i, j), where i and j take values in the range [1; n].

Also, we note $\overline{a_{i,j}}$ the average values of the z parameter in the node of the network (i, j) where i and j take integer values within the related by the mobile window used.

$$\overline{a_{i,j}} = \sum_{i=-k}^{i=k}\sum_{j=-k}^{j=k} a_{ij}$$

Dimensions of window used is $4k^2$ where k is the side of a square cell for the grid used.
The variation of the correlation factor between two sets of parameters brings information for geological and tectonic assumptions. This correlation factor between two sets of data can be calculated, similarly as in mobile averages with windows of different sizes, passing through the entire network of points, bringing information from depths. The correlation between two sets of parameters may be some indicators that they are dependent on common causes.

2.2. Spectral analysis

The Fourier series is a linear combination of mono-frequential signals and describes the behavior of the original signal in time and frequency. It highlights the temporal evolution of the signal and its frequency content. If you

apply direct Fourier transform to a signal is obtained the spectral function of the signal (spectral characteristic), which is a signal parameter. Spectral function is a complex quantity, which can be continuous or discrete, periodic or no periodic.
If the spectral function is discrete is called complex amplitude spectrum and characterization sizes in polar coordinates are called amplitude spectrum, respectively phase spectrum.
Even if the signal is periodic but the time window isn't chosen to be a multiple of the signal period (an integer number of periods), the spectral function obtained may be distorted. This may occur where signal acquisition isn't adapted to the signal periodicities or where periodicities of the signal purchased are not known.
If the time window is chosen correctly then the actual virtual sequence coincides with infinite duration signal, otherwise the virtual signal is distorted compared the real signal.
Using a time window for signal processing is equivalent to the filtering problem, but the goal is to mitigate potential discontinuities at the end of finite segment of the data evolution over time.
In order to achieve the best possible accuracy, the spectral window used (Fourier transform of the time window) must satisfy the following basic requirements:
• main lobe of the window should be very narrow;
• main lobe contains most of the window energy;
• the energy of the secondary lobes must be evenly distributed between them
Generally, these three requirements cannot be met by any window because the first two requirements are contradictory. From this point of view, we can say that there is no optimal window, each providing a compromise between the three requirements.
Bartlett temporal window provides a strong suppression of side lobes of the corresponding spectral window, however, increases the width of the main lobe and reduces its amplitude.
The Hamming time window provides a stronger suppression of the side lobes and minimizing the main lobe amplitude for the chosen frequency.
A large time window leads to a good resolution in frequency, but a low resolution in time domain (narrowband spectrogram) and a short time window determine a good location in time, but a poor frequency resolution (broadband spectrogram).
If the assessment of the power spectrum is based on direct application of Fourier transform followed by mediation, then we deal with the averaged periodogram. Mediation is usually done by dividing the signal into a variable number of segments, possibly overlapping, followed by Fourier transform calculation of all these segments (average for minute, hourly or daily of the geomagnetic signals).
Given the need for a high-performance signal analysis, many variations of spectral analysis of this type have been developed, generally called periodograms. Thus, one of the most popular periodogram mediated assessment procedures is attributed to Welch, who is a modification of the original segmentation scheme, developed by Bartlett. [Matlab-2015a].
Modern approaches of spectral analysis are designed to overcome some of the distortions produced by traditional methods and are very effective especially for short segments of analysis.
According to the Heisenberg uncertainty principle, is not possible accurate and simultaneous localization in both time domain and frequency domain.
Wavelet analysis preserves the information in the time domain and those in the frequency domain.
We performed a Fourier analysis to view the predominant frequencies for each point and can be distinguished range of frequencies.

We used the MATLAB code:
*load table.txt; X1= table (:,1); X2= table (:,2); X3= table (:,3); X4= table (:,4); X5= table (:,5); X6= table (:,6); X7= table (:,7); X8= table (:,8); N=length(X1); t=1:1:N; fe=1/N; x=X1'; Xt=fft(x); Xm=abs(Xt); X=Xm(1,1:N/2+1)/(N/2); f=[0:N/2]*fe; subplot(211); plot(t,x); grid; xlabel('t[min]'); ylabel('x(t)[ ]'); title(' '); subplot(212); stem(f,X); xlabel('f[o.5Hz]'); ylabel('X(f)'); grid; title(‘’)*

To investigate these variations of temperature, in the coordinates time-frequency, we use wavelet analysis.

The values on the scale determines the compression of wavelet. The lower scale are correlates better with high frequencies. Small scale coefficients of continuous wavelet transform CWT highlight the fine features of the input signal. Increasing the scale values of scale allow highlight low frequency content of the signal. Wavelet cross-spectrum of two series of data, x and y, is:

$C_{xy}(a,b) = S\left(C_x^*(a,b)C_y(a,b)\right)$, where $C_x(a,b)$ and $C_y(a,b)$ represent of continuous wavelet transform CWT of series x and y, in function of scale a and position b. Exponent * represent complex conjugate and S is an operator of smoothing.

For real values of the time series, cross-wavelet spectrum has real value. For complex values of time series, cross-wavelet spectrum is complex values. Wavelet coherence of two series of data, x and y, is:

$$\frac{S\left(C_x^*(a,b)C_y(a,b)\right)}{\sqrt{S(C_x(a,b))^2}\sqrt{S(C_y(a,b))^2}}$$

Because the wavelet coefficients are complex valued, the coefficients provide phase and amplitude information of the signal being analyzed. Analytic wavelets are well suited for studying how the frequency content in real world nonstationary signals evolves as a function of time been a good choice when doing time-frequency analysis with the CWT.

We used this MATLAB code:

```
load table.txt; SX=table(:,1); signal = SX; lev   = 5; wname = 'db1'; nbcol = 64; [c,l]
=wavedec(signal,lev,wname);
len = length(signal); cfd = zeros(lev,len); for k = 1:lev; d = detcoef(c,l,k); d = d(:)'; d = d(ones(1,2^k),:);
cfd(k,:) = wkeep1(d(:)',len); end
cfd =  cfd(:); I = find(abs(cfd)<sqrt(eps)); cfd(I) = zeros(size(I)); cfd    = reshape(cfd,lev,len);
cfd = wcodemat(cfd,nbcol,'row'); h211 = subplot(2,1,1); h211.XTick = []; plot(signal,'r'); title('Analyzed
signal.'); ax = gca; ax.XLim = [1 length(signal)]; subplot(2,1,2); colormap(cool(128)); image(cfd); tics = 1:lev;
labs = int2str(tics'); ax = gca; ax.YTickLabelMode = 'manual'; ax.YDir = 'normal'; ax.Box = 'On'; ax.YTick =
tics; ax.YTickLabel = labs; title('Discrete Transform, absolute coefficients.'); ylabel('Level'); figure;
[cfs,f] = cwt(signal,1,'waveletparameters',[3 3.1]); hp = pcolor(1:length(signal),f,abs(cfs)); hp.EdgeColor =
'none'; set(gca,'YScale','log'); xlabel('Sample'); ylabel('log10(f)');
```

3. EXAMPLES FOR ROMANIAN TERITORY

The gravimetric data in Romania are available at the International Gravimetric Bureau. We filtered these data with various mobile windows, with mobile average method, with tendency polynomial surfaces and the analytical continuations for the Bouguer anomaly (at different ceilings) in Romania, in conjunction with the Moho isobaths and the tectonic elements.

In fig.1 and fig.2 we can show the rezidual map of Bouguer anomaly, after was extract tendency surface with order 3 and order 6. Than, in fig.3 this tendency surfaces overlap with deep of Crust made from data of seismic profile in Romania (Radulescu F. – 1988, Ioane - 1995).

In fig.4 we made Fourier analysis of Free Air anomaly and calculated the residual map and in fig. 5 we made wavelet analysis (decomposition and fusion) of Bouguer anomaly (image 1) and elevation (image 2); black is maximum value and white is minimum value.

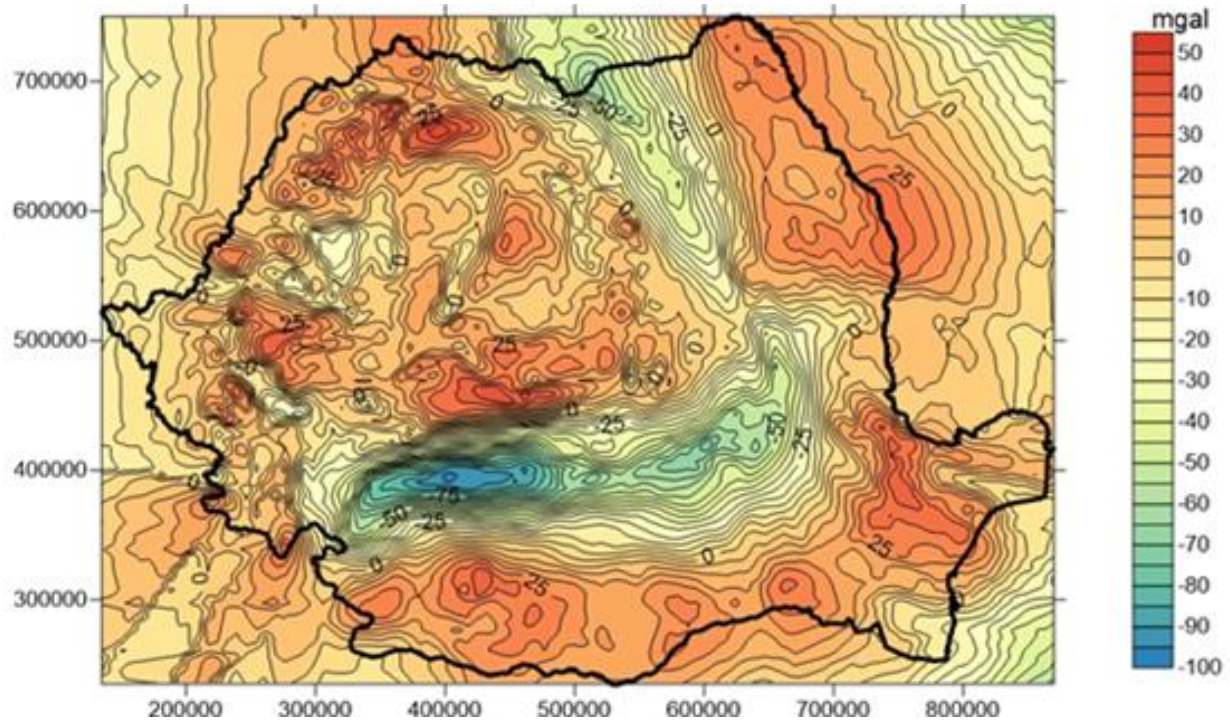

Fig. 1 – Rezidual map of Bouguer anomaly, after was extract tendency surface with order 3.

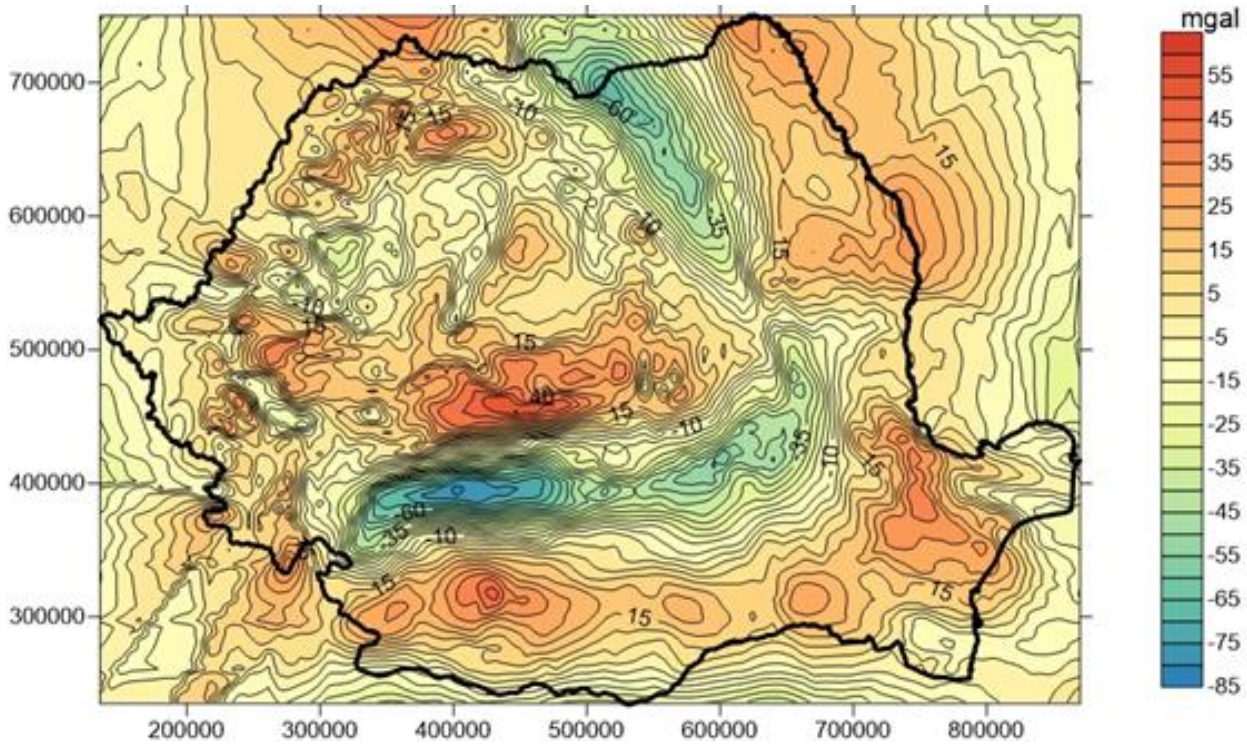

Fig. 2 – Rezidual map of Bouguer anomaly, after was extract tendency surface with order 6.

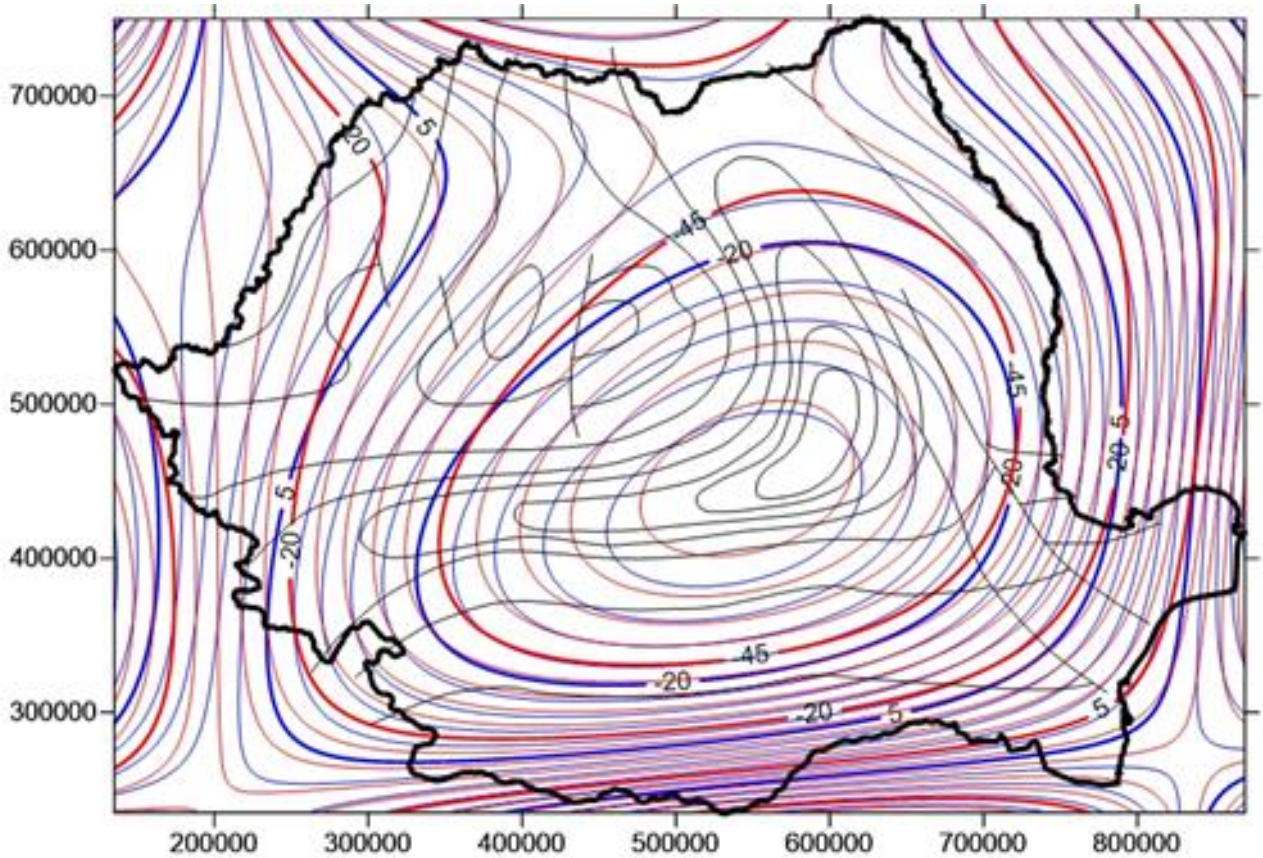

Fig. 3 –Tendecy surfaces of Bouguer anomaly with order 3 (with red lines); Tendecy surfaces of Bouguer anomaly with order 6 (with blue lines); Map with deep of Crust (with black lines – after Radulescu F., 1988).).

Tendecy surfaces of Bouguer anomaly with order 3 has ecquation:
$Z=A+BX+CY+DX^2+EXY+FY^2+GX^3+HX2Y+IXY^2+JY^3$, where coeficients A,...,J are:

A=	-39.1978956384	, B=	0.2801389396	, C=	0.2259832372	, D=	-0.0001630090	, E=	-0.0018658984
F=	-0.0000004369	, G=	0.0000002854	, H=	0.0000003663	, I=	0.0000014334	, J=	-0.0000001853

Tendecy surfaces of Bouguer anomaly with order 6 has ecquation:

$Z_{ord.6}=A+BX+CX^2+DX^3+EY+FXY+GX^2Y+HX^3Y+IY^2+JXY^2+KX^2Y^2+LX^3Y^2+MY^3+NXY^3+OX^2Y^3+PX^3Y^3$

where coeficients A,...,P are:

A=	-896.5115703326	, B=	5.3598654924	, C=	-0.0044335874	, D=	-0.0000008798	, E=	6.9021045916
F=	-0.0437772562	, G=	0.0000483387	, H=	-0.0000000063	, I=	-0.0154970146	, J=	0.0001026575
K=	-0.0000001351	, L=	0.0000000000	, M=	0.0000107958	, N=	-0.0000000738	, O=	0.0000000001
P=	0.0000000001								

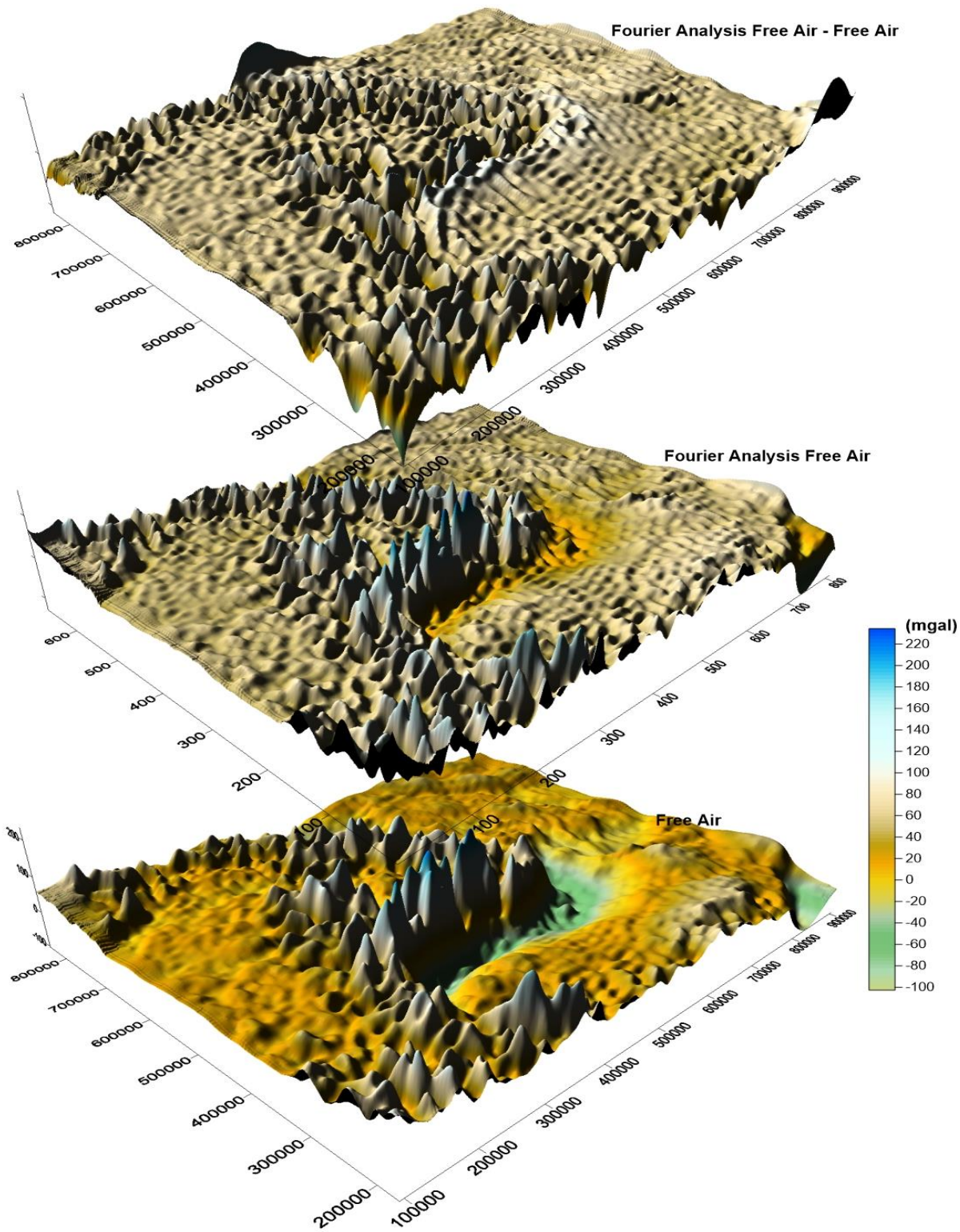

Fig. 4 – Fourier analysis of Free Air anomaly

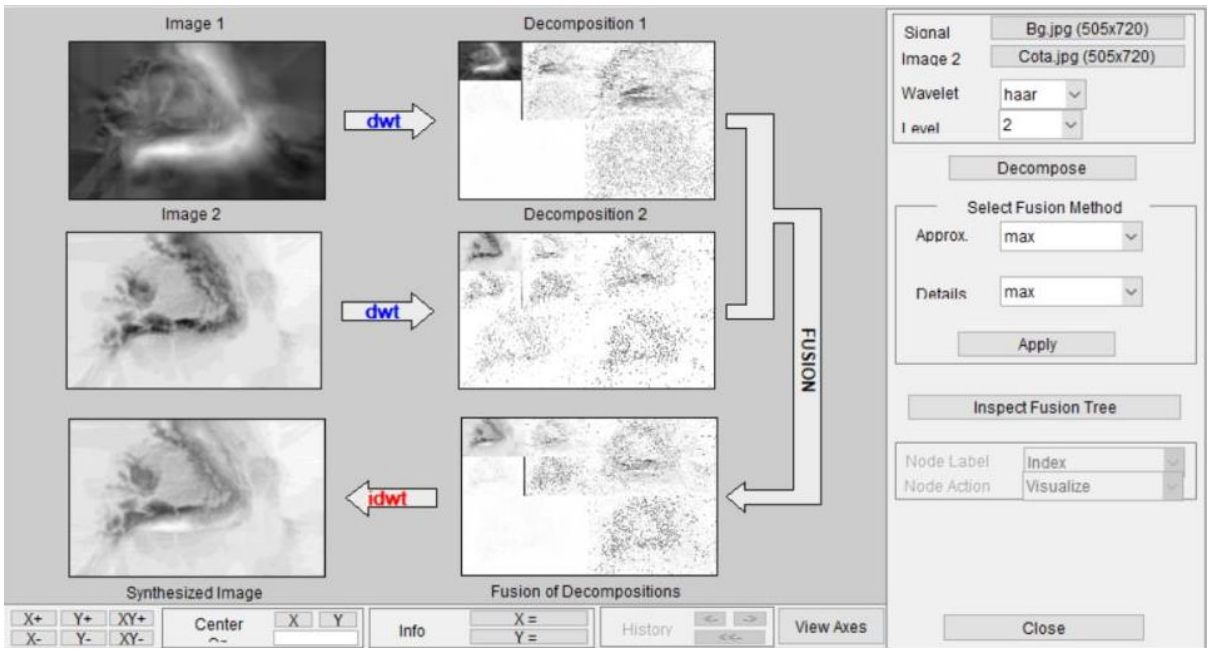

Fig.5 – Wavelet analysis (decomposition and fusion) of Bouguer anomaly (image 1) and elevation (image 2); black is maximum value and white is minimum value.

4. CONCLUSIONS

The calculation of analytical expressions of the polynomial trends based on the least squares' method, highlight quantifiable pattern of the regional trend caused by the deep structures.

Calculating the residual values resulting from the difference between the initial values and the trend values from the network nodes used, we highlighted the superficial local effects. We also obtained information about the regional trend caused by geological structures at medium and large depths, by calculating the difference between magnetic parameters, obtained with different moving average windows or tendency surfaces with different degrees, interpolated in same network.

The types of filters presented in the paper, provide us with information with different degrees of regionality and from different depths, after all the geological and geophysical information has been corroborated. These filters can bring both information about local and surface effects (residual maps, through "high pass" filters), mid-depth structures (through "band pass" filters), and deep structure (tendency maps, through "low pass" filter).

Spectral analysis in modern approaches are designed to overcome some of the distortions produced by traditional methods, they been very effective. In Fourier spectral analysis in conformity with uncertainty principle, is not possible accurate and simultaneous localization in both time domain and frequency domain.

Wavelet analysis preserves the information both in the time domain and those in the frequency domain.

5. ACKNOWLEDGMENTS

We thank for support by the Ministry of Research for financing of the project: "The realization of 3D geological / geophysical models for the characterization of some areas of economic and scientific interest in Romania", with Contract no. 28N / 2019.

Also, we address our thanks for scientific publications, reports and gravity data, to International Gravimetric Bureau (BGI).

REFERENCES

Asimopolos N.S. (2017a). PhD Theses: Contributions to deciphering the deep structure of the Vrancea seismogenic area and adjacent regions using gravimetric and geodetic data, University of Bucharest, Faculty of Geology and Geophysics, 272 pp.

Asimopolos L., Asimopolos N.S. (2017a). Filtering Gravity Data Through Polinomial Trend Surfaces DOI: 10.3997/2214-4609.201702625, 5pp.

Asimopolos N.S., Asimopolos L. (2017b). The importance of terrain corrections of gravity data in hydrological modeling SGEM2017 Vienna GREEN Conference Proceedings, Vol. 17, Issue 33, 363-370 pp; DOI: 10.5593/sgem2017H/33/S12.045, ISBN 978-619-7408-27-0 / ISSN 1314-2704

Asimopolos L., Asimopolos N.S. (2017b). Multi-parametric and correlative studies of the hydrogeological processes SGEM2017 Vienna GREEN Conference Proceedings, Vol. 17, Issue 33, 283-290 pp; DOI: 10.5593/sgem2017H/33/S12.035 ISBN 978-619-7408-27-0 / ISSN 1314-2704

Farhang-Boroujeny B. (2013). Adaptive Filters: Theory and Applications. John Wiley & Sons, Ltd. West Sussex, 529 pp.

Harbaugh J. (1972). Aplicaţiile calculatoarelor în geologie. Edit. Tehnică. Bucureşti. 328 pp.

Ioane, D., Radu, I. (1995). Global geopotential models and gravity data for the territory of Romania, In: Sunkel, H., Marson, I. (Eds.), Gravity and Geoid. Joint IGC/ICG Symposium Graz (1994). IAG Symposium No. 113, Springer, Heidelberg, 640-646.

Karakus D., Safak S., Onur A. H. (2011). A new aproximation method for the trend hypersurface analysis for elevation of drilhole data. Archives of Mining Sciences. Institut Mechaniki Górotvoru. Krakow. **56**(1): 47-58 pp.

MATLAB and Statistics Toolbox Release (2015a). The Mathworks Inc: Natick, MA, USA, 2015, 654pp.

Rădulescu Fl. (1988). Seismic models of the crustal structure in Romania, Rev.Roum.Geol.Geophys.Geogr.Ser.Geophys., 32, 13–17

Unwin D. (1978). An introduction to trend surface analysis – Concept and Techniques in Modern Geography, CAT MOG 5, ISSN 0305-6142, 40 pp.

Poularikas D. & Ramadan Z. M. (2006). Adaptive filtering primer with MatLab. Edit. CRC/Taylor & Francis Group. Boca Raton. 240 pp.

TECTONIC MODEL BASED ON SEISMIC PROFILES, CORROBORATED WITH GEOLOGICAL AND GEOPHYSICAL DATA, IN THE CLUJ-TURDA-GHERLA AREA OF ROMANIA

Asimopolos L. [1], Asimopolos N.S. [2]

[1] *Dr., Geomagnetic Observatory Department, Geological Institute of Romania, Bucharest*
[2] *Dr., Regional Geology Department, Geological Institute of Romania, Bucharest*
Email: asimopolos@gmail.com, laurentiu.asimopolos@igr.ro

ABSTRACT:

The interpretation of seismic profiles corroborated with geophysical anomalies (gravimetric and magnetic), stratigraphic and sedimentologic data improved insights in the evolution of the Transylvanian Basin.
The quantification of the results from the seismic profiles, which have a radial development from Cluj, allowed us to use modern modeling programs for Cluj-Turda -Gherla area. We used 3D GeoModeller software made by Intrepid Geophysics that allowed us to make a 3D geological model in the study area.
This quantification involved the placing in a three-dimensional grid of all data of knowledge so as: the seismic profiles, the Bouguer anomaly profiles, the magnetic data profiles, the tectonic of the area, the 1: 50000 geological maps, the petrophysical samplings of the samples taken from the study area, and so on. The NV area of the Transylvanian basin has a particular structure in which there is a monocline that sinks to the SE. An important fault is at the edge of the sloping area, the Valley Calda - Gădălin - Gherla fault, and in SE it develops the area of crevices.
The western marginal zone between Cluj and Turda is separated from the area by a fault or a fault system. It consisted of a succession of monoclines with falling to E or NE, which is a remnant of the connecting area between the Zlatna Basin and the Transylvanian Basin, interrupted by the lifting of the Campia Turzii - Sănduleşti, which includes Mesolithic and Mesozoic limestone. This lifting continues inside the Transylvanian Basin, under the Miocene sediments, with Puini lifting.
The sloping crest area thus forms a sharp angle between Gherla - Cluj - Turda, and overlaps with the part of the Transylvanian Basin where the salt has a large thickness, capable of bearing a detachment of sediments above it, sliding and rotating them.
These slides have a complicated structure, recent field mappings for maps 1: 50,000 show a structure of slides that was born in at least two tectonic stages, as the initial slides are faltered and cracked by a younger tectonic stage.

KEYWORDS: seismic profiles, geophysical data, geological maps, processing data, 3D modelling

1. INTRODUCTION

The western marginal zone between Cluj and Turda is separated from the area by a fault or a fault system. It consisted of a succession of monoclines with falling to E or NE, which is a remnant of the connecting area between the Zlatna Basin and the Transylvanian Basin, interrupted by the excavation of the Cheile Turzii - Sănduleşti, which includes ophiolites and Mesozoic limestones. This lifting continues inside the Transylvanian Basin, under the Miocene sediments, with Puini lifting [Krézsek C., 2006; A. de Leeuw, 2013; Orasanu I, 1998,2010; Papp D.,2011, Qiang S.2017].
The geological area with salt thus forms a sharp angle between Gherla - Cluj - Turda, and overlaps with the part of the Transylvanian Basin where the salt has a large thickness, capable of bearing sediments above it, sliding and rotating.

Recent field mappings show a structure of slides that was born in at least two tectonic stages, as the initial slides are broken and cracked by a younger tectonic stage.
3D modeling [https://www.intrepid-geophysics.com/ig/index.php?page=Home] of the area could lead to the determination of the direction and succession over time of tectonic stress from each stage.
The consequences of this scientific approach could have important consequences in further research into the reserves of gas and salt deposits inside the basin, as well as in geological research in the Marginal Transylvanian areas, less researched than the central area with methane gas deposits [Krézsek C., 2006; Veliciu S., 1985].

2. GEOLOGICAL AND GEOPHYSICAL DATA

The Transylvanian basin with its Neozoic sediments covers a former Cretaceous mountain chain that closed the branch of Tethys, joining the Tisa and Dacia continental blocks. These are fragments of the European Plate that were detached from it with the opening of Tethys. Their likeness to the European Plate took place during the Alpine orogenesis, especially the tectonic phases in the Middle and Upper Cretaceous. The Dacia unit, located south and east, consisted of metamorphic rocks with lower Palaeozoic sedimentary affected by an early metamorphism. The non-metamorphosed sediments consist of discontinuous Carboniferous-Permian-Mesozoic sediments.
The Tisza Bloc, of which the Apuseni Mountains also belong, consist of a succession of nappes placed in the middle Cretacic, consisting of a meso- and epi-crystalline foundation and a Permian Mesozoic blanket. Sediments have Adriatic affinities due to their more derivation during the opening of Tethys. From Triasic to Middle Cretaceous, a branch of the Vardar Ocean (Transylvanian) evolved to separate the two blocks and was subdivided, and its remains are now in the form of the obelisks over the Dacia block. Associated with this suture, there are also rock bodies of an island of Laramic age volcanism. At the same time, the Transylvanian and Bucovinian nappes in the Eastern Carpathians were replaced by the nappes in Turonian the western part of Apuseni mountains (Bihor, Codru and Biharea) were put in place. Turonian-Campanian sediments up to Maastrichtian cover locally nappes. They are affected in turn by the later tectonics in Neozoic, which gave birth to the arched chain of the Carpathians and the inter Carpathian basins, including the Transylvanian Basin [Krézsek C,2006; Hauser F,2007; Qiang S., 2017; Sandulescu M., 1984].

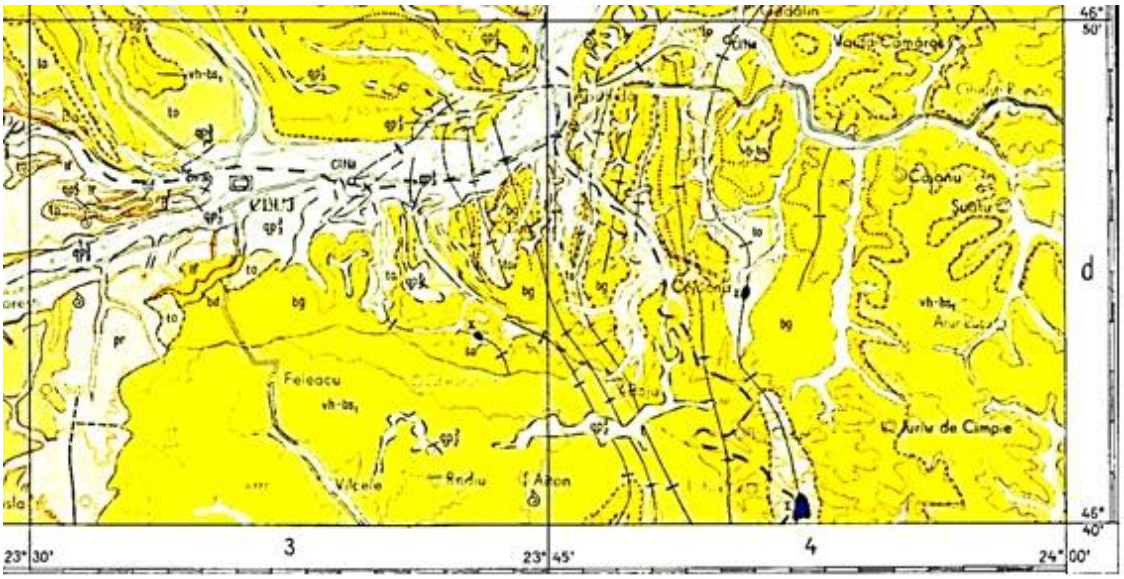

Fig.1 - Extract from geological map 1: 200000, sheet Cluj, L-34-XII, perimeter $46^0$50'-$46^0$40' and $23^0$30'- $24^0$00', 1967-IGR

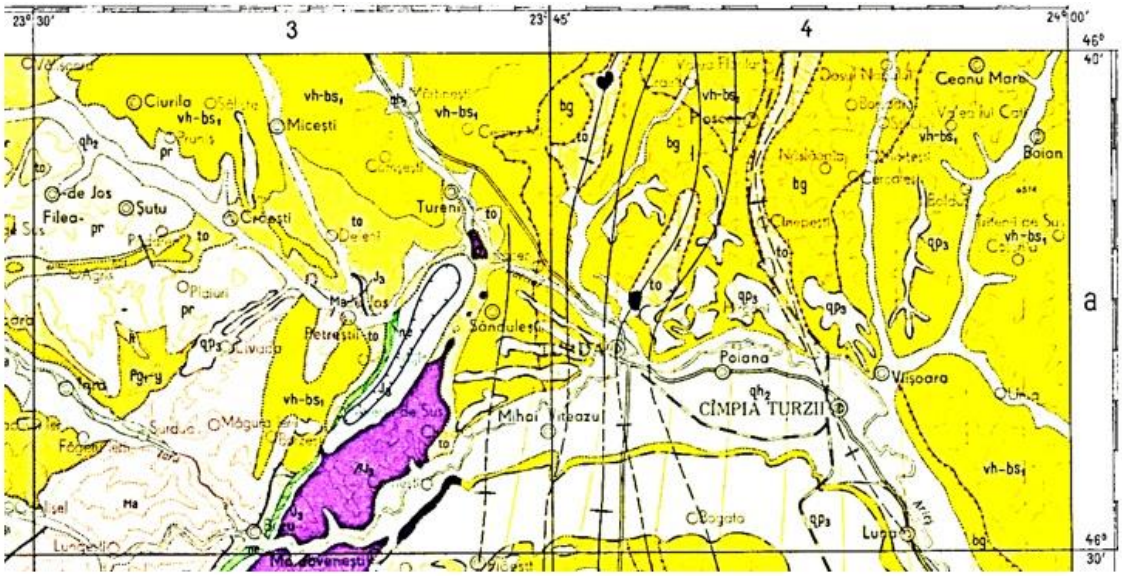

Fig.2 - Extract from geological map 1: 200000, sheet Turda, L-34-VIII, perimeter $46^0$40'-$46^0$30' and $23^0$30'- $24^0$00', 1967-IGR

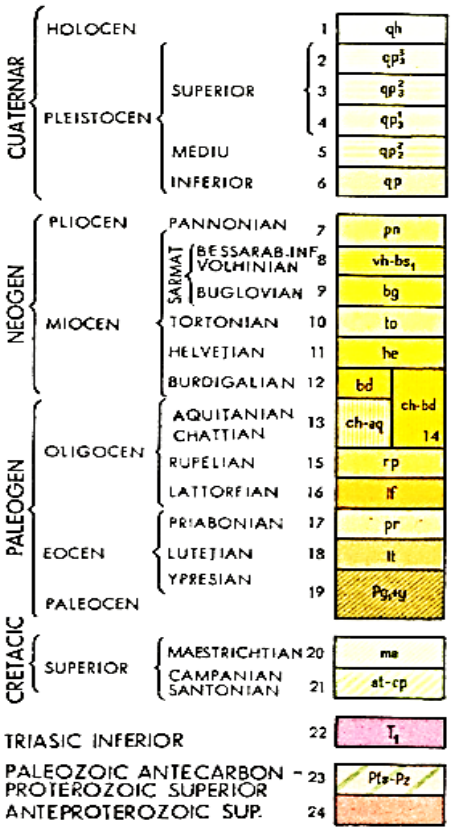

Fig. 3 – Legend for maps from fig.1-2.

In fig. 1 and fig.2 are extracts from geological maps scale 1: 200000, sheets Cluj and Turda. In fig. 3 is geological legend and in fig. 4 is geological map of Romania, scale 1: 1000000 with indexing of maps scale 1: 200000. Also is represented the study area for geophysical parameters (square of 200 Km * 200 Km).

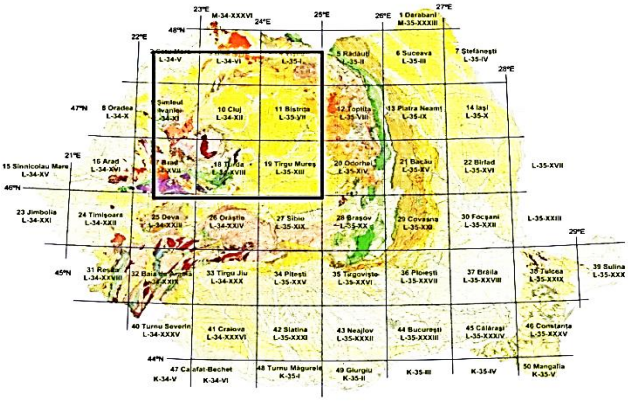

Fig.4 - Geologic map of Romania (after Geological Institute of Romania – 1978).

We complete the geophysical and geological information from the digitized maps at the level of Romania and made multiparametric maps using the Surfer program, interpolated with the Kriging method, using a suitable grid that would not lose anything in the resolution of the initial map but in the same time not to introduce unnecessary and redundant information.

Also, we used seismic profiles (fig. 5) completed with geomagnetic/gravity data (Stefanescu M.- 1985 - IGR) and boreholes in the study area with petrographic characterization of the formations.

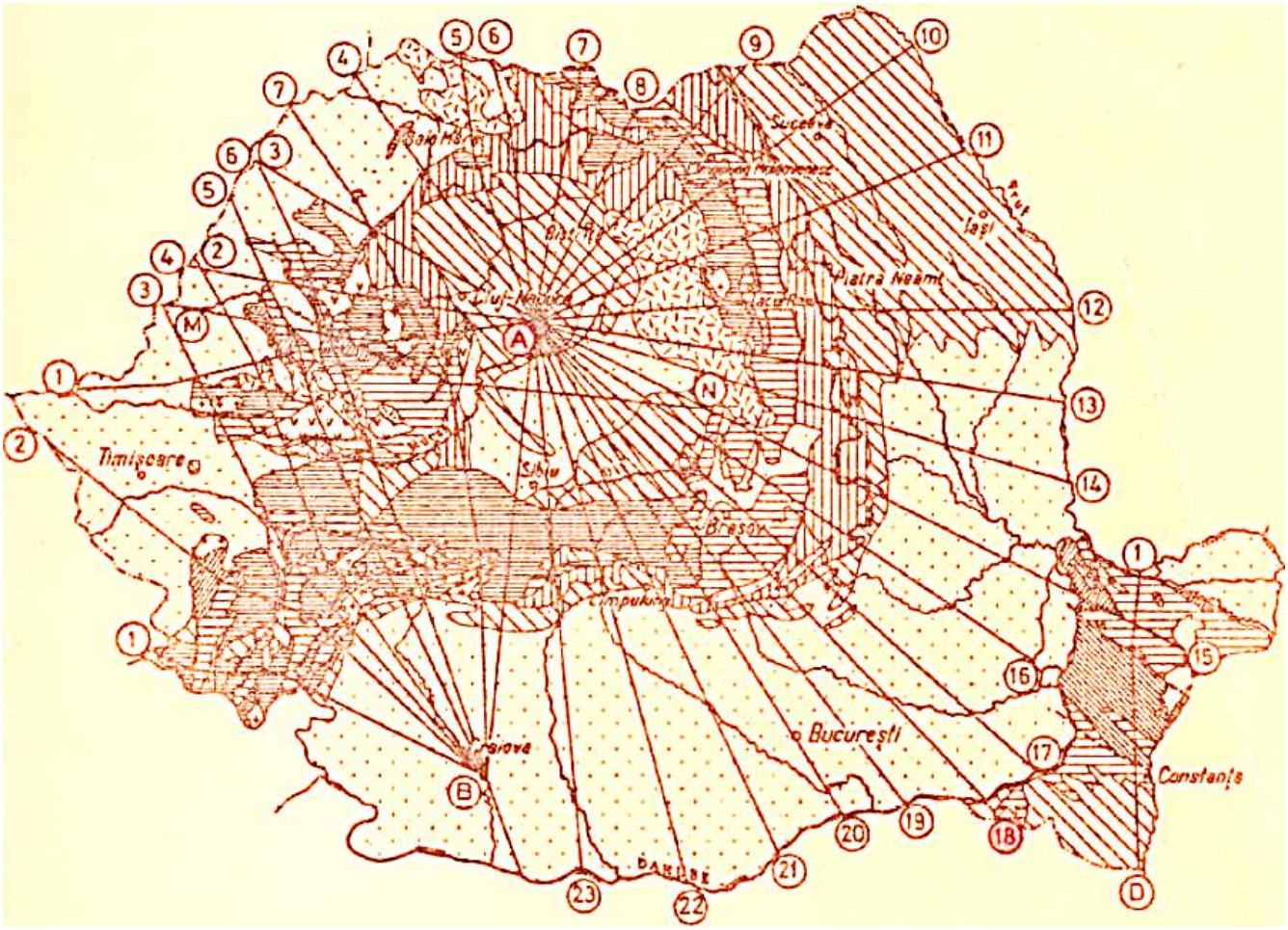

Fig.5 – Seismic profile on map of Romania (after Stefanescu M. et.al. - Geological Institute of Romania – 1985).

Data from geologically interpreted of seismic sections were included in a database, by overlaying a grid and digitizing the information as in the figure 6.

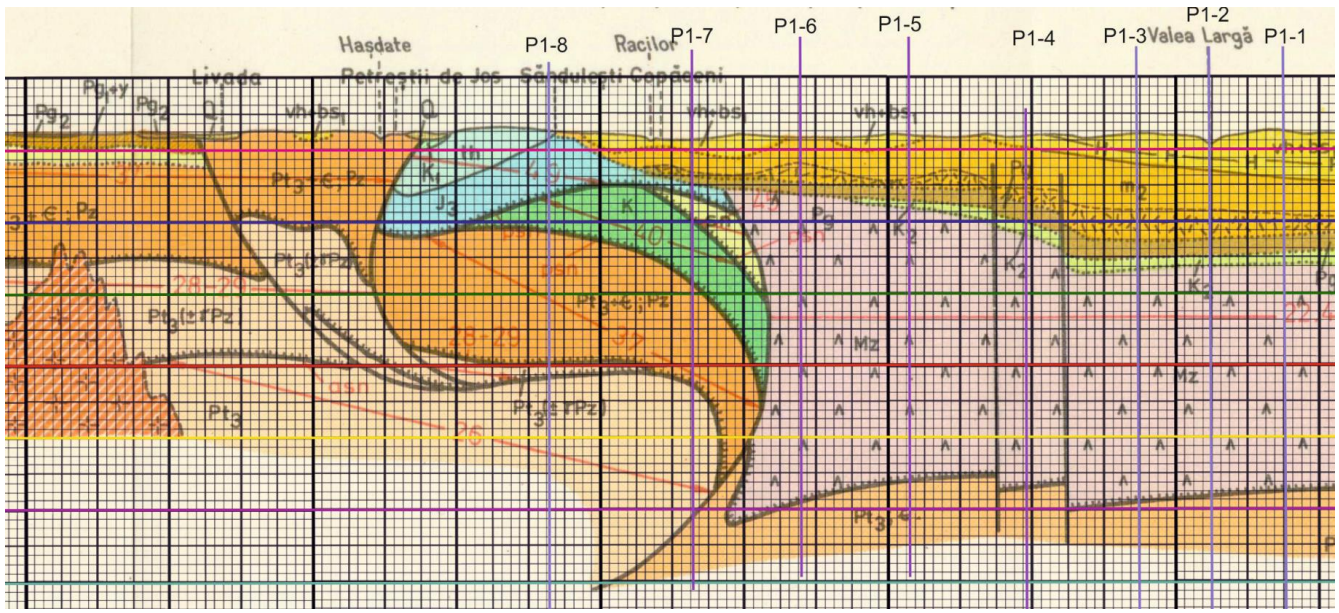

Fig.6 – Digitizing the information from geologically interpreted of seismic sections (after Stefanescu M. et.al. - Geological Institute of Romania – 1985).

The boreholes in the study area with petrographic characterization of the formations was included in Google Earth, as in the figures 7.

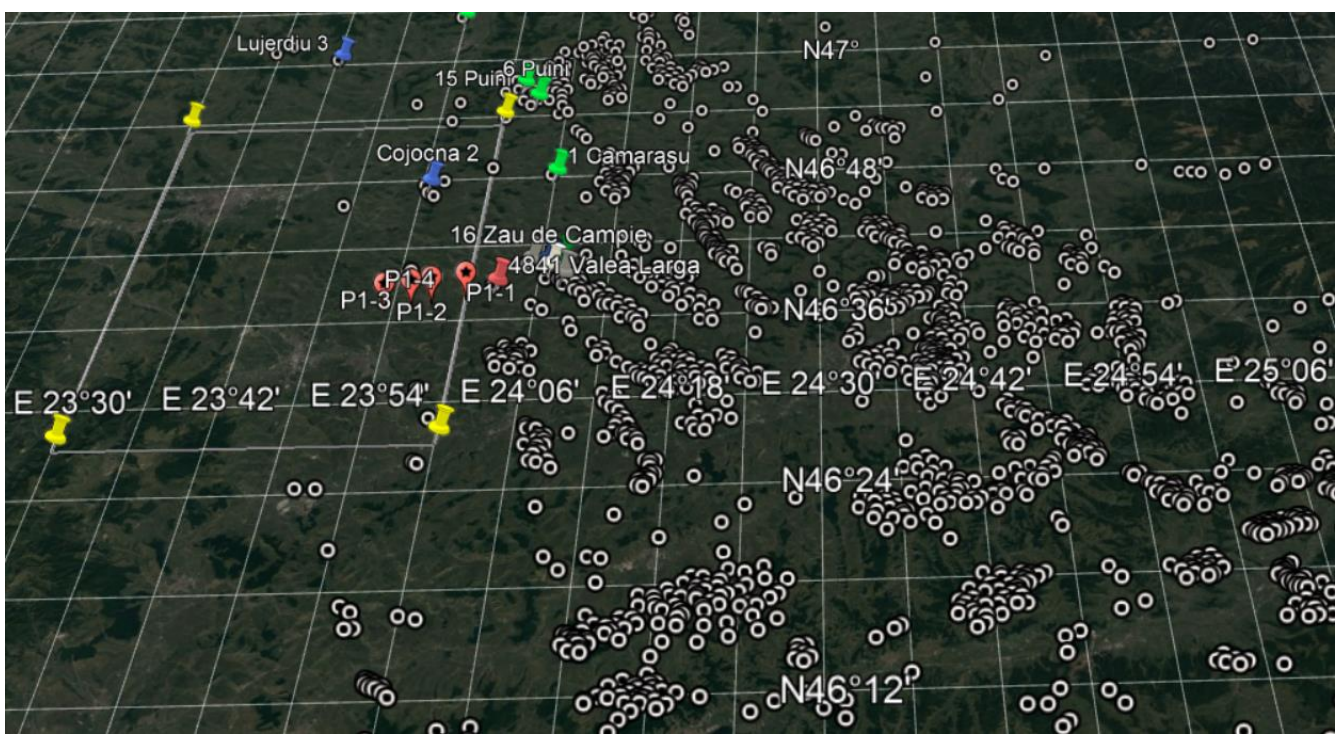

Fig. 7 – Localizations of boreholes from study area in Google Earth

N_Gauss	47-18-20.898
E_Gauss	22-23-54.686
N_S70	648379
E_S70	303314
Marcaj	
Official_w	Abram 1
On_offshor	Onshore
Operator_n	S.C. PETROM SA
Surface_la	N 47 18 20.898
Surface_lo	E 022 23 54.686
Surface_co	Digitised
Surface_or	Assumed
Spud_date	1.97401e+07
Completion	1.97405e+07
Well_class	Appraisal
Technical_	Completed
Content_st	Oil
Status_com	
Field_name	Abram
Elevation_	0
Water_dept	0
Td_m	2350
Ptd_m	0
BH_age	
Objective_	Sand and sandstone
BH_formati	
Rig_name	
Rig_contra	
Rig_type	Land rig
F31	Land
Province	Bihor
basin	Pannonian Basin
Date_comme	Estimated day and month
Objective1	Miocene

N_Gauss	47-18-10.433
E_Gauss	22-25-15.708
N_S70	648000
E_S70	305005
Marcaj	
Official_w	Abram 16
On_offshor	Onshore
Operator_n	S.C. PETROM SA
Surface_la	N 47 18 10.433
Surface_lo	E 022 25 15.708
Surface_co	Digitised
Surface_or	Assumed
Spud_date	1.98601e+07
Completion	1.98605e+07
Well_class	Appraisal
Technical_	Completed
Content_st	Oil
Status_com	
Field_name	Abram
Elevation_	0
Water_dept	0
Td_m	2265
Ptd_m	0
BH_age	
Objective_	Sand and sandstone
BH_formati	
Rig_name	
Rig_contra	
Rig_type	Land rig
F31	Land
Province	Bihor
basin	Pannonian Basin
Date_comme	Estimated day and month
Objective1	Miocene

FID_	1760
N_Gauss	46-03-22.158
E_Gauss	23-57-55.667
N_S70	506760
E_S70	419962
Marcaj	
Official_w	Brosteni 1
On_offshor	Onshore
Operator_n	SNGN ROMGAZ
Surface_la	N 46 03 22.158
Surface_lo	E 023 57 55.667
Surface_co	Digitised
Surface_or	Assumed
Spud_date	1.97001e+07
Completion	1.97005e+07
Well_class	New-field wildcat
Technical_	Plugged & Abandoned
Content_st	Dry
Status_com	
Field_name	
Elevation_	0
Water_dept	0
Td_m	1350
Ptd_m	0
BH_age	
Objective_	
BH_formati	
Rig_name	
Rig_contra	
Rig_type	Land rig
F31	Land
Province	Alba
basin	Transylvanian Depres
Date_comme	Estimated day and

Fig. 8 – Examples of information of boreholes accessed from Google Earth.

The geophysical and geologic interpretation of the data by forward and inverse modeling gave the following results:

The sedimentary succession can be subdivided into 7 layers with a total thickness of up to 22 km. It is composed of the Carpathian nappe pile and the post-collisional (post-Early Cretaceous) Paleo to Neogene Transylvanian Basin, which covers the local Late Cretaceous to Paleogene Tarnava Basin [Krézsek C, 2006].

The lowest layer is a low-velocity zone with 5.30 km/s and other with 5.5-6.0 km/s, sandwiched between higher-velocity layers.
Different crustal blocks characterized by clearly distinct geometries and velocity structures were identified: the Tisza-Dacia crustal block, which underlies the Transylvanian Basin and most of the Eastern Carpathian Orogen and the Moesian Platform crustal block, which underlies the Focsani Basin.
The sedimentary sequence is composed of the East Carpathian flysch nappes, the Neogene infill of the Transylvanian Basin.

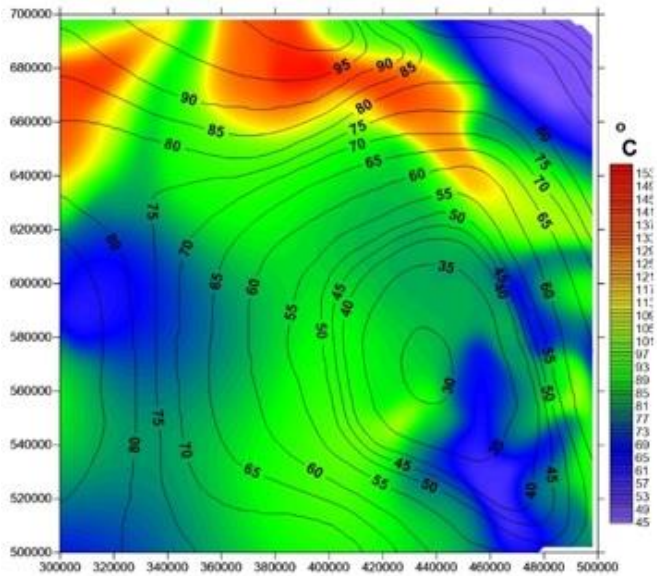

Fig.9 - Temperature of 3000m, with colour shades and overlaps with isolines geothermal flow (mW/m^2) with values written over them [data from Veliciu S, 1985]

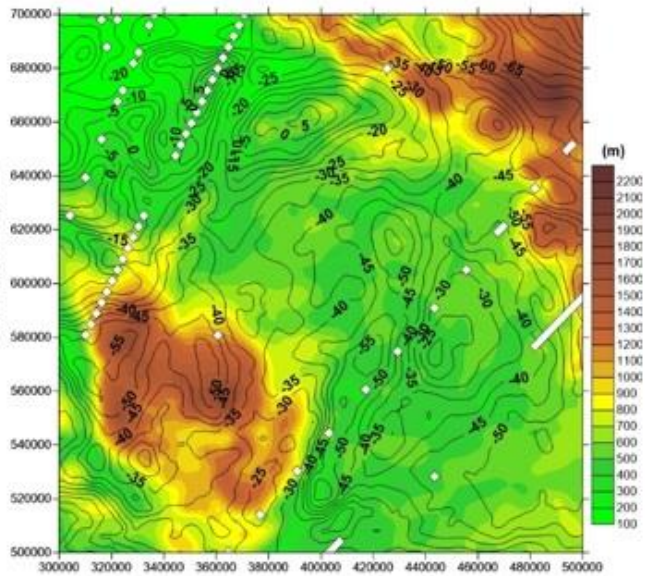

Fig.10 - The altitude with colour shades and overlaps with isolines of Bouguer anomaly (mgal) with values written over them.

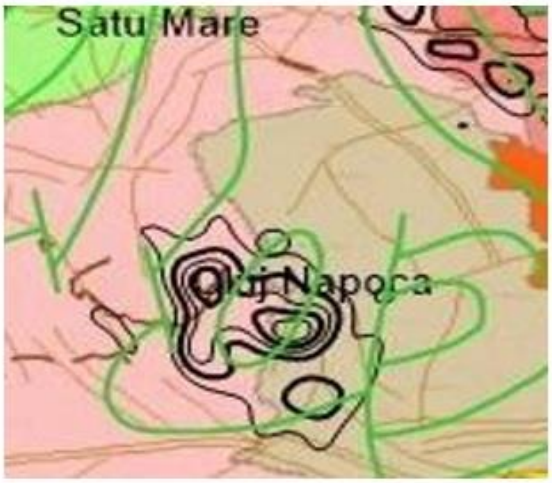

Fig.11 – The difference between quasi-geoid and geoid (with black) superimposed over structural elements and deep of Moho surface (green)

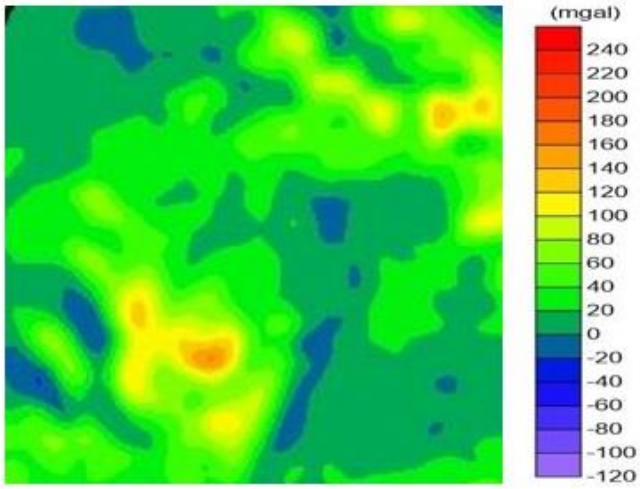

Fig.12 – Free Air anomaly (mgal) [data from http://bgi.obs-mip.fr]

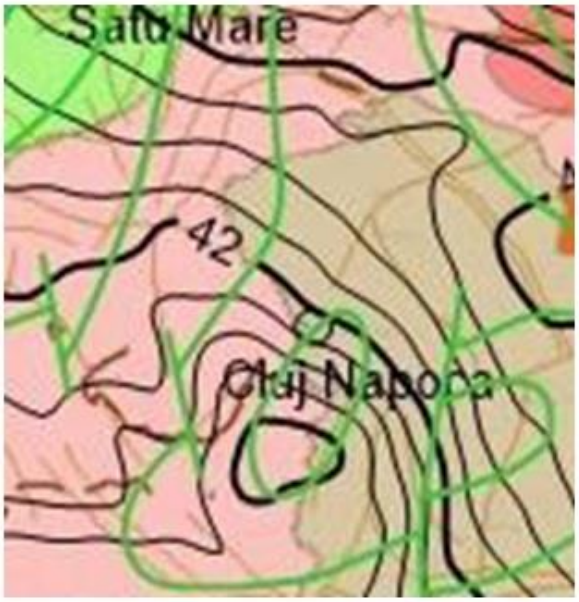

Fig.13 - Geoid (m). [data from http://bgi.obs-mip.fr]

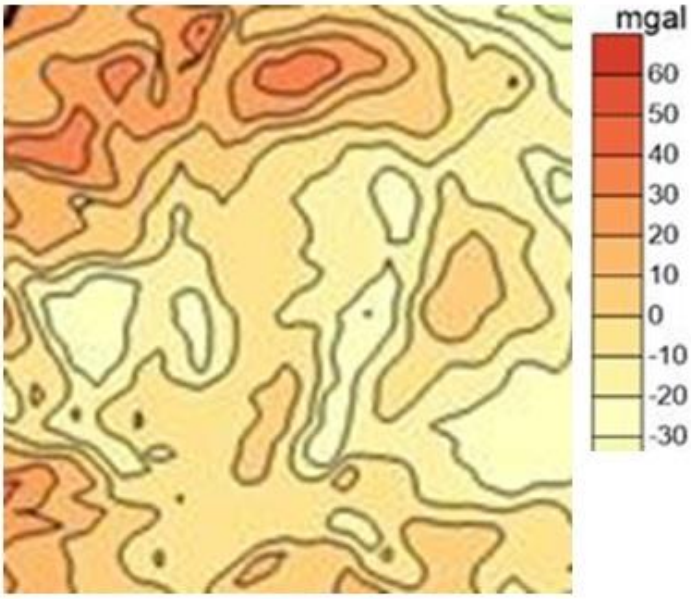

Fig.14 – Rezidual Bouguer anomaly (mgal) [data from http://bgi.obs-mip.fr]

In the figures 9-14, we have exemplified where we performed geophysical studies, taking into account the following parameters: temperature 3000 m, geothermal flow, Bouguer anomaly, Free Air anomaly, altitude of the geoid to the ellipsoid and topography from the studied area. The gravimetric parameters [data from http://bgi.obs-mip.fr] were compared with the geothermal parameters and the tectonic elements in the studied area.

In fig. 15-16 we made the map vertical geomagnetic map ΔZ and vertical geomagnetic anomaly map ΔZa from digitalized data after maps from I.G.R. – 1983.

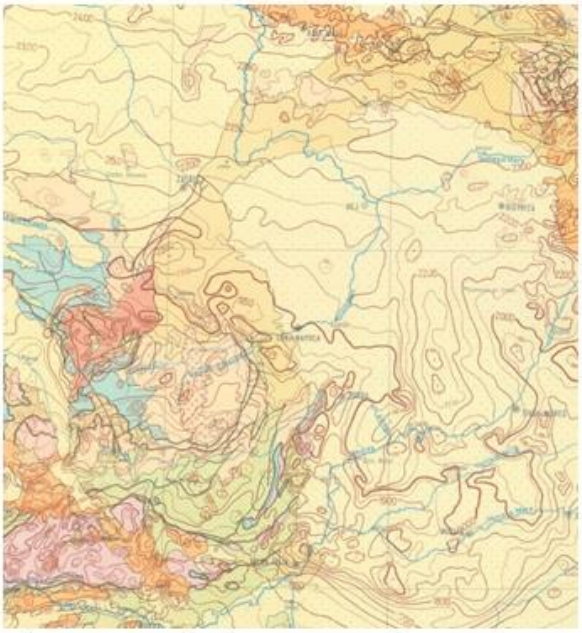

Fig.15 – Vertical geomagnetic map ΔZ

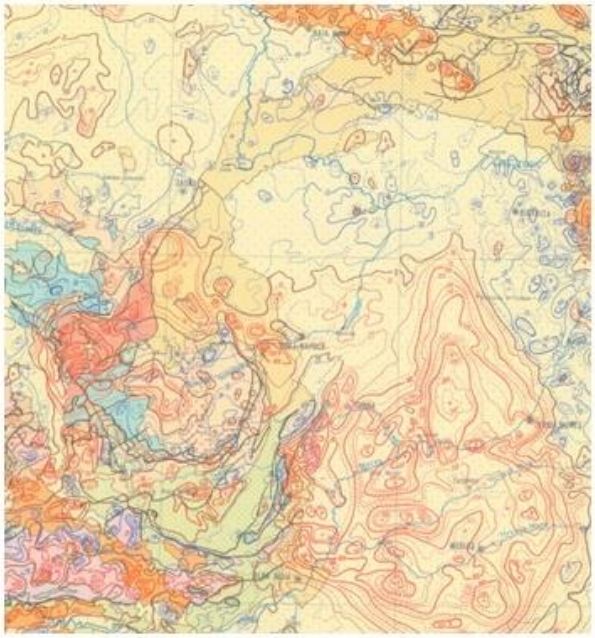

Fig.16 – Vertical geomagnetic anomaly map ΔZa

3. CONCLUSION

The tectonic evolution of the Transylvanian Basin can be treated, in accordance with [A de Leeuw,2013; Sandulescu M.,1984] in a synthesized manner and in accordance with geophysical information.
The Transylvanian Basin basement is shared with the Eastern Pannonian Basin and consists of a stack of basement-involved thrust sheets, which were assembled by the Middle Cretaceous. These involve Paleozoic crystalline units, ophiolites and island-arc volcanic and sedimentary cover of Triassic to Mid Cretaceous age.
The assembled tectonic units evolved from a Triassic to Lower Cretaceous intercontinental rift.
Was differentiate three basial domains: foredeep basins formed in the front of the Carpathian accretionary wedge, wedge-top basins on the Carpathian accretionary wedge and intra-Carpathian basins formed on top of the backstop.
The ophiolites and their cover do not appear to be significantly thickened by subduction-related thrusting in the subsurface of the central Transylvanian Basin.
Alternatively, they are relatively thin oceanic successions abducted onto the passive margin of Dacia were not involved in the subduction.
The deepening of siliciclastic deposition may be related to the onset of Middle Cretaceous subduction of the "Transylvanian Ocean" which, in turn, triggered increased subsidence in the foredeep area of the Transylvanian subduction zone.
The complex geological aspects begin to be clarified once the Geological Maps 1: 50,000 were made. There is a marginal area in the North-East part, which is a monocline which sinks to the South and South-East. This marginal area is delimited by the sloping area through an important fracture, in the direction of Valley Calda - Gadalin - Gherla. Southwest of this fracture is the area with salt.
The eastern marginal zone between Cluj and Turda is a succession of monoclines falling to the East or North-East, which is a remnant of the connecting area between the Zlatna Basin and the Transylvanian Basin interrupted by the Mesozoic calcination Gorge Turzii - Sandulesti, . This lifting continues inside the Transylvanian Basin, under the Miocene sediments, with Puini lifting.
Recent survey shows a structure of salt that was born in at least two tectonic stages, as the initial salt are flawed and cracked by a younger tectonic stage. To solve some details of the geothermal potential of the NW part of the Transylvanian Basin it is essential to know the geophysical parameters and to estimate the lithospheric volumes of the geothermal energy storage as well as the transmission mechanisms, in accordance with [Qiang S, 2017]. This is possible by using an iterative software for modelling-inversion (for example, 3D Geomodeller) in which all data needs to be entered in a specific format. Only after such a 3D study [Asimopolos L, 2017; https://www.intrepid-geophysics.com/ig/index.php?page=Home] can we reach a conceptual model as well as the mechanical properties and porosity of the rocks.

4. ACKNOWLEDGEMENTS

We thank for support by the Ministry of Research for financing of the project: The realization of 3D geological / geophysical models for the characterization of some areas of economic and scientific interest in Romania, with Contract no. 28N / 2019.
Also, we address our thanks for scientific publications, reports and gravity data, to: Bureau Gravimétrique International (BGI), International Association of Geodesy (IAG) and International Centre for Global Earth Models (ICGEM).

REFERENCES

Asimopolos L., Asimopolos N.S. (2017). Filtering Gravity Data Through Polinomial Trend Surfaces DOI: 10.3997/2214-4609.201702625, 5pp.

Hauser F., V. Raileanu, W. Fielitz, C. Dinu, M. Landes, A. Bala, C. Prodehl (2007). Seismic crustal structure between the Transylvanian Basin and the Black Sea, Romania, Tectonophysics 430 (2007) 1–25

Krézsek C., Albert W. Bally. (2006). The Transylvanian Basin (Romania) and its relation to the Carpathian fold and thrust belt*:* Insights in gravitational salt tectonics. Mar. Pet. Geol 23\4 405-442

A. de Leeuw, S. Filipescu, L. Maţenco, W. Krijgsman, K. Kuiper, M. Stoica (2013). Paleomagnetic and chronostratigraphic constraints on the Middle to Late Miocene evolution of the Transylvanian Basin (Romania): Implications for Central Paratethys stratigraphy and emplacement of the Tisza–Dacia plate- Global and Planetary Change 103 (2013) 82–98

Oraseanu I. (1998). Hidrogeological recherches for still waters in codru Moma and Padurea Craiului (Apuseni Mountains, Romania). Proeedings of the Int. Symp. Mineral and thermal groundwater, Miercurea Ciuc, Romania, 24-27 june, p. 223-232.

Oraseanu I., Iurkiewicz A., ed. (2010). Karst hydrogeology of Romania, Oradea

Papp, D. C., Cociuba, I. (2011). Application of stable hydrogen isotope models to the evaluation of groundwater and geothermal water resources: case of the Pădurea Craiului limestone aquifer system, Geochemistry: Exploration, Environment, Analysis, 11, 2, 79-91.

Qiang Sun, Shen-en Chen, Qiao Gao, Weiqiang Zhang, Jishi Geng, Yuliang Zhang (2017). Analyses of the factors influencing sandstone thermal conductivity, Acta Geodyn. Geomater., 14(2) (186): 173-180

Sandulescu M. (1984). Tectonica Romaniei – Editura Tehnica

Stefanescu M. et.al. from Geological Institute of Romania (1985). Seismic profiles with geological and geophysical data on territory of Romania.

Veliciu S., Negut A., Vamvu V. (1985). Geothermal map of Romania (Geothermal flow – [mW/m^2], Temperature of 3000m-[^{0}C], scale 1:1.000.000), Geological Institute of Romania, 1985.

http://bgi.obs-mip.fr

https://www.intrepid-geophysics.com/ig/index.php?page=Home

GEOPHYSICAL AND GEODETIC CONSIDERATIONS REGARDING THE EARTHQUAKES ZONE FROM VRANCEA, ROMANIA

Asimopolos N. S.[1] and Asimopolos L.[2]

[1] *Dr., Regional Geology Department, Geological Institute of Romania, Bucharest*
[2] *Dr., Geomagnetic Observatory Department, Geological Institute of Romania, Bucharest*
Email: asi_nata@yahoo.com, natalia.asimopolos@igr.ro

ABSTRACT:

The Vrancea seismological area is located in the Oriental Carpathian region, known as the "Carpathians Curvature". Within the active geodynamic region two types of major geotectonic units can be separated: the orogen and platforms “vorland units”.
Characteristic of Oriental Carpathians is the structure of geologic nappes in both the internal and external areas of the chain. Thus, we distinguish from the inside (west) to the outside (east) the following systems of nappes: Transylvanian nappes, external Dacites (with Cretaceous tecto-genesis) and Moldavian nappes (with Miocene tectono-genesis).
Periodically, in the Vrancea area there are intermediate but also normal earthquakes, of which at least two per century are catastrophic, so we can recall the 1940 earthquake with the magnitude of 7.4 and 133 km, the 1977 magnitude 7.2 and the depth of 100 km, 1986 with a magnitude of 7.1 and a depth of 130 km, 1990 with a magnitude of 6.7 and 6.2 and a depth of 90 km, respectively 79 km and one in 2004 with a magnitude of 6 and a depth of 98.6 km, their effect was on large areas in Romania, Bulgaria and the Republic of Moldova, so in the Carpathian-Balkan area, but also felt in Poland and Hungary.
Thus, the Vrancea region (with center at 45.7ºN, 26.5º E) appears as an isolated area, the epicenters of earthquakes being arranged in a completely continental environment in a triangle with the sides of about 30 km.
In this paper, we draw a detail of the depth structure in the Vrancea area where it is supposed to be the contact of three large tectonic units: the East European Platform, the Moesian Platform and the intra-arc basins - the Transylvanian Basin and the Pannonian Basin, in fact the Intra- Alpine. We also present details of the crust in the Vrancea area and adjacent areas.
The data used in this study is obtained by digitizing geophysical and geological maps and extracting data from these, in particular gravimetric and magnetometry data, along four seismically and geological sections from the Curvature Carpathians.

KEYWORDS: earthquakes zone, geophysical data, geodetic data, seismic profiles

1. INTRODUCTION

The purpose of this paper is to show the importance of geophysical data filtering and filtering parameters, in correlation with the depth from which we want to obtain information regarding the distribution of geological structures.
On the territory of Romania there are three distinct lithospheric units: The East European plate, the Moesic plate and the Intra Alpine plate, which meet directly in the Vrancea area. The mutual contact of Intra Alpine plate Moesic plate shows clear subduction relationships associated with the Benioff rupture system. The intensification of subduction in the Vrancea segment is due to the faster advance of the Black Sea microplate, pushed by the Turkish microplate, which has the highest displacement speed in the whole of the Mediterranean basin.

In time there was many geodynamic hypotheses. One hypothesis is involving a NE-SV paleo subduction, the south-east edge of the plate being decoupled from the rest of the plate. Others involves the production of the Vrancea earthquakes not within the gravitational fall plate fragment, but in the area of separation (approximately vertically) between it and the rest of the slab.
However, the two hypotheses have gaps about the material above the breaking surface of the plate fragment in gravitational fall respect to the rest of the plate (40 to 70 km deep), depths that do not admit astenospheric material nor lithospheric material. The particular seismicity of the Vrancea region, the crust deformations and the lack of volcanism usually associated with the subduction zones have been channeled in three directions in the conception of the various researchers: subduction of the ocean crust "in place", ocean crust rupture and roll-back, respectively lithospheric delamination.
The greatest weight in literature is supported by works in which the scenario of a subduction of an oceanic lithosphere (Roman, 1973, Constantinescu et al., 1973, Airinei, 1977, Fuchs et al. Constantinescu and Enescu, 1985) are based on seismological studies and are generally velocity models that take into account simplified geological models without taking into consideration the complex of possible sources of anisotropy from the crust-mantle and lithospheric-astenosphere mantle.
Based mainly on seismic surveys, models of breaking the lithospheric slag were developed, followed by a delamination of the lithospheric shell along a horizontal plane under the crust, and the roll-back to the SE associated with increasing the slope of the underlying lithosphere (Sperner et al., 2001, Knapp et al., 2005) or the existence of a triple unstable junction (Beşuţiu, 2001, 2006).

2. THE GEOLOGICAL STRUCTURE OF THE VRANCEA AREA

Vrancea area is located in the Carpathian region, known as the "Oriental Carpathians Curve". Within the active geodynamic region two types of major geotectonic units can be separated (Săndulescu, 1984): orogen and platforms (vorland units).
Characteristic of Oriental Carpathians is the structure in nappes both the internal and external areas of the mountain chain. Thus, we distinguish from the inside (west) to the outside (east) the following systems: Transylvanian nappes, external dacites (with Cretaceous tectono-genesis) and Moldavian nappes (with Miocene tectono-genesis).
The Transylvanian nappes (put in place at the end or during the Albian age), the most internal and the highest in the area of the Carpathian-Mesozoic region of the Oriental Carpathians, are the nappes of Mesozoic and/or Triassic, Jurassic and Cretaceous sedimentary formations, mostly calcareous and marno-greasy. Jurasic thickness being moderate, ranging from 800-1000 m, they tectonic cover the wildflisch formation of the bucovinian nappes (the highest nappe of the Median Dacites) in Haghimaş and Perşani mountains.
Median Dacian nappes (East-Carpathian Central nappes) are shear blades of Pre-Cambrian and Paleozoic metamorphic formations covered by Mesozoic sedimentary formations. The nappes cover each other and from top to bottom (in the retro-tectonic sense from the inside to the outside) the Bucovinian nappe and several infra-Bucovinian nappes, each characterized by specific sedimentation sequences at one or more levels.
The tectono-genesis, revealed by several faults, occurred in the Albian-Aptian period, with two moments of maximum: Intra-Aptian and the end of the Albian.
The Dealu-Mare fault - a vertical and a horizontal composite fault - which confines the Vlădeni corridor to the south, separates two sectors in the innermost part of the curvature of the Mesozoic lens, due to the different erosion of the mentioned fault - affects structurally different units. To the north of the Dealu Mare fault, only the Bucovinian and the Transylvanian nappes are located in the lower and further departed compartment west of the crystalline-Mesozoic area.
The crystalline-Mesozoic zone at the inside of the curvature maintains a real homogeneity of geological composition (though it is fragmented by important transversal faults), structurally without a limit between the Oriental Carpathians and the Southern Carpathians.
Curbicortical Flish, consists mainly of predominantly cretaceous deposits which sometimes develop flish (Albian age), with thicknesses not exceeding 1200 m.

The hypotheses at the level of Romania launched in the conception of the authors of St. Airinei (1977), C. Roman (1973), L. Constantinescu (1973, 1984), were the existence of several microplates (some subplates or even blocks), located between major Eurasian (or East European) and African major plates.

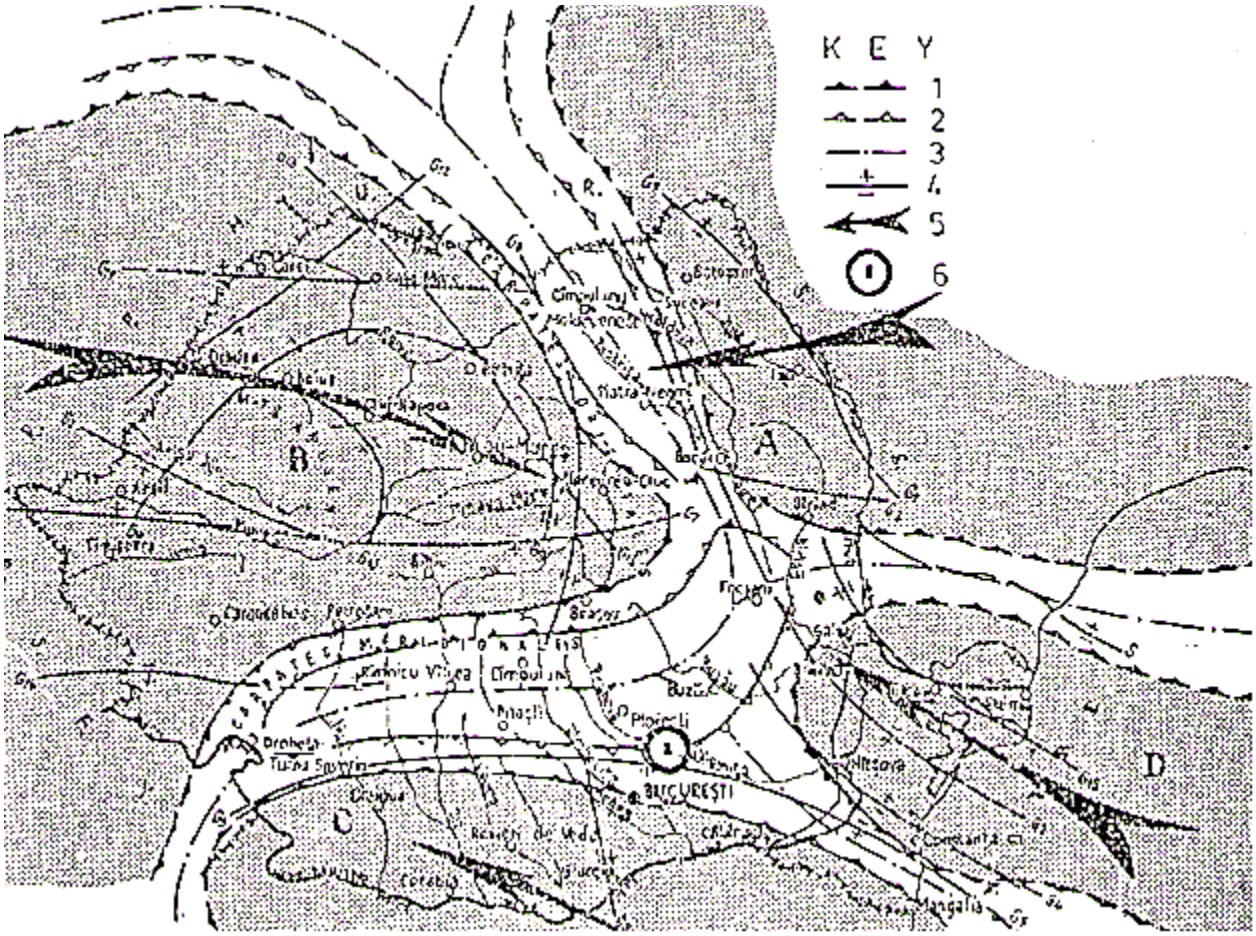

Fig. 1. The system of the lithospheric segments on the territory of Romania in the current positions and with the meanings of motion, viewed in the context of the tectonic plate concept (after St. Airinei, 1977).

1. limit of maximum regional gravity anomaly
2. limit of regional gravimetric anomaly
3. gravimetric axis
4. field of crust faults
5. directions of movement of lithospheric plates and microplates
A-extremity of SV of the Eurasian Plate; B- inter Alpin microplate;
C-Moesic microplate; D - Black Sea microplate.

Interpretation of the eastern data of the long seismic segment Vrancea 2001 (450 km) (Hauser et al., 2007) indicated a multi-layer structure with variable thicknesses and velocities. The sedimentary stack comprises up to 6 layers (L1-L6) with seismic speeds of 2.0-5.9 km / s and reached a maximum thickness of over 15 km in the Focsani Basin Area. The underlying crust (L7-L10) showed total variations of considerable thickness as well as its individual subdivisions. The model shows the structure of these blocks at lateral speed along the seismic line that remained nearly constant at about 6.0 km / s and 7.0 km / s above Moho.

Under the Transylvanian basin, the crust appeared to be 34 km thick, and under the Carpathians, Moho is deeper than 41 km, reaching 46 km in the Focsani basin, but the crystalline crust does not exceed 25 km in thickness and

is covered by up to 15 km of sedimentary rocks. The crust in northern Dobrogea reaches a thickness of approximately 43 km and has been interpreted as the thick crust in Eastern Europe, which is usually thin 1 km to 2 km (Hauser, 2007, Knapp, 2005).

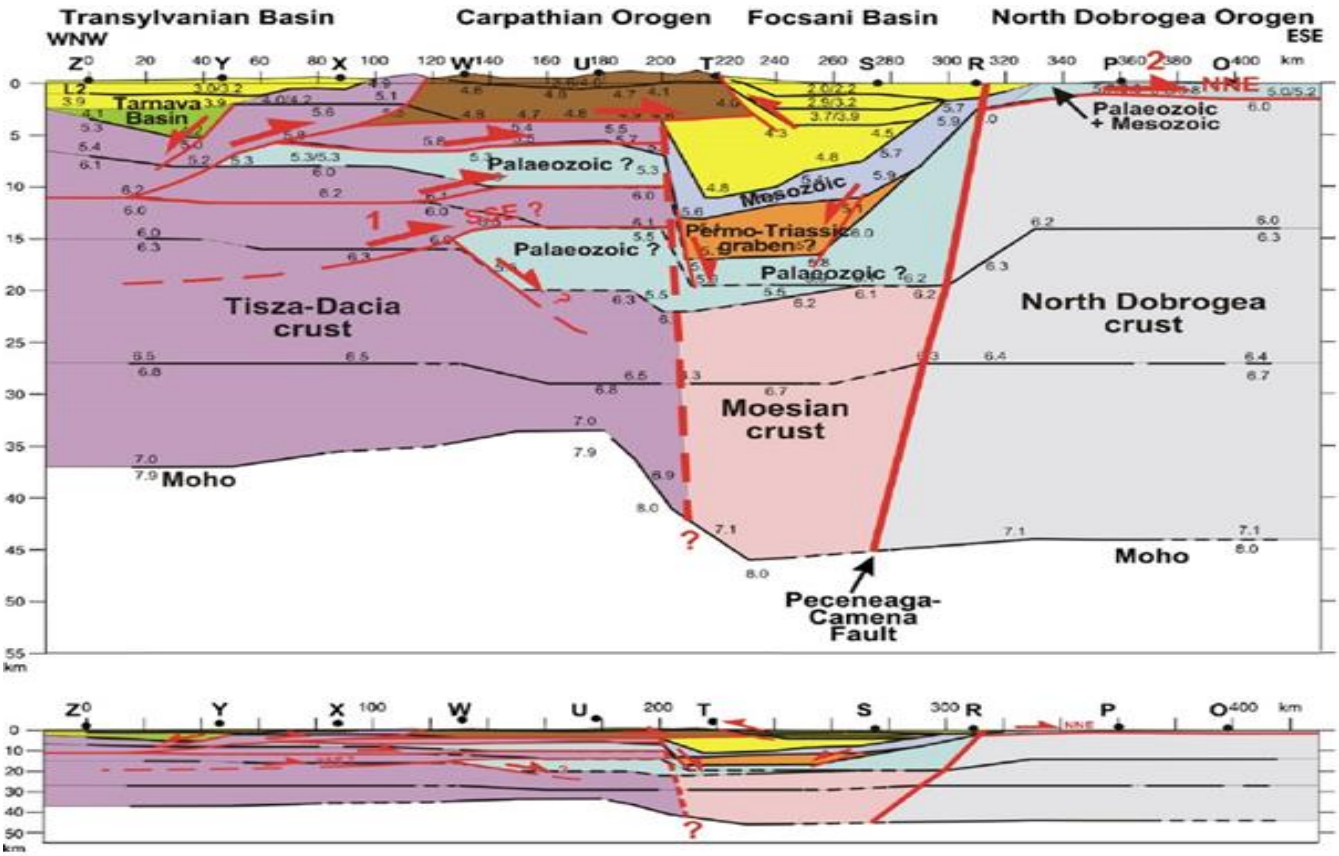

Fig. 2 - Crustal P-wave cross section along the WNW-ESE profile in Romania. P-wave velocity in km/s (from Hauser, 2007).

Along the Peceneaga - Camena fracture, as well as its extension to the NW, south of Focsani, there are two continental lithospheric portions with different net features similar to the contacts between two Paleozoic platforms, made by the known Teyssere - Tornquist. The differences are also found in the south-eastern prolongation of the fracture in terms of the thickness of the consolidated crust (without sediment), from the Black Sea to the Turkish coast.

The Peceneaga - Camena fault and its extension to the NV and SE are found both in the crust and subcrustal field, it is a major active fracture, near it along the proximity of the contact and the seismological data show that there are earthquakes, both normal and deeper 60 km.

3. THE GEOPHYSICAL STUDY OF THE VRANCEA AREA

The data used in this study is obtained by extracting geophysical data, in particular gravimetric and magnetometry data, along four geological sections from the Curvature Carpathians.

It is difficult to estimate the physics-geological significance of anomalies due to the existence of numerous density contrasts, disposed at different vertical levels. Between the different sections of the foundation there are no large contrasts of density, as it results from the drilling data or outflow areas. The density variation range for the base formations ranges from 2.70 to 2.80 g / cm3. Due to this fact, gravimetric research, although it brings information

on the structural elements, makes it difficult to emphasize the junction between the foundation sectors with a different tectonic genesis.
The gravity field shows a significant variation, from -110 mgal (in the Vălenii de Munte area) to -20mgal (in the Sfântu Gheorghe area). Such a variation cannot be attributed to the local effects of the surface of the crust but to the regional effects caused by much deeper sources of lithospheric nature.
The gravimetric minimum in the Odobeşti-Focsani sector corresponds to the major depression of the Carpathians of the Curvature, clogged with thick Sarmatian-Pliocene deposits (Focsani Depression).
Fly and molasses formations, as well as sedimentary formations in platform screens show that they are very poorly magnetized. Andesitic tuffs, occurring at different depths, are responsible for the local magnet maxima and gravimetric minima.
Regional magnetic anomalies are given by foundation segments with a different petrographic position.
Figure 3 shows the location of the geological sections A13, A14, A15 and A18 (Ştefănescu M. et al, IGR, 1985). Interpretative section with the magnetic susceptibilities and the densities characteristic of the geological formations on the Three Sate-Fîntîni segment 192 km) within the A14 profile (Tăul Zăului-Three Sate-Vlăhiţa-Sînmartin-Plăieşu de Jos-Poiana Sărată-Fîntîni-Bălţi-Tichileşti) are in (Sandulescu M., 1984, 2009).

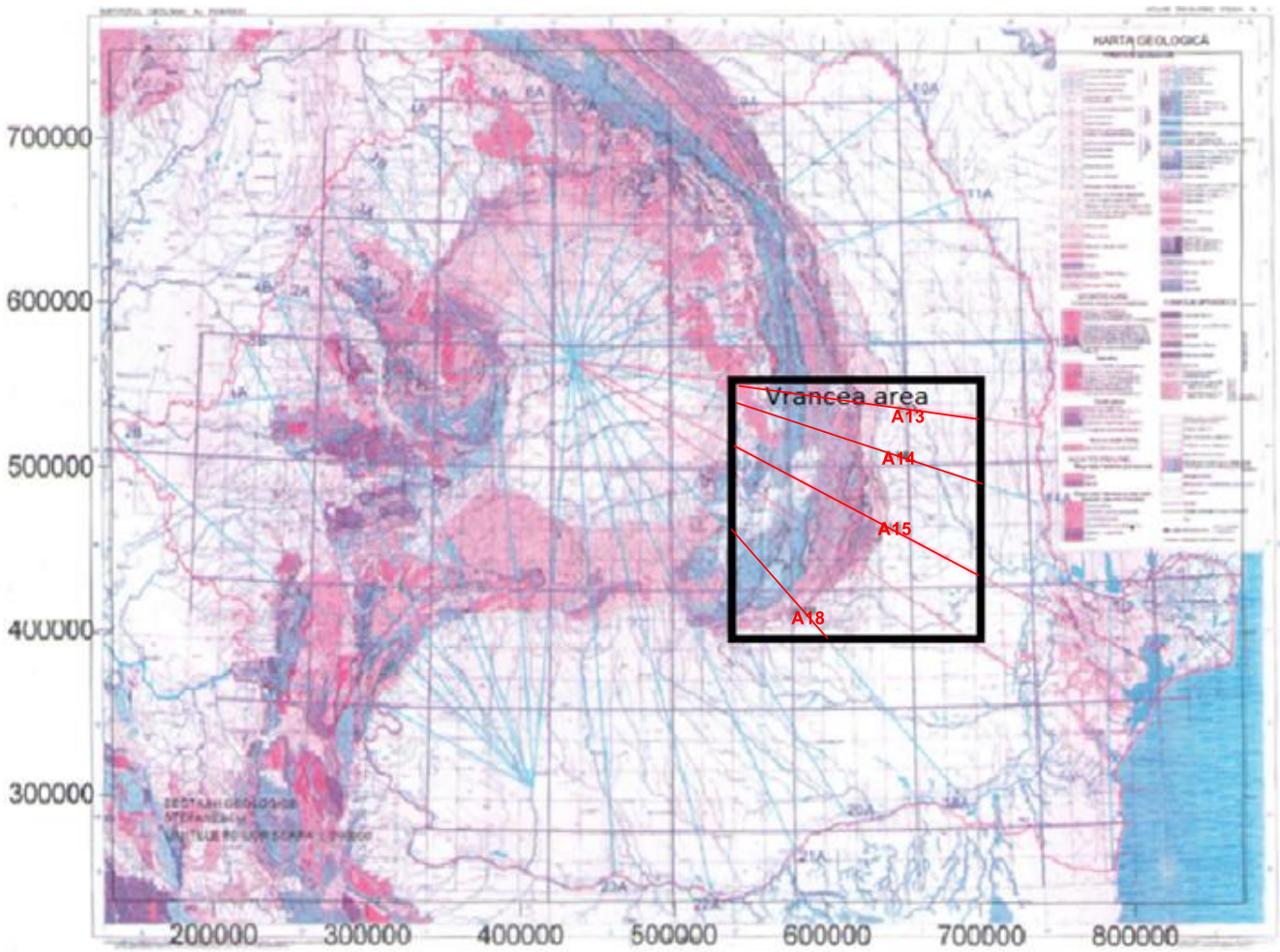

Fig. 3 - Section along seismic profile A13, A14, A15 și A18 (IGR, 1985, M. Stefanescu et al)

After the digitization of national maps, scale 1: 1.000.000 for the vertical magnetic field ΔZ, and for the Bouguer ΔgB anomaly (density 2.67 g / cm3) we interpolated the data with the Surfer program, the Kriging method. Then

we digitized the topographic surface, the vertical magnetic field ΔZ and the Bouguer ΔgB anomaly (density 2.67 g / cm3) along the geological sections A13, A14, A15 and A18.
We made the analytical continuations in the upper half-space of the gravity anomaly for the sections A13, A14, A15 and A18, from 100m to 100m, from the level of each point on the profile to the top of + 1800m. In fig.4 is analytical continuations for the sections A13, where blue line is elevation (m) in each point, isostatic anomaly and its analytical continuations (values between -18 mGal to 43 mGal), Bouguer anomaly and its analytical continuations (values between -85 mGal to -25 mGal) and disturbing gravity anomaly and its analytical continuations (values between -95 mGal to 65 mGal)

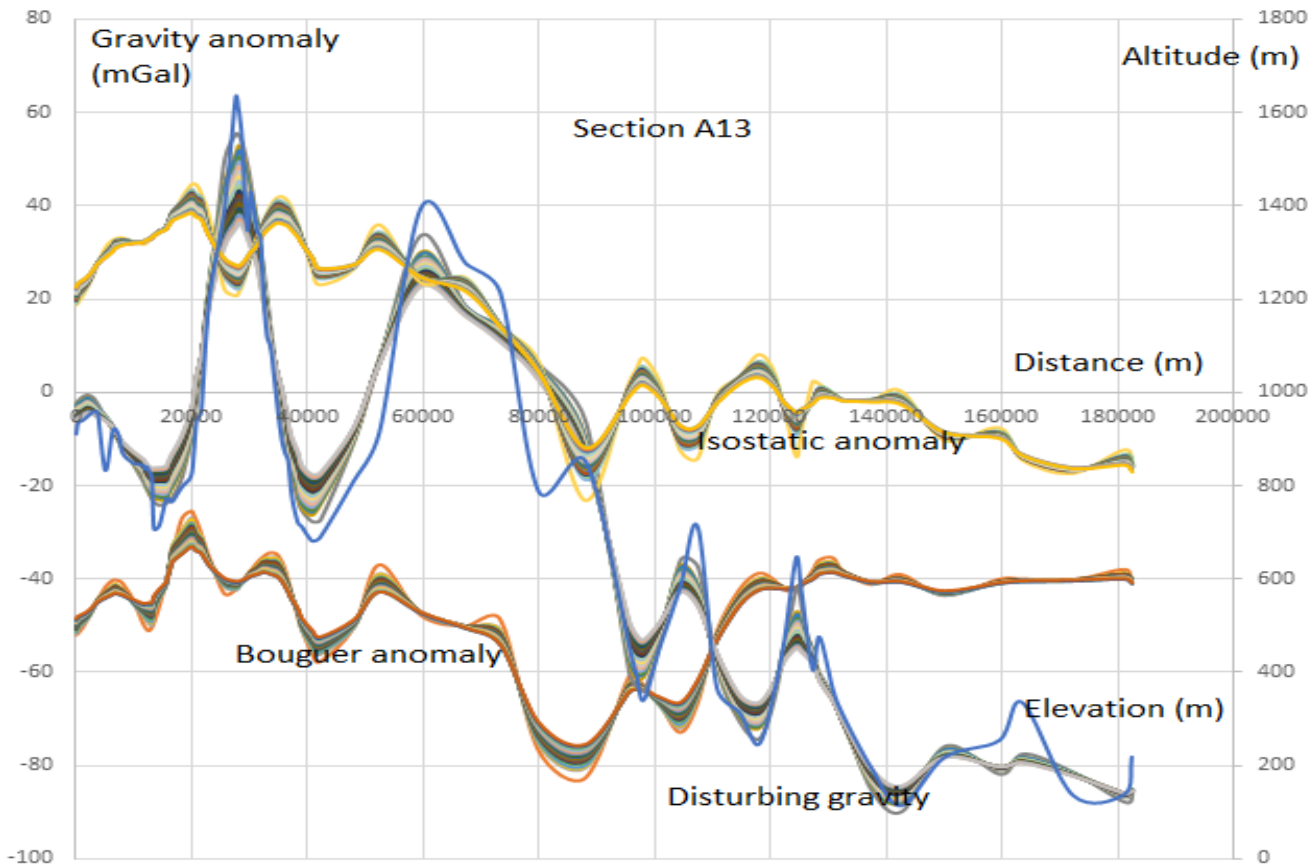

Fig.4 - Analytical continuations in the upper half-space of the Bouguer anomaly, disturbing gravity anomaly and isostatic anomaly, for the sections A13

An analysis of the Bouguer anomaly, gravity perturbation and isostatic anomaly were performed.
The horizontal axis is the distance expressed in meters, the left-hand vertical axis is in mGal and the right-hand vertical axis is in meters and is for quota representation.
Bouguer anomaly and her analytical continuation in the upper half-space of 100m in 100m are grouped as values, the differences being maximum 10 mgal. Also, the isostatic anomaly is grouped along with its analytical sequels. The disturbance of gravity and its analytical continuity correlate very well with the altitude of the points on the profile on the topographic surface (Barthelmes 2013, Balmino 2011, Blakely 1995).
It is also noted the very similar trend of the Bouguer anomaly with isostatic anomaly, for each level of the analytical continuation and for each studied section.
In Figs. 5 (A, B, C, D, E, F) and 6 (A, B, C, D, E, F) show the effects of mobile averages and tendency surfaces for Bouguer and Free Air anomalies. These images in each figure are presented in the order of the degree of

averages (the size of the window used), which is reflected in the extension and depth to which the information refers.

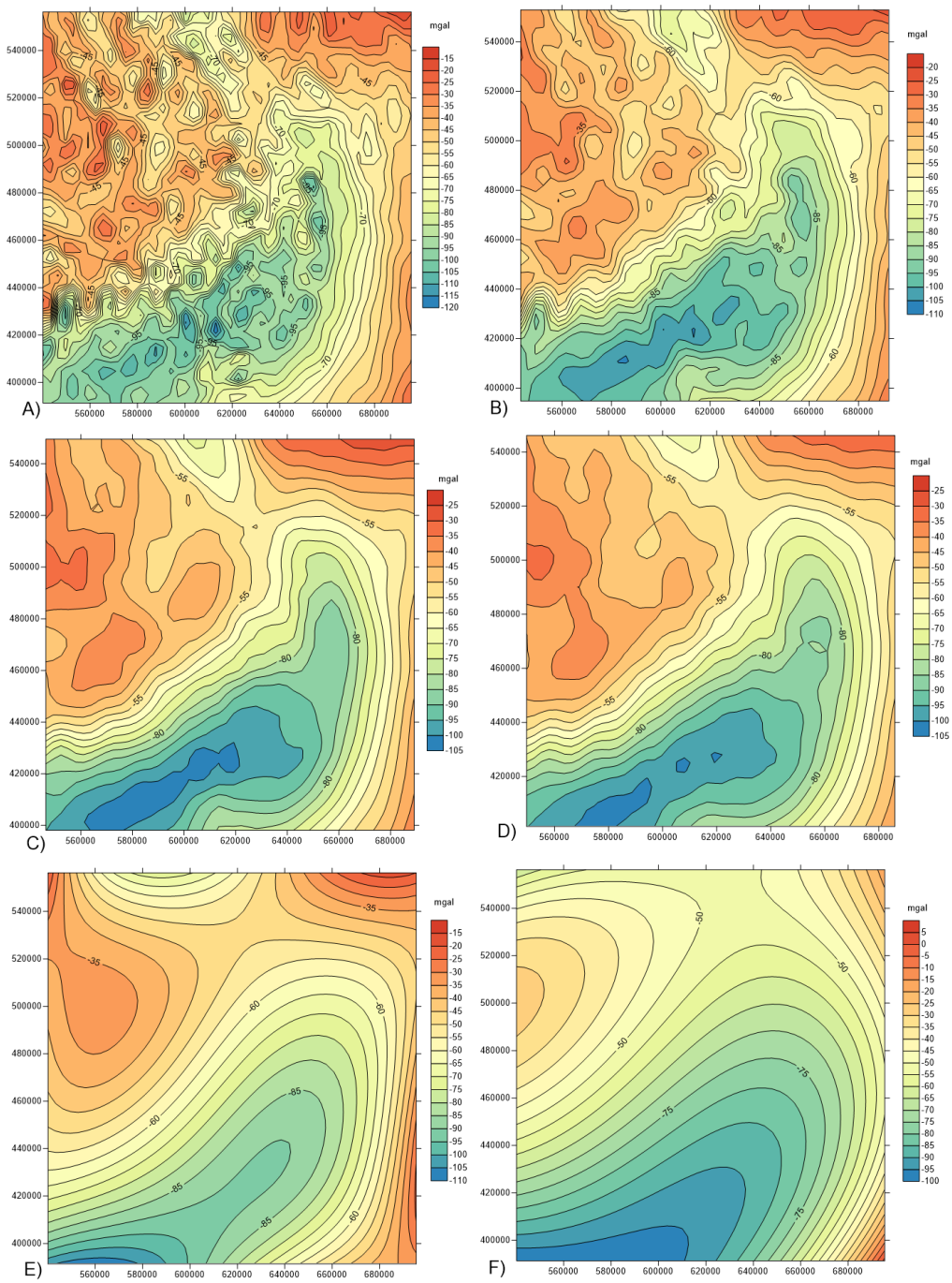

Fig. 5 - Bouguer Anomaly in the Vrancea area (coordinates are in meters – STEREO 70 and data are from BGI - International Gravimetric Bureau database):
A) The representation of unfiltered data;
B) Representation of the data averaged in moving windows of 9 values (3 lines * 3 columns);
C) Representation of the data averaged in moving windows of 25 values (5 lines * 5 columns);
D) Representation of the data averaged in moving windows of 49 values (7 lines * 7 columns);
E) The tendency surface with 6th order; F) The tendency surface with 3rd order.

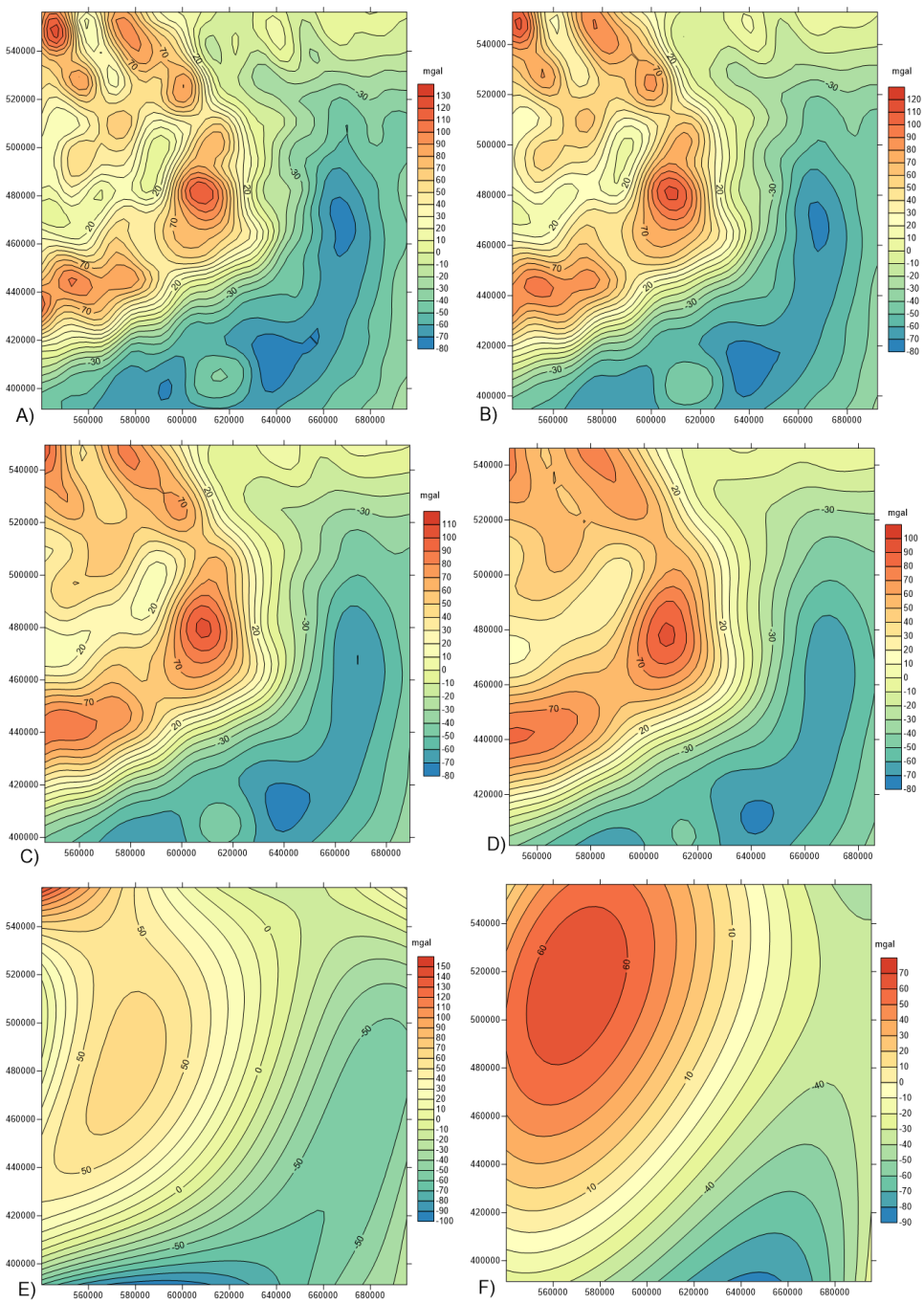

Fig. 6 - Free Air Anomaly in the Vrancea area (coordinates are in meters – STEREO 70 and data are are from BGI - International Gravimetric Bureau database):
A) The representation of unfiltered data;
B) Representation of the data averaged in moving windows of 9 values (3 lines * 3 columns);
C) Representation of the data averaged in moving windows of 25 values (5 lines * 5 columns);
D) Representation of the data averaged in moving windows of 49 values (7 lines * 7 columns);
E) The tendency surface with 6th order; F) The tendency surface with 3rd order.

In both figures (Fig.5 - Bouguer anomaly and Fig. 6 - Free Air anomaly) are presented 6 images of filters with different filtering thresholds (Asimopolos N.S., Asimopolos L. – 2011, 2017, 2018),. Thus, in the images A are presented the original data and in the images B, C and D show the mobile averages with 9 values, 25 values and 49 values respectively, reflecting an increase in the wavelength, the regionality of the anomalies and the depth of their causes. In the images E and F are tendency surfaces for Bouguer and Free Air anomalies (6th degree and 3rd degree). They reflect anomalies with a higher degree of regionality, greater wavelength and deeper causes. For these tendency surfaces the analytical equations were calculated.

4. CONCLUSIONS

In the comparative study in Vrancea area, between the mobile media method, the trend lines and the analytical continuations for the Bouguer anomaly in Romania from the published terrestrial data, it can be noticed that the used filtering methods (the analytical continuations in the upper hemispace at different ceilings, the mobile mediations with different windows and trending areas of varying degrees) yielded results that correlate very well. It is noticed that with the increase of the ceiling to which the values of the anomalies are recalculated, they become more and more attenuated, owing to the increasingly reduced gravity effect given by the density differences of the underground geological masses and their distribution. Similarly, if the window size is increased for mobile mediation or if the degree of the polynomial trend is decreasing.
All the knowledge about geophysical data must be filtered according to the depth of the model we want to achieve. For a small depth model, we need to enter the residual data. As the depth of the model increases, the filtered data with different windows must be entered, going to the regional models and very deep to the trending surfaces. Trending surfaces with higher degree reflect a lower depth and trending surfaces with lower degree reflect a higher depth. The limit case for the largest depth is given by the regional trend plan.
In the 3D geological / geophysical models we need to use geophysical data appropriate to the depth we are reporting.
In Vrancea region Miocene subduction of oceanic crust was accompanied by rollback of the subduction zone and slab steepening after continental collision had started in Mid Miocene.
Vertical extension axes from earthquakes focal to a depth of 300-350 km, but at intermediate-depth (75-130 km) are the strogest earthquakes.

5. ACKNOWLEDGMENTS

We thank for support by the Ministry of Research for financing of the project: “The realization of 3D geological / geophysical models for the characterization of some areas of economic and scientific interest in Romania”, with Contract no. 28N / 2019.
Also, we address our thanks for scientific publications, reports and gravity data, to: International Gravimetric Bureau (BGI), National Oceanic and Atmospheric Administration (NOAA) and GFZ Potsdam.

REFERENCES

Airinei, St. (1977). Microplăcile litosferei de pe teritoriul României reflectate în anomaliile gravimetrice regionale, St. Cercetări Geologice,Geofizice, Geografice, 15 (1), 19-30
Asimopolos, N.S., Asimopolos, L. - Highlighting the deep tectonic elements of the eastern carpathians by analyzing the morphology of geoid, Geoinformatics & Geodesy and Mine Surveying, Issue 2.2, SGEM 2018, vol.18, pag. 821-828
Asimopolos, L. , Asimopolos, N.S.- Methods of smoothing and filtering geological and geophysical data, Geology & Applied and Environmental Geophysics, Issue 1.1, SGEM2018, vol. 18, pag.237-244

Asimopolos, L. , Asimopolos, N.S.- - Determination of the associated pattern for geomagnetic perturbations, Geology & Applied and Environmental Geophysics, Issue 1.1, SGEM 2018, vol.18, pag.755-762, ISBN 978-619-7408-35-5, ISSN 1314-2704, DOI: 10.5593/sgem2018/1.1

Asimopolos, N.S., Asimopolos, L. (2017). Separation of gravimetric anomalies with different degrees of regionality – "Oltenia. Studii si comunicari. Stiintele Naturii, Tom 33, vol.2, pag. 27-34

Asimopolos, N.S., Asimopolos, L. (2017). The effects of terrain corrections on gravity data - "Oltenia. Studii si comunicari. Stiintele Naturii", Tom 33, vol.1, pag. 33-38

Asimopolos, N.S., Andrei, J., Asimopolos, L. (2011). The gravity exploration in Romania - Surveying Geology & Mining Ecology Management, SGEM2011, vol 2 – pag 303 – 309,

Balmino, G., Vales, N., Bonvalot, S., Briais, A. (2011). Spherical harmonic modeling to ultra-high degree of Bouguer and isostatic anomalies. *Journal of Geodesy. DOI* 10.1007/s00190-011-0533-4

Barthelmes F. (2013). Definition of Functionals of the Geopotential and Their Calculation from Spherical Harmonic Models - Scientific Technical Report STR09/02 Revised Edition, January 2013 - Theory and formulas used by the calculation service of the International Centre for Global Earth Models (ICGEM) http://icgem.gfz-potsdam.de/ICGEM/

Beşuţiu, L. (2001). Vrancea active seismic area: a continental unstable unstable triple junction. Revue Roumaine de Geophysique, 45, 59-72

Beșuțiu, L., Zlăgnean, L. (2006). Vrancea intermediate-depth seismicity within the geodynamic framework of the SE Carpathians foreland: in Sledzinski et. al (Eds) Geodynamics of the Balkan Peninsula, A Monograph Reports on Geodesy, 5 (80), 399-403

Blakely, R. J. (1995). Potential theory in gravity and magnetic applications, *Cambridge University Press.*

Constantinescu, L., Cornea, S., Lazarescu, D. (1973). An approach to the seismotectonics of the Romanian Eastern Carpathians. Rev. Roum. Geol. Geophys. Geogr., Ser. Geophys. 17 (2), 133–143.

Constantinescu, L., Enescu D. (1984). A tentative approach to posibily explaining the occurrence of Vrancea earthuaque, Revue Roumaine de Geophysique, 28

Constantinescu, L., Enescu D. (1985). Cutremurele din Vrancea în cadrul științific și tehnologic, Ed. Academiei, 322 p

Cornea, I., I. Dragoescu, M. Popescu, and M. Visarion (1979). Harta miscarilor crustale vertical recente pe teritoriul R. S. Romania, Stud. Cercet. Geol. Geofiz. Geogr. Geofiz., 17, 3-20.

Hauser F., Răileanu V., Fieltz W., Dinu C., Landes M., Bala A. and Prodehl C. (2007). Seismic crustal structure between the Transylvanian Basin and the Black Sea, Romania, *Tectonophysics*, 430, 1–25

Knapp J. H., Knapp Camelia, Răileanu V. Matenco L., Mocanu V., Dinu C. (2005). Crustal constraints on the origin of mantle seismicity in the Vrancea Zone, Romania: The case for active continental lithospheric delamination.*Tectonophysics*. Elsevier. 410: 311-323.

Roman C. (1973). Rigid Plates, Buffer Plates and Sub-Plates-Comment on 'Active Tectonics of the Mediterranean Region 'by D. P. McKenzie, *Gcophys. J. R. astr. Soc.* (1973) 33, 359—373

Săndulescu M. (1984). Geotectonica României, Ed. Tehnică, 336 p

Săndulescu M. (2009). The geotectonic framework of a peculiar seismogenetic area the Vrancea seismic zone (Romanian Carpathians) – *Tectonics*

Sperner, B., F. Lorenz, K. Bonjer, S. Hettel, B. Müller, and F. Wenzel (2001). Slab break-off - abrupt cut or gradual detachment? New insights form the Vrancea Region (SE Carpathians,Romania), Terra Nova, 13, 172-179.

Ștefănescu M., Working Group (1988). Geological Cross Sections at scale 1: 200 000, A13-A15 și A18, Geological Institute of Romania

http://bgi.omp.obs-mip.fr/

http://www.ngs.noaa.gov/GEOID/geophysics.shtml

http://icgem.gfz-potsdam.de/home

GEODYNAMIC MANIFESTATIONS RECORDED IN OBSERVATORIES FROM ROMANIA, AFTER THE BIG EARTHQUAKES

Asimopolos N.S. [1], Asimopolos L. [2], Sandulescu A.M. [2], Asimopolos A.A. [3]

[1] *Dr., Regional Geology Department, Geological Institute of Romania, Bucharest*
[2] *Dr., Geomagnetic Observatory Department, Geological Institute of Romania, Bucharest*
[3] *PhD Student. Assist., Faculty of Transportation, Polytechnic University, Bucharest, Romania*
Email: asi_nata@yahoo.com, natalia.asimopolos@igr.ro

ABSTRACT:

Observatories and geodynamic stations are thus located in the territory of our country so that the data gathered within them contain information with maximum geodynamic value, able to lead to elucidation of causal-related phenomena both the deformations of the terrestrial globe and the fields variation of the Earth in time.
Complex geodynamic observatories were equipped, whenever possible, not only with equipment designed to track phenomena directly related to earth globe deformations, but also with seismicity monitoring, variation of natural fields of the Earth, variation in temperature and air pressure as well as the level variation in groundwater.
With their location, geodynamic observatories can provide both information about the globe as a whole and information on some aspects of the evolution of the tectonic plates that constitute the territory of our country.
In this paper we present the effects of major seismic events on a global scale, recorded in the geodynamic observatories in Romania.
The sensors we used for monitoring of data are very diverse, namely: gravimeters, magnetometers, seismographs, pendulums of various sizes, clinometers with liquid, barometers and thermometers. These sensors are located in very stable areas such as mining galleries in mountain areas. In these areas thermal stability is very high, +/- 1^0C / year, ensuring a good functioning of the sensors.
We have made correlations with mobile windows between different sensors and the seismic data recorded at different seismological observatories in the world during catastrophic earthquakes.
Thus, in our work we present the effect of the major earthquake of Sumatra on December 26, 2004, Pakistan on October 8, 2005 and Japan on March 11, 2011, followed by a giant tsunami.
For all these events there was a very good correlation of the data recorded in Romania with the seismic data recorded in their epicentral areas and with the seismic data recorded in various observatories in the world. Of course, these correlations occurred after several tens of minutes, during which the effect of seismic phenomena was propagated from sources to receptors. This time depends on the distance between the sources and the sensors, as well as on the phenomena pursued (gravitation, magnetism or micro vibrations) with different types of sensors.

KEYWORDS: geodynamic observatories, gravimeters, magnetometers, seismographs

1. INTRODUCTION

Within the Geodynamics Observatories there are various types of sensors, including: pendulums, clinometers, gravimeters, temperature sensors and pressure sensors. The scientific activity is carried out in various directions for the study of the spatial-temporal evolution of the relative displacements between the tectonic blocks that come into contact in the active geodynamic areas. A special type of studies is the elaboration of the methodology for the optimal building and placement of some sensors able to reflect in physical parameters related to cumulative / triggering tensions in active geodynamic areas.

In order to increase the precision of the sensors, evaluated by the signal to noise ratio, in EDAS concept (Environmental Data Acquisition System), developed at the Royal Observatory of Belgium, selected passive transducers that need a minimum in energy transfer from the surrounding medium. The effect of sensors on the medium is thus minimized (M.van Ruymbeke,1998,2001,2001b).
Based on the continuous measurements we can study the spatial-temporal evolution of the geomagnetic, gravitational and geothermal fields with implications in geodynamics, seismology, volcanology, tectonics and in all geosciences.
Information monitored from various sensors, with various transfer features and functions, allow for integrated multidisciplinary geoscience studies.
Complex geophysical measurements in active geodynamic areas include, besides geodynamic measurements, electromagnetic surveys, electrometric measurements, soil vibration measurements, which ensure knowledge of the vertical distribution of some of the physical parameters that characterize the tectonic blocks.
The depths of investigation go from the surface to very large depths that can exceed the thickness of the Lithosphere.

2. DATA ACQUISITION SYSTEMS

At the Royal Observatory in Belgium has been designed the Environmental Data Acquisition System (EDAS) with an improvement in precision for environmental instrumentation (M.van Ruymbeke,1998,2001,2001b).
EDAS contains sensors (devices such as thermometers, barometers, gravimeters, tilt meters, tensiometers and others), loggers and software for monitoring and processing data.
They produce data files that follow a standard sequence that contains the date, time, and values recorded in the ASCII columns. The family of EDAS sensors and interfaces are adapted to monitor different geophysical parameters and they have a great accuracy in relatively stable temperature environments.
Otherwise an EDAS temperature sensor should be added to the system to demodulate the effects of temperature from real measurements and eventually, to apply transfer functions and theoretical corrections.
Was necessary to consider the environment in which the instruments were installed as environment is an intrinsic part of the transducer. To increase sensor accuracy, evaluated by the signal / noise ratio, was selected passive transducers, resistive and capacitive, that require a minimum energy transfer from the environment.
Have been developed a series of voltage to frequency converters. The interfaces are relaxation oscillators using voltage comparators to send a frequency modulated signal proportional to the value of capacitors or resistors.
The oscillator delivers a signal at a frequency given by the inverse of the values of R and C components attached to it. This signal is used to trigger a mono-stable circuit with a pulse length determined by two other components R’ and C’. The final signal is a pulse with modulation, with a ratio depending of the four components R, R’, C and C’. The microDAS data acquisition system and later nanoDAS provides more than six-month autonomy for four channels at 24-bit recording every minute.
This acquisition system contains the RS-232 RS-232 interface and is adapted for long-term measurements with increased stability in time keeping.
The µDAS Grapher software has been developed for data collection of collected data and graphic module is interactive and intuitive.
For various processing, ASCII files can be used in MatLab (The MathWorks, Inc. – 2001).

3. GEODYNAMIC MANIFESTATIONS RECORDED IN OBSERVATORIES

3.1. The effect of the Sumatra earthquake

(produced at December 26, 2004, 0 h 58 min 53 sec GMT, produced at a 30 km depth, magnitude M = 9, latitude = 3.29N and longitude = 95.94E) on sensors located in geodynamic observatories in Romania, namely Căldăruşani, Ursoiu and Crăciuneşti.

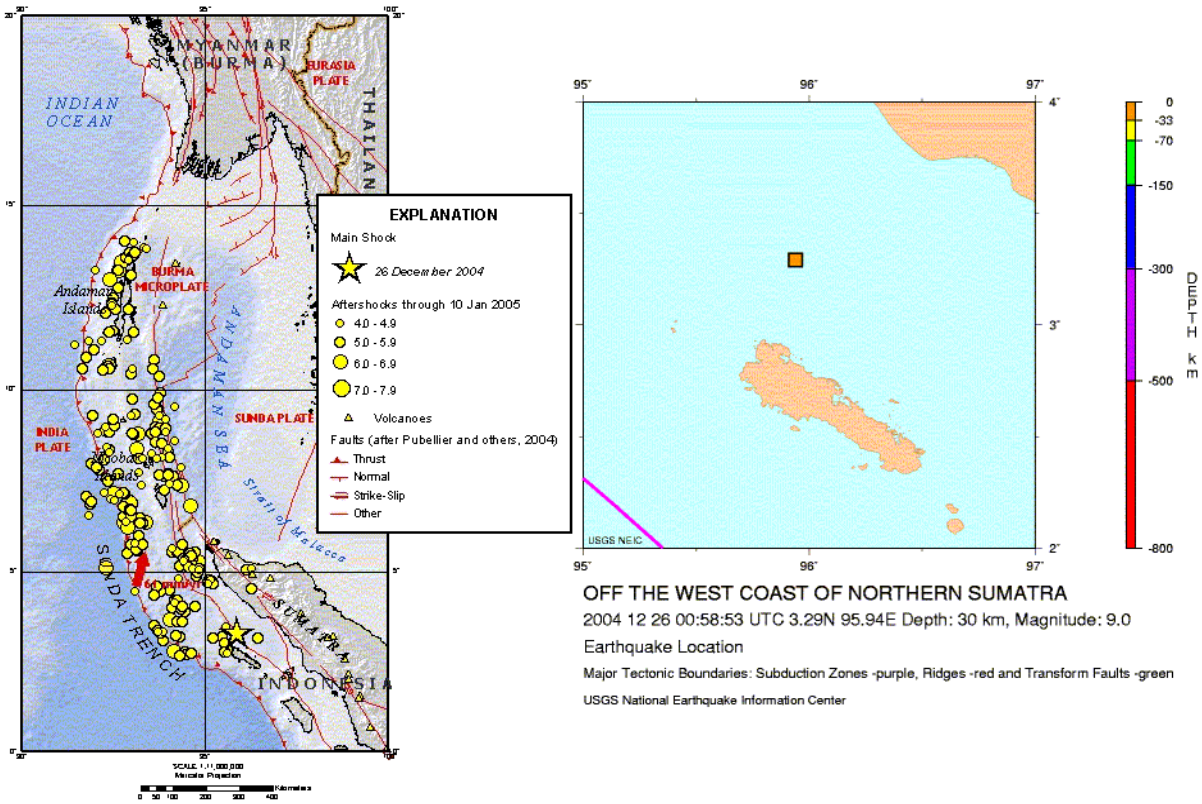

Fig.1 – Coordinate of the Sumatra earthquake and countries affected by earthquake (https://thisdayinwaterhistory.wordpress.com/2012/12/25/december-26/1226-countries-affected-by-2004-dec-tsunami-graphic-courtesy-bbc/, https://en.wikipedia.org/wiki/Effect_of_the_2004_Indian_Ocean_earthquake_on_India)

In order to highlight the effect of the earthquake on these sensors, a five-hour representation interval was chosen (0-5 GMT, 26.12.2004), considering that the event occurred at 0h 58min 53sec GMT, and the seismic wave took about 1 hour to be registered, due to the distance of about 7,000 km from the outbreak to the observatories in Romania.

In the first step, the graphical representations of the normalized signals ($y_i = x_i / \bar{x}$, where y_i are the normalized values, x_i represent the recorded values and $\bar{x}$ mean value) recorded in the geodynamic observatories, with a sampling rate of 1 minute (Fig. 2-3).

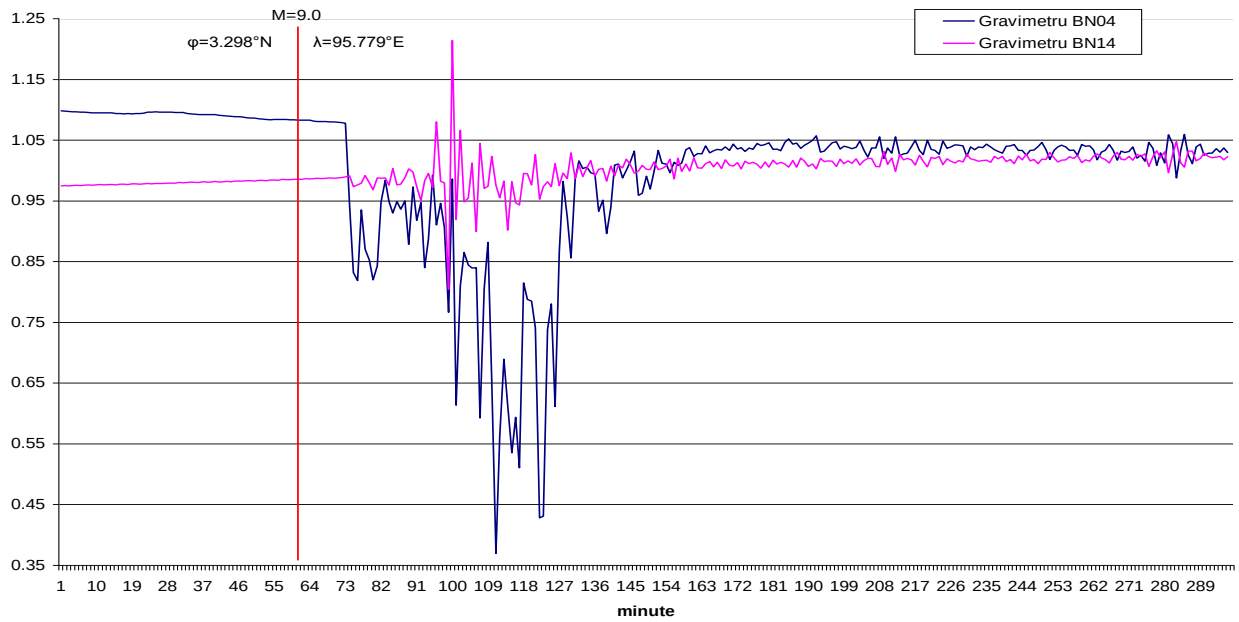

Fig.2 – Normalized values for two gravimeters at Căldăruşani Observatory, in the time interval 0 - 5 GMT from the date December 26, 2004.

In Fig 2 we notice that the two gravimeters located at the Caldarusani Observatory reacted 10 minutes after the earthquake.

The two gravimeters showed different sensitivity. Thus, the first gravimeter (the blue line) began with a sudden drop in the values, after which the oscillations related to the earthquake began. The second gravimeter (the red line) debuted gradually with oscillations, without changing the baseline. Although they had a different behavior on the earthquake-related oscillations, however, during their earthquake their signals correlate very well.

For each time series, complex statistical analyzes such as the selection covariance between two recorded time series, the covariance ratio and the product of the standard deviations of the analyzed variables, called the correlation coefficient, were performed. We have made the correlation coefficient between the different sensors within each observer, as well as the correlations between sensors of the same type in different observatories. We used a mobile window of 11 values and 21 other values and we reported the value obtained at the half of the window used. We packed with these moving windows the entire set of values, calculating the correlation index at each moment: We packed with these moving windows the entire set of values, calculating the correlation index at each moment:

$$r = \frac{n * \sum_1^n x_i * y_i - \sum_1^n x_i * \sum_1^n y_i}{\sqrt{\left[n * \sum_1^n x_i^2 - \left(\sum_i^n x_i\right)^2\right] * \left[n * \sum_1^n y_i^2 - \left(\sum_1^n y_i\right)^2\right]}}, \text{ where:}$$

r = correlation coefficient; n = the number of samples taken into account in each mobile window; x_i, y_i = instantaneous values for the analyzed time series.

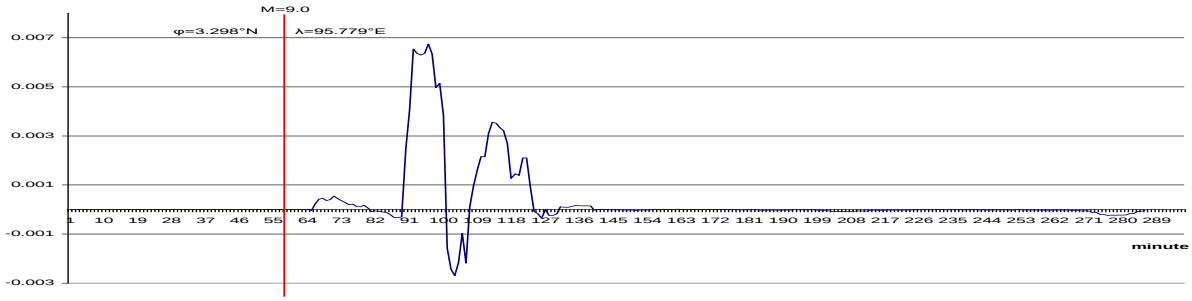

Fig.3 – Correlation coefficient between normalized values for two gravimeters at Căldăruşani Observatory, in the time interval 0 - 5 GMT from the date December 26, 2004.

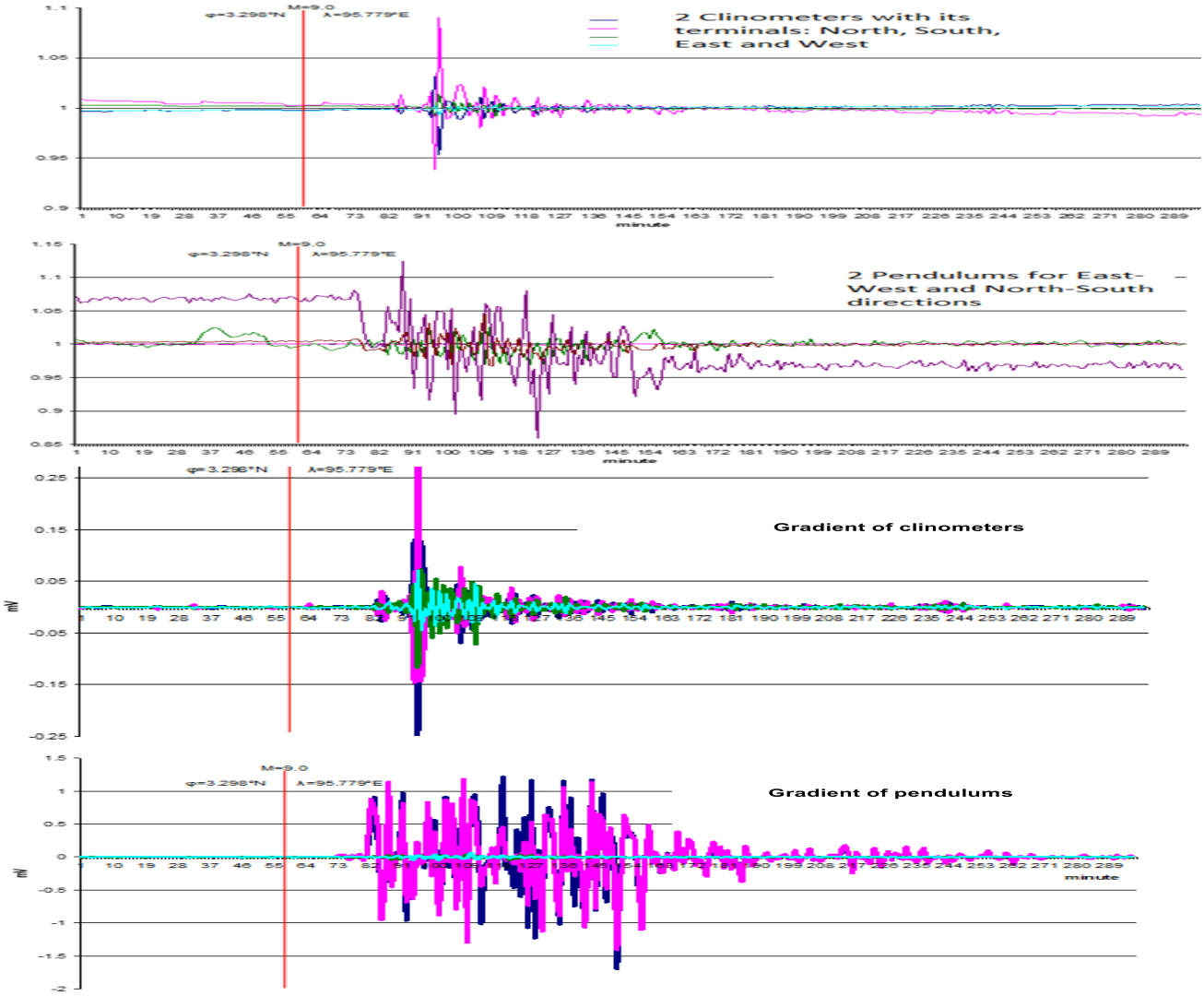

Fig.4 – Normalized values for clinometers and pendulums at Căldăruşani Observatory, in the time interval 0 - 5 GMT from the date December 26, 2004. The red line is the moment of earthquake from Sumatra with magnitude 9. In the last two images are gradient of clinometers and gradient of pendulums.

In Fig. 4, we notice that the two clinometers and two pendulums, located at the Caldarusani Observatory, had a delay to the first impulse compared to gravimeters. Thus, the pendulums reacted 5-10 minutes after the gravimeters, and the clinometers reacted 20-25 minutes after gravimeters. This delay is clearer in gradient graphs.

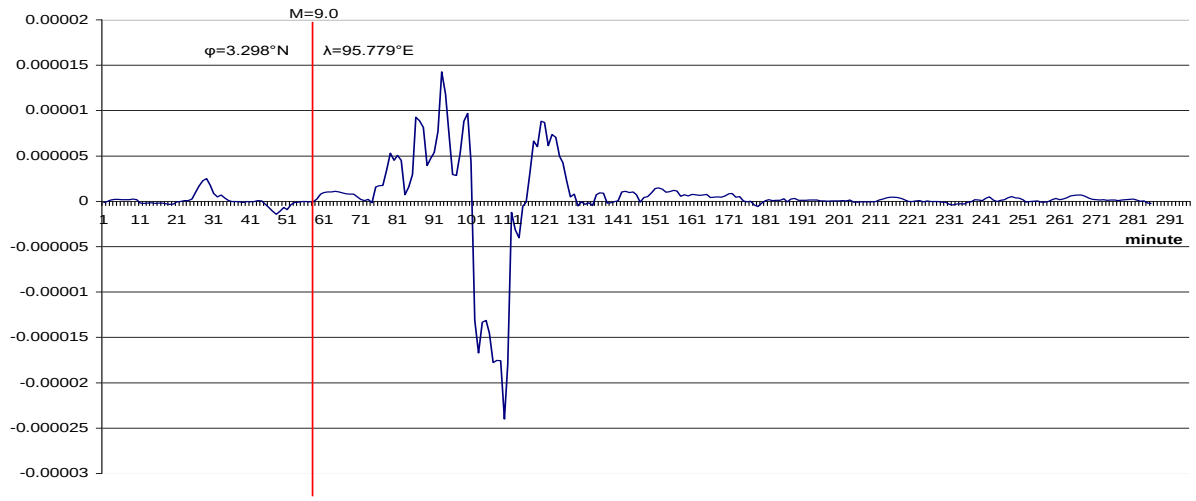

Fig.5 – Correlation coefficient between normalized values for two pendulums at Căldăruşani Observatory, in the time interval 0 - 5 GMT from the date December 26, 2004.

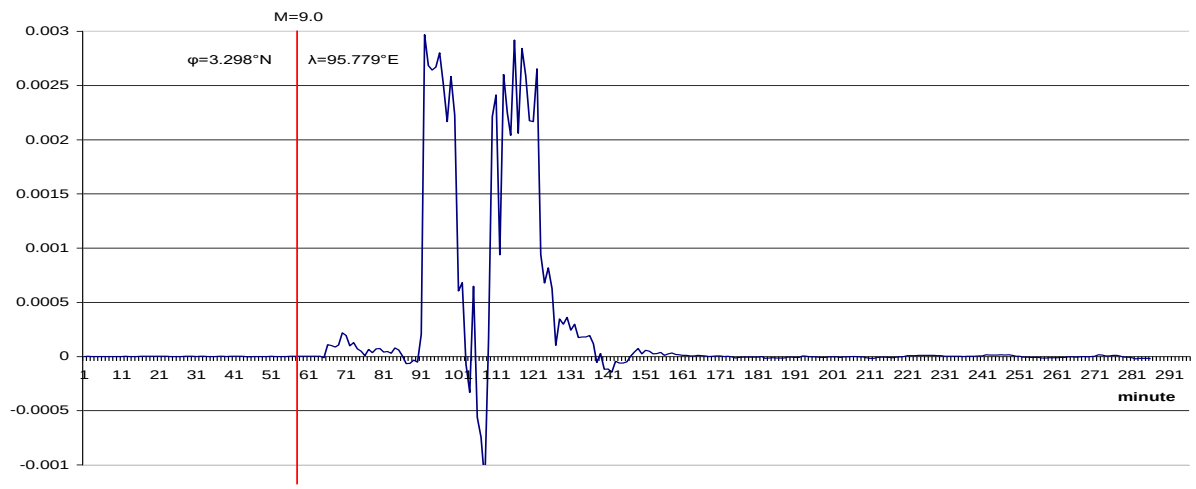

Fig.6 – Correlation coefficient between normalized values between one gravimeter at Căldăruşani Observatory and one gravimeter at Ursoiu Observatory (localized at 400 Km distance from Căldăruşani Observatory), in the time interval 0 - 5 GMT from the date December 26, 2004.

In fig. 3, 5 and 6 we note an increase in the correlation coefficient between the two sets of data during the earthquake.

The evolution of the area affected by the earthquake in the period up to 2007 is presented in Fig. 7

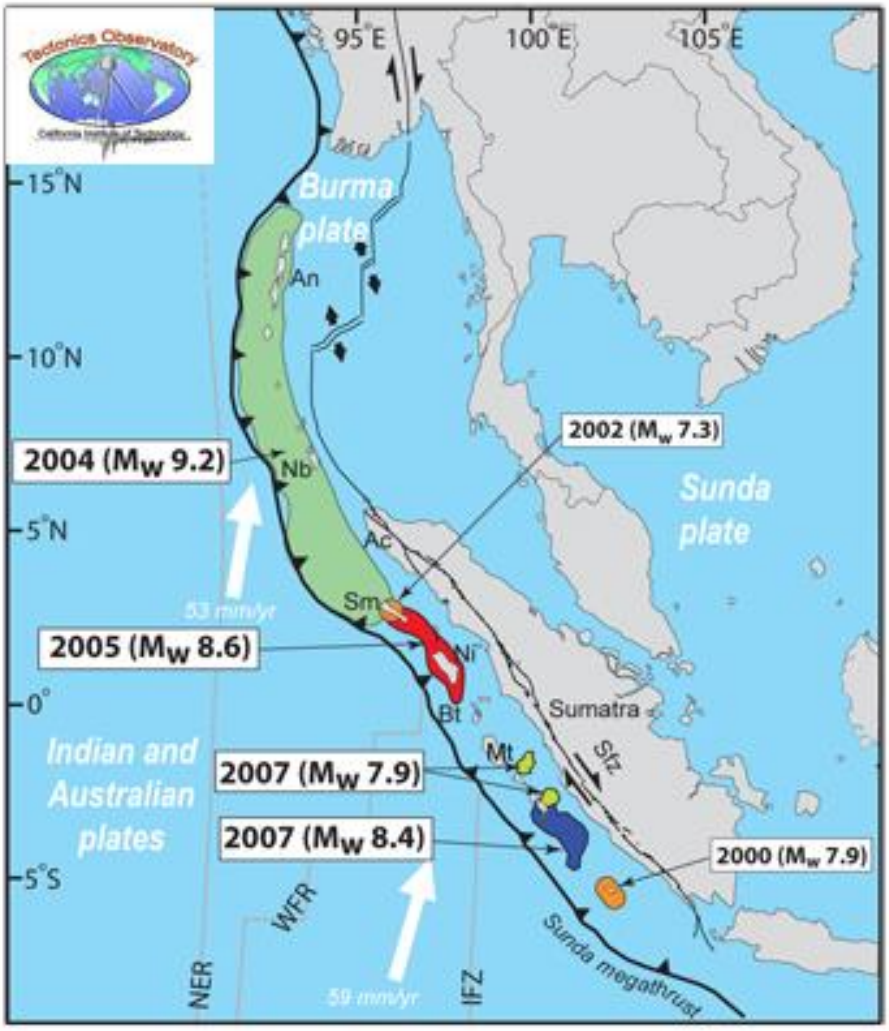

The giant 2004 Sumatra earthquake ruptured the greatest fault length of any recorded earthquake, spanning a distance of 1500 km, or longer than the state of California. Rather than tearing the land apart all at once, the rupture started beneath the epicenter marked in the figure below and progressed northward along the fault at about 2 km/sec (1.2 miles/second). The whole rupture lasted about 10 minutes.

The portion of the fault that ruptured lies deep in the earth's crust, in places as much as 50 km (31 miles) below the ocean floor. There the two tectonic plates, which had been stuck together, suddenly broke free, the upper plate sliding back upward and to the west by as much as 20 m (65 feet) along the plate boundary.

Fig. 7 - Map of Sumatra region showing the extent of the ruptured fault lines for the three most recent giant quakes. Green shows 2004, red shows 2005 and blue and yellow show 2007.
(http://www.tectonics.caltech.edu/outreach/highlights/sumatra/what.html)

3.2. The effect of the Pakistan earthquake

(produced at October 08, 2005, 03 h 50 min 36 sec GMT, produced at 26 km depth, magnitude M = 7,6; latitude = 34,493N and longitude = 73,629E) on sensors located in geodynamic observatories in Romania

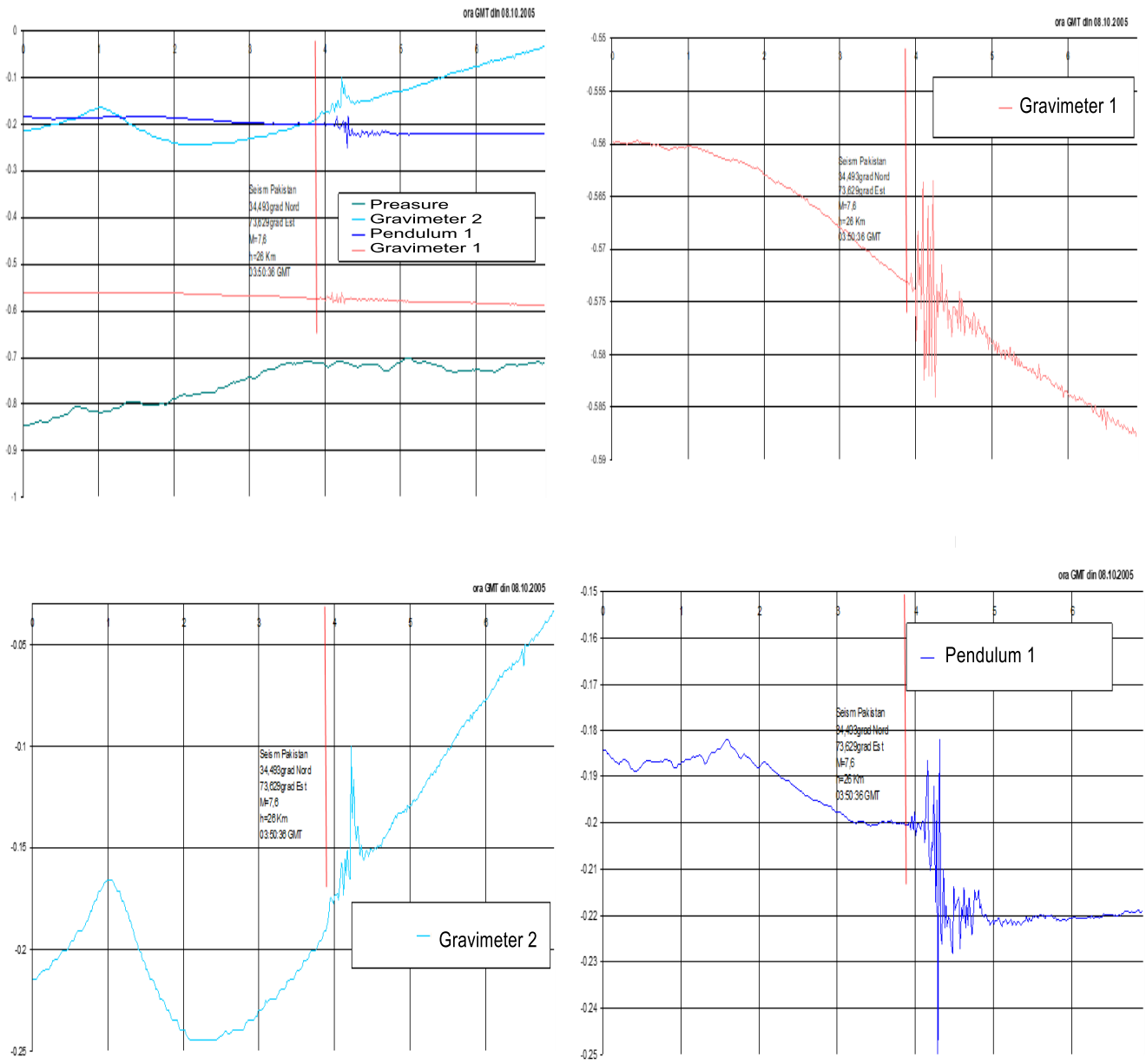

Fig.8 –Values for geodynamic sensors at Căldăruşani Observatory, in the time interval 0 - 7 GMT from the date October 08, 2005. The red line is the moment of earthquake from Pakistan with magnitude 7,6.

3.3. The effect of the Australia earthquake

(produced at January 27, 2006, 16 h 58 min GMT, magnitude M = 7,6; latitude = 5,51 South and longitude = 128,19 East) on sensors located in geodynamic observatories in Romania

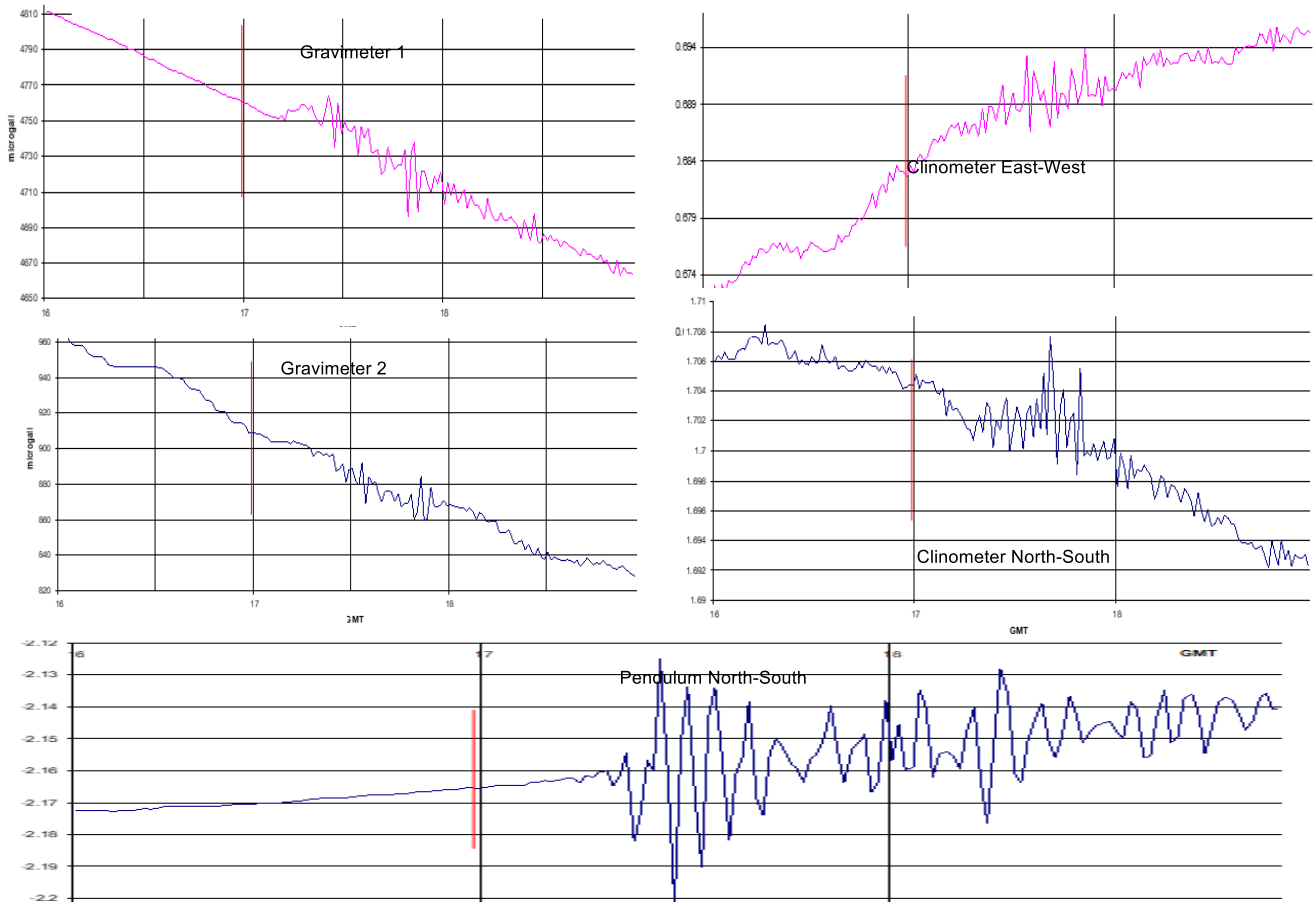

Fig.9 –Values for geodynamic sensors at Căldăruşani Observatory, in the time interval 16 - 19 GMT from the date October 08, 2006. The red line is the moment of earthquake from Australia with magnitude 7,6.

In figures 8 and 9 we note very good correlation between geodynamic sensors data and the earthquake event.

4. CONCLUSIONS

Following the records and processing for the three geodynamic observatories, we can state that the results obtained highlighted the major seismic events, although they occurred thousands of kilometers away. Gravimeters, pendulums and clinometers responded very well to the signal received. In longer records, there is also a good correlation with the theoretical terrestrial tide. The correlation between the sensors, both from each observer and between sensors in different observers, can be appreciated as very good. Also, comparison with other observatories data located on different Earth's meridians shows a very good correlation taking into account time corrections depending on the geographical coordinates of each observatory.

Analyzing the behavior of each type of sensor, we notice that the clinometers and pendulums, had a delay to the first impulse compared to gravimeters. Thus, the pendulums reacted 5-10 minutes after the gravimeters, and the clinometers reacted 20-25 minutes after gravimeters. This delay is clearer in gradient graphs.

Presented types of analysis as well as other statistical and spectral analyzes can be a subject of further studies for the Vrancea earthquakes in which we will take into account the data obtained in the geodynamic observatories,

particularly located in stable areas such as Căldăruşani, Ursoiu, Crăciuneşti, Tulnici and Daniel gallery in Romania.

5. ACKNOWLEDGMENTS

We thank for support by the Ministry of Research for financing of the project: "The realization of 3D geological / geophysical models for the characterization of some areas of economic and scientific interest in Romania", with Contract no. 28N / 2019.
We also thank the Institute of Geodynamics of the Romanian Academy, where we carried out the measurements in its Geodynamic Observatories.

REFERENCES

M.van Ruymbeke, A.Somerhausen (1998). Experiments in Laboratory and Field with Precise Thermometry, Seminar der Dr. Wilhelm Heraeus und Else Heraeus-Stiftung, pp.23-35.

M van Ruymbeke, F. Beauducel, A. Somerhausen (2001). The Environmental Data Acquisition System (EDAS) developed at the Royal Observatory of Belgium - Journal of the Geodetic Society of Japan Vol. 47, No. 1, (2001), pp. 40 – 46

M van Ruymbeke, A. Somerhausen, B. Ducarme, R. Vieira, J. Arnoso and E. J. Velez (2001). Projects of the Royal

Observatory of Belgium (ROB) at the Lanzarote Laboratories, J. Geod. Soc. Japan

The MathWorks, Inc. (2001). Signal Processing Toolbox User's Guide - Revised for Version 5.1 (Release 12.1), pp. 800

https://thisdayinwaterhistory.wordpress.com/2012/12/25/december-26/1226-countries-affected-by-2004-dec-tsunami-graphic-courtesy-bbc/, https://en.wikipedia.org/wiki/Effect_of_the_2004_Indian_Ocean_earthquake_on_India

http://www.tectonics.caltech.edu/outreach/highlights/sumatra/what.html

THE EFFECT OF FOUNDATION TYPE ON SEISMIC PERFORMANCE OF REINFORCED CONCRETE FRAMED BUILDINGS

Safkan I.[1], Derogar S.[1], and Anywar J.[2]

[1] *Asst. Prof., Civil Eng. Department, European University of Lefke, Northern Cyprus*
[2] *Undergrad. Stud., Civil Eng. Department, European University of Lefke, Northern Cyprus*
Email: sderogar@eul.edu.tr

ABSTRACT:

It is known that the seismic response of structures is influenced by the soil-structure interaction relationships. Type and size of the foundation is also reported to affect the global response. This paper aims to investigate the influence of different characteristics of soil structure interaction on the seismic response of reinforced concrete structure. An 8 story reinforced concrete structure was simulated with two different foundation type where the first model is fixed based structure where the soil structure interaction is not considered and the second model is pile raft foundation. OpenSeesPL Computer program was used to model the structure and real earthquake records were incorporated for the analysis of the structure. The results are presented and highlighted in terms of soil amplification, and superstructure seismic response.

KEYWORDS: Soil structure interaction, , piled raft foundation, soil amplification

1. INTRODUCTION

Structures built on soft soil or rigid soil, generally interact differently under earthquakes. This was observed in the earthquake disaster occurred in Mexico on the 19th and 21st of September 1985 (Esteva, 1988), two earthquakes with magnitude of 8.1 and 7.5 occurred at a part of the plate boundary besides the Mexican subduction zone prior known as the Michoacan gap. The major shocks where composed of two subevents which way 26 seconds apart, the peak acceleration observed in the epicenter area was unexplainably low about 0.2g and was recorded 20 kilometers from the epicenter.

A large city built on soft clay soil, approximately 360 kilometers away from the epicenter region had the earthquake effects, where it has left deep scares in the economy and the daily life in the city. The peak earthquake acceleration recorded in the city was approximately the same as the acceleration recorded in the epicentral region. The casualties of this earthquake were at least 10,000 dead, with 50,000 people left homeless and loss of materials reached 4 billion dollars in cost. Champilo et. al., (1989) investigated the source characteristics and propagated waves from the epicenter to the Mexico City and the authors concluded that the earthquake catastrophe of Mexico City in 1985 was due to a large local amplification, caused by the extremely soft clay layer underlying the city. The importance of these events and of their consequences has brought an increased pressure to understand the behavior of Soil-Structure Interaction, in order to improve the seismic safety of multi-story structures.

Liquefaction during an earthquake is a major reason to causes hazardous damage to the buildings. Liquefaction damage prompts the soil to excessive settlement, loss of bearing capacity, sand boils, slope failure and landslides, lateral spread, etc. Structures built in seismic active regions are susceptible to experience liquefaction of the underlying soil caused by excessive pore pressure development. The two most commonly considered soil improvement techniques in practice are stone columns and piled foundations. Among the different improvement techniques, the most popular technique adopted for liquefiable soil improvement is the installation of stone columns. Yoshimi and Kuwabara (1973) introduced the use of stone columns as an improvement for liquefaction

hazards for the first time. Stone columns generally improve liquefiable soil by the high stiffness, permeability and strength properties of stone columns. A considerable number of research has been done regarding to the performance of stone columns to improve soil liquefaction. Seed and Booker (1977) proposed a stone column model designed for liquefiable soil improvement by assuming the infinite permeability of the stone column. Non dimensional charts have been introduced for the determination of the spacing of stone columns. Sasaki and Taniguchi (1982) performed a large scale test aiming to determine the effective area of stone columns to minimize liquefaction. Yang and KO (1998) observed that the tendency of liquefiable soil is greater at points far from the drain (cited in Ben Salem, et. al., 2016).
A study conducted by Asgari et. al., (2013), focused on stone column and pile-pinning methods, comparing the behavior of each method in retaining permanent seismic deformations. However, different stiffness properties of soil were not investigated.
This study, parametrically assess, different stiffness properties of clay on stone columns and piles. Relative difference in between the type or size of the foundation will be discussed in this paper.

2. METHOD

Substructure was modeled using OpenseesPL software. Both the pile and stone column foundation models were analyzed considering different soil conditions such as loose and dense clay. Once the acceleration and displacement properties at surface level was obtained, then structural analyses were conducted on 8 story frame model.

2.1. Modeling substructure

Table 1 provides the soil parameters utilized in the analyses.

Table 1. Soil parameters of clay

Parameters	Loose clay	Medium loose clay	Medium clay	Dense
Mass density (ρ) (kg/m^3)	1620	1870	2090	2130
Shear wave velocity (m/s)	150	300	500	700
Cohesion (c) (kPa)	22	32	55	75

2.1.1 Stone column

The main constitutive soil modeling parameters used in this study of stone column, for: loose clay, medium loose clay, medium clay, medium dense clay and dense clay, are the main constitutive soil modeling parameters used in the study of stone column which are represented in table 1, with the soil layer having a total depth of 10 *m*. Different soil models achieved by using a variety of shear wave velocities.
Nowadays, stone columns are preferred as an economical solution for the stabilization of underlying soil. Stone Column case utilizes same stabilization material property for but as column shape and with different area replacement ratio (ARR). Area replacement ratio of 5%, 10%, 25%, 50% and 100% were utilized for modelling in this study.

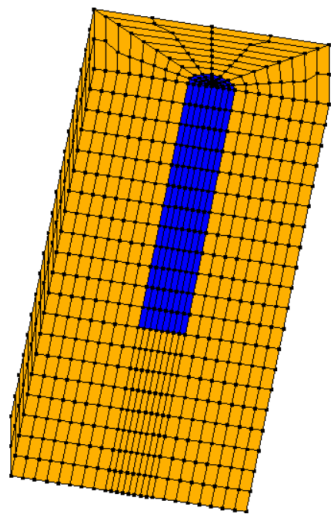

Figure 1. Stone Column Cell finite element model (OpenSeesPL, 2018)

2.1.2 Piled foundation

The unit cell finite element model consisted of a pile embedment in to two layers soil strata. As illustrated in Figure. 2a, the top soil layer thickness is 10m underlain by a 5m thick dense bottom layer. The pile diameter was designed to be 1m and the pile was embedded into the bottom layer by a specified embedment length. The soil domain used in this study was discretized using eight node brick elements with up formulation such that soil deformation and water pressure can be solved simultaneously. The model used pile beam elements for the purpose of accurately capturing the bending behavior of piles. The beam element used has no radial dimension, thus the actual diameter of the pile was modeled using rigid links placed normal to the axis of the pile axis, as illustrated in Figure. 2b. In addition, the rigid links form node- to-node contact with the surrounding soil elements, so that the contact and spacing between the pile and soils can be realistically simulated. The base of the model was assumed to be non-sloping and homogeneous within the individual layers.

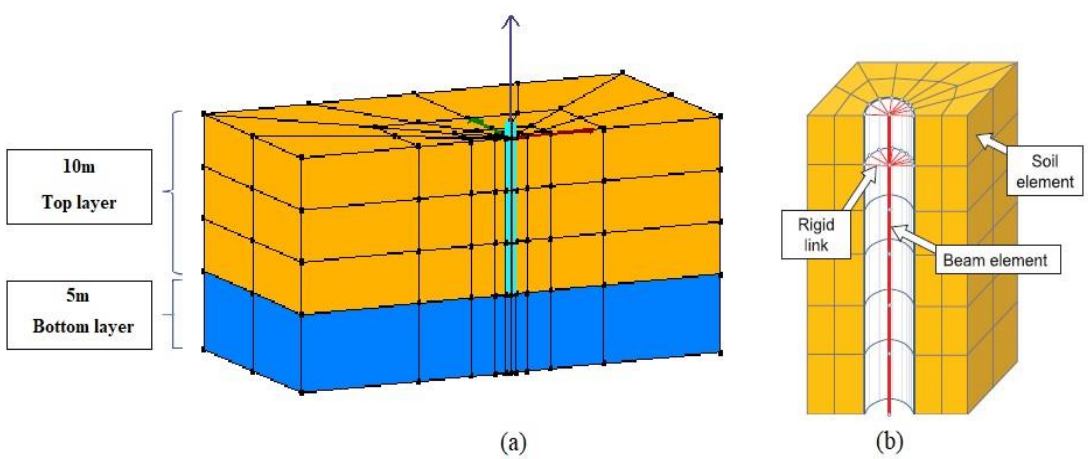

Figure 2. Pile finite element model

A pressure dependent multi-yield elastoplastic material model as shown in fig 3 (Opensees 2019) was used for modelling. The characteristics of a pressure depended multi-yield material require modelling the regular medium dense soil by replicating drained soil conditions. For the purpose of simulating a soil under fully undrained condition, the material should either be fitted in a fluid solid porous material, or with a solid-fluid coupled element with a low permeability. For the simulation of partially drained soil behavior, the pressure dependent multi-yield material must be coupled with a solid-fluid fully integrated element with the right permeability values (Opensees 2019).

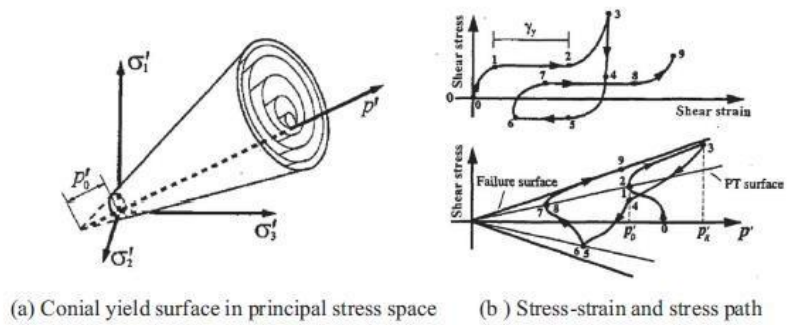

Figure 3: Pressure dependent multi-yield. (Opensees 2019)

2.2. Superstructure

For this study, the finite element software SeismoStruct was used for modelling and analyzing the eight story reinforced concrete 2D structure (Fig 4) subjected to nonlinear time history analysis. The time history input was obtained from initially exported from Opensees PL analyses and was applied to the base nodes of the 2D structure. The stone column and pile reinforced clays soils were assessed individually by using El Centro and Chile, Llolleo seismic motions.

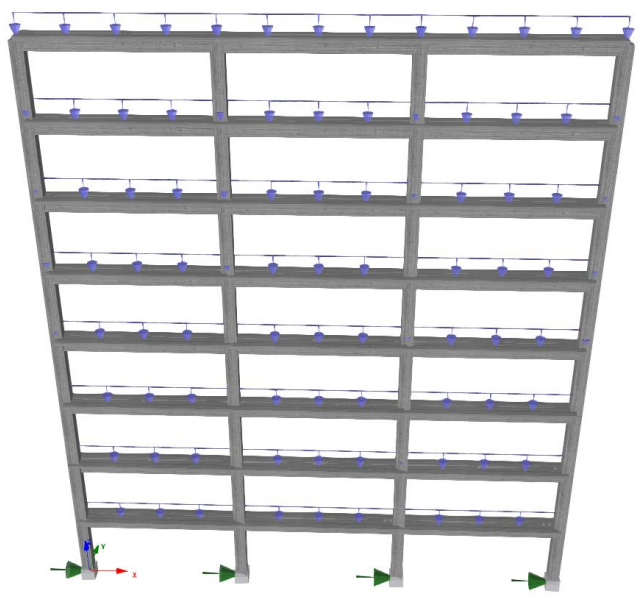

Figure 4. 2D frame analysis model

The reinforced concrete frame was adopted from one of the existing building from Cyprus which was recently designed by considering the local seismic design codes. The section properties are considered as given in table 2 below.

Table 2. Reinforced concrete building frame section properties

	Section Height (m)	Section Width (m)	Reinforcement
Beam	0,7	0,3	2 ϕ 20 Bottom 4 ϕ 20 Top
Column	0,8	0,3	20 ϕ 18

In total 2 strong motion data were utilized for assessing the influence of foundation type on superstructure. Table 3 gives the statistics of selected ground motions. The relatively high peak ground acceleration characteristics of these two motions are considered to influence the amplification characteristics of soil in nonlinear behavior.

Table 3: Statistics of the utilized ground motions.

Earthquake	Year	Length of record (s)	Magnitude	PGA (g)
El Centro	1940	31	7.1	0.27
Chile, Llolleo	1985	116	7.8	0.95

3. RESULTS AND DISCUSSION

The analyzed ground motions` frequency content were especially magnified at short period range. The longer period range for the Chile earthquake was monitored to not to change in a significant manner. On the other the El Centro data was observed to damp the energy on long period range when 4m deep embedment length was considered.

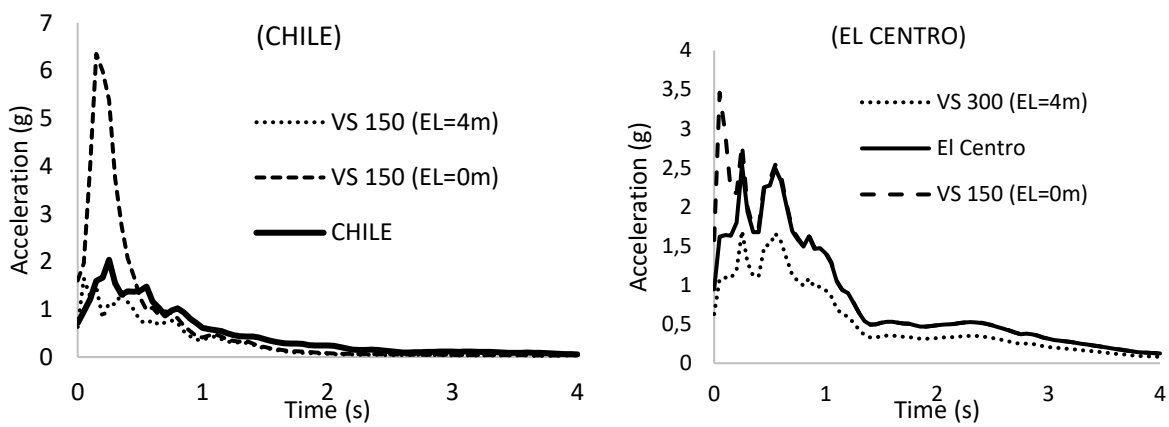

Figure 5. Influence of Pile Embedment Length on Spectral Coordinates

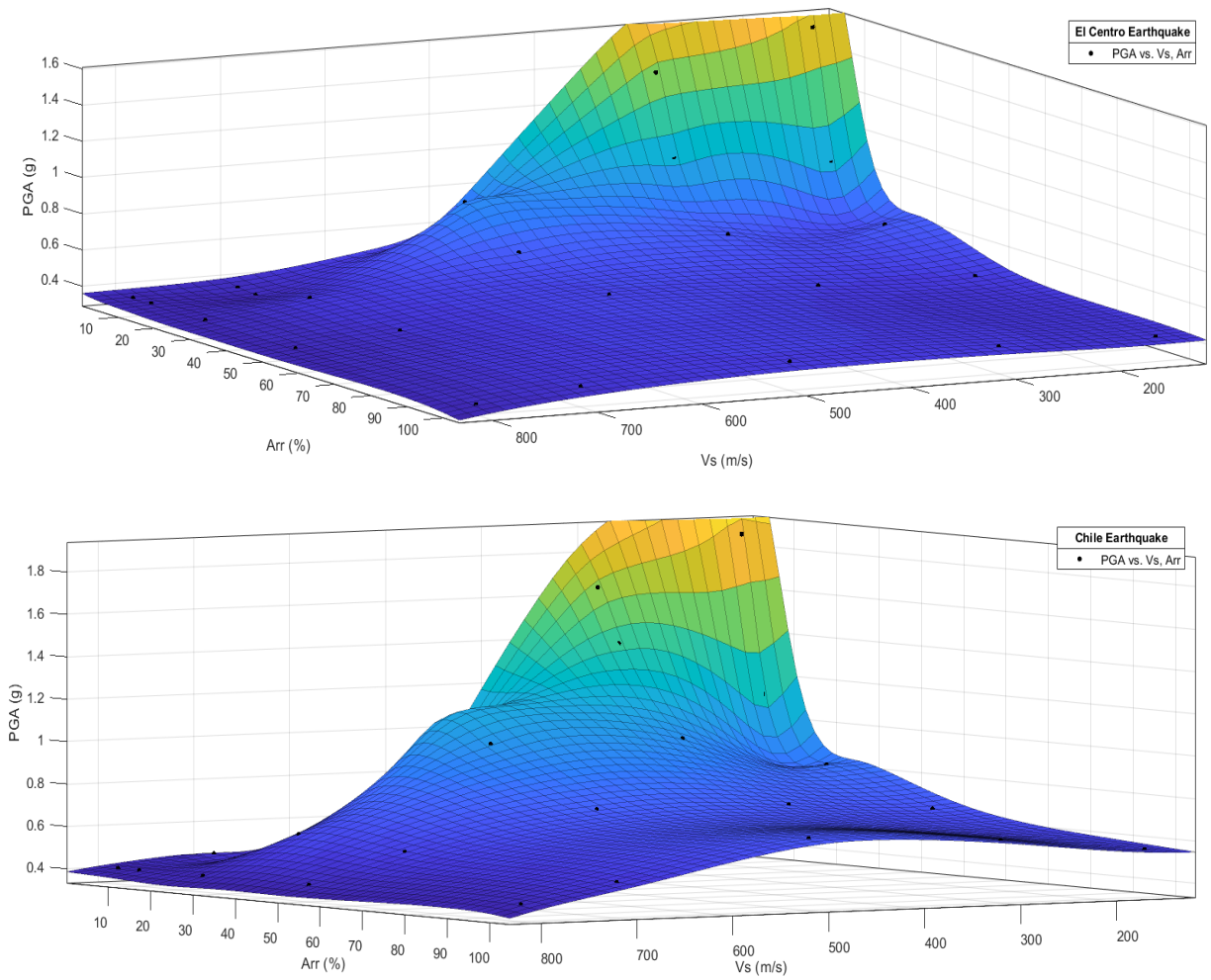

Figure 6. Peak Ground Acceleration respect to ARR of stone column and Vs conditions

As result of analyses, a multidimensional relationship were developed in between ARR of stone column, Vs of surrounding soil and PGA (Fig.6) When loose soil condition (Eg. Vs< 200) was considered, significant amplification of ground acceleration was observed for ARR<25%. Although the reduction was gradual for stiffer soil conditions, there is a jump at Vs: 500m/s and ARR: 20%. This may be argued as the secondary mode effects of stone column due to the specific stiffness-mass ratio.

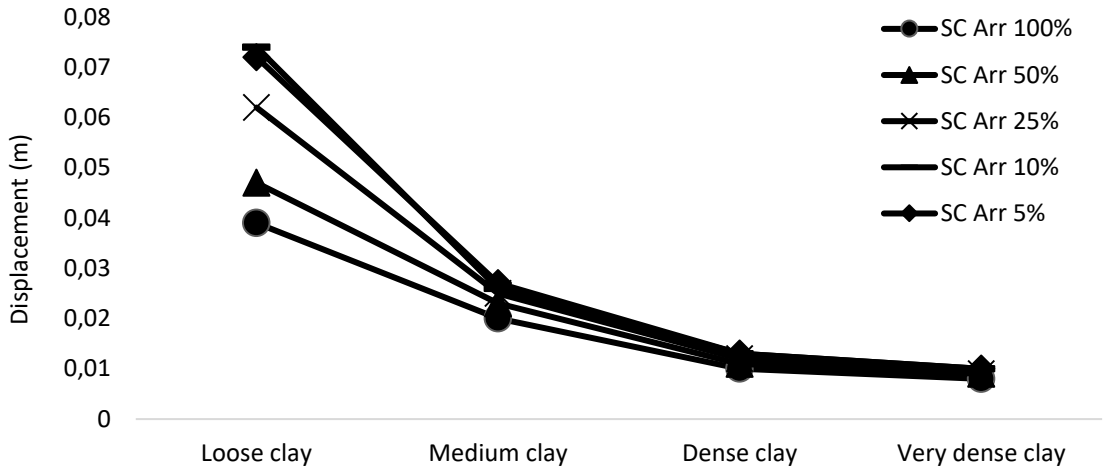

Figure 7. The effect of stone column ARR on peak structural response at different soil conditions

Significant variance of structural response was observed for the loose clay stone column samples. The peak storey displacement was observed to be 0.075m for the 5% ARR and 0.04m for the 100% ARR. On the other hand insignificant difference on response was monitored for the medium and dense clay soil conditions. Furthermore, the difference in between the 50% and a100% ARR was also found to be negligible.

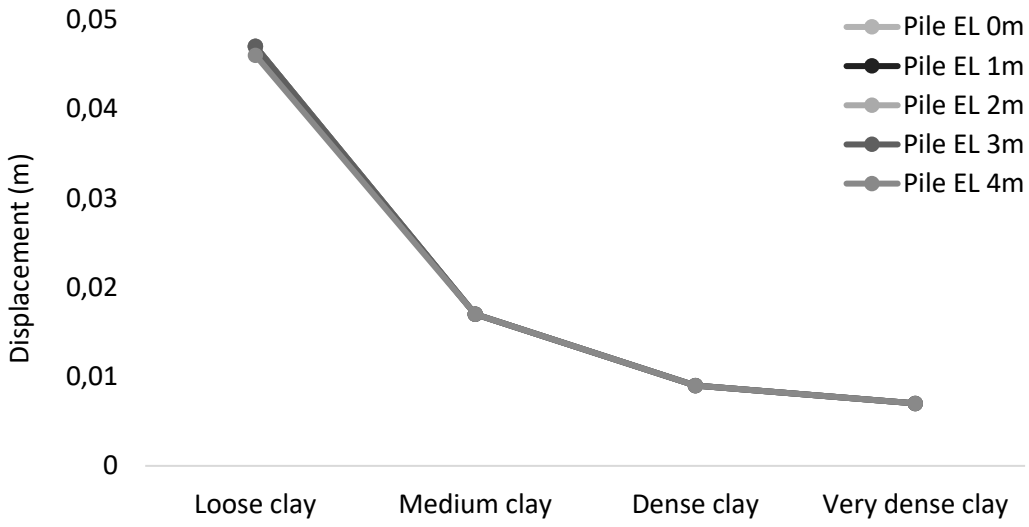

Figure 8. The effect of stone column ARR on peak structural response at different soil conditions

Negligible structural response was obtained for the different pile embedment length values for the soft soil conditions. On the other hand, no structural response difference was obtained for the firm soil conditions. This may be due to the insignificant difference at long period range of response spectra. Similar trend was also observed on firm soil conditions, where no amplification of acceleration characteristics were monitored.

4. CONCLUSION

In this study, the effect of stone column and pile reinforcement in loose soil and on structural displacement was investigated. In addition the effect of different soil types on the amplification or damping of spectral acceleration was studied. The modeling analysis was done by the aid of finite element computer software Opensees PL and SeismoStruct.

The results of this study showed that an increase in the consistency of soil, increases the damping of spectral acceleration, the critical stone column ARR and pile embedment length that gives the best response to loose soil under earthquake loading is 50% ARR for stone column and 2m embedment length of pile into dense soil.

REFERENCES

Asgari, A., Oliaei, M. and Bagheri, M. (2013). Numerical simulation of improvement of a liquefiable soil layer using stone column and pile-pinning techniques. *Soil Dynamics and Earthquake Engineering* **(51)**: 77–79.

Ben Salem, Z., Frikha, W., and Bouassida, M. (2016). Effect of granular column in- stallation on excess pore pressure variation during soil liquefaction. *Int. J. Geo- mech*, 10.1061/ (ASCE) GM.1943-5622.0000516, 04015046.

Lu, J., Elgamal, A., & Yang, Z. (2011). OpenSeesPL: 3D lateral pile-ground interaction user manual (Beta 1.0). Department of Structural Engineering, University of California, San Diego. http://soilquake.net/openseespl/OpenSeesPL_UserManual.pdf

Sasaki, Y., & Taniguchi, E. (1982). Shaking table tests on gravel drains to prevent liquefaction sand deposits. *Soils Found*. 22(3), 1–14.

Seed, H. B., & Booker, J. R. (1977). Stabilization of potentially liquefiable sand de- posits. *J. Geotech. Eng. Div.*, 103(7), 757–768.

Yang, T. F., & KO, H.-Y. (1998). Reduction of excess pore-water pressure by the gravel drainage method during earthquakes. Centrifuge '98, T. Kimura, O. Ku- sakabe, and J. Takemura, eds., A. A. Balkema, Rotterdam, Netherlands, 301–306.

Yoshimi, Y., & Kuwabara, F. (1973). Effects of subsurface liquefaction on the strength of surface soil. *Soils Found*. 13, 67–81.

SEISMIC VULNERABILITY ASSESSMENT AT URBAN SCALE: CASE OF THE GREAT-BLIDA (ALGERIA)

Boukri M.[1], Farsi M.N.[2], Mebarki A.[3], Ait Belkacem M.[4], Yousfi N.[5], Belazougui M.[6]

[1] *Senior Researcher, Centre National de Recherche Appliquée en Génie Parasismique (CGS), Algiers, Algeria*
[2] *Research Director, Centre National de Recherche Appliquée en Génie Parasismique (CGS), Algiers, Algeria*
[3] *Senior Researcher, Centre National de Recherche Appliquée en Génie Parasismique (CGS), Algiers, Algeria*
[4] *Senior Researcher, Centre National de Recherche Appliquée en Génie Parasismique (CGS), Algiers, Algeria*
[5] *Prof. Université Paris-Est, Laboratoire Modélisation et Simulation Multi Echelle, Marne-La-Vallée, France*
[6] *Director, Centre National de Recherche Appliquée en Génie Parasismique (CGS), Algiers, Algeria*
Email: mehdi.boukri@gmail.com

ABSTRACT:

This work presents an integrated framework for seismic damage assessment at urban scale in Algeria. Its main objective is the proposal of simplified methodological and operational approaches to assess urban vulnerability and socio-economic losses. It relies on the performance of probable seismic scenarios in urban areas exposed to earthquakes. This will enable decision makers to take adequate preventive measures and develop appropriate mitigation strategies, i.e. crisis prevention and management plans to reduce the losses. It deals with the assessment of building seismic risk of urban areas in Algeria by using the RADIUS Model (Risk Assessment Tools for Diagnosis of Urban Areas against Seismic Disaster) after a prior adaptation to the Algerian context. It estimates also the expected number of victims and their spatial distributions. This concept is adopted to estimate the urban seismic risk of the Great-Blida, South-West of Algiers region, (consisting of 4 cities, namely Blida, Ouled-Yaïch, Bouarfa and Beni-Mered), by performing an earthquake scenario. In order to draw reliable results, an extensive survey was carried out concerning the buildings (approximately 46,000 units). The data were mapped and stored in databases using GIS tools. The results of this earthquake scenario show that serious damages would be observed in the studied area. The results reported in this study will drive the decision-making, by the local authorities, adapted to the specific socio-environmental vulnerability context at the Great-Blida urban scale.

KEYWORDS: seismic urban vulnerability, earthquake scenario, victims, mitigation, RADIUS, Great-Blida

1. INTRODUCTION

The seismic risk to which the urban agglomerations are exposed has become a world concern because of the potential losses in human lives and assets, because people continues to invest in hazard-prone regions at an accelerated rate, the poor urbanization strategies and also the society's unawareness and lack of education towards this risk.

During the last decades, since El Asnam earthquake (Ms = 7.3, October 10, 1980), which took the precious lives of more than 2,600 people, severely destroying and damaging over 60,000 buildings, Boukri et al. (2013), Algeria has experienced several destructive earthquakes. These earthquakes show that there is significant seismic activity in Algeria that can cause considerable human and economic losses in urban areas near epicentral areas.
This activity mainly concerns the northern part of the country, Boukri et al. (2014), where the big cities are located. Depending on economic development and population growth, it is essential to assess the seismic risk.

To protect a city against earthquake disasters requires, as a first step, to model and predict theoretically the consequences, i.e. the structural damage as well as the socio-economic losses that may occur after an earthquake. In reality, it is critically important to estimate the effects of a potential earthquake in order to be prepared for disaster management, to organize relief operations, to anticipate and to take appropriate measures to reduce vulnerability and losses and thus ensure resilience.

Among the most effective actions, it is appropriate to conduct studies in order to simulate potential Earthquake damage scenarios, Dolce et al. (2003), that may concern and affect an urban area and its surroundings. In fact, local or government authorities and institutions take optimal decisions based on rigorous predictive estimations, also taking into account acceptable uncertainties. In reality, they rely on the theoretical results to take the appropriate measures before (prevention based on the results of vulnerability studies), during (elaboration of an emergency plan) and after (reconstruction and recovery) the earthquake. These studies provide a first insight of the spatial distribution of damage and their extent, in order to develop an action plan to reduce human and economic losses, Ansal et al. (2010). To perform an earthquake damage scenario, the mathematic convolution of the following 4 items is required: (a) seismic hazard (b) inventory of elements exposed to risk (c) vulnerability of exposure, Cutter (2012), and (d) local site conditions and site effects, with the use of reliable methodologies allowing appropriate damage calculation.

Generally, this kind of action is anticipated and achieved by the private financial sector. Nevertheless, it is widely accepted that the assessment and quantification of potential losses that may occur, in a given moment, are of great interest not only for private insurers, reinsurers and investors, but also for governments, stakeholders and local authorities. Indeed, the budgets for adaptive response, relief and reconstruction could be significant at the scale of a city or a country, Boukri et al. (2013).

This paper proposes to adapt an integrated earthquake loss estimation methodology to the Algerian urban context, namely the RADIUS Model (Risk Assessment Tools for Diagnosis of Urban Areas against Seismic Disaster) (OYO, 2000) after a prior adaptation to the Algerian building context, Boukri et al. (2015) and Boukri et al. (2017).

Within this framework, this concept is adopted and applied to estimate the urban seismic risk of the Great-Blida region (consisting of 4 cities, namely Blida, Ouled-Yaïch, Bouarfa and Beni Mered) taken as example of application, regarding an earthquake scenario.

2. OVERVIEW OF THE GREAT BLIDA

The Great-Blida consists of four municipalities: Blida, Ouled-Yaïch, Beni Mered and Bouarfa. It represents the largest conurbation of the department (Wilaya) of Blida (see Figure 1). It is located in the Central Northern part of Algeria; it extends on the plain of Mitidja to more than 260 m above the sea level. The Great-Blida shelters a population of 321,485 inhabitants out of 1,002,935 inhabitants throughout the province, which represents a high population density (1,390 inhabitants/km²), according to the last General Census of Population and Housing (2008), NOS (2008). Given its geographical location, the Great-Blida is a crossroads for exchange and connection between the West and the South of the country. It represents, also, a significant administrative, military, economic and scientific pole, in addition to other potentialities it has. For that, Blida has always experienced significant population flows from different parts of the country.

2.1. Seismic hazard in Blida region

The historical and instrumental seismicity shows that the Blida region is located in a very active seismic zone, Roussel (1973) and CGS (2013). The region experienced strong earthquakes during the last centuries generating seismic intensities ranged between X and XI, CGS (2013), which severely affected the city of Blida and its

surroundings. Besides those which occurred in 1716 (February 3), 1756 (March 1), and 1760 (May 16), the earthquake, which occurred in 1825 (March 2), is considered as the most severe (magnitude ~7.4, Beghoul et al. (2010); an MMI intensity (Modified Mercalli Intensity Scale) ~X, Novelli et al. (2015); ~ 7,000 as global death toll), destroying almost completely the old city of Blida (~ 3,000 as local death toll). It is also worth quoting the earthquake in 1867 (January 2) which destroyed Mouzaïa village, located 12 Km West of Blida city (I_0=X-XI) Novelli et al. (2015).The strongest earthquake, instrumentally recorded in the region of Blida, is that of 1959 (November 7), with a magnitude Ms = 5.6.

The Blida region is surrounded by a set of active faults, namely, Sahel, Menaceur, South Mitidja, Blida and Khemis El Khechna faults, as illustrated in Figure 1, Boukri (2014). The maximum magnitude intervals of these faults, given in Table 1 were estimated in the probabilistic seismic hazard assessment study of the Algiers region carried out by the National Earthquake Engineering Research Centre (CGS), CGS (1998) and CGS (2013).

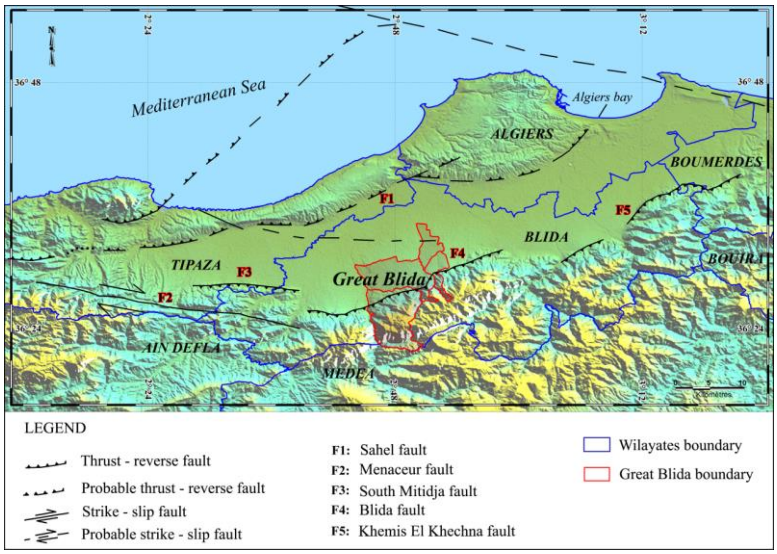

Figure 1. a) Location of the Great-Blida; b) Map of active faults in Blida region CGS (2013) and Boukri (2014)

Table 1. Seismic characteristics of active faults in the Blida region (CGS, 1998; CGS, 2013)

Fault	Length (Km)	Dip [°]	Mecanism	Depth (Km)	Maximum Magnitudes [Mw]
Sahel (F1)	70	45 towards N	Reverse fault	10	6.75
Menaceur (F2)	46	90 towards N-O	Strike-Slip faulting	10	6.75
Sud Mitidja (F3)	50	45 towards S	Reverse fault	10	6.75
Blida (F4)	45	55 towards SE	Reverse fault	10	6.5-7.0
Khemis El Khechna (F5)	58	55 towards SE	Reverse fault	10	6.75 - 7.0

2.2. Local site conditions

The Great-Blida perimeter is mostly located on the plain of the Mitidja basin (municipality of Beni-Mered and the northern parts of the municipalities of Blida and Ouled-Yaïch), whereas the other part, concerning the municipality of Bouarfa as well as the southern parts of the municipalities of Blida and Ouled-Yaïch, overlooks the piedmont and the mountains of *Atlas Blideen*. According to the seismic microzoning study of Blida province conducted by the National Earthquake Engineering Research Center CGS (2013), the Great-Blida features heterogeneous geological formations, as shown in Figure 2a.

Furthermore, geophysical investigations based on H/V spectral ratios measurements campaign were carried out by the National Earthquake Engineering Research Center (CGS) in this area, Boukri (2014) and Bouchelouh et al. (2017). More than 700 H/V measurement points have been performed, which allow to determine the shear velocity (Vs) of the geological formations in each mesh (the study zone being subdivided into cells by adopting a mesh grid). According to the collected results, local soil classification of the urban area of the Great-Blida has been identified for each mesh, following the RADIUS methodology and prescription of the current Algerian Seismic Code (RPA99 version 2003), RPA (2004), as shown in Figure 2b.

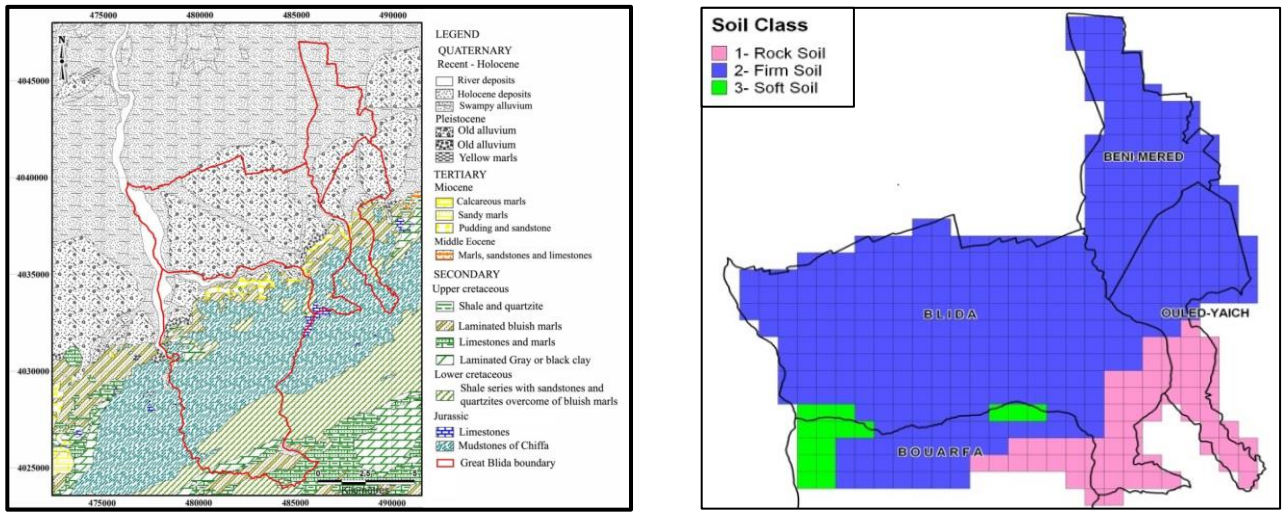

Figure 2. a) Geological map of the Great-Blida region CGS (2013), b) Local soil classification by meshes of the study area

3. BUILDING INVENTORY OF THE GREAT-BLIDA URBAN AREA

3.1. Zoning

Due to the variety of the urban fabric, the Great-Blida layout is subdivided it into 27 urban subdivisions (sectors). Each sector contains a group of meshes, named according to its most popular neighbourhood, as shown in Figure 3. According to the RADIUS methodology and for a rational seismic damage assessment, the study area (Urban perimeter of the Great-Blida) is subdivided into 412 meshes of 500 meters aside (see Figure 4).

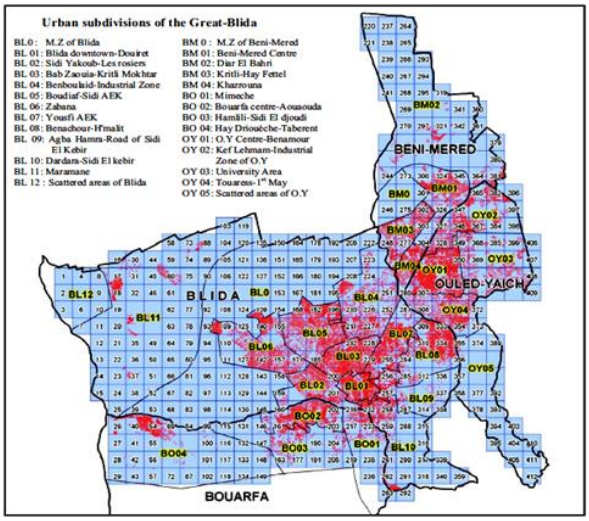

Figure 3. Representation of the Great-Blida urban area discretisation by mesh and urban subdivisions (sectors)

3.2. Buildings database

An extensive and systematic inventory has been performed out for the whole buildings within the pilot zone (see Figure 4). A building inventory form has been adopted, for this purpose as illustrated in Figure 4, Boukri et al. (2014), Boukri et al. (2015), Boukri et al. (2017). The urban buildings data have been digitized in an extensive GIS database carried out for this purpose, using a very high resolution (50 cm) Geo-Eye satellite image (see Figure 5) providing a precise geometric location of this building units.

National Earthquake Engineering Research Center (CGS)

BUILDING INVENTORY FORM OF THE GREAT-BLIDA

Name:…….. Date……/……/……..
N° of inventory form:……..
District:……..
Islet: ……
Address: ……

Construction Type:
Building ☐ Single house ☐ Hangar ☐ Mosque ☐ Precarious ☐
Other (precise) ……..

Construction Use:
Dwelling ☐ Hospital ☐ Commercial ☐ Administrative ☐ Sports ☐
Industrial ☐ School ☐ Socio-cultural ☐ Hydraulic ☐
Other (precise)……

Structure Type:
Reinforced concrete ☐ Masonry ☐ Steel ☐ Wood ☐
Other (precise)……
If Reinforced concrete: Moment frame ☐ Shear wall ☐ Dual ☐
If Masonry: Confined ☐ Non-Confined ☐

Date of construction (approximately):
Before 1981 ☐ 1981-1999 ☐ 1999-2003 ☐ After 2003 ☐
Number of stories: Number of basement:
Existence of under floor space: Yes ☐ No ☐

Dimension of the structure : X = …….m ; Y= ……m , Nb of bays:…
Plane regularity: Regular ☐ Light irregularity ☐ Irregular ☐
Elevation regularity: Regular ☐ Light irregularity ☐ Irregular ☐

Building implantation:
- On an unstable ground (settlement) Yes ☐ No ☐
- At the edge of a cliff Yes ☐ No ☐
- At top or bottom of a hill Yes ☐ No ☐
- At the border of a river Yes ☐ No ☐
- On a rough ground with break of significant slope Yes ☐ No ☐

Construction is at: Corner ☐ Middle ☐ Isolated ☐
If existence of seismic joint:…… (Thickness):……cm

General state of the construction:
Good ☐ Average ☐ Bad ☐

General observations:

Figure 4. Building inventory form Boukri et al. (2014)

Figure 5. Example of the Great-Blida building digitization under GIS platform using the high-resolution Geo-Eye satellite image (po_902114_0000000)

4. DAMAGE ASSESSMENT PROCEDURE AND EARTHQUAKE SCENARIO

4.1. Buildings

The building seismic damage assessment, corresponding to the earthquake scenario of the Great-Blida, is based on the RADIUS methodology adapted to the Algerian building context as developed in Boukri et al. (2015) and Boukri et al. (2017).

According to this approach, the building classification of the building has been established for Ten (10) classes or typologies, as illustrated in Table 2. Each building class is defined by a vulnerability function, which expresses the correlation between a characteristic earthquake parameter (intensity, acceleration, etc.) and the damage rate defined as the ratio of repair costs to the replacement cost of the building. These vulnerability functions are based on past earthquakes experience, Boukri et al. (2017). The damage levels considered in RADIUS methodology are complete damage (partial or total collapse) "D5" as well as severe or very severe damage "D4".

Table 2. RADIUS's vulnerability classes adapted for the Algerian buildings context, Boukri et al. (2017)

Building Class	Details
RES1	Informal constructions
RES2	Masonry/Reinforced concrete constructions not complying to any building code (built Before 1981) and having up to 3 stories
RES3	Masonry/Reinforced concrete Constructions not complying to any building code (built Before 1981) and having more than 3 stories
RES4	Reinforced Concrete constructions built according to various versions' of the Algerian building code (Post 1981)
EDU1	School and administrative Buildings up to 2 stories.
EDU2	School and administrative buildings, with more than 2 stories.
MED1	Buildings of hospital use, up to 3 stories
MED2	Buildings of hospital use, of more than 3 stories
COM	Shopping centres
IND	Industrial facilities (factories or hangars in masonry, concrete or steel frame)
Nota: The first Algerian Seismic Algerian Code for buildings was issued in 1981	

4.2. Casualties

The RADIUS methodology uses the model of Coburn et al. (1992a and) Coburn et al. (1992b) to estimate the number of deaths and injuries (moderate and severe).

5. SCENARIO EARTHQUAKE

According to the active fault models analysis in the Blida region, it appears that the most threatening seismic source is the Blida fault, which crosses the municipalities of Bouarfa, Blida and Ouled-Yaïch between the Atlas and the plain. This fault extends from the South of El-Affroun chain towards the East for about 45 kms, CGS (2013). The studies undertaken by Boudiaf (1996) show that the Eastern section of the fault (Ouled Yaïch-Bouinan segment) is more obvious on aerial photographs. This segment of 20 kms length, CGS (2013) and Boukri (2014), would have been at the origin of the devastating earthquake of 1825 (March 2), followed by a significant aftershock causing the ruin of Blida city and its surroundings.

Therefore, to perform the earthquake scenario in the study area, this fault is selected as a seismic model (scenario earthquake). This model is characterized by the following parameters:

- *Blida fault*: Maximum magnitude (Mw = 7); Focal depth: 10 km; Ground motion prediction equations (GMPE): Joyner and Boore, OYO (2000) and Boukri et al. (2015); Epicentral distance: 0.1 Km (see Figure 6). It corresponds to the projection of the assumed epicentre on the central axis of the study area to the centre of the first neighboring perpendicular mesh "232".
-
- Time of occurrence: **1st case:** It is assumed that the seismic event occurs at 10:00 am during a working day, assuming thus that most active people is at workplaces, children at school, and hospitals at normal service conditions. **2nd Case:** It is assumed that the seismic event occurs at 09:00 pm, i.e. almost the whole population is inside the study area.

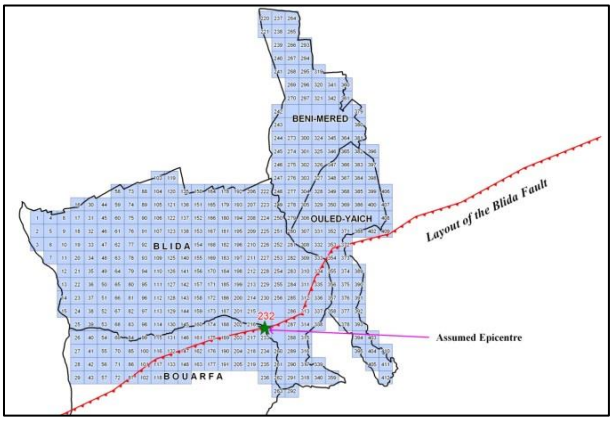

Figure 6. a) The Blida fault layout crossing the Great-Blida perimeter, b) Green star indicates the assumed epicentre

6. ESTIMATION OF DAMAGE

The spatial distribution of damaged building and casualties (only the number of injuries is given in this paper) mesh by mesh and in each sector (urban subdivisions) of the Great-Blida urban perimeter is summarized in Table 3 and illustrated on the corresponding GIS damage maps (See Figures 7-10).

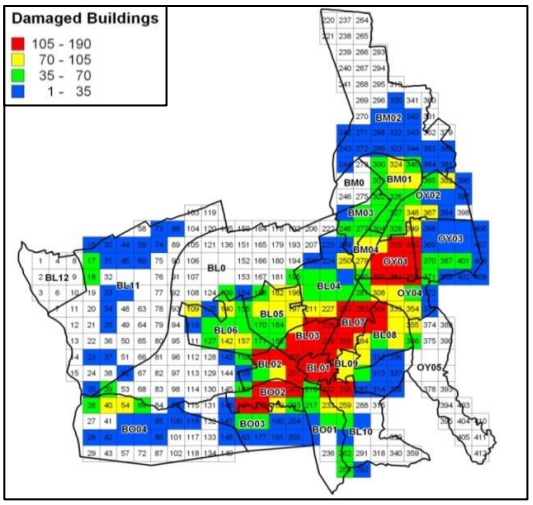

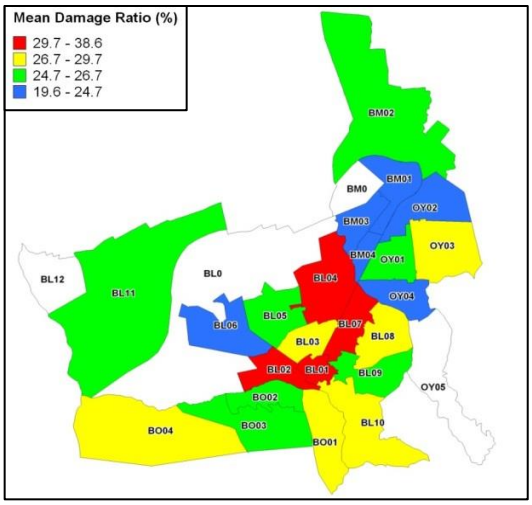

Figures 7 and 8. Damaged buildings mesh by mesh and sectors in the urban perimeter of the Great-Blida

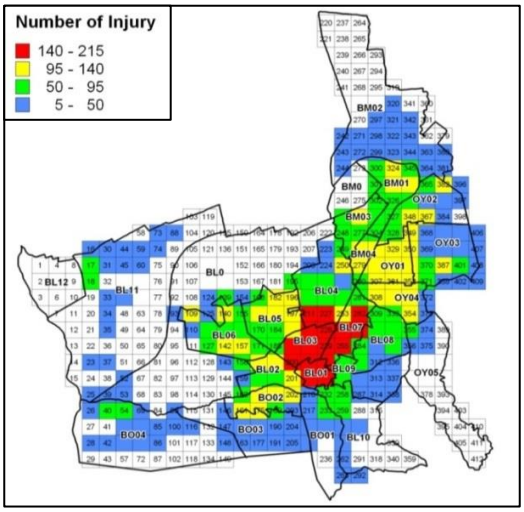

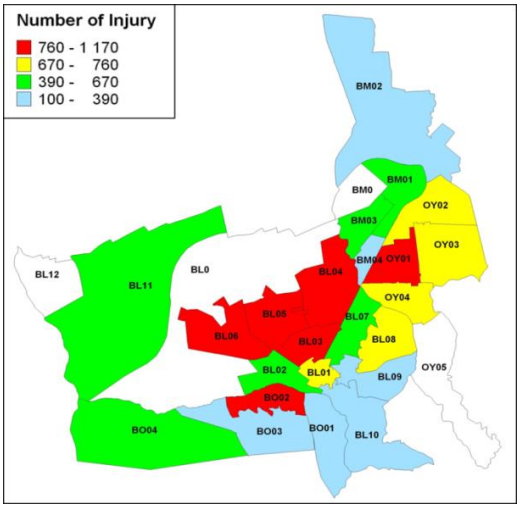

Figures 9 and 10. Distribution of injuries' mesh by mesh (Day scenario) and by sectors (Night scenario)

Table 3. Number and mean damage ratio of damaged buildings and number of injuries (day and night scenarios) in each urban subdivision

Sector	Number of buildings	Number of damaged	Mean damage ratio of buildings	Population (Night)	Population (Day)	Injury (Night)	Injury (Day)
BL01	1,967	759	38.60	6,795	6,342	884	706
BL02	1,546	502	32.48	6,532	6,267	520	559
BL03	2,816	828	29.40	16,392	12,394	1,206	984
BL04	2,115	659	31.14	10,495	11,905	769	1,057
BL05	2,930	753	25.71	21,966	14,767	1,465	1,009
BL06	3,056	735	24.07	23,780	16,913	1,553	1,159
BL07	2,509	780	31.07	12,932	8,871	983	669
BL08	3,153	846	26.83	24,091	12,963	1,502	691
BL09	1,159	301	25.94	7,983	4,466	534	263
BL10	1,785	518	29.00	9,630	5,681	666	353
BL11	1,640	407	24.83	14,507	8,360	870	445
BL12	0	0	0	0	0	0	0
BM01	1,720	405	23.53	13,255	9,084	780	553
BM02	924	229	24.81	7,054	4,779	406	285
BM03	1,580	310	19.65	15,631	9,580	921	558
BM04	1,175	288	24.54	8,871	5,897	559	380
BO01	935	253	27.04	6,954	3,866	470	232
BO02	2,970	780	26.25	22,195	12,780	1,496	780
BO03	997	259	25.95	7,223	3,937	467	216
BO04	1,898	548	28.89	13,642	7,833	864	444
OY01	3,973	981	24.70	29,962	18,724	1,913	1,167
OY02	2,008	490	24.39	16,875	10,994	1,012	681
OY03	1,574	444	28.19	11,008	9,804	714	758
OY04	1,902	471	24.76	13,711	10,394	879	733
OY05	0	0	0	0	0	0	0
Great-Blida	**46,332**	**12,545**	**27.08**	**321,485**	**21,6601**	**21,433**	**14,682**

7. FINANCIAL LOSSES ESTIMATION

It also seems worth estimating, even approximately, the financial losses that may result from the earthquake seismic that may occur in the Great-Blida urban area. For simplicity's sake, this estimate focuses, initially, only on losses related to buildings. According to the General Population and Housing Census in Algeria, NOS (2008), conducted in Algeria in 2008, this urban agglomeration consists of 63,185 dwellings. The average price per square metre of new housing is estimated about 50,000 DZD/m², based on the assumption that the average surface area of each dwelling is S_{du} = 70 m². The expected results of estimating financial losses in the housing stock are shown in Table 4, see Equation 1:

$$C_{fl} = (N_d . D_{mr}) . S_{du} . C_{sq} \quad (1)$$

Table 4. Financial losses estimation in the Great-Blida dwelling stock

N_d : Dwelling	**D_{mr}** : Mean damage ratio	**N_{dd}** : Damaged dwellings Number	**Nb_{dd}** : Damaged living area (m²)	**C_{sq}** : Price/m²	**C_{fl}** : Amount of financial losses
63,185	27.08%	17,110	1,197,700	50 (*kilo*-DZD)	**60** (*Giga*-DZD)

8. CONCLUSION

In the present work, an integrated methodology for urban-scale seismic vulnerability assessment based on GIS has been adopted, i.e. (GIS-Based Model RADIUS). This methodology requested a prior adaptation to the Algerian context and it has been adopted in order to study the seismic intensity distribution, and the buildings seismic damage located in an Algerian study area. It predicts, also, the number of human losses and their spatial distributions. These seismic damage results are represented on GIS damage maps, helpful for the authorities and stakeholders in decision-making.

The use of thematic cartography and mapping of the seismic damage results, in the affected areas, thanks to Geographic Information Systems (GIS) provides a precise location and summarized assessment of the most exposed and potentially impacted urban areas, assets and facilities.

Once this approach has been adapted to the Algerian context, the damage assessment through earthquake scenarios is performed out in urban areas exposed to major seismic risk. Its application to the Great-Blida urban area, potentially subjected to seismic risk, focuses on the case of 04 municipalities: *Blida*, *Ouled-Yaïch*, *Bouarfa* and *Beni-Mered*. Its main purpose is to estimate seismic damage for buildings as well as socio-economic losses (human and financial issues).

The urban buildings, assets and facilities data have been digitized in an extensive GIS database carried out for this purpose, using a very high resolution (50 cm) Geo-Eye satellite image.

The earthquake scenario assumes an earthquake of magnitude Mw = 7 generated from the Blida fault that crosses the study area and which proves to be the most threatening. For such scenario, the results show that the probable mean damage ratio of the study area, in terms of buildings, is about 27%. These damages reflect the concentration of an old urban heritage in the Great Blida urban perimeter, amplified by the epicentre proximity. This is equivalent to about 17,110 dwelling losses. In terms of surface, the losses would be close to 1,200,000 sqm of floors, which represents a financial loss of about 60 Giga-DZD (~ 0.8 Giga-$), in terms of buildings reconstruction or renewal cost. Regarding the human losses, as expected, it is shown that a seismic event occurring in the evening, at around 9pm, has worse consequences compared to a day occurrence, at around 10 am.

REFERENCES

Ansal A, Kurtulus A, Tönük G (2010). Seismic microzonation and earthquake damage scenarios for urban areas. *Soil Dynamics and Earthquake Engineering* **29**: 1319–1328.

Bouchelouh A, Bensalem R, Zaourar N, Machane D, Moulouel H, Oubaiche EH. The miocene roof mapping using microtremor recording and electrical survey method in blida city, Algeria. *Pure and Applied Geophysics* **175(1)**: 287-301.

Boudiaf A (1996). Etude sismotectonique de la région d'Alger et de la Kabylie (Algérie) : utilisation des modèles numériques de terrains (MNT) et de la télédétection pour la reconnaissance des structures tectoniques actives : contribution à l'évaluation de l'aléa sismique. PhD Thesis, Université Montpellier II, Science et Techniques du Languedoc, 274p, France.

Boukri M, Farsi MN, Mébarki A, Naili M, Belazougui M, Amellal O, Guessoum N, Mezazigh B (2017). Seismic vulnerability appraisal according to the Algerian building context. *Proceedings of 11th International Conference on Earthquake Resistant Engineering Structures*, 05-07 July, Alicante, Spain.

Boukri M, Farsi MN, Mébarki A, Naili M, Belazougui M, Amellal O, Guessoum N, Mezazigh B et al. (2015). Réduction du risque sismique urbain en Algérie : Adaptation et application de la méthodologie RADIUS. Actes du 9ème Colloque National AFPS 2015, (30 November-02 December, IFSTTAR, Paris, France.

Boukri M (2014). Vulnérabilité sismique du bâti Algérien : Développement d'un outil d'aide à la décision, PhD Thesis, University of Blida1, Algeria.

Boukri M, Farsi MN, Mébarki A, Belazougui M, Amellal O, Mezazigh B, Guessoum N, Bourenane H and Benhamouche A (2014). Seismic risk and damage prediction: case of the buildings in Constantine city (Algeria). *Bulletin of Earthquake Engineering* **12(6)**: 2683-2704.

Boukri M, Farsi MN, Mébarki A, Belazougui M (2013). Development of an integrated approach for Algerian building seismic damage assessment. *Structural Engineering and Mechanics* **47(4)**: 471-493.

CGS (2013). Vulnerability and seismic risk study of Blida, Report, National Earthquake Engineering Research Center, CGS, Algeria.

CGS (1998). Probabilistic hazard assessment of the Algiers region. Report, National Earthquake Engineering Research Center, CGS, Algeria.

Coburn AW, Spence RJS (1992a). Earthquake Protection. *John Wiley and Sons*, 355p.

Coburn AW, Spence RJS (1992b). A. Pomonis, Factors determining human casualty levels in earthquakes: Mortality prediction in building collapse. *Proceedings of the 10th World Conference on Earthquake Engineering*, Madrid, Spain.

Cutter SL (2012). Vulnerability to environmental conceptual framework for responses to natural hazards. *International. Journal of Disaster Risk Reduction* **1**: 5-16.

Dolce M, Masi A, Marino M, Vona M (2003). Earthquake damage scenarios of the building stock of Potenza (Southern Italy) including site effects. *Bulletin of Earthquake Engineering* **1**: 115-140.

RPA99 version 2003 (2004). Algerian Seismic Code, Ministry of Housing and Urban Planning, DTR-BC 2.48, Algeria.

Novelli VI, D'Ayala D, Makhloufi N, Benouar D, Zekagh A (2015). A procedure for the identification of the seismic vulnerability at territorial scale. Application to the Casbah of Algiers. *Bulletin of Earthquake Engineering* **13**: 177-202.

Beghoul N, Chatelain JL et al. (2010). Seismic empirical relations for the Tellian atlas, north Africa, and their Usefulness for Seismic Risk Assessment. *Pure and Applied Geophysics* **167**: 277–321.

NOS (2008). General Census of Population and Housing of 2008, National Office of Statistics, Algeria.

OYO Corporation (2000). RADIUS Methodology, Report IDNDR.

Roussel J (1973). L'activité sismique en Algérie de 1951 à 1970 inclus. *Extrait du Bulletin de la Société d'Histoire Naturelle de l'Afrique du Nord* **64(3-4)** : 185-210.

"ADAPTIVE NEURO-FUZZY INFERENCE SYSTEMS" FOR ESTABLISH GROUND MOTION PREDICTION EQUATION: AN EXAMPLE BASED ON THE NGA-WEST 2 DATA

Ameur M.[1], Derras B.[2], Zendagui D.[3]

[1] *Dr, Civil Engineering, University of Tlemcen/RISAM laboratory, Tlemcen, Algeria*
[2] *Pr, Civil Engineering, University of Saida/Civil ingeneering, Saida, Algeria*
[3] *Pr, Civil Engineering, University of Tlemcen/RISAM laboratory, Tlemcen, Algeria*
Email: b_derras@mail.univ-tlemcen.dz

ABSTRACT:

Adaptive Neuro Fuzzy Inference Systems (ANFIS) is used here to obtain the robust Ground Motion Prediction Equation (GMPE). Avoiding a priori functional form, ANFIS provides fully data-driven predictive models. A large subset of the NGA-West2 database is used, including 2335 records from 580 sites and 137 earthquakes. Only shallow earthquakes and recordings corresponding to stations with measured V_{s30} properties are selected. Three basics input parameters are choice: the moment magnitude (M_w), the Joyner-Boore distance (R_{JB}), and the time-averaged shear-wave velocity down to 30 m (V_{s30}). ANFIS model output is the Peak Ground Acceleration (*PGA*), Peak Ground Velocity (*PGV*) and 5% damped Pseudo-Spectral Acceleration (*PSA*) at periods from 0.01 to 4 s. A procedure similar to the random-effects approach is developed to provide between and within event standard deviations. The total standard deviation (σ) varies between [0.303 and 0.360] (log_{10} units) depending on the period. The ground motion predictions resulting from such simple three explanatory variables ANFIS models, are shown to be comparable to the most recent NGA results (e.g. Boore et al. 2014; Derras et al. 2016). The main advantage of ANFIS compared to Artifical Neuronal Network (ANN) is its simple and one-off topology: five layers. Although the functional form is not imposed a priori, our results exhibit a number of physically sound features: magnitude scaling of the distance dependency, near-fault saturation distance increasing with magnitude and amplification on soft soils. The ability to implement ANFIS model using an analytic equation and Excel or another simple script is demonstrated, which opens a vast field for its use.

KEYWORDS: Ground motions; Neuro-Fuzzy; PGA; ANFIS; and NGA.

1. INTRODUCTION

Seismic hazard analysis (SHA) depends on Ground Motion Prediction Equations (GMPEs) that quantify the amplitude of the Ground Motion (GM) as a function of distance, magnitude and site condition proxies. Given the variety of factors complicating earthquake shaking, attenuation relationships have a large degree of uncertainty. This uncertainty is strongly affected by quantity and quality of the dataset and also by the approach used to obtain the GMPEs. The empirical regression least square is commonly used. In these approaches type, the knowledge of a priori functional form is required. However, GMPEs has differences in the way they can be used to model magnitude and distance dependencies of ground-motion parameters of engineering interest (Derras et al. 2012). The problem arises because of the lack of complete understanding of the relative importance of the factors that control GM. Moreover, the functional forms used for GMPEs have evolved considerably, and they involve more and more independent variables (Douglas and Edwards 2016). As a consequence, the problem of balancing model complexity and data constraints becomes increasingly relevant for the generation of empirical GM models (e.g. Chiou and Youngs 2014). This problem generates a time and a cost additional and a epistemic ground-motion aleatory variability.

A possible solution to avoid specification of any functional form is to use a data-driven approach. The availability of increasingly data collected recently by modern accelerometric networks (e.g. KiN-Net, RESORCE and NGA-West2) and the development of artificial intelligence methods offer the opportunity to develop data-driven ground-motion models. In this context, we cite the work of (Derras et al. 2014; Ahmad et al. 2008; Liu et al. 2006; Kerh and Ting 2005) in which the authors used Artificial Neural Networks (ANN) to develop GMPEs fully driven by the data. Nonetheless, the design of the ANN model requires several choices concerning the number of hidden layers and the corresponding number of nodes and the method used to avoid the overfitting problem (Derras et al. 2012).

To avoid being embarrassed by all these choices, which are not always correct, we use a complementary approach in this document. This is the fuzzy-logic (FL) which was introduced by (Zadeh 1965). He introduced the concept of fuzzy sets to approximate human reasoning with adequate representation of imprecise knowledge, uncertain which are based on linguistic terms.

The joint use of ANN and FL allows taking advantage of both. The learning capacity of the first and the clarity and the unique architecture type of the second can substantially shorten the learning process. To do this, a hybrid method is proposed in this work named ANFIS: Adaptive Neuro-Fuzzy Inference System (Jang 1991, 1993). ANFIS is the integration of a fuzzy inference system with a back-propagation algorithm. In recent years, the ANFIS has received growing interest from the earthquake engineering community for e.g. generation of shear modulus and damping ratio (Akbulut et al. 2004), a Comparison of ANFIS and ANN for the prediction of the peak ground acceleration in Indian Himalayan region (Mittal et al. 2012), earthquake magnitude prediction (Mirrashid 2014) and risk management of natural disasters : A Fuzzy-Probabilistic Methodology and its application to seismic hazard (Karimi 2006).

In this study, the Peak Ground Acceleration (PGA), Peak Ground Velocity (PGV) and 5% damped Pseudo-Spectral Acceleration (PSA) from 0.01 to 4 s are determined from three simple parameters related to magnitude, distance and site conditions. The input parameters considered here are the Joyner & Boore distance R_{JB} (km), moment magnitude M_w, and the time averaged shear-wave velocity down to 30m V_{S30} (m/s). The first goal of this paper is to show the capability of ANFIS to predict the same tends and level of the GM intensity and the GM variability given by classical GMPEs (e.g. Boore et al. 2014). The second goal is to explain that the build of GMPE by ANFIS is easier than by ANN: the ANFIS present a unique architecture and the over-fitting problem does not arise. Finally, we demonstrate that with ANFIS we can obtain an analytic GMPE.

After a short presentation of the NGA-West2 dataset selection used for the present study, a section is dedicated to the presentation of the ANFIS approach and its specific implementation in the present application. The following section concentrates on the results of the application to the NGA-West2 data. We then use the obtained results to discuss the respective influences of each considered input parameter. The result of the use ANFIS model to predict the GM is compared to more complex NGA-West2 model of (Boore et al. 2014) in terms of the median and aleatory variability predictions, and also with model of (Derras et al. 2016) in terms of standard deviation.

2. NGA-WEST2 DATASET

The NGA-West 2 is a research program on the (NGA: Next Generation Attenuation) models for shallow crustal earthquakes in active tectonic regions. The NGA-West 2 flat files contain site and source information, along with R_{JB} parameters and the corresponding Ground Motion (GM) Intensity Measures (IMs).This database is described in (Ancheta et al., 2014). The database includes 21540 records, 5540 events. A subset of the database has been used in the current study. We have eliminated all records with a depth over then 25 km, to focus around crustal earthquakes (Derras et al., 2014). The unrepresentative free field recordings were deleted. So only classification stations GMX C1 was selected (Abrahamson et al., 2013). We have kept the main shock and eliminated all replicas, (boummer et al. 2010). In addition, we maintained that sites with V_{S30} values measured (Derras et al., 2016), a moment magnitude M_w and Joney & Boore distance R_{JB}. In that, the majority of events dataset for Japan, Taiwan and the California.

Finally, after these selections process we obtain a dataset of 2335 records, 137 earthquakes, and 580 site, with the range of M_w =[3,2 - 7,9], covering a distance (R_{JB}) of 0.01 to 358 km, and a value of measured V_{S30} varies from 110 - 1540 m/s. While the corresponding range of PGA is of [3.59 $\times 10^{-6}$ to 1.76] g. The PGV values belong to the interval [8.78 × 10-4 - 115] cm/s, and a margin of PSA that ranges from 4.16 × 10-8 g to 4.81 g, for the period T = [0.01 to 4] s.

2.1. Dataset distribution

The distributions of the dataset linking M_w, R_{JB}, V_{S30}, and PGA are displayed on (Figure 1). (Figure 1a) shows the M_w as function as R_{JB} with different ranges of PGA, and the distribution of PGA dependence with R_{JB} distance is displayed on the (Figure 1b), for different ranges of magnitude M_w. Figures 1 clearly show the attenuation of the ground motion with distance, and the presence of the scale-magnitude effect.

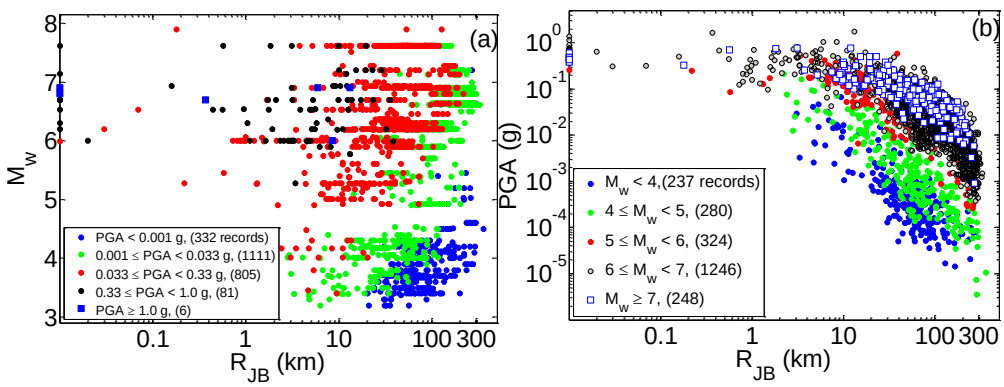

Figure 1. Distribution of the NGA-West 2 dataset considered in this study. The left plots correpond to the Magnitude (M_w) - distance (R_{JB}) distribution. For this plot, the bins with different colors correspond to five sample-size subsets with increasing PGA values from 0.001 to 1 g. On the right plot, the distribution of PGA versus distance (R_{JB}) is shown. In this plot, the distribution is given by bins of Magnitude, M_w=[4 - 7]

The cumulative distribution function (CDF) of the dataset with respect to the exlanatory variables, magnitude M_w, R_{JB} distance, V_{S30} and PGA are given in Figure 2. The R_{JB}, V_{S30} and PGA distributions are found to follow a log normal law, while M_w follow a normal law. In our ANFIS models, we thus used the logarithm values of R_{JB}, V_{S30} and spectral ordinates PSAs.

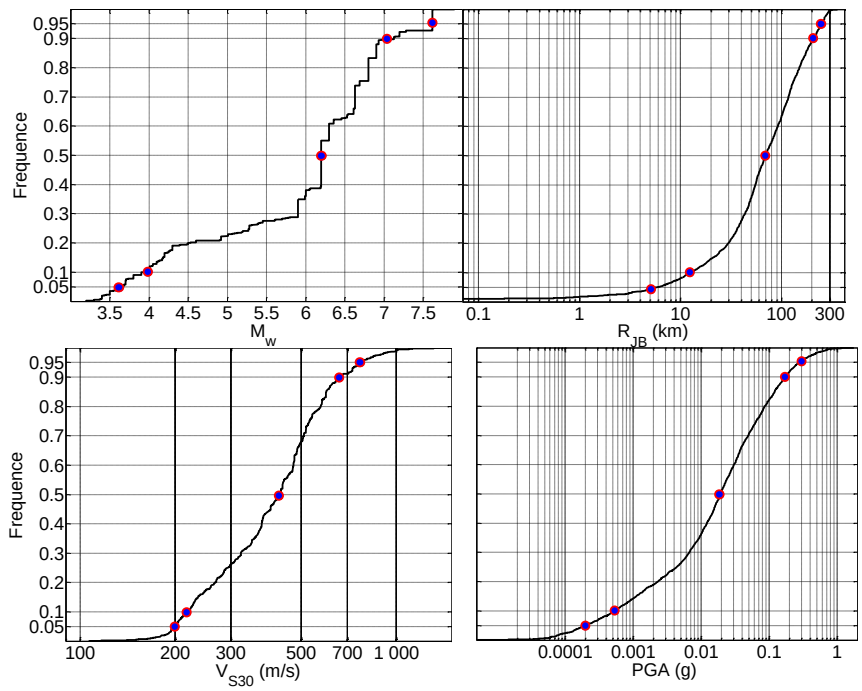

Figure 2. Cumulative distributions function (CDF) of the NGA-West 2 dataset, with respect to the metadata. Magnitude M_w (top left), distance R_{JB} (top right), V_{S30} (bottom left) and PGA (bottom right). The blue-red circles represent the extreme and the medians values of the M_w, R_{JB}, V_{S30} and PGA: 5 %, 10%, 50%, 90% and 95% of the empirical CDF respectively

3. METHODOLOGIE

In this work, three parameters were used describing the source effect, the wave propagation effect, and the site effect, which are (M_w, R_{JB}, and V_{S30}) respectively. The output parameters taken into account are *PGA*, *PGV* and the *PSA* at periods ranging from 0.01 to 4 s, are considered representative parameters of the ground motion.
The random-effect regression algorithm made popular within engineering seismology by (Abrahamson and Youngs, 1992) is arguably the most commonly used approach for developing empirical ground-motion models. In our ANFIS models we used this type of approach in order to facilitate the comparability with classical GMPEs. This resulted in a two-phase building process:

3.1 Fixed model

To predict the *PGA*, *PGV* and *PSA* we used an Adaptive Network Fuzzy Inference System (ANFIS) which is a kind of Artificial Neural Network (ANN) that is based on Takagi–Sugeno-Kang : TSK (takagi and sugeno 1985; sugeno and kang 1986) fuzzy inference system. ANFIS is a multi-layer feed forward network in which each node performs a particular function (node function) on incoming signals as well as a set of parameters pertaining to this node (jang 1993).ANFIS include five layers : inputs parameters, the four hidden layer and output layer, as illustrated in Figure 3.

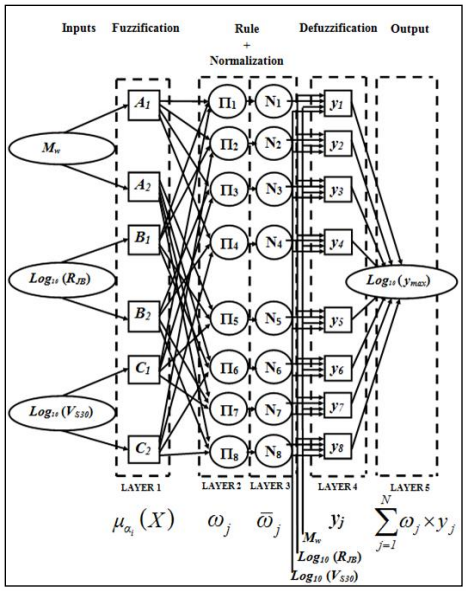

Figure 3. Structure of ANFIS model using to predict PGA or PGV or PSA. There are five fixed layers in this model; The inputs parameters are M_w, $\log_{10}(R_{JB})$ and $\log_{10}(V_{S30})$. is the membership function for each inputs parameters

The inputs parameters are the M_w, R_{JB}, and V_{S30}. The first hidden layer is called a fuzzification layer. This layer is characterized by the membership function (MFs). It is noted that there are several membership functions. The classical membership functions (gauss, trapeze and triangular) were considered, as listed in Table 1.

Table 1. Influence of different membership functions on total σ at T = 0.00, 0.20, 1.00 and 2.00 s.

Membership functions	Triangular	Trapezoidal	Gaussian
PGV	0.2799	0.2757	0.2739
PSA (T = 0.00 s)	0.3219	0.3103	0.3118
PSA (T = 0.20 s)	0.3467	0.3372	0.3379
PSA (T = 1.00 s)	0.3036	0.3037	0.3008
PSA (T = 2.00 s)	0.3130	0.3132	0.3218

The best combination of membership functions which gives a small σ and simple model is a triangular type function, which can be written as follows:

$$\mu_{\alpha_i}(X) = \begin{cases} \dfrac{X - a_i}{b_i - a_i} & if \quad a_i \le X \le b_i \\ \dfrac{c_i - X}{c_i - b_i} & if \quad b_i \le X \le c_i \end{cases} \qquad i = 1, 2 \qquad (1)$$

Where X is corresponding either M_w, R_{JB} or V_{S30}. αi is the linguistic input variable : ai for X=M_w, bi for X= R_{JB} or ci for X= V_{S30} (Figure 3).

In this study each input parameter is assumed to have two associated MFs. ai, Bi, and Ci are called a premise parameters, where the node of this layer is a node adaptive to reflect different adaptive capabilities, we use both circle (fixed) nodes and square (adaptive) nodes.

In the second layer, the outputs are obtained by the products of the corresponding degrees of membership in the layer 1, based on the application of the operator product "T-norm" (jang 1997) as following:

$$\omega_j = \prod_{J=1}^{N} \mu_{\alpha_i}(X) = \mu_{A_i}(M_w) \times \mu_{B_i}(R_{JB}) \times \mu_{C_i}(V_{S30}) \qquad j = [1 \text{ to } 8] \qquad (2)$$

Where ωj is the rules firing strengths for whose each node in this layer. The number of rules (N) equal to $(i)^I$, when I is the number of inputs parameters.

In the third layer we normalize the ωj by:

$$\overline{\omega_j} = \frac{\omega_j}{\sum_{j=1}^{N} \omega_j} \qquad j = [1 \text{ to } 8] \qquad (3)$$

The fourth layer has adaptive nodes and the output can be calculated by TSK:

$$y_j = p_j \times M_w + q_j \times R_{JB} + r_j \times V_{S30} + s_j \qquad j = [1 \text{ to } 8] \qquad (4)$$

So the output of this layer can be written as follows:

$$\overline{\omega_j} \times y_j = \overline{\omega_j} \times (p_j \times M_w + q_j \times R_{JB} + r_j \times V_{S30} + s_j) \qquad j = [1 \text{ to } 8] \qquad (5)$$

Where, p_j, q_j, r_j and s_j, are the coefficients of linear combination; the parameters in this layer are referred to as consequent parameters. This layer can be called defuzzification layer.

In the last layer, we have only single node, which represents either PGA, PGV or PSA for a fixed period. The output parameter is given by:

$$log_{10}(y_{max}) = \sum_{j=1}^{N} \overline{\omega_j} \times y_j \qquad j = [1 \text{ to } 8] \qquad (6)$$

Where the y_{max} can be presented PGA, PGV or PSA at periods [0.01 to 4 s].

The classical training rule based on the gradient method is known for its slowness and tendency to become trapped in local minima. To avoid both those problems, we propose here, a hybrid training rule. So, to obtain the premises and consequent parameters, we use two-pass training cycles (shi et al. 1996) :1) forward pass: premise parameters are fixed and consequent parameters are computed using a least squared error (LSE) algorithm, 2) backward pass: consequent parameters are fixed and premise parameters are computed using a gradient descent algorithm (usually back-propagation), (jang 1997).

3.2 Random-Effect Model

A procedure similar to the random-effect approach was then used to provide the between-event and within-event sigma, as described in (Derras et al., 2014). For each period, the final ANFIS model is obtained using the maximum likelihood approach developed by abrahamson and youngs (1992). In addition to the median, this approach provides the aleatory uncertainly values. The performance of the ANFIS scheme is measured by the sigma $\sigma(T)$ value classically used in GMPEs, which is decomposed into the between-event (τ) and within-event (ϕ) variabilities: both are zero-mean, independent, normally distributed random variables with standard deviations τ and ϕ (al atik et al. 2010). The between-event and within-event residuals are assumed uncorrelated, so that the total σ at a period T of the ground motion model can be calculated according to equation 7:

$$\sigma(T) = \sqrt{\tau(T)^2 + \phi(T)^2} \tag{7}$$

Finally, the models were established for each output parameter *PGA*, PGV, and PSA at different periods, with the same input parameters M_w, R_{JB}, and V_{S30}, the final implementation of the ANFIS model elaborated, was performed using Matlab software on the toolbox "fuzzy logic". The resulting model is defined by the following equation:

$$Log_{10}\left(PSA_{ij}\right) = Log_{10}\left(P\hat{S}A_{ij}\right) + \eta_i + \varepsilon_{ij} \tag{8}$$

Where $P\hat{S}A_{ij}$ and PSA_{ij} are, respectively the median predicted (equation 9) and observed values, η_i is the between-event residual for the event i (137), and ε_{ij} is the within-event residual for recording j (2335) of events i. The relationship between the between-event and within-event standard deviation τ and ϕ is given by (equation. 7) under the random effects procedure. In the following sections, we present two analyses: ground motion aleatory variability analysis and ground-motion median analysis.

4. GROUND-MOTION MODEL ANALYSIS

4.1 Analysis of Residuals

The random-effects model leads ηi and εij residuals. For classical GMPE techniques, these residual should: (left) show a log normal distribution; and (right) be free from any trend with respect to any of the explanatory variables. The ηi and εij residuals normal probability distributions for four periods T = [0.0, 0.2, 1.0 and 2.0] s are shown in follow figure:

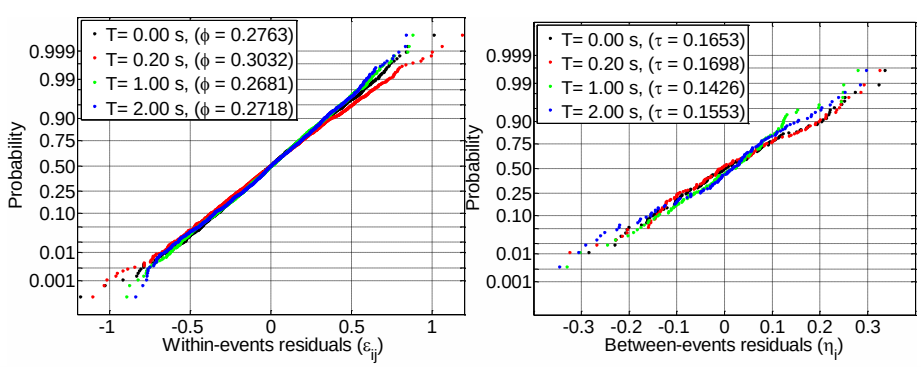

Figure 4. Normal probability plot of the residuals, at T=0.00 s (black dot), T=0.20s (red dot), T=1.00 s (green dot) and T=2.00s (blue line). Top : Probability-εij. Bottom Probability-ηi

Generally, they thus appear to fit a distribution very well, up to about ±3ϕ and ±3τ for all considering periods.

4.2 The functional form

The functional form provided by the ANFIS approach, represents the prediction median of the ground-motion parameters. The classical geometric mean horizontal components $\log_{10}$ of ground motion parameters PGA(g) or PGV (m/s) or PSA(g) [0.01– 4 s], are given by the following equation:

$$\log_{10}(y_{max}) = \frac{1}{b}\left(\begin{array}{c} a_{20}+M_w(a_6+a_7M_w)+\log_{10}R_{JB}(a_5+a_9\log_{10}R_{JB})+\log_{10}V_{S30}(a_4+a_{13}\log_{10}V_{S30})+ \\ M_w(a_{10}\log_{10}R_{JB}+a_{18}\log_{10}V_{S30}+a_{15}(\log_{10}V_{S30})^2+a_{10}(\log_{10}R_{JB})^2+M_w^2(a_8\log_{10}R_{JB}+ \\ a_{11}\log_{10}V_{S30})+\log_{10}R_{JB}(a_{17}\log_{10}V_{S30}+a_{14}(\log_{10}V_{S30})^2)+(\log_{10}R_{JB})^2(a_{12}\log_{10}V_{S30})+ \\ M_w(\log_{10}R_{JB})(\log_{10}V_{S30})(a_{19}+a_3M_w+a_2\log_{10}R_{JB}+a_1\log_{10}V_{S30}) \end{array}\right) \quad (9)$$

$$b=a_{21}\log_{10}V_{S30}+a_{22}\log_{10}R_{JB}+a_{23}M_w+a_{24}M_w\log_{10}R_{JB}+a_{25}(\log_{10}R_{JB})(\log_{10}V_{S30})+a_{26}M_w\log_{10}V_{S30}+ a_{27}M_w(\log_{10}R_{JB})(\log_{10}V_{S30})+a_{28}$$

4.3 Range of Applicability

Table 2. Intervals of validity of metadata (M_w, R_{JB}, V_{S30}) using in the proposed ANFIS model.

	M_w	R_{JB} (km)	V_{S30} (m/s)
Min	3.6	6	200
Max	7.6	200	760

Table 2 watch the validity ranges of input seismological parameters (M_w, R_{JB}, V_{S30}) that we recommend (for the ANFIS model) for the best of PSA, PGA and PGV prediction. These validity ranges were adopted from the data set analysis presented in the (Figures 1 and 2); thus, from residual analysis presented in Figure. 5 when we show the distribution of between-event residuals versus M_w, and of within-event residuals versus R_{JB} and V_{S30}, for T = 0.0 s.

The mean and standard deviations of the residuals for different metadata ranges are also indicated (Figure 5) in order to identify possible localized bias. If we consider the applicability range of ANFIS fully data-driven models [5-95] % of CDF, The residual do not exhibit a trend with magnitude M_w, V_{S30} and R_{JB} except for long distance where R_{JB}> 200 km. To have a stable model, we limit the applicability range at 200 km.

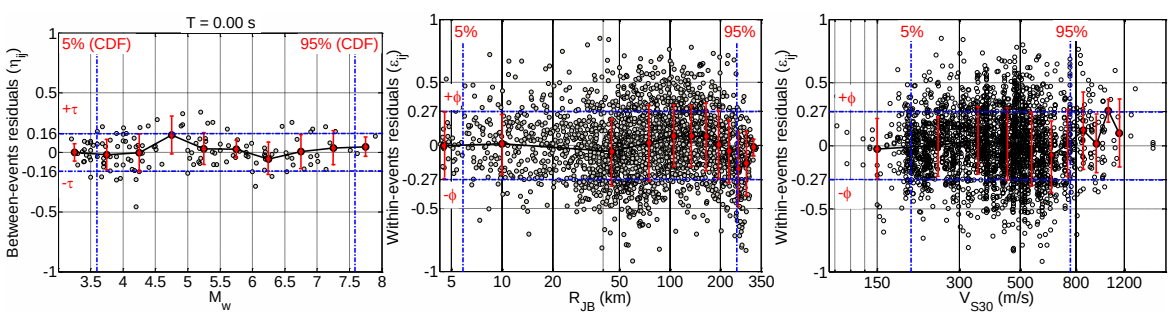

Figure 5. Distributions of the residuals for the PGA from the ANFIS model. Between-events residuals with M_w (top). Within-event residulas vs R_{JB} (middle) and against V_{S30} (bottom).

We illustrate also the Mean residuals ± standard deviations in the different metadata ranges. The circles show average residuals, the vertical bars are the symmetrical error bars for two standard deviations; and the horizontal bars represent ±1 standard deviation. The two dotted vertical blue lignes represent the values at 5 % and 95 % of the CDF (Figure 2)

5. COMPARISON BETWEEN ANFIS AND BOORE (2014) MODELS

A comparison of the median ground motion values from the (Boore et al. 2014) GMPE and our proposed model (Equation 9) is presented. The reason for that we have chosen (Boore et al. 2014) is it because it is a simple model with few seismic parameters. The different comparisons are mentioned in the (Figures 6 and 7). All the parameters used in (Boore et al. 2014) which were unknown were assigned their default values (i.e. δZ1.0 = 0, unknown style of the fault).

5.1 ANFIS model curve

Figure 6 Compares the peak ground acceleration curves vs R_{JB} for M_w=4, 5, 6 and 7, the results are shown here for a target V_{S30} = 400 m/s and V_{S30} = 760 m/s. This result shows that the ground-motion model derived using the ANFIS method and the NGA-West 2 database converge as compared with Boore 2014 model.

In addition to that, the trends of the curves are appropriate, they look like to the recent GMPEs: the decay of the ground-motion intensity with distance depends on the magnitude, mainly at short distances: near-fault saturation for large magnitudes.

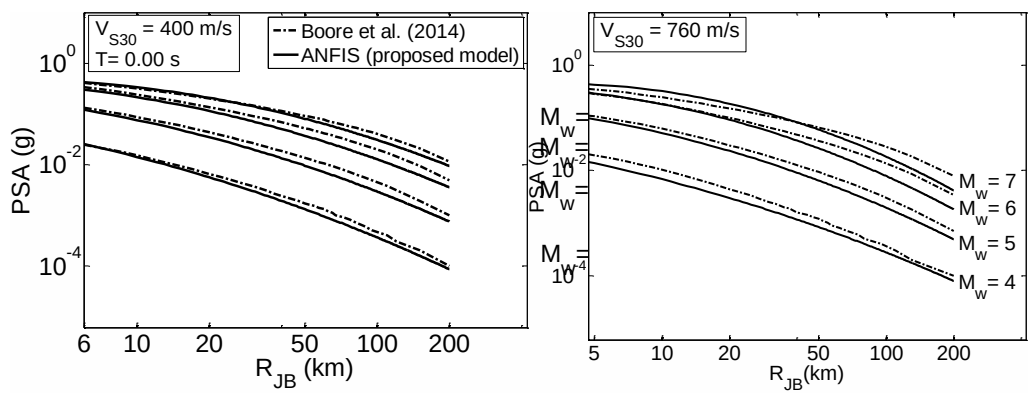

Figure 6. Ground-motion predictions as a function of the Joyner & Boore distance for four different magnitudes and for V_{S30} = 400 m/s and VS_{30} = 760 m/s. Solid lines represent the PGA given from ANFIS approach. The dotted lines illustrate the ground motion obtained by (Boore et al. 2014)

5.2 Response spectra

The median response spectra PSA for M_w = 4, 5, 6 and 7 with V_{S30} = 400 m/s at Joney Boore distance equal to R_{JB} = 30 km are compared in Figure 7. The predicted spectra prove similar to the two models ANFIS and (Boore et al. 2014). Whereas, the classical GMPE of PSA are slightly larger than ANFIS approach for short periods. Inversely, the amplitudes given by ANFIS are rather large, than those providers by (Boore et al. 2014) for medium and long periods.

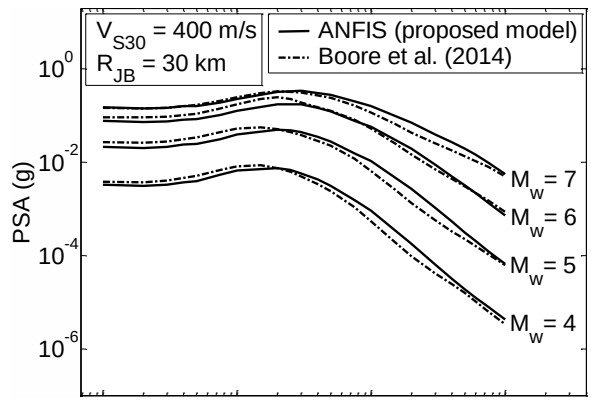

Figure 7. Comparison of median spectra predicted for M_w= [4, 5, 6 and 7], V_{S30} = 400 m/s with two values of Joyner & Boore distance R_{JB}=30 km and R_{JB}=70 km, between the present model (solid line) and the (Boore et al. 2014) model (dashed line).

5.3 Comparison of sigma with other studies

As we have carried out in (Derras et al. 2016), we close this series of comparison by the period dependencies of the aleatory variability models (Figure 8). In (Boore et al. 2014) the σ depends on M_w, distance, and even site conditions, this comparison is performed for a M_w = 4, M_w = 7, V_{S30} = 270 and V_{S30} = 600 m/s (Boore et al. 2014) at R_{JB} = 70 km. For (Derras et al. 2016), the only parameter controlling σ is the type of V_{S30} (measured or inferred), here we take only the case where V_{S30} are measured. For propose ANFIS model, we have used only measured V_{S30}, so this model is independent of M_w, R_{JB} and V_{S30}. If we compare the both driven-data models (ANN and ANFIS), we notice that ANFIS model gives σ less than ANN model. σ is found almost always low for ANFIS compared to (Boore et al. 2014), except for long periods (T > 2.0 s) and for M_w = 4.

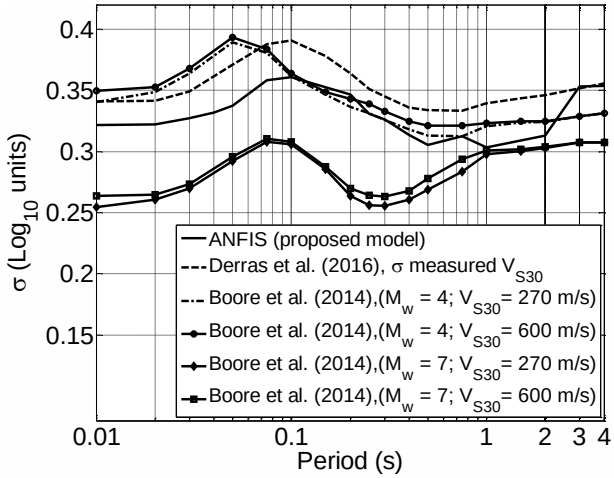

Figure 8. Comparison of the total aleatory variability σ of the present ANFIS model, (derras et al. 2016) model (for the mesuread V_{S30}), and those associated to (Boore et al. 2014) model, displayed here for four cases: two sites and two magnitudes. The two sites are, respectively, relatively soft (V_{S30} = 270 m/s), and stiff (V_{S30} = 600 m/s). The two events are moderate (M_w= 4) and large (M_w = 7)

The σ values are much lower than the corresponding values for ANFIS as compared to the model of (Boore et al. 2014) especially at large M_w. The origin of such large differences certainly has to be investigated further, as they

certainly deeply impact PSHA results. Adding a few additional parameters (style of faulting, hypocenter depth) could help reduce the variability for large events.
These comparisons show that the derived ANFIS ground-motion model has the same ability as traditional GMPEs to predict the amplitude and variability of ground-shaking within the NGA-West 2 dataset.

6. CONCLUSION

This work was especially devoted to test the ability the Adaptive Neuro Fuzzy Inference Systems approach (ANFIS) to capture the maximum of the physically sound features predictive ground-motion models. Avoiding the specification of any a priori functional form, ANFIS provide fully data-driven predictive models and allow the testing of the relative importance of the effects of independent variables on seismic ground motion. All tests have been carried out with the predictive ground-motion models derived through ANFIS method based on a subset of the NGA-West2 database.

The series of tests carried out with the ANFIS approach brought interesting answers to several much-debated issues: 1) The residual analysis has shown an absence of significant bias, linked to R_{JB}, M_w and V_{S30}. 2) We have shown that the ANFIS is carefully designed, its predictions are robust and not more sensitive to the dataset. 3) Despite the absence of any a priori assumption on the functional dependence, these results exhibit a number of physically sound features: magnitude scaling of the distance dependency, near-fault saturation distance increasing with magnitude, indications for non-linear effects in softer soils. 4) The ANFIS model does predict significant non-linearity on the site response as in (Derras et al. 2017) in which the KiK-net data have been used , which include a large number of sites with well constrained weak and strong motion recordings at the surface and depth). 5) even though it has only three explanatory variables (M_w, R_{JB}, and V_{S30}), the ANFIS-GMPE model is very consistent with (Boore et al. 2014). It proves in particular successful in reproducing the correct scaling with M_w, distance (including larger decay for small magnitudes and short distance saturation) and V_{S30}. One of the advantages of the ANFIS approach is the absence of bias associated with an a priori choice concerning the functional form. One associated drawback, however, is the impossibility to use such models outside the range of input parameters considered for the learning dataset. 6) Finally, we can conclude that the present "ANFIS" model gives weaker σ than (Derras et al. 2016). In addition, of the simplicity with which we could implement this type of model: unique architecture and faster learning.

REFERENCES

Abrahamson NA, Youngs RR (1992). A Stable Algorithm for Regression Analyses Using the Random-Effects Model. *Bull Seismol Soc Am* 82:505–510

Abrahamson NA, Silva W, Kamai R (2013). Update of the AS08 Ground-Motion Prediction Rquations Based On The NGA-West2 dataset. *Pacific Eng Res Cent Rep* 174

Ahmad I, El Naggar MH, Khan AN (2008). Neural Network Based Attenuation of Strong Motion Peaks in Europe. J Earthq Eng 12:663–680. doi: 10.1080/13632460701758570

Akbulut S, Hasiloglu AS, Pamukcu S (2004). Data Generation for Shear Modulus and Damping Ratio In Reinforced Sands Using Adaptive Neuro-Fuzzy Inference System. *Soil Dyn Earthq Eng* 24:805–814. doi: 10.1016/j.soildyn.2004.04.006

Al Atik L, Abrahamson N, Bommer JJ, Scherbaum F, Cotton F, Kuehn N (2010). The Variability of Ground Motion Prediction Models and its Components. *Seismol Res Lett* 81:794–801

Ancheta TD, Darragh RB, Stewart JP, et al (2014). NGA-West2 Database. *Earthq Spectra* 30:989–1005. doi: 10.1193/070913EQS197M

Bommer JJ, Douglas J, Scherbaum F, Cotton F, Bungum H, Fäh D (2010). On the selection of Ground-Motion Prediction Equations for Seismic Hazard Analysis. *Seismol Res Lett* 81:783–793

Boore DM, Stewart JP, Seyhan E, Atkinson GM (2014). NGA-West2 Equations for Predicting PGA, PGV, and 5% Damped PSA for Shallow Crustal Earthquakes. *Earthq Spectra* 30:1057–1085. doi: 10.1193/070113EQS184M

Chiou BSJ, Youngs RR (2014). Update of the Chiou and Youngs NGA Model for the Average Horizontal Component of Peak Ground Motion and Response Spectra. *Earthq Spectra* 30:1117–1153. doi: 10.1193/072813EQS219M

Derras B, Bard PY, Cotton F, Bekkouche A (2012). Adapting the Neural Network Approach to PGA Prediction: An Example Based on the KiK-net data. *Bull Seismol Soc Am* 102:1446–1461. doi: 10.1785/0120110088

Derras B, Bard PY, Cotton F (2014). Towards Fully Data Driven Ground-Motion Prediction Models for Europe. *Bull Earthq Eng* 12:495–516. doi: 10.1007/s10518-013-9481-0

Derras B, Bard PY, Cotton F (2016). Site-Conditions Proxies, Ground-Motion Variability and Data-Driven GMPEs: Insights from NGA-West 2 and RESORCE Data Sets. *Earthq Spectra* 32:2027–2056. doi: 10.1193/060215EQS082M

Douglas J, Edwards B (2016). Recent and Future Developments in Earthquake Ground Motion Estimation. *Earth-Science Rev* 160:203–219. doi: 10.1016/j.earscirev.2016.07.005

Jang JSR (1991). Fuzzy Modeling Using Generalized Neural Networks and Kalman Filter Algorithm. *In AAAI* (Vol. 91, pp. 762-767)

Jang JSR (1993). ANFIS: Adaptive-Network-Based Fuzzy Inference System. *IEEE Trans Syst Man Cybern* 23:665–685. doi: 10.1109/21.256541

Jang JSR, Sun CT, Mizutani E (1997). Neuro-Fuzzy and Soft Computing: A Computational Approach to Learning and Machine Intelligence. *Prentice Hall*

Karimi I (2006). Risk Management of Natural Disasters : A Fuzzy-Probabilistic Methodology and its Application to Seismic Hazard

Kerh T, Ting SB (2005) Neural Network Estimation of Ground Peak Acceleration at Stations Along Taiwan High-Speed Rail System. *Eng Appl Artif Intell* 18:857–866. doi: 10.1016/j.engappai.2005.02.003

Liu B, Ye L, Xiao M, Miao S (2006). Peak Ground Velocity Evaluation by Artificial Neural Network for West America *Region. Springer, Berlin, Heidelberg, pp 942–951*

Mirrashid M (2014). Earthquake Magnitude Prediction by Adaptive Neurofuzzy Inference System (ANFIS) Based on Fuzzy C-means Algorithm. *Nat Hazards* 74:1577–1593. doi: 10.1007/s11069-014-1264-7

Mittal A, Sharma S, Kanungo DP (2012). A Comparison of ANFIS and ANN for the Prediction of Peak Ground Acceleration in Indian Himalayan Region. *Springer India*, pp 485–495

Shi Y, Mizumoto M, Yubazaki N, Otani M (1996). A learning algorithm for tuning fuzzy rules based on the gradient descent method. In Fuzzy Systems: *Proceedings of the Fifth IEEE International Conference on* (Vol. 1, pp. 55-61)

Sugeno M, Kang GT (1986). Fuzzy Modelling and Control of Multilayer Incinerator. *Fuzzy Sets and Systems*, 18(3), 329-345

Takagi T, Sugeno M (1985). Fuzzy Identification of Systems and its Applications to Modeling and Control. *IEEE transactions on systems, man, and cybernetics*, (1), 116-132

Zadeh LA (1965). Fuzzy Sets.pdf. *Inf Control* 8:338–353. doi: 10.1109/2.53.

İNCE DANELİ ZEMİNLERİN SIVILAŞMA POTANSİYELİNİN DEĞERLENDİRİLMESİ

Emiroğlu T.[1], Arsoy S.[2]

[1] *Araş. Gör., İnşaat Müh. Bölümü, Kocaeli Üniversitesi, Kocaeli*
[2] *Prof. Dr., İnşaat Müh. Bölümü, Kocaeli Üniversitesi, Kocaeli*
Email: tansu.emiroglu@kocaeli.edu.tr

ÖZET:

Konum itibariyle Türkiye, sismik yükün sebep olacağı her türlü zemin ve yapı hasarı riski ile karşı karşıyadır. Zemin sıvılaşması deprem bölgelerinde sıkça rastlanan ve üzerine çalışılmaya devam edilen bir zemin hasarı çeşididir. Sismik yük etkisiyle, zeminde hali hazırda bulunan suyun ivedilikle tahliye olamaması durumunda dayanım kaybı yaşanması ile meydana gelmektedir. Bu sebeple boşluk suyunun drenaj süresini belirleyen her parametre sıvılaşma potansiyelini de etkilemektedir. Bu parametrelerden bazıları dane boyutu, şekli ve dağılımıdır. Zemin sıvılaşması için en riskli zemin gevşek ince daneli kumlar olmakla beraber kohezyonsuz ve plastik olmayan zeminlerde de sıvılaşma gözlenebilmektedir. Plastik olmayan siltli zeminler ve nadir durumlarda killi zeminler de sıvılaşma için elverişli olabilmektedir. İnce daneli zeminlerin sıvılaşma durumundaki davranışı iri daneli zeminlerden farklıdır. Çalışma kapsamında ince daneli zeminlerin sıvılaşma potansiyelinin tahmin edilmesi için ülkemizde ve dünyada yapılan araştırmalar sonucunda yaygın olarak kullanılan 9 yaklaşım birlikte sunulmuştur. Ülkemizde yapılan çalışmalardan Adapazarı kriteri ile Tezcan-Özdemir yaklaşımı, dünya genelindeki çalışmalardan ise Çin kriteri, modifiye Çin kriteri, Andrews-Martin yaklaşımı, Polito yaklaşımı, Bray vd. yaklaşımı, Seed vd. yaklaşımı ile kıyı ve liman tesisleri için geliştirilen Japon kriteri ele alınmıştır. Yöntemlerde sıvılaşma potansiyelini belirleyebilmek için plastik limit, likit limit, plastisite indisi ve doğal su muhtevası yaygın olarak kullanılmaktadır. Bunların haricinde, ince dane oranı, serbest basınç mukavemeti, hassaslık derecesi, kum etki katsayısı ve üniformluk katsayısı da ince daneli zeminlerin sıvılaşma potansiyelinin belirlenmesinde faydalanılan zemin parametreleridir. Yapılan araştırmada ele alınan yöntemlerin kullanım alanları, avantaj ve dezavantajları birlikte incelenmiştir. Sıvılaştırma analizini gerçekleştirecek olan saha veya ofis mühendisinin elindeki verilerle hangi yöntemleri kullanabileceği ve bu yöntemlerin sonuçlarıyla ilgili bazı karşılaştırmalar yapılarak uygulamacılara faydalı olabilecek tavsiye ve önerilerde bulunulmuştur.

ANAHTAR KELİMELER: İnce dane oranı, zemin sıvılaşması, silt

ASSESSMENT OF LIQUEFACTION POTENTIAL OF FINE-GRAINED SOILS

ABSTRACT:

Because of its location, Turkey is faced with structural and geotechnical damages due to seismic load. Soil liquefaction is a type of geotechnical damage, continued to be studied and frequently observed in seismic zones. Seismic loading causes loss of strength in soil in case the pore water cannot be drained immediately. Therefore, each parameter that determines the drainage time of pore water affects the liquefaction potential. Some of these parameters are grain size, shape and gradation. The most prone soil for liquefaction is loose fine-grained sands but liquefaction can also be observed in cohessionless and non-plastic soils. Non-plastic silty soils and, rarely, clayey soils may also be prone to liquefaction. The behavior of fine-grained soils in liquefaction is different from that of coarse-grained soils. The scope of this study is to present 9 methods, which are commonly used to estimate the liquefaction potential of fine-grained soils. Adapazari criterion and Tezcan-Ozdemir approach from Turkey

are the methods included in this study. Worldwide methods are Chinese criterion, modified Chinese criterion, Andrews-Martin approach, Polito approach, Bray etc. approach, Seed etc. approach and Japanese criterion which was developed for port and harbour facilities. Plastic limit, liquid limit, plasticity index and natural water content have been widely used variables in the liquefaction evaluation methods. In addition to these, fine content, shear strength, sensitivity, sand effect coefficient and CU are the soil parameters used in determining the liquefaction potential of fine-grained soils. In this study, the conditions of use, advantages and disadvantages of the methods are discussed and presented. Recommendations are also included for the practicing liquefaction analysts based on the comparisons performed in this study.

KEYWORDS: Fine content, soil liquefaction, silt

1. GİRİŞ

Türkiye nüfusunun büyük bir çoğunluğu, Türkiye'nin iki büyük fay hattı olan Kuzey Anadolu Fayı ve Doğu Anadolu Fayı civarında konumlanmıştır. Bu sebeple Türkiye, deprem etkisiyle oluşacak olan tüm yapı ve zemin hasarları riski altındadır. Zemin sıvılaşması deprem bölgelerinde büyük maddi ve manevi zararlara sebep olabilen tehlikeli bir zemin yenilmesi türüdür. Yapılaşmanın bulunduğu arazinin zemin özellikleri ve depremselliğine bağlı olarak sıvılaşma potansiyeli belirlenmektedir. Zemin özelliklerine bağlı olarak sıvılaşma geçmiş ve gelecekte önemli bir yenilme olarak dikkat çekmektedir.

Zemin sıvılaşması, sismik yük etkisi ile hızlı şekilde artan boşluk suyu basıncının zeminde geçici bir dayanım kaybına sebep olmasıdır. Boşluk suyu basıncındaki artışı kontrol eden temel zemin parametrelerinden biri permeabilitedir. Yüksek geçirimliliğe sahip zeminlerde (çakıl vb.) suyun boşlukları tahliye etmesi daha kolay olduğundan bu tür zeminlerde sıvılaşma gözlenmemektedir. Kohezyonlu zeminlerde daneler arası çekim kuvveti dayanım kaybını engelleme eğiliminde olduğundan bu tür zeminlerde de ender durumlar haricinde sıvılaşma beklenmemektedir. Bu koşullar altında sıvılaşabilen zeminler başta ince temiz kumlar ve plastik olmayan siltlerdir. İri ve ince daneli zeminlerin yükleme altındaki davranışı birbirinden farklı olduğundan, sıvılaşma potansiyelinin değerlendirilmesinde farklı yaklaşımlar kullanılmaktadır. Çalışma kapsamında ince daneli zeminlerin sıvılaşma potansiyelinin belirlenmesinde kullanılmakta olan temel yaklaşımlar birlikte incelenmiştir.

2. İNCE DANELİ ZEMİNLER İÇİN SIVILAŞMA POTANSİYELİ

Zeminde geçirimliliği etkileyen parametrelerin hepsi, sıvılaşma potansiyelini etkilemektedir. Dane boyutu, dağılımı ve şekli bunlardan bazılarıdır. 0,002-0,075 mm arasında dane boyutuna sahip zeminler silt olarak adlandırılmakta ve sıvılaşma için uygun olabilmektedir. Bu zeminlerde Atterberg limitleri sıvılaşma potansiyelinin belirlenmesinde sıkça kullanılan parametrelerdir. Çin kriteri olarak bilinen, en yaygın kullanılan yaklaşım (Wang, 1979) bu alandaki çalışmaların temelini oluşturmaktadır. 1999 Kocaeli depreminden sonra siltli zeminlerde sıvılaşma gözlenmiş ve ülkemizdeki akademik çalışmaların bu alanda ağırlık göstermesinde etkili olmuştur. Çalışma kapsamında dünya genelinde kabul görmüş olan ince daneli zemin sıvılaşma kriterlerinin yanında ülkemizde çalışılmış olan yaklaşımlar beraber incelenmiştir.

2.1. İnce daneli zeminlerin sıvılaşma riskinin tayini için başlıca global yaklaşımlar

İnce daneli zeminlerin sıvılaşma potansiyelinin belirlenmesi için yapılan çalışmaların temelini Çin kriteri oluşturur (Wang, 1979). Çalışmada, boyutu 0,005 mm'den küçük olan dane yüzdesinin %15'e eşit veya küçük olan zeminlerin aşağıdaki koşulları sağlaması durumunda sıvılaşmaya elverişli olduğu sunulmaktadır,

- $w_n \geq 0{,}9.LL$
- $LL \leq 35$
- $I_L \leq 75$

Çin kriterinin üzerinde çalışılıp düzenlenmesi ile modifiye Çin kriteri elde edilmiştir. Yaklaşımın ilk haline ilave olarak zeminin, SPT darbe sayısı, hassaslık derecesi ve serbest basınç mukavemeti değerleri dikkate alınarak daha hassas sonuçların elde edilmesi amaçlanmıştır. Bu yaklaşımda ince daneli bir zeminin sıvılaşabilmesi için Çin kriterine ek olarak zeminde, $N_{60} \leq 4$, $q_U \leq 50$ kPa ve hassaslık derecesi > 4 olmalıdır. Şekil 1'de Çin kriteri ve Modifiye Çin kriterinin sıvılaşma koşulları grafiksel olarak sunulmuştur.

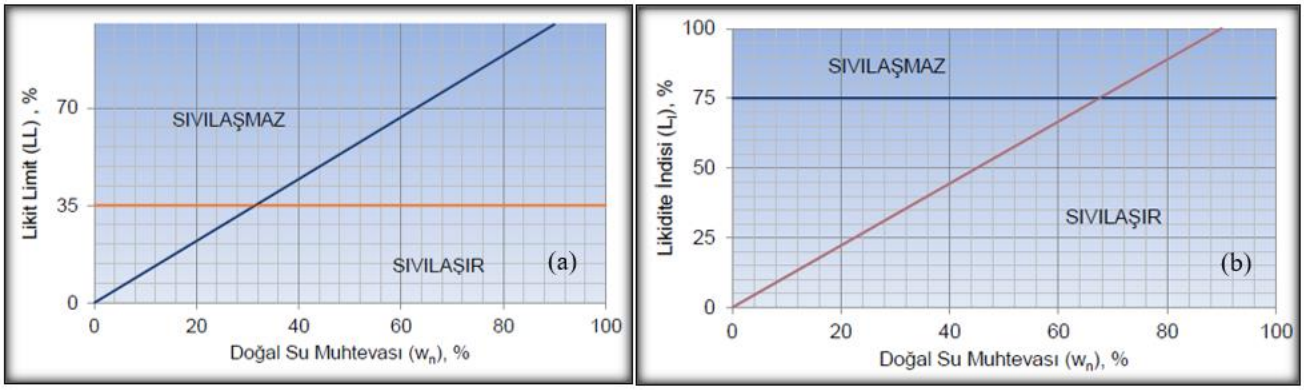

Şekil 1. Çin Kriteri (a) ve Modifiye Çin Kriterine (b) göre sıvılaşma koşulları

Andrews ve Martin tarafından, ince daneli zeminlerin sıvılaşma potansiyelinin, likit limit ve kil içeriğinin dikkate alınarak belirlenebileceğini savunulmuştur. Metoda göre kil olarak kabul edilecek olan dane boyutunun 0,002 mm'den küçük olması gerekmektedir (Andrews ve Martin, 2000).

İnce daneli zeminlerin sıvılaşma potansiyelinin belirlenmesi üzerine yapılmış olan bir başka global çalışma Polito tarafından yapılmış ve kilit parametre plastisite indisi olarak seçilmiştir (Polito, 2001).

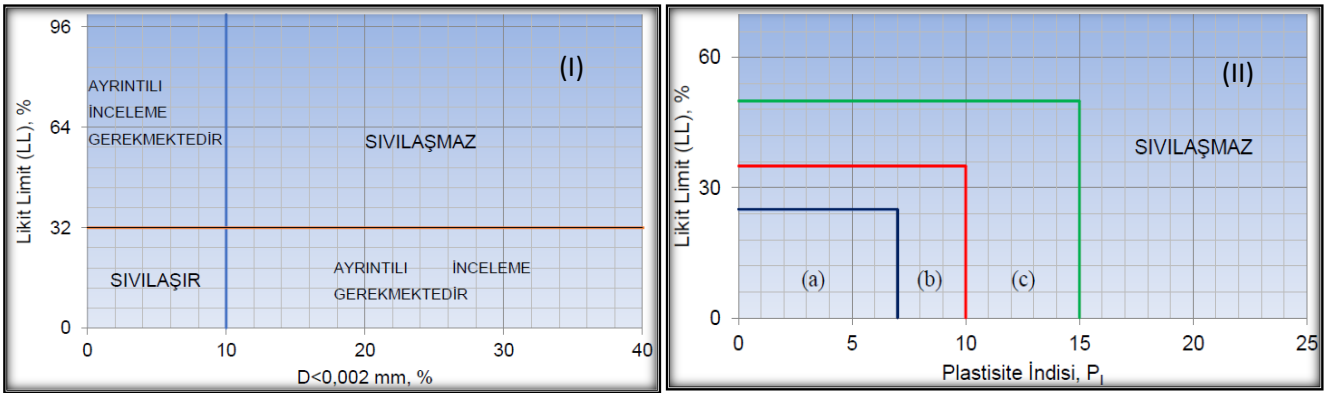

Şekil 2. Andrews-Martin (I) ve Polito (II) tarafından önerilen sıvılaşma kriterleri. (a) sıvılaşan zemin, (b) ayrıntılı inceleme gereken zemin, (c) çevrimsel hareketliliğe karşı duyarı zemin

2006 yılında Bray vd. ince daneli zeminlerde sıvılaşma için kendi kriterlerini ortaya koymuştur. Bu çalışmaya göre plastisite indisi ve su muhtevası-likit limit ilişkisine göre zemin davranışı tahmin edilmektedir. Yönteme dair sıvılaşma kriterleri Tablo 1'de sunulmuştur (Bray ve Sancio, 2006).

Tablo 1. Bray vd. tarafından önerilen yaklaşıma göre sıvılaşma koşulları

Zemin Davranışı	Plastisite İndisi	w/LL
Sıvılaşma ve çevrimsel hareketliliğe karşı duyarlı	$P_I \leq 12$	$w/LL \geq 0{,}85$
Sıvılaşma ve çevrimsel hareketliliğe karşı kısmen duyarlı	$12 < P_I \leq 20$	$0{,}8 < w/LL \leq 0{,}85$
Sıvılaşmaya elverişsiz	$P_I > 20$	$0{,}8 < w/LL$

Japon kriteri, deprem bölgelerinde kıyı ve liman tesislerinde karşılaşılan sıvılaşma olaylarından yola çıkarak hazırlanan bir yaklaşımdır (Green ve Ziotopoulou, 2015). Sarsma tablası deneyi ile deprem sonrası gözleme dayalı veriler kullanılarak yola çıkılmıştır. İyi derecelenmiş (C_U>3,5) ve kötü derecelenmiş (C_U<3,5) zeminler için ayrı ayrı hazırlanan sıvılaşma bandı, granülometri eğrisi üzerinde sunulmuştur (Şekil 3).

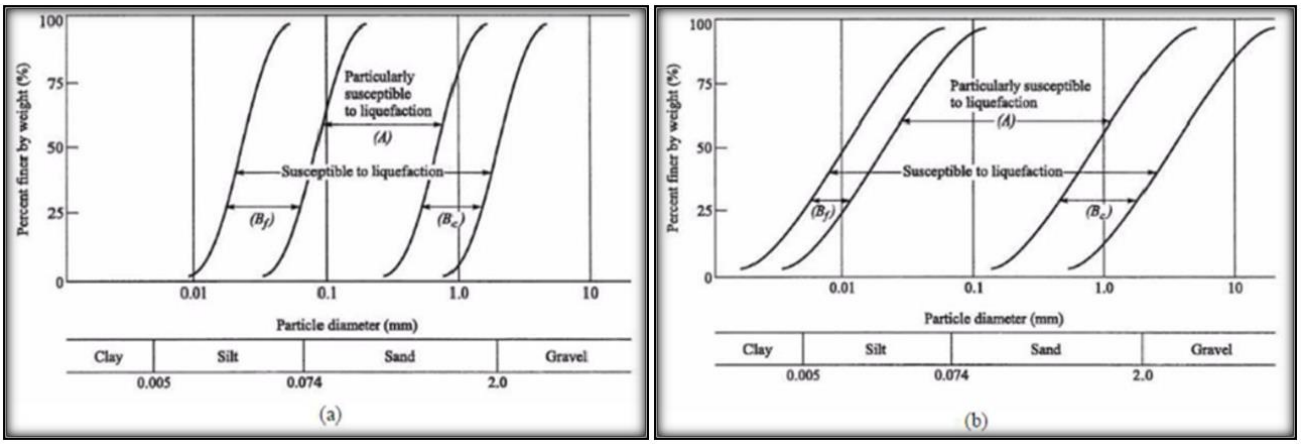

Şekil 3. Kötü derecelenmiş (a) ve iyi derecelenmiş zeminler (b) için Japon kriteri

2.2. İnce daneli zeminlerin sıvılaşma riskinin tayini için Türkiye'de yapılan başlıca yaklaşımlar

1999 Kocaeli depremi ile birlikte, özellikle Sakarya ili ve çevresinde gerçekleşen zemin sıvılaşması sonucu meydana gelen hasarlar, ülkemizde bu konu üzerine çalışılması ihtiyacını doğurmuştur. İnce dane oranının fazla olduğu zeminlerde meydana gelen sıvılaşma vakaları üzerine yapılan çalışmalar sonucunda oluşturulan iki temel yaklaşım Tezcan ve Özdemir'in sıvılaşma kriterleri ve Adapazarı kriteridir.

Tezcan ve Özdemir'e ait olan yaklaşıma göre, ince dane oranı (D<0,002 mm) %30'a eşit veya küçük olan zeminlerde, aşağıda sunulan koşulların sağlanması durumunda sıvılaşma beklenir.

- $w_n \geq 0{,}7.LL$
- $LL \leq 50$
- $I_L \leq 75$
- $I_P \leq 75$

Sakarya nehri sebebiyle oluşan çökellerin, sıvılaşmaya elverişli koşullarda bulunan kısımlarında meydana gelen sıvılaşma vakalarının incelenmesi ile oluşturulan bir diğer yerel yaklaşım, Adapazarı kriteridir. Türkiye'de, ince daneli zeminlerde sıvılaşma potansiyelinin belirlenmesi üzerine yapılan çalışmalar arasında Adapazarı kriteri, en popüler yaklaşım olmayı başarmıştır. Zeminin kum etki katsayısı (η) 1 ~ 0,51 aralığında ise ince daneli olarak kabul edilir ve bu yaklaşım kullanılabilir. Adapazarı kriterine göre ince daneli bir zeminin sıvılaşabilmesi için aşağıdaki koşulları sağlaması gerekmektedir (Bol vd., 2010).

- $w_n > 0{,}9.LL$

- LL ≤ 33
- Kil içeriği < %10

3. METOTLARIN KARŞILAŞTIRILMASI

Bölüm 2'de, ince daneli zeminlerin sıvılaşma potansiyelinin belirlenmesinde kullanılan başlıca yerel ve global yaklaşımlar sunulmuştur. Metotlar birlikte incelendiğinde, ince daneli zeminlerin davranışını tanımlayan Atterberg limitlerinden likit ve plastik limitin aktif olarak kullanıldığı görülmektedir. Likit limit zeminin sıvı bir malzeme gibi davrandığı andaki su muhtevasıdır. Likit limitine ulaşmış ve aşmış olan bir zemin için statik durumdaki bir sıvılaşma gerçekleştiği düşünülebilir. Bu parametreler kullanılarak dinamik durumdaki sıvılaşma riski tahmin edilebilir. Sıvılaşma mekanizmasının kilit noktası zeminin su içeriği ve bundan kaynaklanacak olan boşluk suyu basıncıdır. Bundan yola çıkarak metotlarda doğal su muhtevası ve likit limit parametrelerinin yaygın olarak kullanılmış olduğu görülmektedir. Tablo 2'de çalışma kapsamında dikkate alınan yaklaşımların kullanılmasında gerekli olan parametreler verilmiştir (Emiroğlu, 2018).

Tablo 2. Çalışma kapsamında ele alınan global ve yerel yaklaşımlarda kullanılan zemin parametreleri

İnce Daneli Zemin Sıvılaşma Analiz Metodu	W_n	LL	LI	PI	İ.D.O.	N_{60}	q_U	Hassaslık	η	C_U
Çin Kriteri	+	+	+	-	+	-	-	-	-	-
Modifiye Çin Kriteri	+	+	+	-	+	+	+	+	-	-
Andrews ve Martin, 2000	-	+	-	-	+	-	-	-	-	-
Tezcan ve Özdemir, 2004	+	+	+	+	+	-	-	-	-	-
Polito, 2001	-	+	-	+	-	-	-	-	-	-
Bray vd., 2006	+	+	-	+	-	-	-	-	-	-
Adapazarı Kriteri	+	+	-	+	+	-	-	-	+	-
Japon Kriteri	-	-	-	-	-	-	-	-	-	+
Seed vd., 2003	+	+	-	+	+	-	-	-	-	-

**w_n: doğal su muhtevası, LL: likit limit, LI: likidite indisi, PI: plastisite indisi, İDO: ince dane oranı, N_{60}: düzeltilmiş darbe sayısı, q_u: drenajsız kayma mukavemeti, η: kum etki katsayısı, C_u: üniformluk katsayısı*

4. SONUÇLAR

Bu çalışmada ince daneli zeminlerin sıvılaşma potansiyelinin tahmininde kullanılan global ve yerel yöntemler, gerekli olan parametrelerin adedi ve ulaşılabilirliği dikkate alınarak sunulmuştur. Yaklaşımlar birlikte incelendiğinde yaygın olarak kullanılan zemin parametrelerinin LL, PL, I_P, I_L ve doğal su muhtevası olduğu görülmektedir. Metotlarda kullanılan zemin parametrelerinin sayısı arttıkça, yaklaşımın gerçekçiliği artarken kullanım kolaylığı azalmaktadır. Yaklaşımlar arasında en çok parametre barındıran Modifiye Çin kriteridir. Atterberg limitlerinin yanı sıra, zemin dayanımı hakkında bilgi veren SPT darbe sayısı ve CPT uç direnci ile birlikte hassaslık derecesi de dikkate alınmıştır. Bu durum dikkate alındığında, en gerçekçi sonuçlara ulaşmayı sağlayacak yaklaşım Modifiye Çin kriteri olarak kabul edilebileceği kanaatine ulaşılmıştır.

Atterberg limitleri ve w_n kullanılmadan, üniformluk katsayısına bağlı olarak sıvılaşma potansiyelinin belirlenmesini hedefleyen Japon kriteri, en az koşul ile en yüzeysel sonuçlar elde edilmesine sebep olacaktır. Ancak zaman sıkıntısı yaşanan durumlarda, sadece zemin sınıflandırılmasının yapılarak hızlı bir şekilde zemin sıvılaşma için ön tahminde bulunulabilir.

Ülkemizdeki veriler ve zemin numuneleri kullanılarak oluşturulan yerel yaklaşımlar ise, proje sahalarını daha iyi örneklediğinden bu bölgelerde sıvılaşma potansiyelinin belirlenmesi için kullanımı oldukça uygundur.

KAYNAKLAR

Andrews DCA, Martin GR (2000). Criteria for liquefaction of silty soils. *12th World Conference on Earthquake Engineering*, 30 Ocak-4 Şubat 2000, Auckland, Yeni Zelanda (İngilizce).

Bol E, Önalp A, Arel E, Sert S, Özocak A (2010). Liquefaction of silts: the Adapazari criteria. *Bulletin of Earthquake Engineering*, **8(4)**, 859-873 (İngilizce).

Bray JD, Sancio RB (2006). Assessment of the liquefaction susceptibility of fine-grained soils. *Journal Of Geotechnical and Geoenvironmental Engineering*, **132(9)**, 1165-1177 (İngilizce).

Emiroğlu T (2018). Serbest arazi koşullarında ve düşey gerilme artışı etkisinde sıvılaşma analizi. Yüksek Lisans tezi, İnşaat Müh. Bölümü, Kocaeli Üniversitesi, Kocaeli, Türkiye.

Green RA, Ziotopoulou K (2015). Overview of screening criteria for liquefaction triggering Susceptibility. *10th Pacific Conference on Earthquake Engineering*, 6-8 Kasım, Sidney, Avustralya.

Polito C (2001). Plasticity based liquefaction criteria. *International Conferences On Recent Advances In Geotechnical Earthquake Engineering And Soil Dynamics*, 26-31 Mart ,San Diego, Kaliforniya (İngilizce).

Wang WS (1979). Some findings ın soil liquefaction. Water Conservancy and Hydroelectric Power Scientific, Araştırma Enstitüsü, Pekin, Çin.

ANALYSIS OF HIGH SPEED RAILWAY BRIDGES CROSSING FAULT-RUPTURE ZONES

Etemadi A.[1], Saglik H.[2]

[1] *Assist. Prof. Dr., Department of Civil Engineering, Istanbul Gelisim University, Istanbul, Turkey*
[2] *Researcher, Department of Civil Engineering, Yıldız Technical University, Istanbul, Turkey*
Email: [1] aetemadi@gelisim.edu.tr, [2]huseyinsaglik20@gmail.com

ABSTRACT:

The construction of bridges on active fault zones is a significant challenge. Surface rupture imposes a significant risk on bridges that crossing or constructed over active fault zones during strong ground motions. In practice, the measure for fault rupture has been disregarded in the seismic design of bridges, as bridge damage is rarely caused directly by fault ruptures. The implemented regulations or policies to address this risk, such as the strategies of prohibiting the construction of new bridges over active faults and setting a safe distance between structures and active faults cannot completely alleviate the risk of destruction to bridges over active faults. The actual surface fault rupture traced may neither follow the distribution marked on the geological map nor occur within the historical earthquake fault zone given the limitations of existing active fault. The variation of both railway transport infrastructures and geotechnical consequences of near-source effects are shown for densely populated environments, Kocaeli and Düzce (Turkey), situated on an alluvial fan at the western part of the North Anatolian fault with its faulting mechanism and high capability of generating damaging earthquakes. This paper describes the design challenges for the high speed train bridges that could be suffered damage due to propagation of a surface fault rupture between segments of viaduct piers. The 3D finite element (FE) model of high speed train bridge is analyzed to evaluate the damaged margin length of the bridge girder to prevent the girder from falling off the pier. Relative maximum displacements between superstructure and interior bent obtained from both time-history analyses and response spectrum analyses by using design spectrum according to Turkish Earthquake Code (TEC) 2007 and 2018 are compared. This analysis showed that the displacement of the superstructure relative to the piers exceeded the capacity of the bearings at an early stage of the earthquake and can cause to damage of the bearings as well as the energy dissipation units.

KEYWORDS: High speed train bridge, Near fault ground motion, Fault-rupture zones, Composite steel-concrete bridge

1. INTRODUCTION

Several ground motions over the past two decades have demonstrated that bridges crossing fault rupture zones may suffer significant damage owing to the combined effects of ground excitation and surface rupture. Although it is greatly recommended to avoid construction a bridge across a fault, it is not always possible to achieve this objective, especially in regions with a dense network of active faults such as Marmara region in Turkey. The observed performance of these essential infrastructures following recent earthquakes 1999 Chi-Chi earthquake (EERI, 2001), 1999 Kocaeli earthquake (EERI, 2000), 1999 Duzce earthquake (Ghasemi et al., 2000), and 2008 Wenchuan earthquake (Kawashima et al., 2009) suggested that conventional bridge design methods might not provide the desired performance levels. When there is no other alternative than to design the bridge structure crossing an active fault, factors such as the spatially varying ground motion due to fault crossing (including

permanent tectonic displacements across the fault), fault crossing location and fault crossing angle need to be considered in the design methodology.

Approximately 120 km of the Turkish State Railways (TCDD) high speed railway line between Halkalı (the Istanbul end of the line) and Ankara, plus the 8 km line from Arifiye to Adapazari, lie within 15 km of the fault rupture. The rupture crossed the railway line at some locations. Approximately 265 km of these lines lie within 80 km of the epicenter of the 1999 Kocaeli earthquake. The 1999 Kocaeli earthquake was caused by primarily right-lateral strike-slip along a rupture zone with a length in the order of 160 to 170 km, including surface faulting observed over a distance of 110 km. Whether, bridges are defined as structures with lengths of 4 meters or more, which essentially agrees with the current fault rupture area definition, there are 181 bridges within 80 km of the north Anatolian fault line. Nearly half of these are within 15 km of the fault rupture. Thirty-two composite bridges, with a combined length of 186 m, are located within 80 km of the epicenter. Three of these, with a combined length of 31 m are located within 15 km of the fault rupture. These are, typically, single span bridges with span lengths of 4 m to 8 m. The longest bridge consists of three 7 m spans. All except one, which was built in 1960, were built in 1912. Some new bridges are being constructed with the expansion of the high speed train network (Byers 2000).

The main objectives of this study are to investigate the seismic performance of the composite steel I-girder bridge, Elvo Viaduct, under a set of near-fault ground motions having surface rupture. For this purpose, FE model of the bridge is analyzed via time-history analysis. The displacements of the superstructure relative to the piers obtained from the time-history analysis were compared with the results of response spectrum given in the Earthquake Code of 2007 (TEC2007) and 2018 (TEC2018).

1.1. Literature review

There is some fault-crossing bridge cases that were damaged in past earthquakes is collected from the literature review. The fault crossing conditions and observed damage modes are reported in the literature (Konakli and Der Kiureghian (2009), Choi et al (2007), Goel and Chopra (2009), Yang and Mavroeidis (2018)). The review findings of experimental, analytical and numerical studies, and to summarize seismic design provisions and recommendations related to fault-crossing bridges was presented by Yang and Mavroeidis (2018). Gloyd et al. (2002) proposed a procedure that requires estimation of seismic demands for two additional load cases, without providing any structural-dynamics-based justification for the proposed load cases. Under the guidance of a technical advisory panel, this approach was used by the CALTRANS engineers and project consultants to design bridges in the SR210/I-215 interchange in San Bernardino, Calif. Choi et al. (2007) investigated experimentally and numerically the effects of fault crossing on the seismic response of a bridge system. Specifically, a quarter-scale, two-span reinforced concrete bridge was subjected to a series of synthetic incoherent ground motions that simulated fault rupture. An identical bridge model had also been tested under spatially uniform excitations. The measured data in the fault rupture study showed a major shift in the location of the most critical pier compared to the bridge that was subjected to uniform motion. It was reported that the shortest columns failed when the bridge was subjected to coherent motions, but the tallest columns experienced the most significant damage during the fault rupture case. Goel and Chopra (2009) developed a response spectrum analysis procedure and a linear static analysis procedure for estimating the dynamic part of seismic demands in linearly elastic/ inelastic range bridges crossing fault rupture zones. They demonstrated that both of these procedures, when combined with the quasi-static demands due to ground offset across the fault, provide estimates of peak responses that are close to the exact results from response history analysis.

Several researchers have also investigated the performance of the Bolu Viaduct during the 1999 Duzce earthquake in Turkey. Konakli and Der Kiureghian (2009) investigated the problem of estimating seismic demands for bridges crossing faults within the framework of the multiple support response spectrum method. A coherency function was developed to describe the variability in support motions for a vertical strike-slip fault, under the assumptions of stationarity and zero residual slip. The structure under consideration in this study, Bolu Viaduct, is located in west-central Turkey. Roussis et al. (2003) presented a comprehensive evaluation of the design of the viaduct's seismic isolation system and an assessment of its performance in the 1999 Duzce earthquake. The collapse of the superstructure was avoided due to the restraint provided by the shear keys in the

transverse direction and the concrete stoppers/cable restrainers in the longitudinal direction. Park et al. (2004) simulated the seismic performance of the Bolu Viaduct traversed by a surface rupture and concluded that bridges built close to known faults must have greater displacement capacities than those designed in the far-field region.
The 1999 Chi-Chi earthquake was triggered by Chelungpu thrust fault and caused enormous surface dislocation, several meters of surface dislocation. The destruction was astonishing. When earthquake striking, the length of surface rupture along the main fault was about 83km, another surface rupture was about 22km long from Fengyuan to the northeastern direction. The thrust fault length is about 105km, which is the longest one in the world. There were severe and large areas of surface rupture and damage. Such huge dislocation of the surface can have damaged almost all types of bridge.
During the 1999 Chi-Chi earthquake, if a relative large displacement occurred on the superstructure and substructure of the bridge that exceeding the bearing capacity, the bearing would be damaged. Moreover, if the support length is insufficient or lack of suitable anti-falling devices, the bridge will fall. Parts of bridges were damaged in this earthquake due to the lack of anti-falling device (Shear Pin Fuse) to prevent falling. Another possible solution to prevent span failures is the installation of cable restrainers across deck joints. The restrainers utilized at expansion joints on the decks of the Bolu Viaduct prevented end girders from dislodging off of their supports during the Duzce earthquake.

2. DESCRIPTION OF THE BRIDGE

The composite high speed (HS) train bridge of the new Torino–Milano line of the Italian HS railway network, the Elvo viaduct, is adopted to investigate fault rupture phenomena. The Elvo viaduct (see Figure1), is consist of 11 simply composite spans, each of 33.7 m, for a total length of about 371 m. A typical cross-section of the composite ballasted deck is formed by four steel I-girders connected by studs, with a concrete slab. The concrete slab has geometrical dimensions of 13.6 m width and 0.4 m thickness and is formed by prefabricated parts (Chellini et al (2009)). The superstructure, consists of reinforced concrete sleepers and UIC60-type rails, lies on the ballast. In each span, it is possible to identify three types of cross-section pattern for diaphragm members: X bracings with two different pattern (Figure2b, 2c) and inverted-V steel bracings (Figure2d) with steel. The diaphragm members consisted of L100x10 and UNP240 profiles. The fixed, mono-directional and bi-directional supports are used to avoid internal stress due to thermal action as shown in Fig.2a, 2e.

2.1. Analytical model development

Herein the FE numerical model of the investigated seventh span of the Elvo viaducts is presented. In order to analyze the experimental dynamic response of the bridges crossing fault-rupture zones, suitable 3D FE model of a single span is implemented using CSI Bridge v20 software. In order to describe the global behavior of viaducts by means of single-span model, the effect of the adjacent spans caused by ballast continuity is introduced by spring elements as proposed by Chellini et al (2009). Four-node shell element with six degree of freedom at each node is applied to model concrete slab and ballast layers. The two-node frame elements are used to model steel I-girders. Full composite action between steel I-girder and concrete slab are provided through the rigid-links. The rigid-body constraints are used between I-girders at appropriate locations as diaphragm members. Ballast layer is connected to the bridge structure by link elements for considering its mechanical properties. The ballasted railway track consists of two lanes representing two rails and mass points representing the sleepers (290 kg for each).
The link elements which prevent three displacement and rotation as fixed bearing are used at the bottom of the main girders. Besides, pin constrains that prevent transverse displacements and roller constrains that prevent vertical displacements are modeled by using link elements according to Figure2-a. Circular reinforced concrete columns with a diameter of 4.86m are fixed at the ground level. The concrete slab is consisted with an elastic modulus of 35 GPa and density of 2500 kg/m^3 while steel members are consisted with an elastic modulus of 206 GPa and density of 7850 kg/m3. For the ballast-binder-sleepers pack, material properties are used with an elastic modulus of 2.2 GPa and density of 1800 kg/m^3.

Figure 1. Overview of the Elvo railway (Chellini et al., (2009))

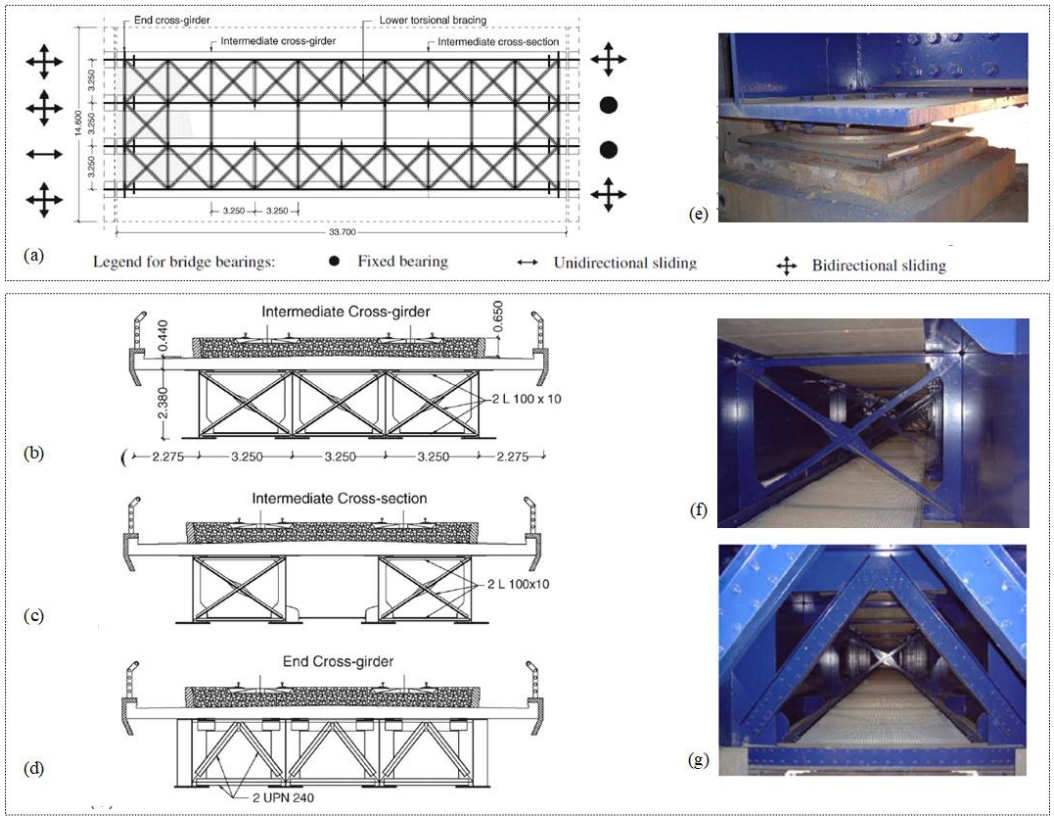

Figure 2 General cross-sections of the Elvo viaduct (dimensions in meters) (Chellini, 2009)

The modal damping ratio ς=2% is considered for the two vibration modes. A suitable structural dynamic identification procedure based on enhanced operational modal analysis has been done by Chellini et al (2009) on the Elvo viaduct. Validation of the proposed FE models is performed by comparing the natural frequencies obtained by single-span FE model and the measured ambient vibration test. As indicated by Table 1, (Figure3a) good agreement is achieved between simulation and experimental results in prediction of the natural frequencies of the bridges. For this study, the Elvo viaduct consisted of 3 interior simply spans which allows different placements of the fault ruptures crossing is modeled as shown in Figure 3b. Main modal shapes and corresponding vibration frequency of the superstructure and global model of three-span bridge are shown in Figure 4. The longitudinal, transversal and torsional mode shapes are exhibited in Figure 4.

Table 1. Comparison of Eigen frequencies computed by FE model and identified from ambient vibration data of the Elvo viaduct

Vibration mode	**Natural frequencies(Hz)**	
	Elvo viaduct	
	Measured	Computed
First bending mode	4.97	4.57
Second bending mode	14.15	12.51
First torsional mode	6.6	5.82
Second torsional mode	6.75	6.46

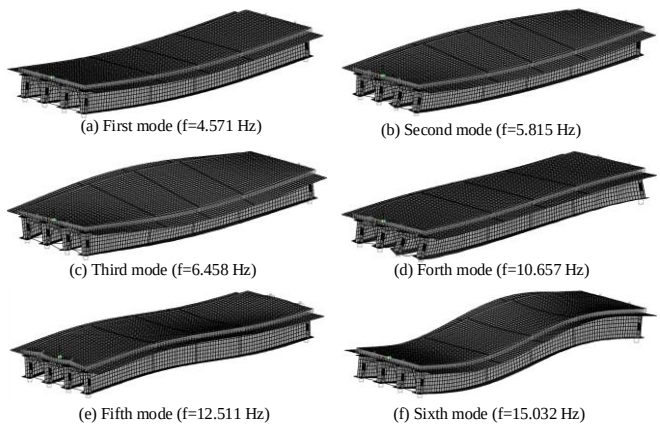

a) Main modal shapes and corresponding vibration frequency of seventh span of the Elvo viaducts

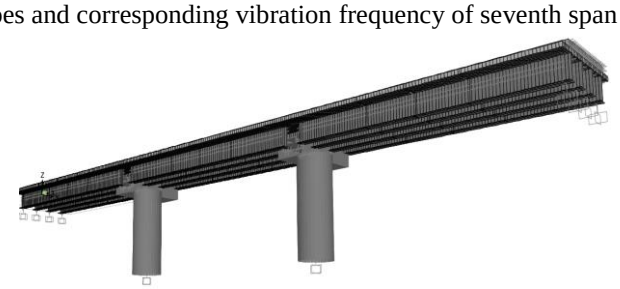

b) 3D FE model of the bridge

Figure 3. Main modal shapes and corresponding vibration frequency of the superstructure and global model of three-span bridge

3. NEAR-FAULT GROUND MOTION SELECTION AND FAULT LOCATION

Figure 5 provides a map of Turkish high-speed railway line, the active faults and the recording stations. The purple line shows the high speed railway line. The PGA seismic hazard map for a return period of 475 years presented in the Figure 5. In the data-set of ground motion records from the given stations, gathered to evaluate deformation demands at bridge supporting zone. Total of 12 near-field ground motions involving fault rupture at the ground surface are collected (Table 2). The majority of ground motions are larger than magnitude 6 (M_w) with short epicentral distances. Important features of the ground-motion data include the peak ground acceleration to velocity (a/v ratio), peak ground displacement; magnitudes as well as a site condition are listed in Tables 2.

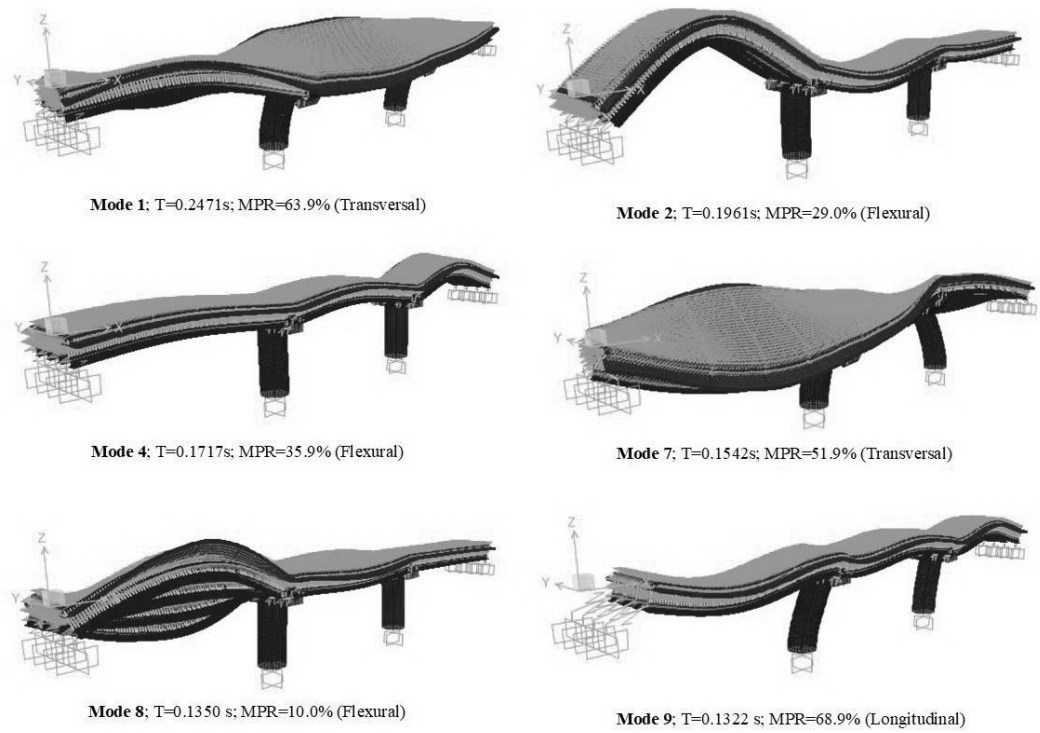

Figure 4. Main modal shapes and corresponding vibration period and mass participation ratios (MPR) of the Elvo railway crossing.

3.1. Fault Locations and Bridge Orientations

As shown in Figure 3b, the Elvo viaduct model has three interior spans, which allows different placements of the fault rupture crossing the bridge. Fault line represents the fault rupture crossing the span-2 between Bent-1 and Bent-2 is considered. The fault line is chosen perpendicular to the bridge axis for all analyzed cases. The EW components of the earthquake records given in Table 2 contain surface rupture and therefore the EW components are chosen as fault line direction. The effect of the surface rupture is modeled by a ground displacement time series in the fault-parallel direction according to EW components of given ground motion across the rupture. In addition, NS components of given ground motions have introduced as ground displacement time series in the fault-normal direction.

Figure 5. Position of record stations, high speed railway network on active faults map of Turkey

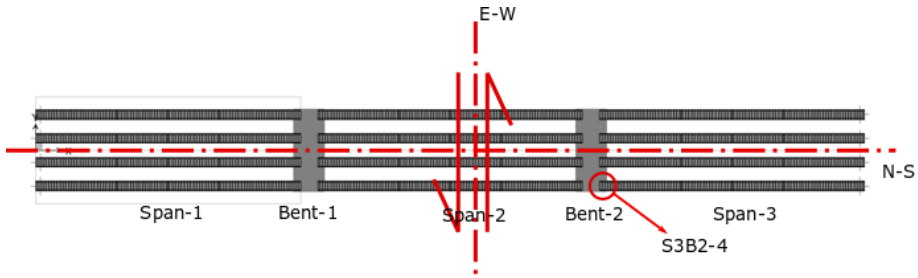

Figure 6. Considered fault rupture

Table 2. Considered near-field ground motions

No.	Earthquake and Date	Station Coordinate	Comp.	Soil Cond.	Mech.	Mag. (M_w)	Dist. (km)	PGA (g)	PGV (m/s)	PGD (m)	a/v Ratio (g/m/s)
1	Düzce, Bolu,Bayındılık ve Iskan Mud, Aug, 1999, (DZC1)	(40.7450N, 31.6100E)	NS	Soil	Strike-slip	7.4	20.41	0.337	0.606	0.638	0.56
2	Düzce, Bolu,Bayındılık ve Iskan Mud, Aug, 1999, (DZC1)	(40.7450N, 31.6100E)	EW	Soil	Strike-slip	7.4	20.41	0.383	0.496	1.058	0.77
3	Düzce: Meteoroloji Istasyonu, Nov, 1999, (DZC2)	(40.8500N, 31.1700E)	NS	Soil	Strike-slip	7.1	8.23	0.407	0.658	0.880	0.62
4	Düzce: Meteorolojı Istasyonu, Nov, 1999, (DZC2)	(40.8500N, 31.1700E)	EW	Soil	Strike-slip	7.1	8.23	0.513	0.860	1.701	0.60
5	Gebze, Tubitak Marmara Aras. Mer, Aug, 1999, (GBZ)	(40.8200N, 29.4400E)	NS	Rock	Strike-slip	7.4	15.00	0.269	0.455	0.826	0.59
6	Gebze, Tubitak Marmara Aras. Mer, Aug, 1999, (GBZ)	(40.8200N, 29.4400E)	EW	Rock	Strike-slip	7.4	15.00	0.143	0.347	1.037	0.41
7	Izmit, Meteoroloji Istasyonu, Aug, 1999, (IZT)	(40.7900N, 29.9600E)	NS	Rock	Strike-slip	7.4	8.00	0.167	0.320	0.476	0.52
8	Izmit, Meteoroloji Istasyonu, Aug, 1999, (IZT)	(40.7900N, 29.9600E)	EW	Rock	Strike-slip	7.4	8.00	0.227	0.543	1.293	0.42
9	Yarimca, Petkin Tesisleri, Aug, 1999, (YPT)	(40.7639N, 29.7620E)	NS	Soil	Strike-slip	7.4	3.28	0.322	0.796	0.653	0.40
10	Yarimca, Petkin Tesisleri, Aug, 1999, (YPT)	(40.7639E, 29.7620E)	EW	Soil	Strike-slip	7.4	3.28	0.231	0.847	1.676	0.27
11	Erzincan,Meteoroloji Istasyonu, Mar, 1992, (ERZ)	(39.7520E, 39.4870E)	F45N	Soil	Strike-slip	6.9	5.00	0.432	1.182	0.401	0.37
12	Erzincan ,Meteoroloji Istasyonu,Mar,1992, (ERZ)	(39.7520E, 39.4870E)	F45P	Soil	Strike-slip	6.9	5.00	0.456	0.583	0.270	0.78

4. BRIDGE SEISMIC RESPONSE

Experience with recent earthquakes in Turkey, shows that bridges built near to known fault lines should have greater displacement capacities than bridges built away from the fault line to prevent unseating damage of bridge superstructures. However, current Turkish earthquake code (TEC 2018) has not developed a design methodology in terms of fault rupture zone, although there are many determined and unknown active fault lines locate on the high population areas and transportation networks in Turkey.

In the new version of the Turkish earthquake code (TEC2018), the design spectrum ordinates can be obtained via website by defining site coordinates and soil condition of interest. Some spectral acceleration used in the response spectrum analysis for the exact location of recording stations (Table 2) are shown in Figure 7. The design spectrum ordinates according to the TEC2007 and TEC2018 are compared with response spectrum of selected ground motions. The govern longitudinal and transversal vibration period of the bridge model is indicated in the figures. As shown, the spectral values by location are obtained below or above the design spectrum ordinates.

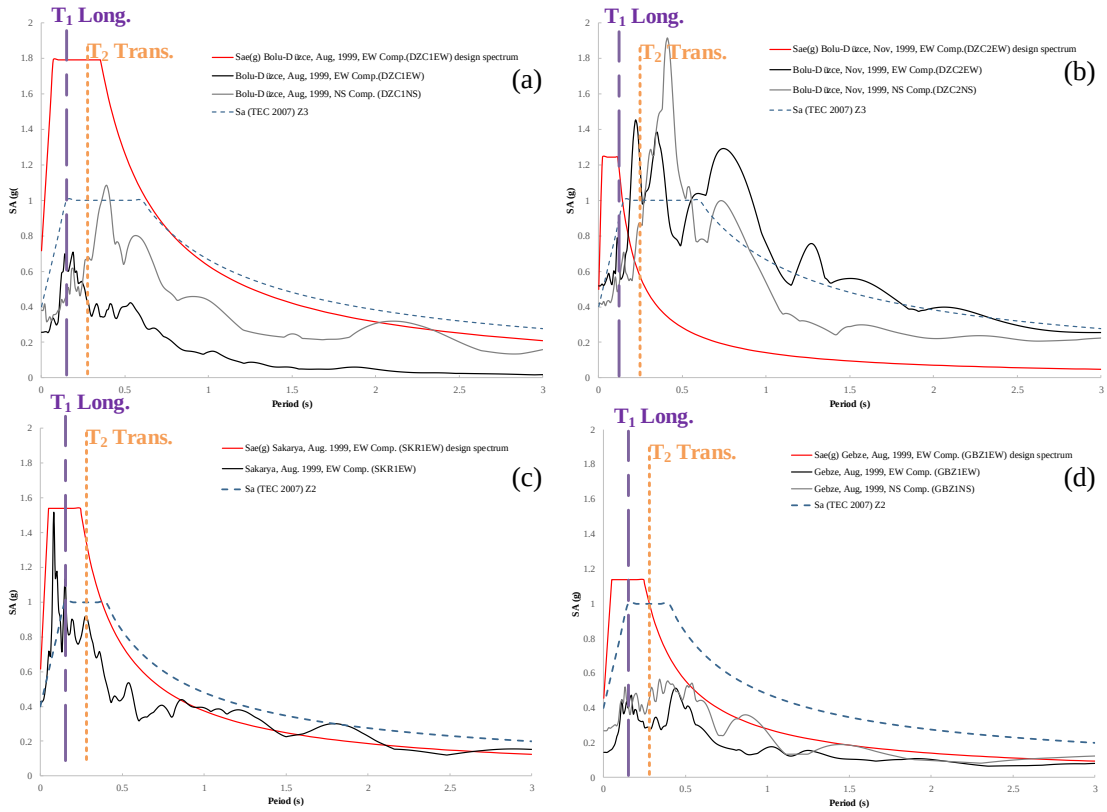

Figure 7. Spectral accelerations for the exact location of recording stations given by TEC2007 and TEC2018

The displacements of the superstructure relative to the piers caused by fault rupture obtained from the time-history analysis are compared with the results of response spectrum analysis by using spectral acceleration values given in the TEC2007 and TEC2018. It should be noted that the displacement values used in the comparison are taken from the #S3B2-4 (third-span, second-bend, fourth girder) relative to the 2-Bent as shown in Figure 6. The displacement time histories for the longitudinal and transverse components of the Duzce, Nov., 1999 (DCZ2) are shown in Figure 8a and 8b, respectively. The relative displacement path for bearings is demonstrated in Figure 8c. This analysis showed that the displacement of the superstructure relative to the piers exceeded the drift capacity of the bearings (almost 8.5 cm permanent displacement) at an early stage of the ground motion, causing damage to the bearing devices.

The relative displacement values obtained from both the time-history analysis and the response spectrum analysis given by the specifications for longitudinal and transverse directions of the bridge are demonstrated in Figure 9. The all relative displacements are higher than response spectrum analysis results. The maximum value of displacement equals to 85 mm which can cause 85% drift ratio by supposing 100 mm bearing height. The displacement values can be obtained higher if ductile materials such as elastomeric bearings are introduced as link element at the top of the bents. It should be noted that, the earthquake specification (TEC 2018) does not take surface rupture phenomena into account and leads to considerable small displacement values than the time-history analysis as seen in Figure 9. Therefore, it is advisable to use time history analysis by considering sufficient quantity of near-fault ground motions including permanent displacement for the bridges built in surface rupture prone zone such as Marmara region. If necessary, additional anti-falling device and/or energy dissipation units can be used to reinforce bearing support locations.

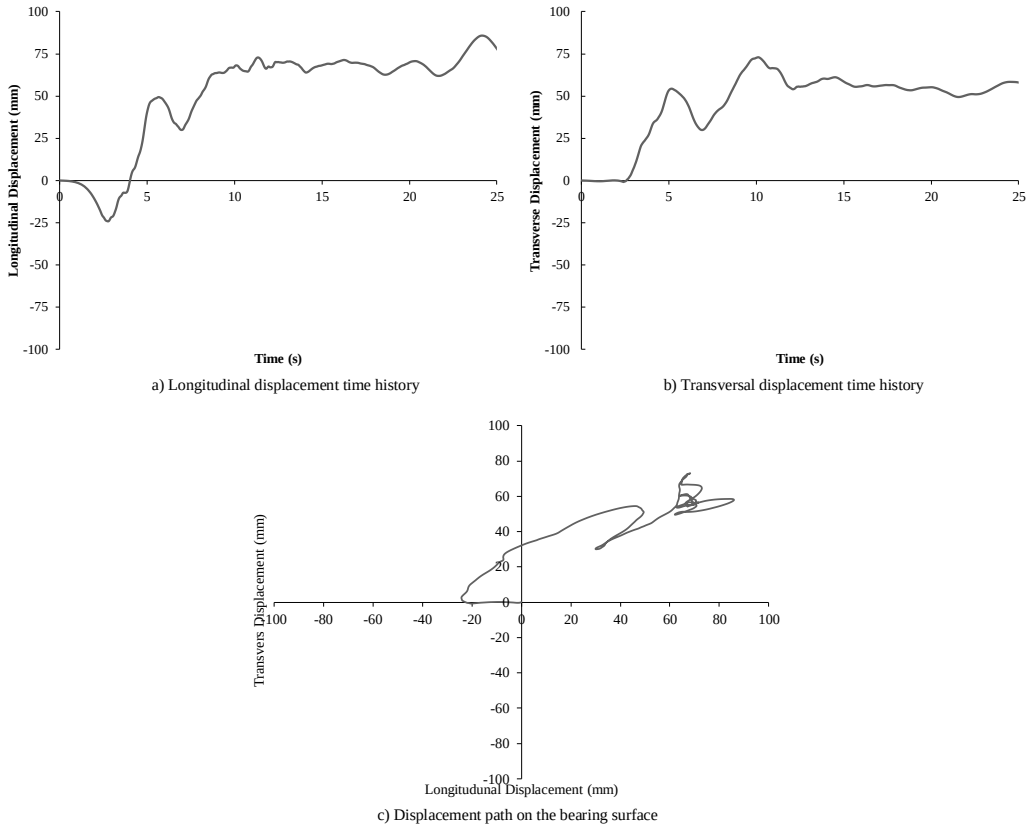

a) Longitudinal displacement time history

b) Transversal displacement time history

c) Displacement path on the bearing surface

Figure 8. Bearing displacement at the second bent under Düzce, Nov, 1999, (DZC2) ground motion

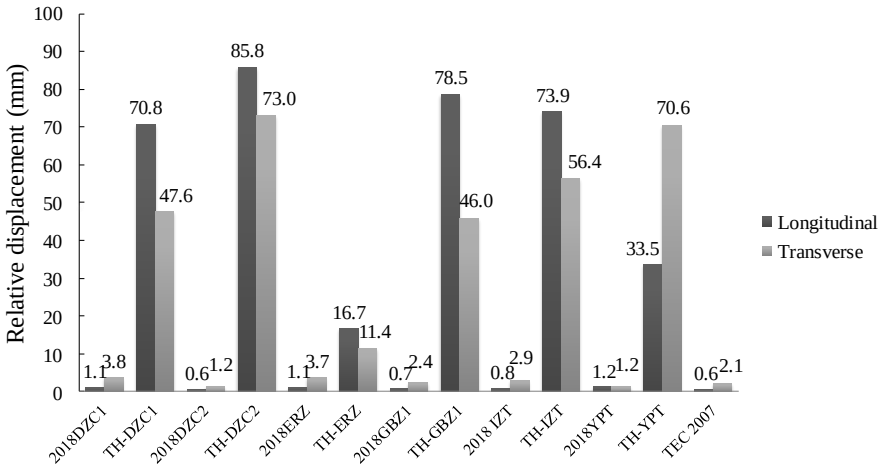

Figure 9. Relative displacements in both longitudinal and transverse directions of the bridge

5. CONCLUSIONS

The seismic response of the composite steel I-girder HS bridge crossing fault-rupture zones is investigated by using near fault ground motions with permanent displacement passing the HS railway line in Turkey. The 3D FE model of three-span bridge is built in CSI Bridge software. Validation of the proposed FE model is performed by comparing the natural frequencies obtained by single-span FE model and the measured ambient vibration test. Some near fault ground motions with permanent displacement close to HS railway network are selected from the

recording stations and compared with corresponding design spectrum as per Turkish Earthquake Code. The displacement time history of fault-parallel and fault-normal components of the given ground motions are implemented into the FE model. Moreover, the response spectrum analyses are conducted by using design spectrum of the recording stations according to TEC2007 and TEC2018. Eventually, relative maximum displacements between superstructure and interior bent obtained from both time-history analyses and response spectrum analyses are compared.

Considering the experience of past earthquakes, high-speed train line in Turkey, has apparently passed very near to the active fault lines in the Marmara region. Furthermore, the mentioned active fault lines have surface rupture characteristics, therefore, the design of the high speed train bridges crossing fault rupture zone need to special analyses considering the fault rupture which is not considered by the current TEC2018. It has been observed that there is a significant difference in terms of relative displacements between the response spectrum analysis proposed by seismic analysis of current Turkish earthquake specifications and the time-history analysis by using ground motions taken from the recording stations. Therefore, it is advisable to use time history analysis by considering sufficient quantity of near-fault ground motions including permanent displacement for the bridges built in surface rupture prone zone. If necessary, additional anti-falling device and/or energy dissipation units can be used to reinforce or retrofit the bearing support locations.

REFERENCES

Byers W G (2000). Effects of the August 17, 1999 Izmit earthquake on the Turkish state railways, *PEB Northern - Proceedings of the 2000 Annual Conferences*, Burlington Northern and Santa Fe Railway.

Chellini G, Nardini L and Salvatore W (2009). Dynamic identification and modelling of steel-concrete composite high-speed railway bridges. *Structure and Infrastructure Engineering*; **7(11)**, 823-841.

Choi H, Saiidi M, Somerville P (2007). Effects of near-fault ground motion and fault- rupture on these is mic response of reinforced concrete bridges, Report No. CCEER-07-06, Center for Civil Engineering Earthquake Research, Department of Civil and Environmental Engineering, University of Nevada, Reno, NV.

Earthquake Engineering Research Institute (EERI), (2000). Chapter 18: Impact on Highway Structures in Kocaeli, Turkey, Earthquake of August 17, 1999 Reconnaissance Report, Earthquake Spectra, Supplement A to Volume 16.

Earthquake Engineering Research Institute (EERI), (2001). Chapter 8: Highway Bridges in Chi-Chi, Taiwan, Earthquake of September 21, 1999 Reconnaissance Report, Earthquake Spectra, Supplement A to Volume 17.

Ghasemi H, Cooper JD, Imbsen R, Piskin H, Inal F, Tiras A (2000). The November 1999 Duzce Earthquake: PostEarthquake Investigation of the Structures on the TEM, Publication No. FHWA-RD-00-146, Federal Highway Administration, U.S. Department of Transportation, Washington, DC.

Gloyd S, Fares R, Sánchez A, Trinh V (2002). Designing ordinary bridges for ground fault rupture. *In: Proceedings of the 3rd national seismic conference and workshop on bridges and highways*, Technical Report MCEER-02-SP04. Buffalo, NY: Multidisciplinary Center for Earthquake Engineering Research.

Goel RK, Chopra AK (2009). Linear analysis of ordinary bridges crossing fault-rupture zones. *Journal of Bridge Engineering-ASCE*;**14(3)**:203–15.

Kawashima K, Takahashi Y, Ge H, Wu Z, Zhang J (2009). Reconnaissance report on damage of bridges in 2008 Wenchuan, China, earthquake. *Journal of Earthquake Engineering* **13(7)**:965–96.

Konakli K, Der Kiureghian A (2009). A response spectrum method for analysis of bridges crossing faults. *In: Proceedings of the 2nd international conference on computational methods in structural dynamics and earthquake engineering*, Rhodes, Greece; 2009.

Park SW, Ghasemi H, Shen J, Somerville PG, Yen WP, Yashinsky M (2004). Simulation of the seismic performance of the Bolu Viaduct subjected to near-fault ground motions. *Earthquake Engineering & Structural Dynamics*; **33(13)**:1249–70.

Roussis PC, Constantinou MC, Erdik M, Durukal E, Dicleli M (2003). Assessment of performance of seismic isolation system of Bolu Viaduct. *Journal of Bridge Engineering-ASCE*; **8(4)**:182–90.

Turkish Earthquake Code (TEC2007) (2007). Specifications for the buildings to be constructed in disaster areas, Ministry of Public Works and Settlement, Ankara, Turkey.

Turkish Earthquake Code (TEC2018) (2018). Specifications for the buildings to be constructed in disaster areas, Prime Ministry Disaster and Emergency Management Authority, Ankara, Turkey.

Yang S, Mavroeidis GP (2018). Bridges crossing fault rupture zones: a review. *Soil Dynamics and Earthquake Engineering*;**113**:545-571.

A STUDY ON THE EFFECT OF TENSION REINFORCEMENT RATIO AND CONCRETE STRENGTH TO RESPONSE OF RC BUILDINGS

Onat O.[1] and Yön B.[2]

[1] *Assis. Prof. Dr., Civil Eng. Department, Munzur University, Tunceli*
[2] *Assoc Prof. Dr, Civil Eng. Department, Munzur University, Tunceli*
Email: burakyon@munzur.edu.tr

ABSTRACT:

This paper focuses on the effect of tension reinforcement ratio and concrete strength to performance of reinforced concrete (RC) structures. For numerical study, two planar RC structures were selected. One of them is 5 stories other of them is 7 stories. Two different concrete class, C20 and C25, were considered and three tension reinforcement ratios were considered for analyses. Incremental dynamic analyses (IDA) were performed on these buildings. IDA is a parametric consequence analysis method that has used commonly in several different forms to assess the structural performance under seismic loadings. This method proposes a set of ground motion acceleration records by selecting and scaling into multiple intensity domain levels to cover the whole array of structural behaviors, from elastic response to global dynamic instability. In this study to execute IDA, eleven seismic acceleration benchmark records were multiplied with various scaling factors from 0.2 to 1.2. Peak responses obtained from IDA curves were generated according to these responses. IDA curves were compared with each other by using suitable graphs. According to analyses results, increasing tension reinforcement of beam elements has not any effect on maximum roof displacement. Whereas, tension reinforcement increases decreased interstorey drift ratio this result damage limitation.

KEYWORDS: Incremental dynamic analysis, maximum responses

1. INTRODUCTION

Tension or compression reinforcement ratio may change due to external effects such as corrosion and deterioration of rebars as reported by Theriaule and Benmokrane (1998). It was reported that two important parameters have influenced on performance of bar ratio change. One of them is propagated as crack width, other of them is crack spacing. These two factors are restricted with tension reinforcement ratio. Fantilli et al. (1999) investigated tension reinforcement ratio on structural performance on the base of bond-slip behavior. Minimum steel bar ratio is affected by bar diameter. Thus, bond slip behavior is profoundly affected by bar diameter. Ashour (2000) experimentally investigated tension reinforcement ratio on the high-strength beam behavior. Increasing compressive strength allowed beam to behave more flexible. Lee and Pan (2003) investigated concrete confinement and spalling of concrete on the base of tension rebar ratio. Lee and Pan draw attention to fulfill ductility of structural members during design phase. Yön et al. (2014) investigated site conditions and effects of seismic zones on RC structures by using IDA. Onat et al. (2016) performed IDA with artificially produced earthquake on the base of Eurocode 8. Their paper aims to investigate global behavior of infill wall on complete structure. Onat et al. (2018) investigated performance of RC structures with shear wall by using IDA. In this paper, it is aimed to investigate the effect of tension reinforcement ratio of beam on ductility and capacity of RC structures. For this purpose, two RC structure were selected. One of them is 5 stories and other of them is 7 stories.

Two different concrete compressive strength were considered. Eleven seismic record were used to perform IDA. However, ten of the seismic records were effectively used to perform analysis.

2. NUMERIC MODEL AND METHOD

Both model in this study were defined with fiber element model which accounts plasticity. This plasticity is spread through to the cross-section and the length of the element. In this hinge model, the structural element is divided in three types of fibers: one type fibers are used for modelling of longitudinal steel reinforcing rods; second type of fibers are used to define nonlinear behavior of confined concrete which consists of core concrete; and third type fibers are defined for unconfined concrete which includes cover concrete. Also, the stress/strain diagram is determined for the nonlinearity by using constitutive laws for each fiber element like rebar, confined concrete and cover concrete, according to defined materials. Figure 1 shows typical fiber modelling for a rectangular reinforced concrete section.

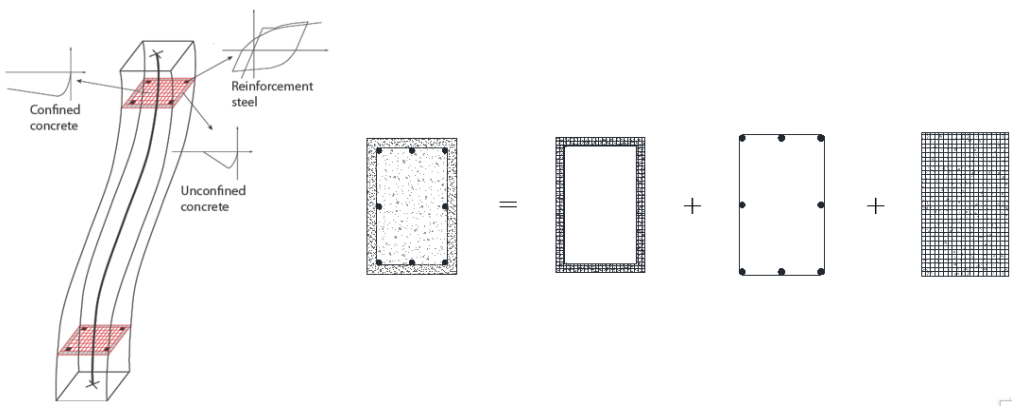

Figure 1. Typical fiber model of a RC element (Rodrigues, 2012)

2.1. Description of numeric model

Numeric models were modelled with 5 storeys and 7 storeys RC frame. Both of the RC frames have 5 bays and width of the bay is 5m. Two different concrete compressive strength were considered C20 and C25. Moreover, yield strength of rebar was considered as 420 MPa. Columns were not jacket in this study. One of the models was presented in Figure 2. Each floor was 3.0 m constant story height. The dimensions for columns were selected as 40cm/40cm for 5 story building and 50cm/50cm for 7 story building. Moreover, dimensions of beams were selected as 25/50 for both buildings. The nonlinear static analyses of the buildings were performed as indicated in Turkish Building Earthquake Code (TBEC) (2018). The building importance coefficient is assumed as 1.0 for the existing building. Boundary condition of the building was supposed as fixed support. Also, the soil differences and damping properties accordance with soil were not considered. For nonlinear analyses, SeismoStruct (2014) program was used which is able to simulate the inelastic structural systems response.

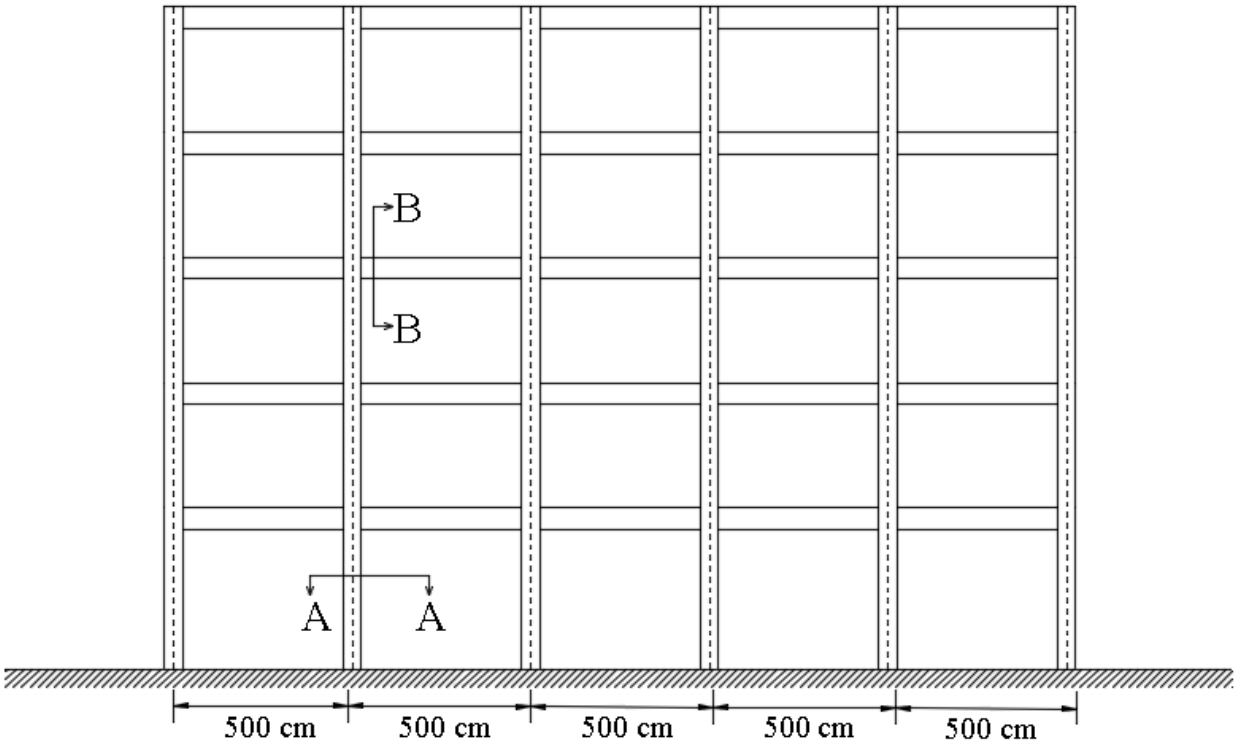

(a)

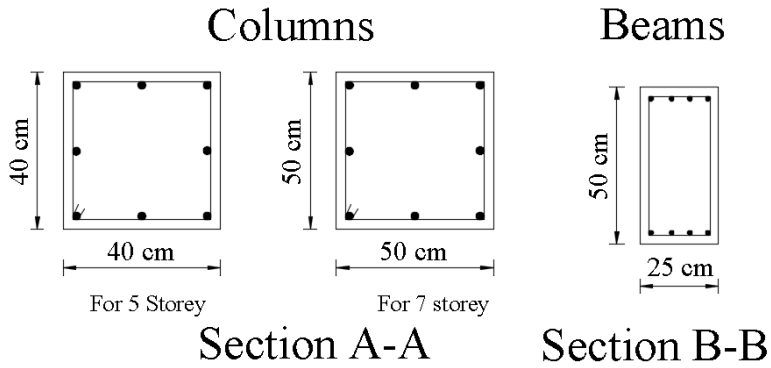

(b)

Figure 2. (a) Generic 5 storey model, (b) Cross sections

2.2. Adopted material models, properties and seismic records

The bilinear elastic plastic material model which includes kinematic strain hardening is used for the rebar. Concrete material is defined by the uniaxial confined concrete model (Figure 3) (Kwon and Kim 2007, Duan and Hueste 2012). The confinement effect is calculated by using Mander (1988) model. Reinforced concrete parameters related to structural elements are illustrated in Table 1.

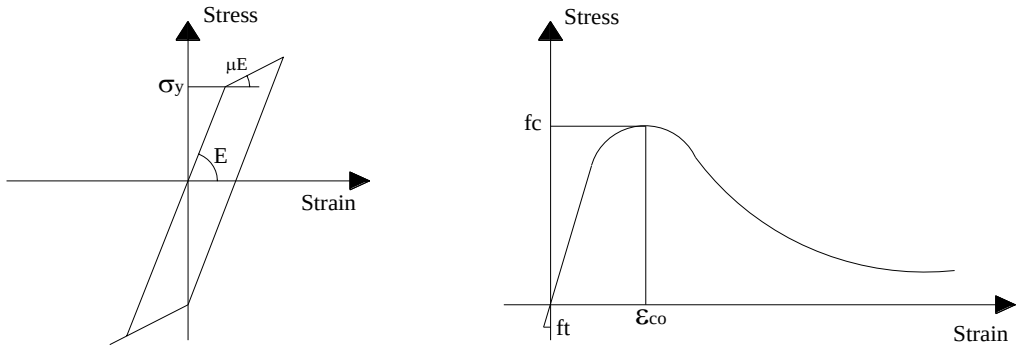

(a) Reinforcing bar (b) Concrete

Figure 3. Material models for reinforcing (a) bar and (b) concrete

Table 1. Reinforced concrete parameters related to structural elements.

Structural Elements		Longitudinal reinforcement	Section	Transverse reinforcement spacing (cm)
Column (50/50 and 40/40)	Confinement zone of column	8Ø16	A-A	15
	Central zone of column		A-A	15
Beam (25/50)	Confinement zone of beam	Top reinforcement 2Ø12	B-B	20
	Central zone of beam	Bottom reinforcement 4Ø12		

Model-I represents $\frac{\rho}{\rho'} = \frac{1}{2}$, Model-II represents $\frac{\rho}{\rho'} = 1$, Model-III represents $\frac{\rho}{\rho'} = \frac{3}{2}$. Where ρ' represents rebar area of compression reinforcement, ρ represents rebar area of tension reinforcement.

Indeed, TBEC 2018 suggests performing IDA with eleven seismic record. However, ten seismic record were used for this study. The reason of this is analysis results could not be drawn from one of the Van earthquake record. Used records were presented in Figure 4 with PGA values below. Earthquake records were scaled between 0.2g and 1.2g. Scaling procedure was followed by used software automatically. Six dynamic analysis were performed for each of the earthquake records from 0.2g to 1.2g with a 0.2g differences. Earthquake characteristics of used seismic records can be seen in Table 2.

Table 2. Selected earthquake acceleration records for dynamic analyses

Number	Earthquakes	Station	Direction	Date	Magnitude	PGA (gal)
1	Kocaeli	Düzce	E-W	August 17, 1999	7.4	373.76
2	Kocaeli	Sakarya	E-W	August 17, 1999	7.4	407.04
3	Düzce	Bolu	E-W	November 12, 1999	7.2	805.78
4	Düzce	Düzce	E-W	November 12, 1999	7.2	513.78
5	Van	Van-Muradiye	N-S	October 23, 2011	6.7	178.5
6	Van	Van	E-W	November 9, 2011	5.6	245.9
7	Erzincan	Erzincan	E-W	March 13, 1992	6.1	470.91
8	Bingöl	Bingöl	N-S	May 1, 2003	6.1	545.53
9	Sultandağı	Afyon	N-S	February 3, 2002	6.1	113.5

10	Dinar	Afton-Dinar	E-W	October 1, 1995	6.0	329.72
11	Ceyhan	Adana-Ceyhan	E-W	June 27, 1998	5.9	273.55

3. RESULTS AND DISCUSSION

The IDA results were plotted with different graphs. Response evaluation of numeric models were performed according to concrete story number of the numeric models. Response of 5 story numeric model with 20 MPa concrete class can be seen in Figure 5.

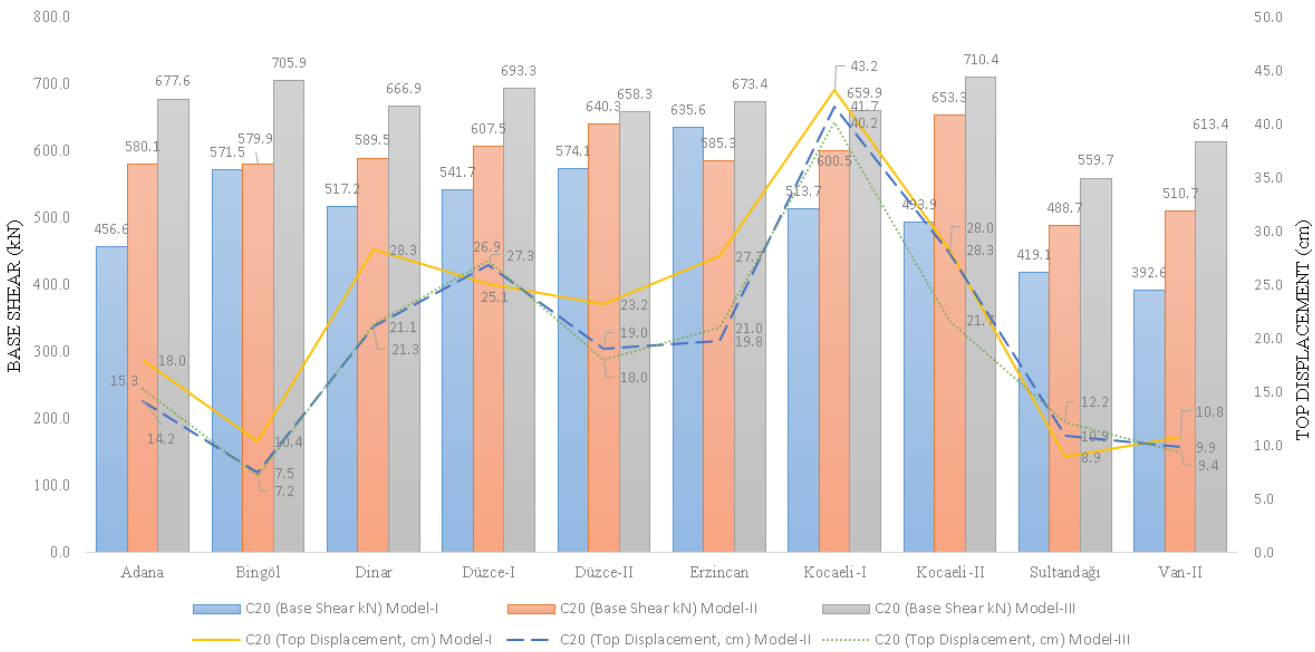

Figure 5. Seismic response of the five-story generic numeric model with C20 concrete

According to IDA results, increasing tension reinforcement ratio provided additional lateral base shear demand. However, there are one exceptional situation for these analyses. Exceptional situation was observed at IDA with Erzincan record. The same reinforcement ratio with tension and compression area decreased global lateral base shear demand. And then 50% surplus tension reinforcement ratio than compression reinforcement ratio provided higher lateral base shear demand than equal situation. Response of 5 story numeric model with 25 MPa concrete class was presented in Figure 6.

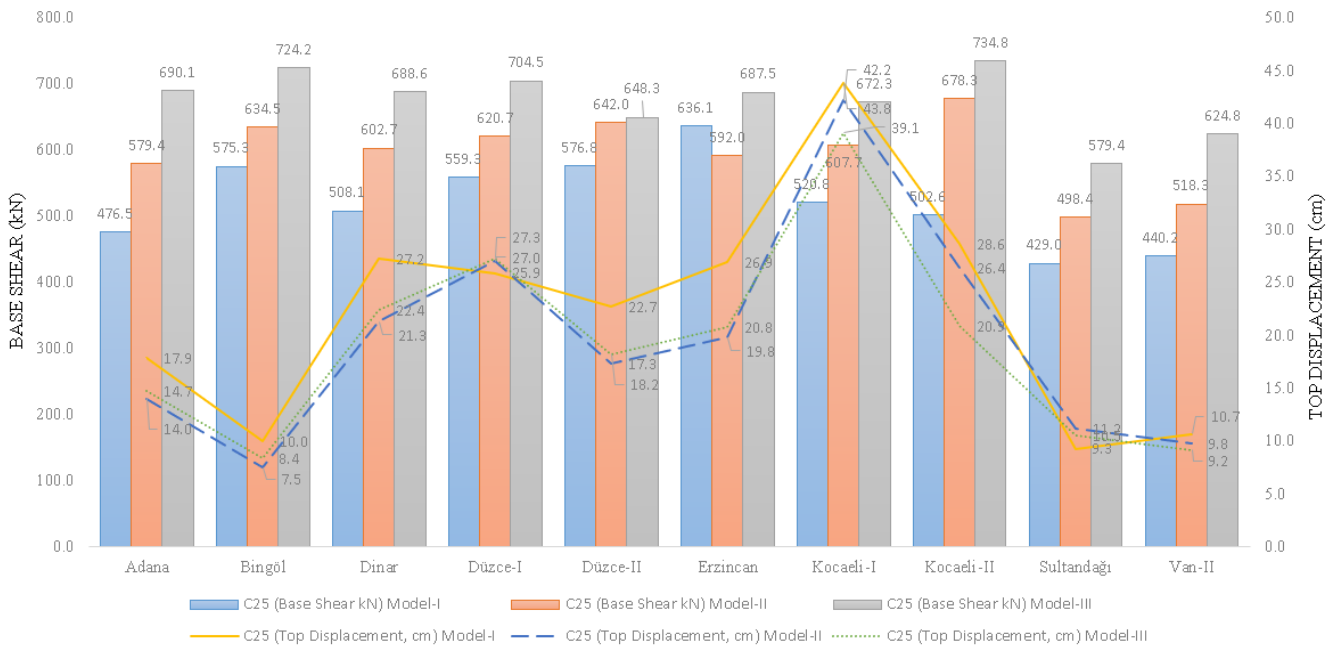

Figure 6. Seismic response of the five-story generic numeric model with C25 concrete

There is an increasing trend at base shear and top displacement with an increasing tension reinforcement ratio. However, one another exceptional situation was obtained at Erzincan record. Obtained maximum resistivity 734.8 kN with Kocaeli-II record and minimum resistivity 579.4 kN with Sultandağı record.

The same earthquake records were used also 7 story generic RC structure to see performance of structure with changing tension reinforcement ratios. The IDA results for 7 story RC structure was plotted in Figure 7 for 20 MPa concrete class.

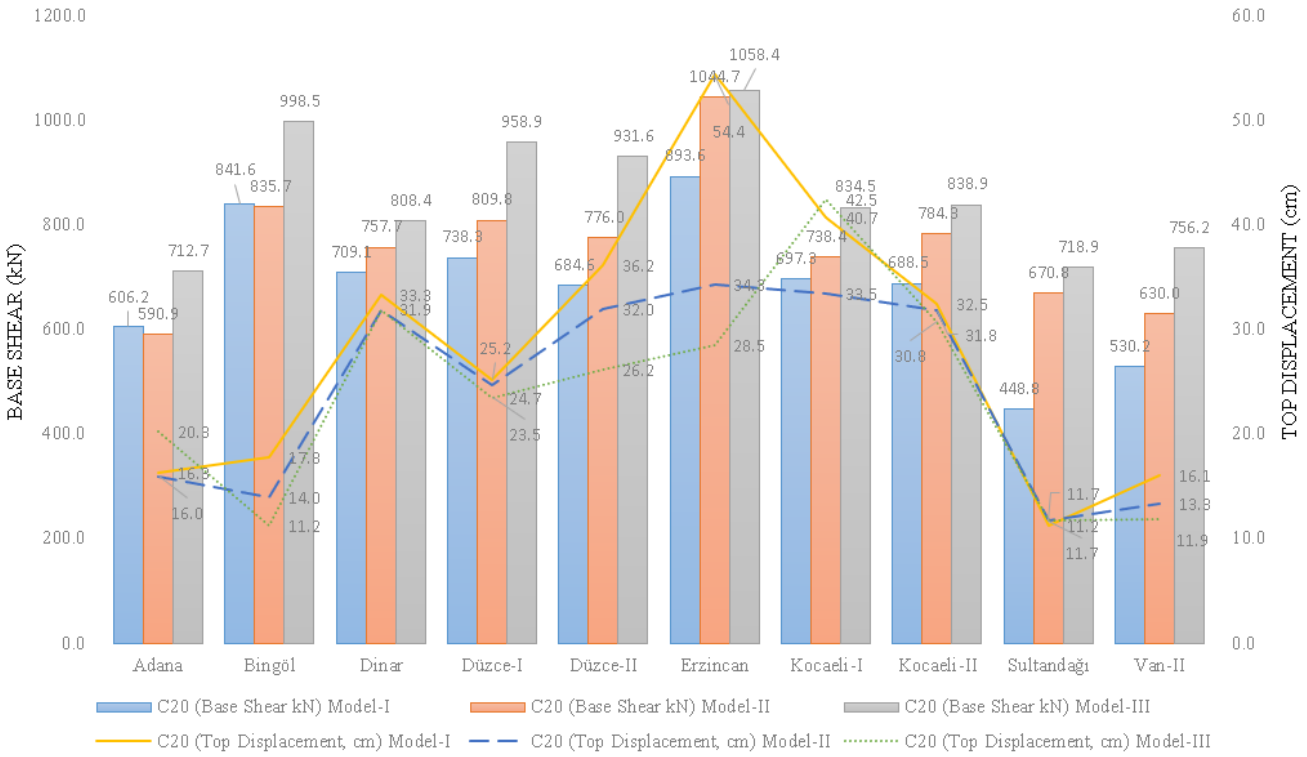

Figure 7. Seismic response of the seven-story generic numeric model with C20 concrete

According to IDA results, lateral base shear demand of the reinforced concrete generic structure increased with increasing tension reinforcement ratio. There are two exceptional results were observed at Adana and Bingöl earthquakes. These exceptional results present that equal reinforcement ratio showed worse performance than Model-I. Rest of the results showed better performance than less reinforcement ratio. The highest displacement values were obtained from Erzincan earthquake record. Moreover, the peak base shear was also obtained from Erzincan earthquake.

The IDA results for 7 story reinforced concrete structure was plotted in Figure 8 for 25 MPa concrete class.

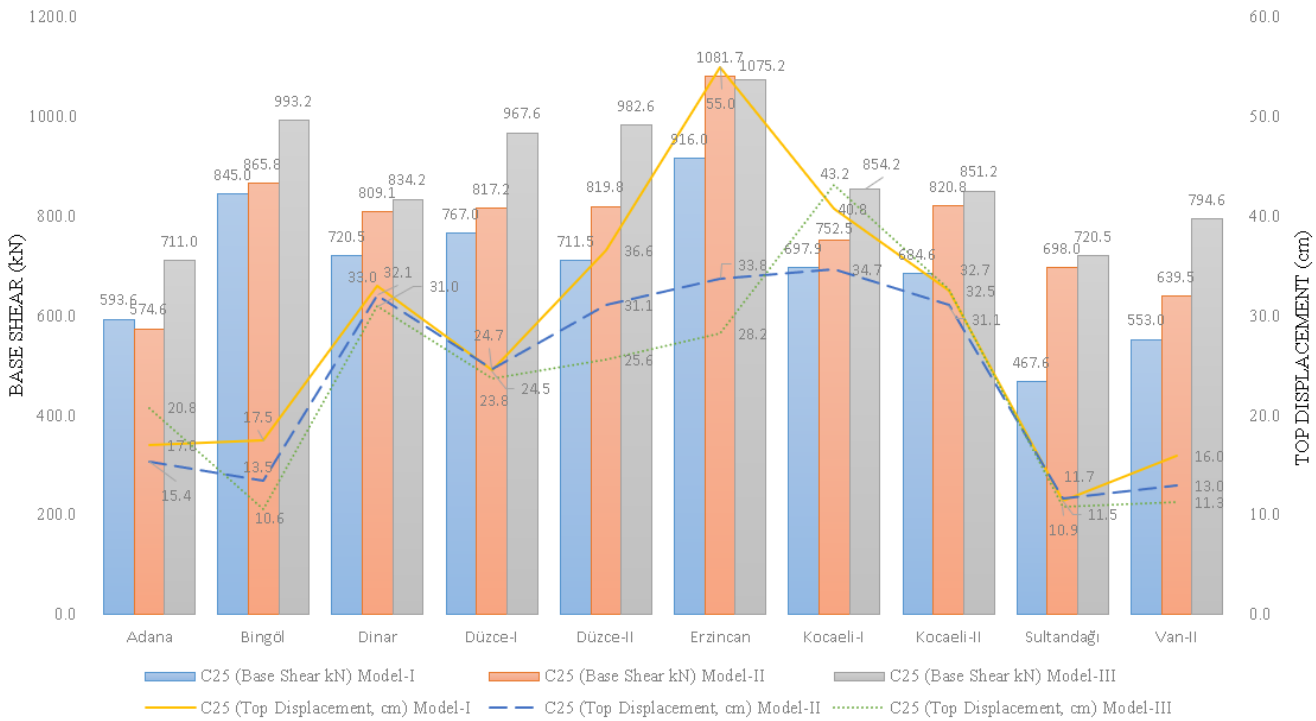

Figure 8. Seismic response of the seven-story generic numeric model with C25 concrete

The IDA results showed that generally lateral base shear demand was increased with increasing tension reinforcement ratio. However, two exceptional results were obtained from Adana and Erzincan earthquake records. The rest of the results similarly showed an increasing trend with the increasing tension reinforcement ratio.

4. CONCLUSIONS

This paper aims to investigate global response of mid-rise RC structures under dynamic analysis. For this purpose, eleven earthquake records were selected and used for IDA. Two different concrete class were used, and three different tension reinforcement ratios used for 5 story and 7 story RC structures with the same plan view. According to IDA results, following results were listed,

- To assess global response of a reinforced concrete structure, IDA analysis presents more option to evaluate results.
- According to IDA results, lateral base shear demand can be increased by increasing tension reinforcement ratio.
- Double compression reinforcement ratio showed a better performance than equal tension reinforcement as an exceptional result.
- Increasing concrete class is a global solution to increase lateral base shear demand of a reinforced concrete structure. However, increasing tension reinforcement is a local solution to increase the performance of the structure.
- Obtained maximum top displacement depends on the earthquake PGA. Top displacement presents an increasing tendency as shown in the figures.
- The investigated reinforced concrete structure should be exposed to low amplitude and low PGA earthquake like Sultandağı earthquake to see either base shear ratio or displacement capacity with a certain range.

REFERENCES

Ashour S A, (2000). Effect of compressive strength and tensile reinforcement ratio on flexural behavior of high-strength concrete beams. *Engineering structures*, **22(5)**: 413-423.

Duan H, Hueste M B D (2012). Seismic performance of a reinforced concrete frame building in China. *Engineering Structures*, **41**, 77–89.

Fantilli A P, Ferretti D, Iori I, Vallini P, (1999). Behaviour of R/C elements in bending and tension: the problem of minimum reinforcement ratio. *European Structural Integrity Society*. 99-125.

Kwon O S, Kim E (2010). Case study: Analytical investigation on the failure of a two-story RC building damaged during the 2007 Pisco-Chincha earthquake. *Engineering Structures*. **32**, 1876-1887.

Lee T, Pan A D (2003). Estimating the relationship between tension reinforcement and ductility of reinforced concrete beam sections. *Engineering Structures*. **25(8)**: 1057-1067.

Mander J B, Priestley M J N, Park R, (1988). Theoretical stress-strain model for confined concrete. *Journal of Structural Engineering (ASCE)*. 1804–1826.

Onat O, Lourenço P B, Koçak A, (2016). Nonlinear analysis of RC structure with massive infill wall exposed to shake table. *Earthquakes and Structures*, **10(4)**, 811-828.

Onat O, Yön B, Calayır Y, (2018). Seismic assessment of existing RC buildings before and after shear-wall retrofitting. *Gradevinar*, **70(8)**, 703-712.

Rodrigues H. (2012). Biaxial seismic behaviour of reinforced concrete columns. PhD Thesis, Universidade de Aveiro, Portugal.

SeismoStruct v7 (2019). A computer program developed for the accurate analytical assessment of structures, subjected to earthquake strong motion. Available online: www.seismosoft.com.

Theriault M, Benmokrane, B, (1998). Effects of FRP reinforcement ratio and concrete strength on flexural behavior of concrete beams. *Journal of composites for construction*, **2(1)**: 7-16.

Turkey Ministry of Environment and Urbanization, (2018) Turkish Building Earthquake Code, Ankara, Turkey.

Yön B, Öncü M E, Calayır Y, (2014). Effects of seismic zones and site conditions on response of RC buildings. *Gradevinar*, **67(6)**, 585-596.

SEISMIC VELOCITY STRUCTRE OF KUCUK AND BUYUK MENDERES GRABEN

Özer Ç.[1*] ve Polat O.[2]

[1] *Dr,Öğr. Üyesi, Deprem Araştırma Merkezi, Atatürk Üniversitesi, Erzurum*
[2] *Prof.Dr, Jeofizik Müh. Bölümü, Dokuz Eylül Üniversitesi, İzmir*
**Email: caglarozer@atauni.edu.tr*

ABSTRACT:

In this study, new absolute P- wave velocity and Poisson ratio model using Local Earthquake Tomography (LET) method at western Anatolia of Turkey are proposed. Recorded more than 15000 local earthquakes at 50 stations, 1456 well located earthquakes with 10368 P- phase reading were selected performing the criteria of a minimum of 12 P- wave observation. The seismic instruments were installed by Earthquake Department of the Disaster and Emergency Management Authority (AFAD) which answers directly to Turkish Prime Ministry. Two depth cross-section tomograms were calculated along Kucuk and Buyuk Menderes graben. Resolution test (checkerboard test) shows that the tomograms are reliable down to 40 km. It is clearly observed that four seismic velocity layer represent the western Anatolia sub-surface down to 40 km. Furthermore, P- wave velocities and poisson ratio are range from 3.5 km/s to 8.5 km/s and from 0.1 to 0.40; respectively. It has known that low velocities and low poisson ratio are indicator of geothermal gasses, while low velocities and high poisson ratios point out the geothermal fluid. We detect low P- velocity and low poisson ratio at Aliaga, Candarli, Doganbey and Menemen. Also we observed low velocity and high poisson ratio along the Guzelhisar, Kizilcukur, Suzbeyli and Yelki. Additionally, low P- velocity and high poisson ratio values which considered being the harbinger of new geothermal fields are defined Bayindir, Karahayit and Menderes down to 7 km. The lower crust-upper mantle discontinuity was identified at between 25 and 33 km.

KEYWORDS: Local earthquake tomography, Kucuk Menderes Graben, Buyuk Menderes Graben, seismic velocity structure

1. INTRODUCTION

The extensional regime manages the western Anatolia tectonic which has complex geology and the N-S extension regime caused E-W faults, generally. Tectonic structures have been advanced like an outcome of the northward motion of the African and Arabian plates notional to the Eurasian plate. The tectonic escape model proposes that extension in western Turkey is managed by the westward movements of Anatolian plate thorough to North and East Anatolian fault zone (Yolsal-Çevikbilen et al. 2014). To monitoring all of the seismic activity, Earthquake Department of the Disaster and Emergency Management Authority (AFAD) installed more than one thousand seismic recorder in Turkey. We used only well coverage 50 seismometers to understand western Anatolia crustal structure. Furthermore, our dataset consists 1456 events which selected from more than 15000 earthquakes and recorded between 2007 and 2013. Clearly, the seismic activity of western Anatolia is concentrate at SW of Kutahya, E part of Denizli, W part of Aydin, N part of Manisa and W part of Izmir (Fig. 1). Also depth distribution of events range from 0 to 30 km, intensely.

The western Anatolia is good example for geothermal energy development, like it contains the high temperature capacity geothermal system in Turkey. Most of highest temperature geothermal places (120-240 °C) are located along the Buyuk Menderes, Kucuk Menderes and Gediz grabens. Besides these geothermal fluids were linked to

circulation of surface waters along faults and the high heat flow values are related to the basement of the Menderes horst-graben system (Serpen et al. 2009; Erkan 2015).

Absolute P- wave velocity and poisson ratio depth cross section are presented along two profiles which are perpendicular each other (Fig. 2). The new seismic velocity model obtained in this study for the western Anatolia show clearly some geothermal reservoir structure (profile-1) and Kucuk Menderes graben seismic velocity structure (profile-2).

Kucuk Menderes Graben (KMG) is 80-km long and 3-10 km wide. It was consisted the pre-Miocene basement rock comprising metamorphic rocks of the Menderes Massif, cut by the Miocene andesitic, basaltic rocks and the upper cretaceous-Paleocene Bornova mélange. Besides, several hot spots can be seen in the KMG from Odemis to Selcuk. Main geothermal area are located at Bayindir, Odemis, Sarigol (Ozer et al. 2018). The main purpose of this study, the highest resolution new seismic velocity and poisson ratio structure have been produced for first time in some geothermal areas and KMG.

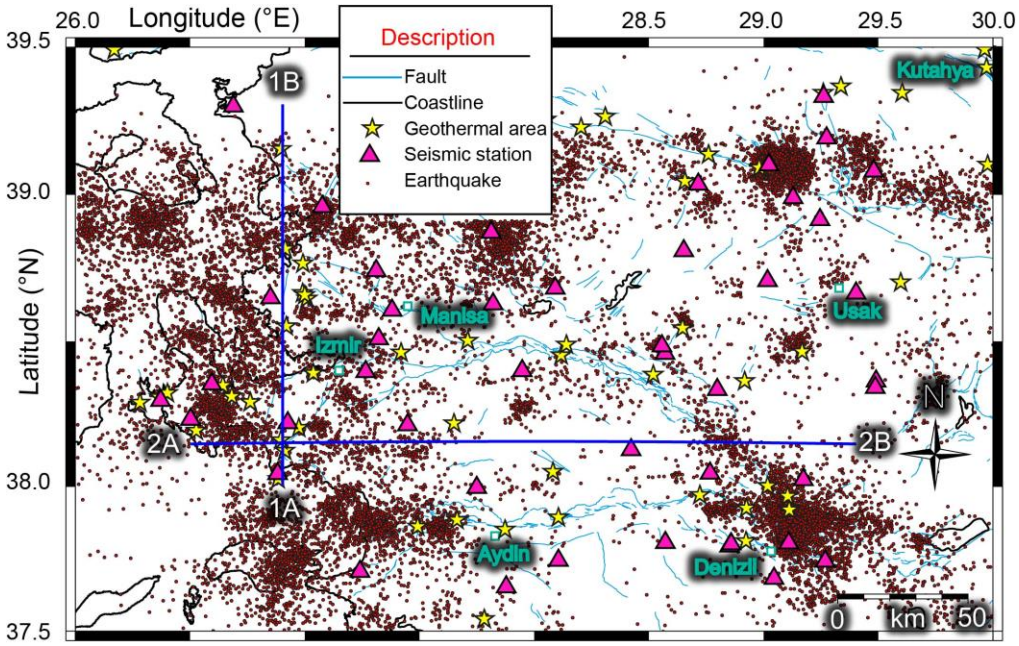

Figure 1. Seismic activity of the western Anatolia, Turkey from 2007 to 2013 showing more than 15000 events recording 50 seismic stations.

2. RESULTS AND DISCUSSION

To predict a probable impact of noise on the resolution, we applied checkerboard synthetic resolution test (Fig. 2). Especially, we created three different checkerboard tests which have different size and empty space. We designed test as periodic positive (blue) and negative (red) velocity anomalies. Model A, B and C anomaly sizes are consisting 50*50 km^2, 30*30 km^2 and 15*15 km^2 with 5 km empty space; respectively (Fig. 2). We added random noise to travel time data having average deviation of 0.1 and 0.2 for the P-and S-wave data. It is frankly observed that three different anomalies prove the data, station coverage and inversion parameters power. Because all of the models are reflect the initial model down to 40 km (Fig. 2).

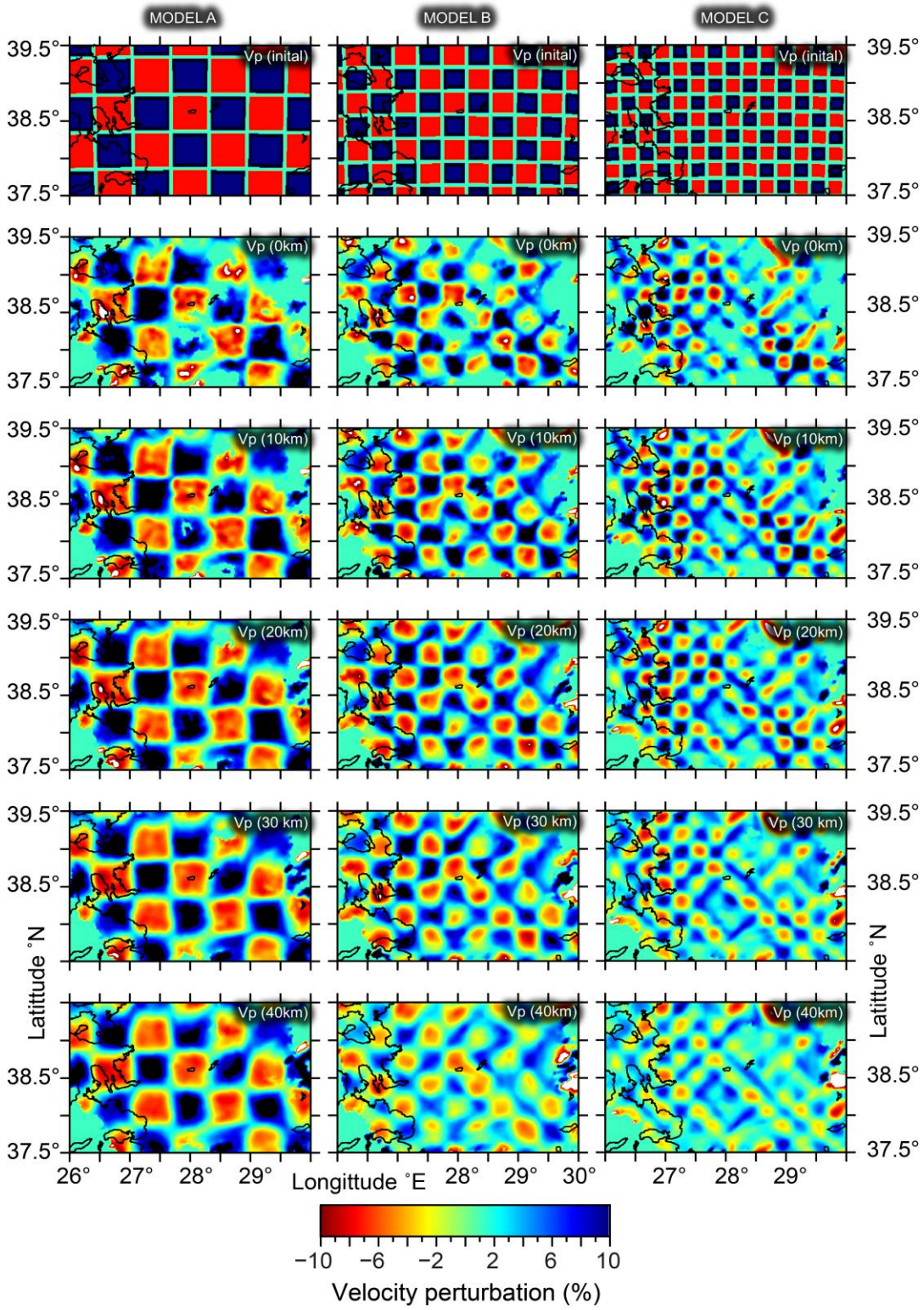

Figure 2. Checkerboard test results. Periodic negative and positive anomalies illustrate 10% velocity changes. We conduct different size of anomaly: 50*50 km^2, 30*30 km^2, 15*15 km^2; respectively.

Some researches assert that absolute velocities and poisson ratios values should be interpreted together (Hauksson 2000; Kaypak 2008; Kaypak & Gökkaya 2012; Muksin et al. 2013). General approach, low velocities and low poisson ratios are responsible for fracture zone which might be contain gas, CO_2 or mixture of them. Conversely, low velocities and high poisson ratio values are related to geothermal fluid. For this purpose, we evaluate the Vp and poisson ratio values together and explored some indicator of geothermal tips at especially Kucuk Menderes Graben, western Anatolia.

In profile 1; we detect low P- velocity and low poisson ratio at Aliaga, Candarli, Doganbey and Menemen. Also we observed low velocity and high poisson ratio along the Guzelhisar, Kizilcukur, Suzbeyli and Yelki. These places may be possible new geothermal area where has not been drilled yet. Furthermore, the Moho depth was determined at approximately range from 22 to 31 km (Fig. 3 and Fig.4; Vp).

In profile 2; while low P- velocity and low poisson ratio are presented thought Doganbey, Sapcilar, Sarigol and Seferihisar regions. Additionally, low P- velocity and high poisson ratio values which considered being the harbinger of new geothermal fields are defined Bayindir, Karanyit and Menderes down to 7 km. The lower crust-upper mantle discontinuity was identified at between 25 and 33 km.

In both profile 1 and profile 2 four main seismic crustal layer appear down to 50 km which velocities are change from 3.5 km/s to 8.5 km. First layer which velocities range from 3.5 to 4.5 km/s are associated with the sedimentary deposits of the basin.

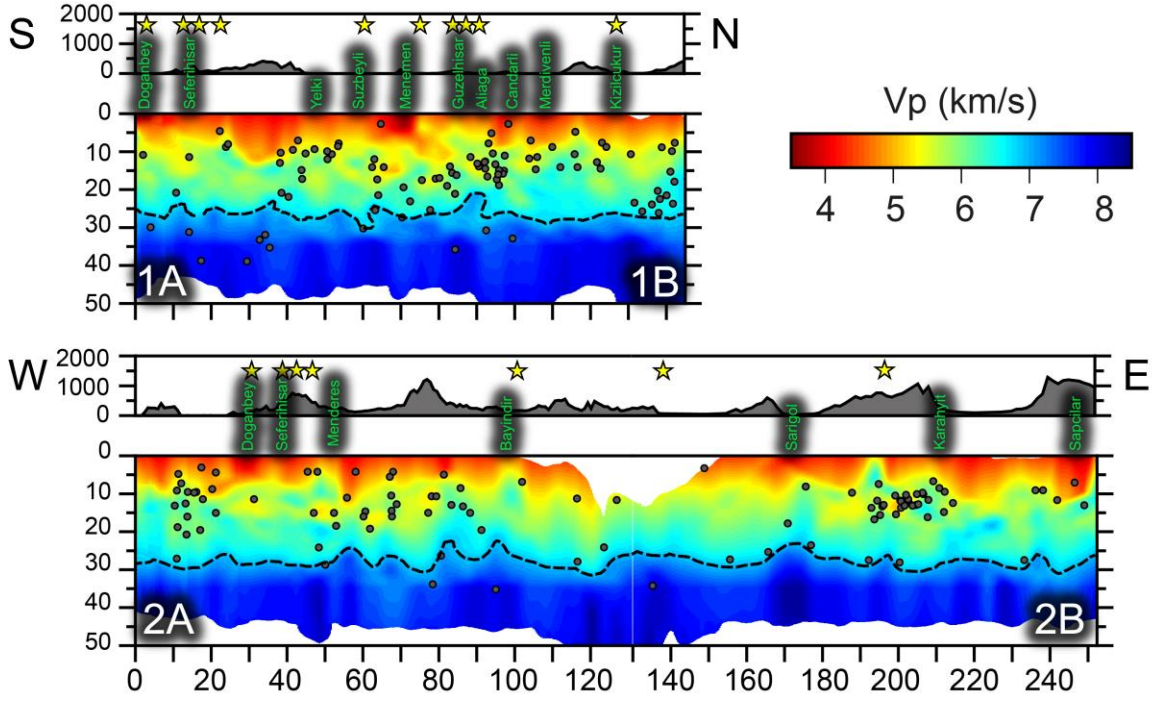

Figure 3. Depth cross-section of P-wave velocity along S-N and W-E directions in the western Anatolia.

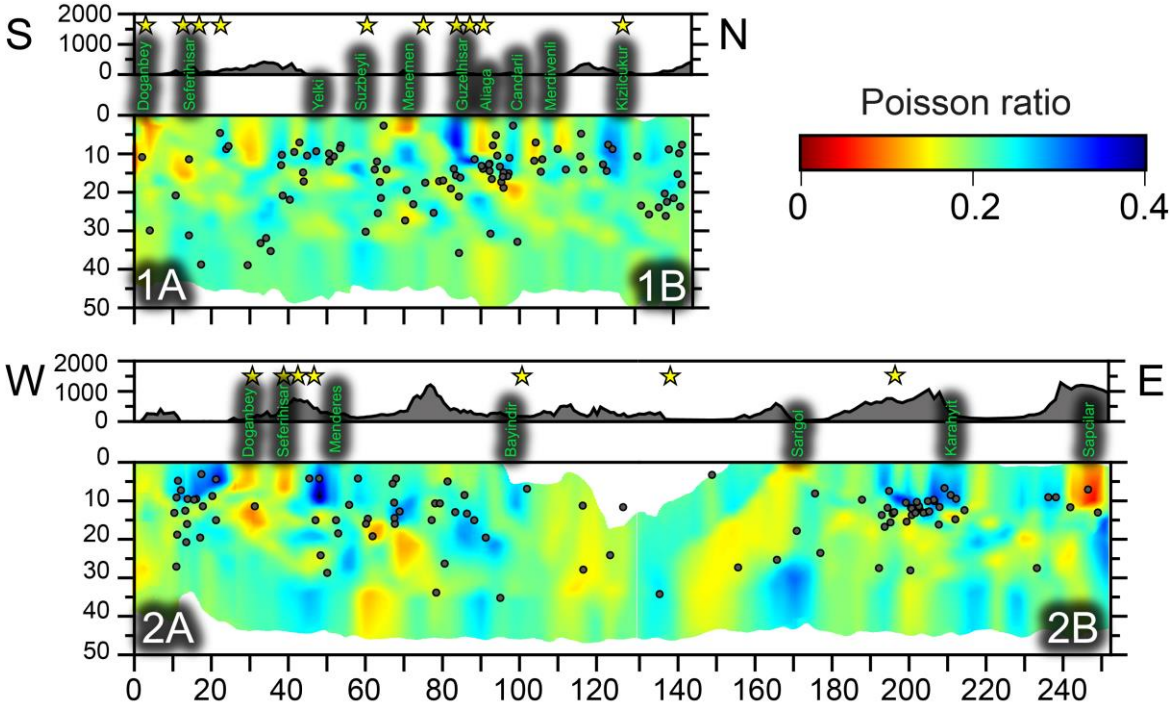

Figure 4. Depth cross-section of Poisson ratio along S-N and W-E directions in the western Anatolia.

3. CONCLUSION

This study presents the first implementation using with Local Earthquake Tomography (LET) algorithm to understand crustal seismic structure at Kucuk Menderes graben, western Turkey. Therefore, high resolution P-wave velocity and poisson values have not been available for this time. Well located 1456 earthquakes selected in more than 15000 earthquakes which recorded AFAD recorders. Generally, we have specified four main crustal seismic layers using P-wave velocity values. Resolution test (checkerboard test) shows that the tomograms are reliable down to 40 km. The upper layer which lies down to ~8 km depths with P- velocities from 3.5 to 4.5 km/s. This layer geology formed generally alluvium and Neogene sediments. Middle layer is located at between 8 and 12 km with velocities ranging 4.5 to 5.3 km/s. Lower crustal layer velocities are range from 5.3 to 6.8 km/s from 12 to 29 km. This velocity may be related to crystalline rocks and gabbro contents. Also the average Moho depth (Crust-Mantle discontinuities) is determined as intrusive shape at ~29 km. The deeper crustal layer velocities are higher than 6.8 km/s.

As it is discussed from some papers (Hauksson 2000; Kaypak 2008; Kaypak & Gökkaya 2012); while seismic velocity values are effected to lithological structure, poisson ratio values are depend on petrological characteristic. We evaluate two tomograms which perpendicular each other and detect tips for geothermal resource. We propose new geothermal areas which may be contain big fluid resources at Bayindir, Guzelhisar, Karanyit, Kizilcukur, Suzbeyli and Yelki.

4. ACKNOWLEDGMENTS

LOTOS algorithm were used the calculation of the tomogram. All images were created using GMT (Wessel et al. 2013; Wessel & Smith 1998). We also thank the General Directorate of Mineral Research and Exploration (MTA) for digitizing the western Anatolia fault data.

REFERENCES

Erkan, K. (2015). Geothermal investigations in western Anatolia using equilibrium temperatures from shallow boreholes, Solid Earth, 6(1), 103-113.

Hauksson, E. (2000). Crustal structure and seismicity distribution adjacent to the Pacific and North America plate boundary in southern California, Journal of Geophysical Research, 105,13875.

Kaypak, B. (2008). Three-dimensional VP and VP/VS structure of the upper crust in the Erzincan basin (eastern Turkey), Journal of Geophysical Research: Solid Earth, 113(7).

Kaypak, B. & Gökkaya, G. (2012). 3-D imaging of the upper crust beneath the Denizli geothermal region by local earthquake tomography, western Turkey. Journal of Volcanology and Geothermal Research, 211-212, 47-60.

Muksin, U., Bauer, K., & Haberland, C. (2013). Seismic Vp and Vp/Vs structure of the geothermal area around tarutung (north sumatra, indonesia) derived from local earthquake tomography. Journal of Volcanology and Geothermal Research, 260, 27-42.

Ozer, C., Gok, E., Polat, O., Three-Dimensional Seismic Velocity Structure of the Aegean Region of Turkey from Local Earthquake Tomography, Annals of Geophysics, 61 (1).

Serpen, U., Aksoy, N., Ongur, T., Korkmaz, E.D. (2009). Geothermal energy in Turkey: 2008 update. Geothermics, 38(2), 227-237.

Wessel, P., Smith, W. H. F., Scharroo, R., Luis J. F., and Wobbe, F. (2013). Generic Mapping Tools: Improved version released. EOS Trans. AGU, 94, 409-410.

Wessel, P & Smith, WHF (1998). New, improved version of generic mapping tools released. Eos, Transactions American Geophysical Union, 79(47), 579-579.

Yolsal-Çevikbilen, S., Taymaz, T. & Helvaci, C. (2014). Earthquake mechanisms in the Gulfs of Gökova, Sıgacık, Kusadasi, and the Simav Region (western Turkey): Neotectonics, seismotectonics and geodynamic implications. Tectonophysics, 635, 100-124.

FINITE ELEMENT SIMULATION OF MASONRY WALLS UNDER CYCLIC LOADING USING A HETEROGENEOUS MODEL

Kömürcü S.[1]

[1] *Res. Assist., Civil Eng. Department, Istanbul Technical University, Istanbul, Turkey*
Email: komurcus@itu.edu.tr

ABSTRACT:

Masonry walls are composite structures that can be modeled using advanced techniques. It is significant to model masonry structures to understand their structural behavior during natural hazards especially earthquakes. Finite element analysis is a robust numerical technique to investigate the structural behavior of the masonry structures and to investigate their earthquake response. In this study, nonlinear behaviors of walls under the effect of cyclic loading are analyzed. The masonry units such as bricks, stones or etc. and mortar between the masonry units are modeled using heterogenous modelling based on 3D finite elements. The loading is applied as displacement controlled and is affected to the wall in two load-steps. First load step is applied as constant vertical compression and the other load step is applied as horizontal cyclic loading. Load deflection curves for the planar cyclic behavior of the walls are obtained successfully. The distributions of the cracks occurred under cyclic loads on the masonry walls are determined as a result of the analysis. It is seen from the numerical results, first cracks occurred at the base course of the wall as a result of the cyclic loading. It can be said from the results; the numerical model produces compatible results with the experiment in the literature and the model can be used for new analysis to investigate the structural design parameters of the masonry walls under planar cyclic loading.

KEYWORDS: crack, finite elements, fracture, masonry, modeling, wall

1. INTRODUCTION

Masonry structures are one of the oldest structure types of the history and have a great significance among the all structures. There are many monumental masonry structures in the world such as buildings, palaces, bridges and towers. Modeling of masonry structures has become a requirement to test the strengths of existing masonry structures and to build modern structures. Masonry modeling is a challenging issue because of their composite nature. The modeling of masonry structures involves uncertainties due to the diversity of the materials that contains. Fracture and friction are often encountered topics for them and are difficult to explain with precise limits.

Masonry structures consist of masonry units (brick, stone or etc.) and mortar. Engineers have investigated the effects of tension, pressure, shear and other effects on the masonry walls and have produced models to design them. There are many examples of experimental works to investigate the structural behavior of masonry walls, see example Raijmakers and Vermeltfoort (1992), Oliviera (2003) and Mojsilovic´ et. al. (2009). Numerical analyzes have been carried out to control and support experimental studies. There are several studies for modeling of masonry to analyze their structural behavior, see example Lorenço (1995), Oller (2014), Pela (2012), Quinteros (2011), Kömürcü and Gedikli (2017). In order to better understand the masonry structures, it is necessary to produce more sophisticated models and analyze the structures. Researchers used heterogeneous modeling technique to model the masonry structures, see examples Nasiri (2017), Abdulla (2017).

In this study, cyclic behaviors of masonry walls are analyzed using a continuous heterogenous model in ANSYS 18.0 software. Generating a nonlinear numerical model for masonry walls and investigation of the structural behavior of them under cyclic loading as closer as an experiment is the focus point of this study. This study also

investigates that the compatibility of using an implicit model for highly nonlinear dynamic analysis of the masonry walls under cyclic loading.

2. MODEL PROPERTIES

The geometry and material properties of the modeled wall belongs to experimental work Mojsilovic´ et. al. (2009) in terms of confirmation of the finite element model. The modeled masonry wall style is known as running bond masonry which composed of stretchers offset by half brick per course. The wall with a base width of 1200 mm and a height of 1200 mm and a thickness of 110 mm are formed by overlaying 14 rows of bricks using 10 mm mortar layer both head joints and bed joints between the bricks as shown in Figure 1.

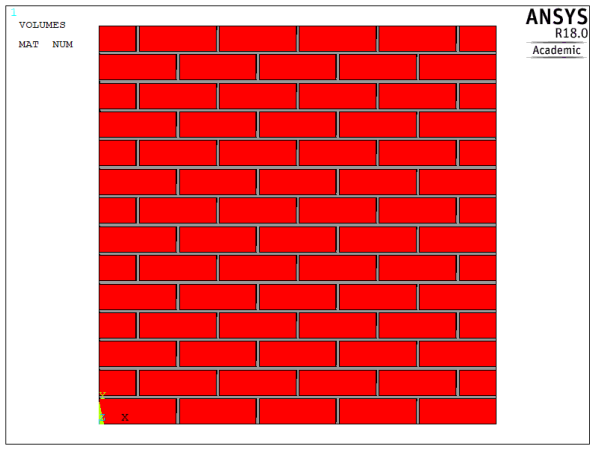

Figure 1. Modeled masonry wall

The walls are constructed with using the same clay brick unit which has dimensions of a=230 mm, b=76 mm and c=110 mm and having 10 holes as shown in Figure 2b. The void area of the brick is %25.

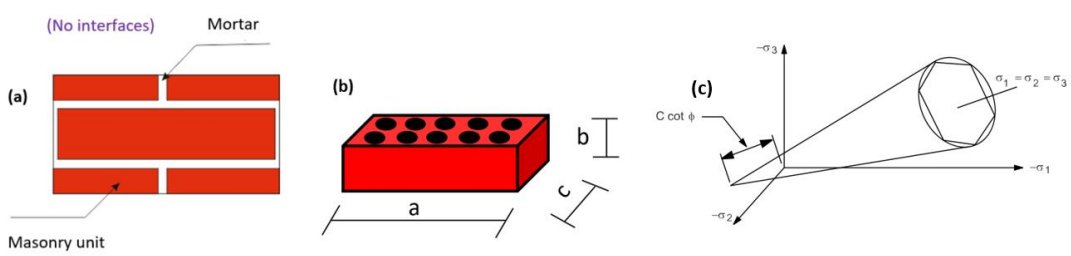

Figure 2. (a) Continuous micro modeling (b) Hollow brick (c) The Drucker-Prager material model

The Modulus of elasticity E and the Poisson ratio v of the bricks and mortar used in this study are E_b=5730 MPa, v_b=0.15 and E_m=565 MPa and v_m=0.15, respectively. The Drucker-Prager fracture criterion is applied in combination with the elastoplastic behavior model. The Drucker-Pager hypothesis appears as a cone in three-dimensional space, where the tip of the cone represents the low tensile strength of the material, while the bottom of the cone represents the pressure strength of the material as shown in Figure 2c. This failure hypothesis is expressed as Equation 1.

$$\left(\frac{\eta-1}{2}\right)(\sigma_1+\sigma_2+\sigma_3)+\left(\frac{\eta+1}{2}\right)\sqrt{\frac{(\sigma_1-\sigma_2)^2+(\sigma_2-\sigma_3)^2+(\sigma_3-\sigma_1)^2}{2}}=f_b \tag{1}$$

In this case, σ_1, σ_2 and σ_3 are the principal stress values, and η and ξ are determined as follows;

$$\eta=\frac{f_c}{f_t} \qquad \xi=\frac{\eta-1}{\eta+1} \tag{2}$$

In these expressions, f_c and f_t parameters show the values of pressure and tensile strength of the masonry wall, respectively. The Drucker-Pager hypothesis is reduced to the Von Mises hypothesis if f_c and f_t are equal. The material parameters required to construct this model are the friction and dilatation angles and cohesion value of the material. The masonry bricks are considered as linear isotropic materials. The nonlinear material properties are only applicated to the mortar between the bricks. The internal friction angle of mortar is φ_{fric}=36.38 ^{0}. The dilatation angle is chosen φ_{dil}=90^0 to ignore volume increasing effect of the material. The cohesion value is c=0.35 MPa. They are considered bonded based on the continuous micro modeling technique as shown in Figure 2a. This means that, there is no separation between the materials. In the continuous micro modeling technique, masonry units and mortar are modeled separately but there are no interfaces at the model. Hence, because of the lack of interfaces, the complexity of the model is dramatically decreased.

The 8 noded SOLID65 element is used at the analysis. Each node has 3 displacement degrees of freedom in x, y and z directions. Brittle materials can be modeled such as rock, stone, brick, concrete etc. using this element. It is a suitable element for modeling the nonlinear behavior of structures in terms of reflecting collapse mechanisms of the materials both tensile and compression ANSYS (2018).

Loading of the masonry walls are carried out in two stages. In the first load step (load step 1) the wall is loaded from the upper side with a vertical pressure of 2.8 MPa. In the second load step (load step 2), horizontal displacement is given to the top nodes of the wall. Each step is repeated three times in a form of a sinusoidal wave as indicated in Equation 3. In this expression, A is the amplitude of the loading and w is the frequency of the loading, t is the time. The loading is applied as using different amplitude and frequency values represented by number i=1 to n.

$$\mathrm{F(t)}=\sum_{i=1}^{n}\mathrm{A}_i\sin(w_i t) \tag{3}$$

The amplitude, loading speed and period values are shown in Table 1.

Table 1. Loading properties

Amplitude (mm)	0.5	1	1.5	2	3	5	7.5	10	15
Loading speed (mm/min)	1	1	1	1	2	2	2	3	4
Period (sec)	120	240	360	480	360	600	900	800	900

The displacement history graph for shear displacement v, versus time t, is shown in Figure 3 as indicated by Mojsilovic´ et. al. (2009). Total time of the experiment is 12480 seconds.

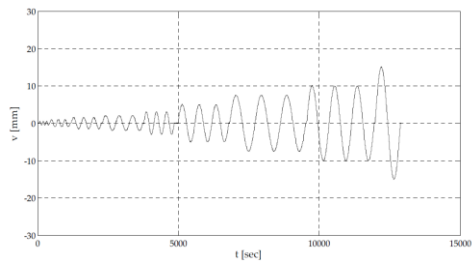

Figure 3. Displacement history

3. VALIDATION OF THE MODEL

The results of finite element analyze are presented in this section to see the validity of the proposed finite element procedure for the shear wall experiment. Results are validated to represent a detailed analysis to understand the cycling behavior of masonry walls. For this purpose, four different loading have been chosen. These sub steps are 1001, 4006, 8031 and 12081. Shear stress values are shown in Figure 4. The shear stress value increases as seen from the results. The directions of maximum and minimum shear stress values are changeable during the analysis. It can be said that; diagonal stress contours are one of the characteristic properties of the shear stress distributions at the analyses of walls exposed to shear wall experiment.

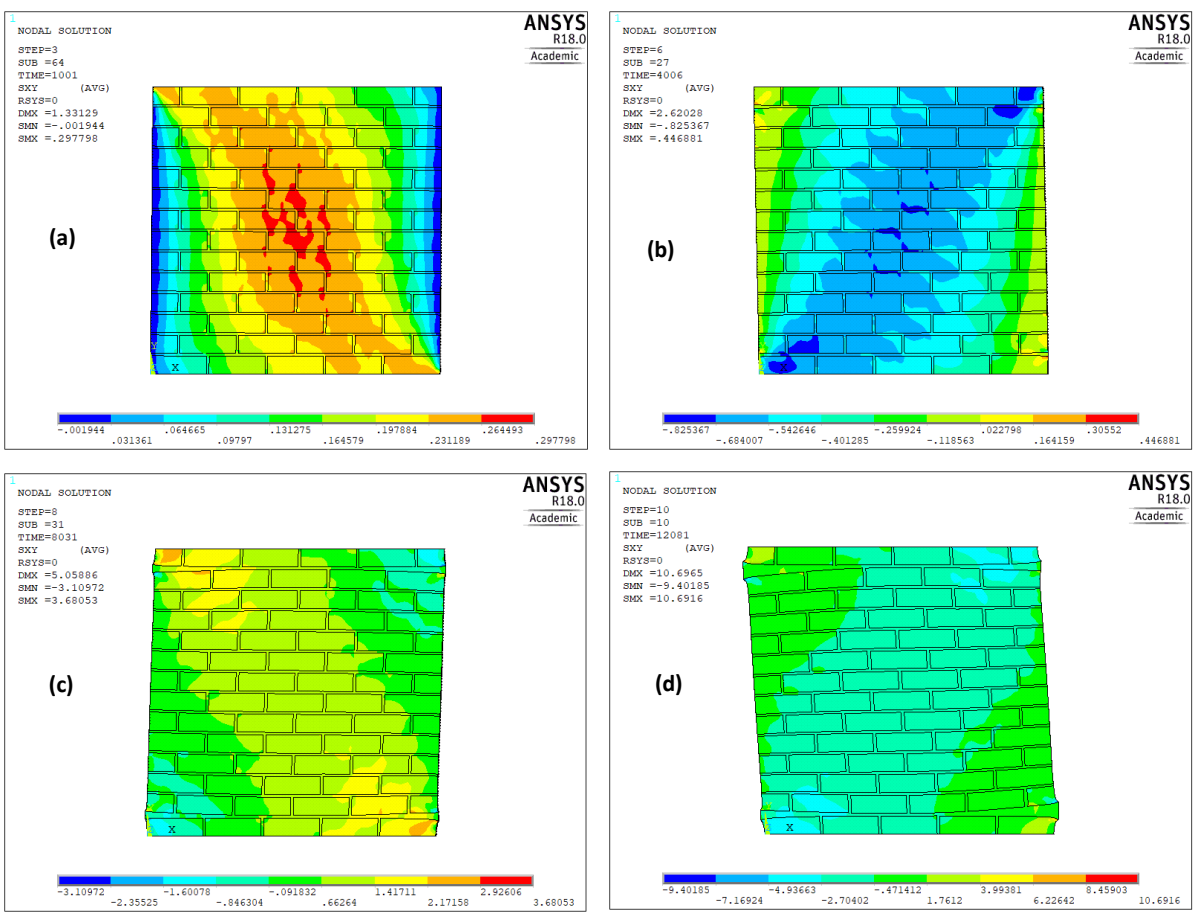

Figure 4. Shear stress distributions

Determination of minimum principal stress value is significant to structural behavior of masonry walls. Minimum stress distributions for different displacement values are shown in Figure 5. This stress value plays a key role to determine the failure mechanisms of the shear wall under the cyclic loading. It can be stated that; at the early level of the analysis, the corners of the walls behave as compression and tension toes. When one corner of the wall works as a compression toe the other parallel corner exposed to tensile stresses. However, at later stages, maximum tensile stress moves towards to the center of the wall due to the nonlinear effects. The minimum principal stress value shows that, the masonry wall collapses by the effects of compression at the end of the analysis.

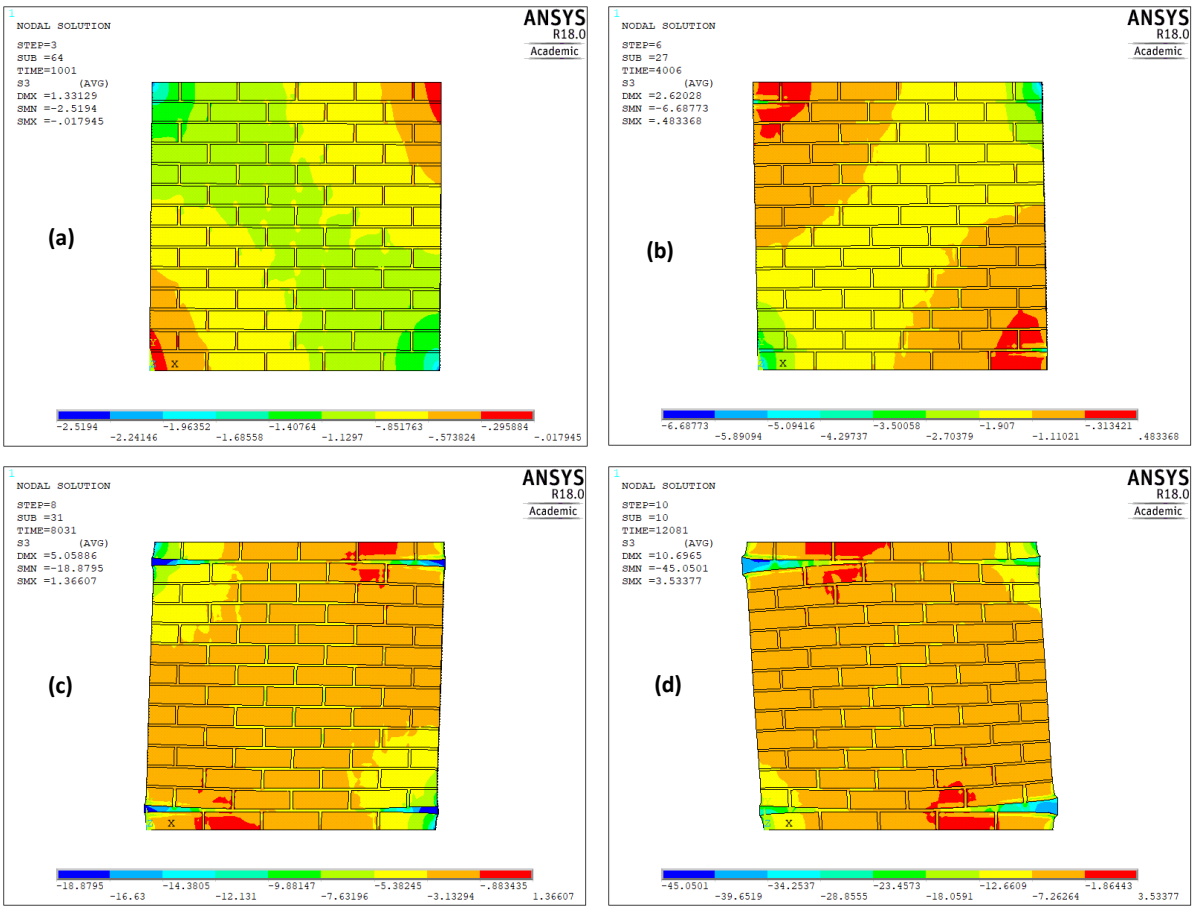

Figure 5. Minimum principal stress distributions

The wall is exposed to plastic deformation during the analysis. Plastic strain distributions for different displacement values are shown in Figure 6. This plastic strain values show the cracking and crushing areas on the wall. In Figure 6a, horizontal cracks occur at the up and down corners both right and left part of the wall. Next, the strain value is 0.02 as shown in Figure 6b. In addition to the horizontal cracks, some vertical cracks are seen at the middle of the wall head joints. Then, the strain value reaches to the level of 0.10 as seen from the Figure 6c, the crack dimensions increases dramatically. At the end of the analysis as in Figure 6d, the strain level is approximately 0.24. It can be seen from the Figure 6d, the initially opened cracks at the middle of the wall closes but the cracks at the up and down corners of the wall increase. Finally, the wall collapses due to the cracks occurred at the corners.

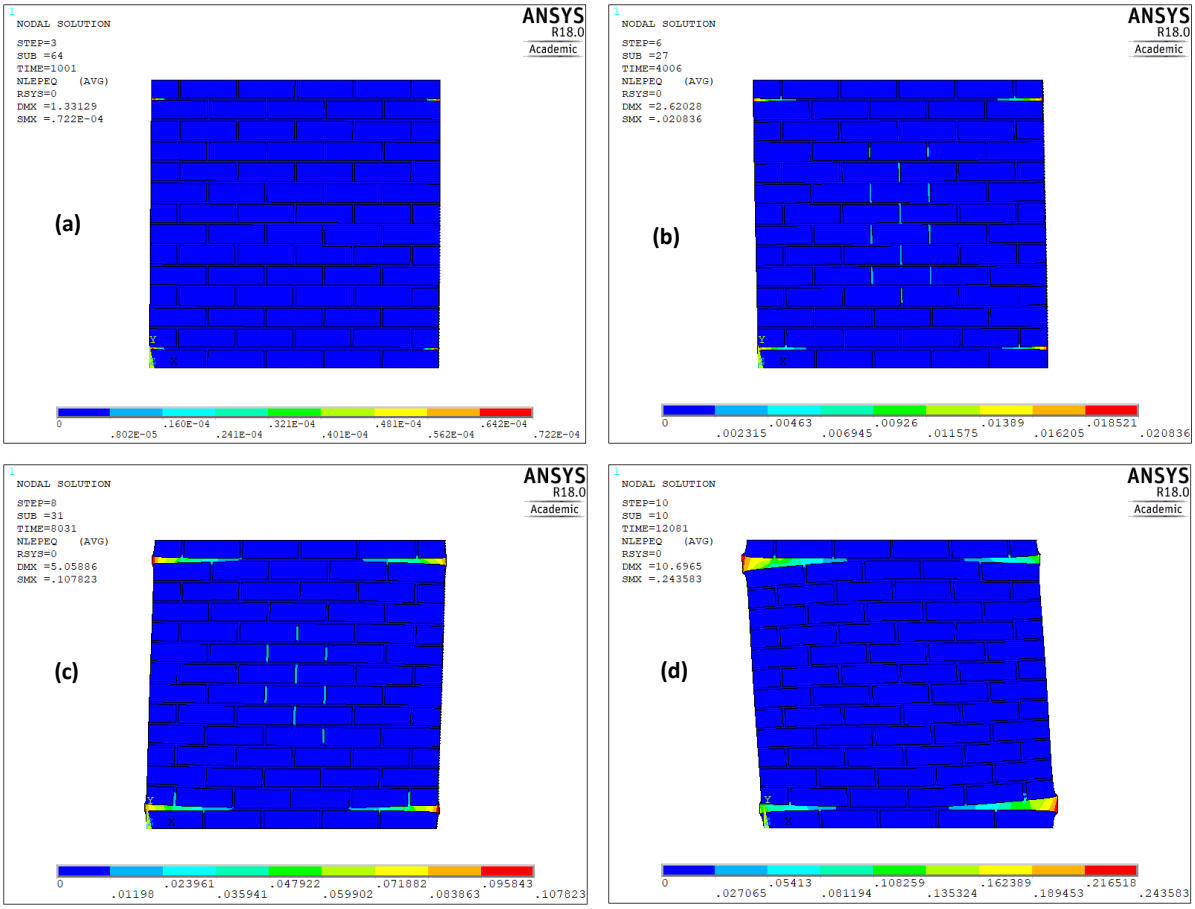

Figure 6. Plastic strain distributions

Load-displacement curve provide enhanced information about the experiments and models. Horizontal displacement at the top of the wall and horizontal reaction force at the base of the wall diagram is called hysteresis as shown in Figure 7. It can be said that; the model has good results for early stages of the analyses. But the model behaves as less ductile at later steps of the analysis and the lateral reaction force has greater than the experimental value. It is stated that, truly representation of later level of the cyclic loading is difficult with using implicit model due to encountered convergence problems. If the convergence problems were solved, the post-peak behavior of the load-displacement curve would be obtained more precisely.

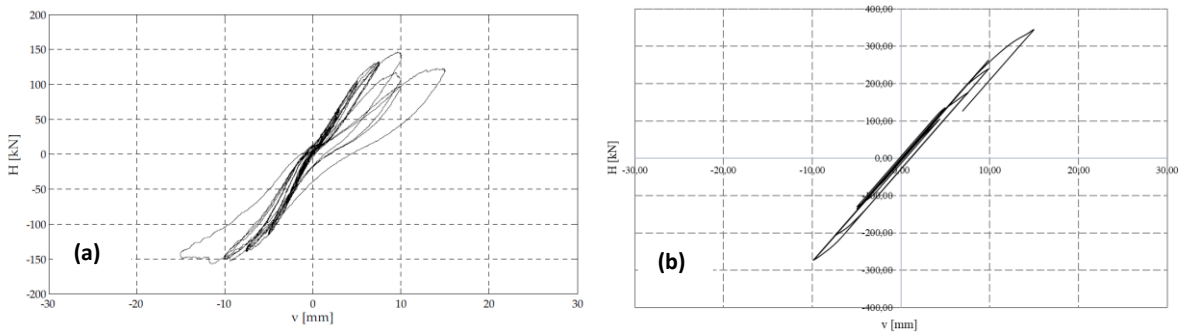

Figure 7. Load-displacement curves: (a) Experiment by Mojsilovic et al. (b) Present numerical model

4. CONCLUSION

In the masonry modeling technique presented in this study, masonry units and mortar are modeled separately but the interfaces between the bricks and mortar are bonded to the materials. It can be said that; the model can represent the nonlinear behavior of masonry wall under cyclic loading efficiently. Stress and strains values can be obtained successfully for the detailed analyses of masonry walls. The plastic strain values also state the information about the collapse mechanism of the wall. The wall failure from the compression at the corners of the wall. It can be emphasized from the hysteresis curve in early stages of the analysis, the structural behavior of the wall is compatible with the experimental values, but the model shows higher results at large amplitude levels of loading in terms of lack of ductility and complexity of the material behavior at that level of the experiment. In conclusion, to provide better understanding both for strengthening of old masonry structures and construction of modern masonry buildings, new modeling techniques as presented in this study should be performed.

REFERENCES

Abdulla K.F, Cunningham L.S, Gillie M (2017). Simulating masonry wall behavior using a simplified micro-model approach. *Engineering Structures*, **151**, 349-365.

ANSYS 18.0 (2018). Element reference. U.S.A.

Kömürcü S, Gedikli A. (2017). Numerical modelling of the in-plane loaded homogenized masonry walls. *Periodicals of Engineering and Natural Sciences* **5(3)**, 314-321.

Lourenço P.B (1995). An Orthotropic Continuum Model for The Analysis of Masonry Structures, Report 03-21-1-31-27, TU Delft, The Netherlands.

Mojsilovic´ N, Simundic G, Page A (2009). Static-cyclic shear tests on masonry wallets with a damp-proof course membrane, vol. 319. ETH, Zurich.

Nasiri E, Liu Y, (2017). Development of a detailed 3D FE model for analysis of the planar behavior of masonry infilled concrete frames. *Engineering Structures*, **143**, 603–616.

Oliviera C (2003). Experimental and Numerical Analysis of Blocky Masonry Structures under Cyclic Loading, Phd. Thesis, Universidade do Minho, Portekiz,

Oller S. (2014). Numerical Simulation of Mechanical Behavior of Composite Materials. Springer, Barcelona, Spain.

Pela L, Cervera M, Roca P (2012). An orthotropic damage model for the analysis of masonry structures. *Construction and Building Materials*, **41**, 957-967.

Quinteros R, Oller S, Nallim L (2011). Nonlinear homogenization techniques to solve masonry structures problems. *Composite Structures* **94**, 724–730.

Vermeltfoort A.Th, Raijmakers T.M.J (1992). Deformation controlled meso shear tests on masonry piers. Report B-92-1156, TNO-BOUWrrU, Building and Construction Research, Eindhoven, The Netherlands.

SİSMİK TABAN İZOLATÖRLÜ YAPILARIN SİSMİK DAVRANIŞININ DALGACIK DÖNÜŞÜMÜ İLE İNCELENMESİ

Kandemir Mazanoğlu E.Ç. [1,2] ve Kara E. [3]

[1] *Doç. Dr., İnşaat Müh. Bölümü, Uşak Üniversitesi, Uşak*
[2] *Deprem Uygulama ve Araştırma Merkezi, Uşak Üniversitesi, Uşak*
[3] *İnş. Müh., Uşak Valiliği Çevre ve Şehircilik İl Müdürlüğü, Uşak*
Email: elif.kandemir@usak.edu.tr

ÖZET:

Bu çalışmada farklı periyoda sahip sismik taban izolatörlü bina türü yapıların dalgacık dönüşümü ile analizi yapılarak deprem altıdaki davranışları incelenmiştir. Dalgacık dönüşümü ile, zaman tanım alanında elde edilmiş yapısal sinyaller frekans tanım alanında irdelenebilmektedir. Böylece hem uzun zaman aralığında hem de kısa zaman aralığında alçak ve yüksek frekans bilgisi elde edilebilmektedir. Dalgacık dönüşümü ile, Fourier dönüşümden farklı olarak frekans-zaman bilgisi sunulmaktadır. Sismik taban izolatörleri yapıların taban seviyesinde yatayda rijitliklerini azalttığı için doğal frekanslarını küçülten bir etki yaratmaktadır. Bu durum taban seviyesindeki yatay yer değiştirmelerin artmasına yol açarken, katlar arası yer değiştirmeleri etkili bir biçimde azaltmaktadır. Çalışmada, çeşitli yükseklikteki bina türü yapıların sismik taban izolatörlü ve izolatörsüz davranışları dalgacık dönüşümü yardımıyla frekans tanım alanında analiz edilmiştir. Modellemeler ve analizler MATLAB programı kullanılarak gerçekleştirilmiştir. Binaların yer değiştirme tepkilerinin sürekli dalgacık dönüşümü yapılarak, izolatör periyodunun ve binanın kat yüksekliğinin frekans içeriklerine etkileri yorumlanmış ve sismik taban izolatörü kapasitesinin tayini üzerinde durulmuştur.

ANAHTAR KELİMELER: Dalgacık dönüşümü, sismik taban izolatörü, deprem.

INVESTIGATION OF THE SEISMIC BEHAVIOR OF SEISMIC BASE ISOLATED STRUCTURES BY WAVELET TRANSFORM

ABSTRACT:

This paper analyzes the seismic behavior of building type structures with base isolation systems with various periods by wavelet transforms. By wavelet transform, structural signals obtained in the time domain can be examined in the frequency domain. Thus, both low and high frequency information can be obtained both in the long time interval and in the short time interval. With wavelet transform, frequency-time information is presented, unlike the Fourier transform. Seismic base isolators create an effect which reduces the natural frequencies of structures as they decrease the rigidity in the base level. This leads to an increase in the horizontal displacements at the base level, however, interstorey displacement decrease dramatically. In this study, seismic base isolated and non-isolated seismic behaviors of buildings of various heights were analyzed in the frequency domain by means of wavelet transform. Models and analyses are constituted in the MATLAB environment. By doing wavelet transform of displacement responses of buildings, the effects of isolator periods and storey numbers on frequency contents are interpreted in addition to emphasizing on determination of the seismic base isolator capacity.

KEYWORDS: Wavelet transform, seismic base isolator, earthquake.

1. GİRİŞ

Ülkemizin büyük bir kısmının aktif faylara ev sahipliği yapmakta olduğu bilinmektedir. Şiddetli depremler sonucu büyük oranlarda can ve mal kayıplarının meydana gelmesi, zaman içinde ülkemizde de deprem yüklerini azaltan sismik taban izolatörlerinin kullanımını yaygınlaştırmaya başlamıştır. Sismik taban izolatörleri yapılara yatayda esneklik sağlayarak, yapının frekansını azaltan, bir başka deyişle, yapının doğal titreşim karakteristiklerinde değişikliğe sebep olan bir etki meydana getirmektedir. Taban seviyesindeki düşük rijitlik nedeniyle yapının baskın periyodu, izolatör periyoduna yaklaşmakta ve taban yer değiştirmesi artarken yapı bir bütün halinde ötelenme yapmaktadır (Sarno vd. (2011), FEMA (1997)).

Dalgacık dönüşümü ile zaman serilerinin frekans içerikleri tanımlanabilmektedir ve bunu Fourier dönüşümünden farklı olarak frekans-zaman bilgisi şeklinde sunarak yapmaktadır. Kısa zamanlı Fourier dönüşümüne (KZFD) benzer olarak dalgacık dönüşümünde pencere görevini ana dalgacık denilen bir fonksiyon üstlenir, fakat bu ana dalgacık dönüşüm işlemi süresince hem ölçeklenir (frekansı değiştirilir) hem de ötelenir (zamanı değiştirilir). Ölçekleme dalganın genişletilip daraltılmasına, öteleme ise zaman ekseninde dalganın kaydırılmasına karşılık gelir (Arı vd. (2008)). Fourier dönüşümü bize frekans bilgisini verir, ancak dalgacık dönüşümü frekans-zaman bilgisini verir. Bu da dalgacık dönüşümünü Fourier dönüşümünden daha üstün kılmaktadır. Dalga ve dalgacık birbirinden farklı kavramlardır. Dalga, sinüs dalgası örneğinde olduğu gibi $\pm\infty$ arasında süreklilik içerirken; dalgacık, sınırlı süreli, ortalaması, başlangıç ve bitiş değeri sıfır olan dalga formudur. Dalgacıklar, düzensiz, sınırlı süreli ve asimetrik olduğundan anomali, titreşim ve sinyal içindeki olayları iyi tanımlamaktadırlar.

Çalışmada 1, 5, 10 ve 15 katlı bina tipi yapıların sismik taban izolatörlü ve izolatörsüz deprem davranışları dalgacık dönüşümü metodu ile incelenmiştir. Analizlerde kullanılacak depremler, büyüklüğü 5 ile 8 arasında ve derinliği 10 km'den küçük olan gerçek deprem kayıtları şeklinde seçilmiştir. Ölçeklendirme işlemi deprem yer hareketi düzeyi DD-1 ve yerel zemin sınıf ZA olan bir bölgeye ait elastik tasarım ivme spektrumuna göre yapılmıştır. Ölçeklendirilmiş deprem kayıtları altında, izolatörlü ve izolatörsüz binaların zaman tanım alanında doğrusal dinamik analizi yapılarak katlar arası yer değiştirme değerleri elde edilmiştir. En üst kat yer değiştirme-zaman serileri dalgacık dönüşümü ile frekans-zaman verilerine dönüştürülmüştür. Elde edilen dalgacık dönüşüm grafikleri yardımıyla, sismik izolatörlerin farklı periyotlardaki ve yükseklikteki binaların frekans içeriklerine etkileri gözlemlenmiştir.

2. YÖNTEM

2.1. Deprem kayıtları

Analizler, ölçeklendirilmiş gerçek deprem kayıtları altında gerçekleştirilmiştir. Elastik tasarım ivme spektrumu İzmir iline ait, DD-1 deprem düzeyi, ZA zemin sınıfı ve %5 sönüm oranı esas alınarak Türkiye Deprem haritaları İnteraktif Web Uygulaması kullanılarak oluşturulmuştur (TDTH (2009)). Ölçeklendirme işlemi Peer Ground Motion Database internet sitesinden kullanıcı tarafından tanımlı spektrum ve ortalama hata kareleri sekmeleri seçilerek yapılmıştır. Şiddetleri 5 ile 8 ve derinlikleri 0 ile 10 km arasında olan deprem kayıtları çıkarılmıştır. 2019 Türkiye Bina Deprem Yönetmeliği'ne göre bir ve iki boyutlu analizlerde en az 11 deprem kaydı kullanılması öngörülmüştür. Kullanılan depremler ile ilgili bilgiler Tablo 1'de gösterilmektedir.

Tablo 1. Çalışmada kullanılan deprem kayıtları

Deprem adı	Büyüklük (Mw)	Derinlik (km)	Baskın periyot (Hz)
Düzce, 1999	7.1	2.65	2.36
Christchurch, 2011	6.2	9.06	1.35
Iwate, 2008	6.9	8.44	0.51
Parkfield, 2004	6.0	0.34	1.38
Imperial Valley, 1979	6.5	0.34	1.61
Erzincan, 1992	6.7	4.38	0.56
Dinar, 1995	6.4	3.36	1.16
Chi-Chi, 1999	7.6	5.80	4.03
Darfield, 2010	7.0	1.54	0.77
Tottori, 2000	6.6	6.88	0.93
San Salvador, 1986	5.8	6.99	1.38

2.2. Sismik taban izolatörleri

İzole edilmiş binaların dinamik analizi için izolasyon sistemi doğrusal viskoelastik davranış ile modelleniyorsa doğrusal analizler yapılabilir. Bu durum lamine elastomerik mesnetler için geçerlidir. Taban izolatörü tarafından üretilen kuvvet, F_b , doğrusal yayın ve sönümlemenin paralel etkisidir (Muthukumar ve DesRoches (2006)):

$$F_b = c_b \dot{x}_b + k_b x_b, \tag{1}$$

burada c_b izolatör sönüm katsayısı, k_b izolatörün rijitliğidir. $\dot{x}_b$ tabanın hız tepkisidir. Yatay rijitlik, taban izolatörünün periyodu (T_b) ve sönüm oranı (ξ_b) gibi önceden belirlenmiş parametrelere göre belirlenir (Chopra (2015)):

$$T_b = 2\pi\sqrt{\frac{M_T}{k_b}}, \tag{2}$$

$$\xi_b = \frac{c_b}{2M_T \cdot \omega_b}, \tag{3}$$

burada M_T izolatörler üzerindeki üst yapının toplam kütlesini, ω_b izolatörün açısal frekansını temsil etmektedir. 2π / T_b ‘den bulunmaktadır (Chopra (2015)):

Şekil 1’deki gibi n katlı, yatay yönde yer değiştirme serbestliğine sahip izolatörlü bir binanın hareket denklemi,

$$[M]\{\ddot{x}\} + [C]\{\dot{x}\} + [K]\{x\} = -\ddot{x}_g[M]\{1\} \tag{4}$$

ile gösterilir. Matrislerin boyutları izolatör ile birlikte $(\mathrm{n}+1) \times (\mathrm{n}+1)$ olur. Burada $[M]$ kütle matrisi, $[C]$ sönüm matrisi, $[K]$ ise rijitlik matrisi olup, $\{1\}$ vektörü $\mathrm{n}+1$ satırdan oluşan birim vektör olmak üzere, $\{x\}$, $\{\dot{x}\}$ ve $\{\ddot{x}\}$ sismik izolasyonlu yapının; rölatif yer değiştirme vektörü, hız vektörü ve ivme vektörüdür. $\ddot{x}_g$ de deprem ivmesini göstermektedir. b alt indisi taban izolatörünü simgelemektedir.

Çalışmada 1 sn, 2 sn ve 3 sn'lik periyotlara ve %10 sönüm oranına sahip sismik izolatörler eklenmiştir. Böylelikle çeşitli rijitlikteki izolatörler etkisindeki yapıların sismik davranışları elde edilmiştir.

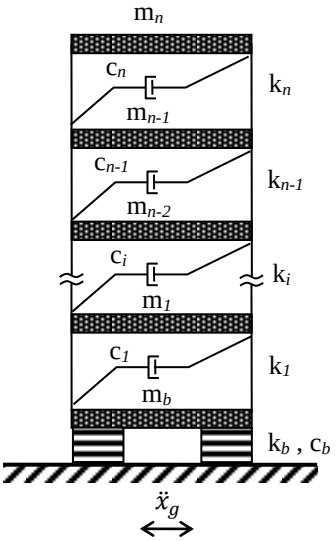

Şekil 1. Sismik taban izolatörlü n katlı bina

2.3. Dalgacık dönüşümü

Zaman tanım alanında $f(t)$ sinyalinin sürekli dalgacık dönüşümü;

$$W(a,b) = \frac{1}{\sqrt{a}} \int_{-\infty}^{\infty} f(t) \psi^* \left(\frac{t-b}{a}\right) dt \tag{5}$$

ile ifade edilir. Burada a ve b değerleri ölçek ve yerdeğiştirme parametreleri olup, $\psi^*(\cdot)$ ana dalgacık fonksiyonu $\psi(\cdot)$'nun karmaşık eşleniğidir. a parametresi dalgacık fonksiyonunu genişletirken, b parametresi fonksiyonun zaman tanım alanında ötelenmesini sağlamaktadır. Dalgacık fonksiyonları ayrık ve sürekli olabilmektedir. Sürekli dalgacık fonksiyonları sismik olayları analiz etmede daha efektif olup, sürekli dalgacıklardan bazıları Şekil 2'de gösterilmiştir.

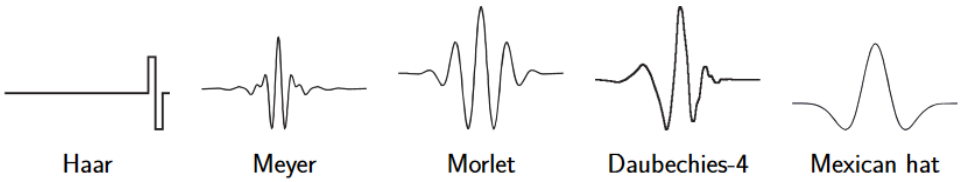

Şekil 2. Dalgacık fonksiyonları

3. ÇALIŞMANIN BULGULARI

Binalar kesme tipi yapı olarak ele alındığı için toplanmış kütle modelleri oluşturulmuştur. Çalışmada kat kütleleri $m = 1 \times 10^5 kg$ ve kat rijitlikleri $k = 6{,}8 \times 10^7 N/m$ olup 1, 5, 10 ve 15 katlı yapılar olarak tasarlanmıştır. Deprem davranışları, zaman tanım alanında veri elde edilmesine olanak sağlayan Newmark-β nümerik metoduyla analiz edilmiştir. Dalgacık dönüşümü de dahil olmak üzere, modellemeler ve yapısal dinamik analizler MATLAB ortamında gerçekleştirilmiştir. Sismik verilerde etkili dönüşüm sağlayan dalgacık fonksiyonu olarak Morlet fonksiyonu kullanılmıştır.

Seçilen deprem kayıtları altında yapılan analizler sonucunda benzer grafikler elde edilmiştir. Bu nedenle, yalnızca Düzce depremine ait sonuçların grafikleri verilmiştir. Şekil 3, Düzce depremi altında izolatörsüz ve 1 sn, 2 sn ve 3 sn periyotlu izolatörlü yapıların en üst kat rölatif yer değiştirmelerinin dalgacık dönüşümlerini göstermektedir. Grafiklerden görüldüğü üzere izolatör periyodu arttıkça enerji yığılmaları genişlemektedir. Beklenildiği üzere, sismik izolatörler yapının frekans değerini azaltan etkiye sahip olduğundan, grafiklerde frekans değerlerinin ölçek ile ters orantılı olarak azaldığı sonucu elde edilmiştir.

Her ne kadar, izolatör periyodunun artmasıyla katlar arası yer değiştirme tepkileri azalsa da enerji yığılmalarının arttığı dalgacık dönüşüm grafiklerinden gözlenmektedir. Aynı sonuç kat sayısının artmasıyla da elde edilmektedir. Tüm depremler altında, yer değiştirme tepkilerinin sürekli dalgacık dönüşümleri incelendiğinde, izolatör periyodu 1 sn olduğunda, yapıda enerji yığılmalarının daha makul bir seviyede kaldığı anlaşılmaktadır.

4. SONUÇLAR

Sismik taban izolatörlerinin yapının katlar arası yer değiştirme tepkilerini önemli ölçüde azalttığı bilinmektedir. Yer değiştirme-zaman serileriyle bu değişimi gözlemek mümkündür. Ancak frekans bileşenlerinin zaman parametresine bağlı olarak değişimini gözlemek ancak dalgacık dönüşümü ile mümkün olmaktadır.

Frekans içeriklerinin karmaşık ve çok olduğu doğrusal olmayan sistemlerde, dalgacık dönüşümü frekans-zaman bilgisi sağlaması bakımından sıklıkla kullanılan bir yöntem haline gelmiştir. Bu çalışmada, dalgacık dönüşümünün deprem mühendisliği alanındaki yeni bir uygulaması sunulmaktadır. Analizler sonucunda frekans içeriklerinin kat seviyelerine ve izolatör periyotlarına göre değişimleri elde edilmiştir. Böylelikle değişken yapısal parametreler altında optimum izolatör kapasiteleri ile ilgili değerlendirmelerde bulunulabilmesi açısından, araştırmacılara kaynak teşkil edebileceği düşünülmektedir.

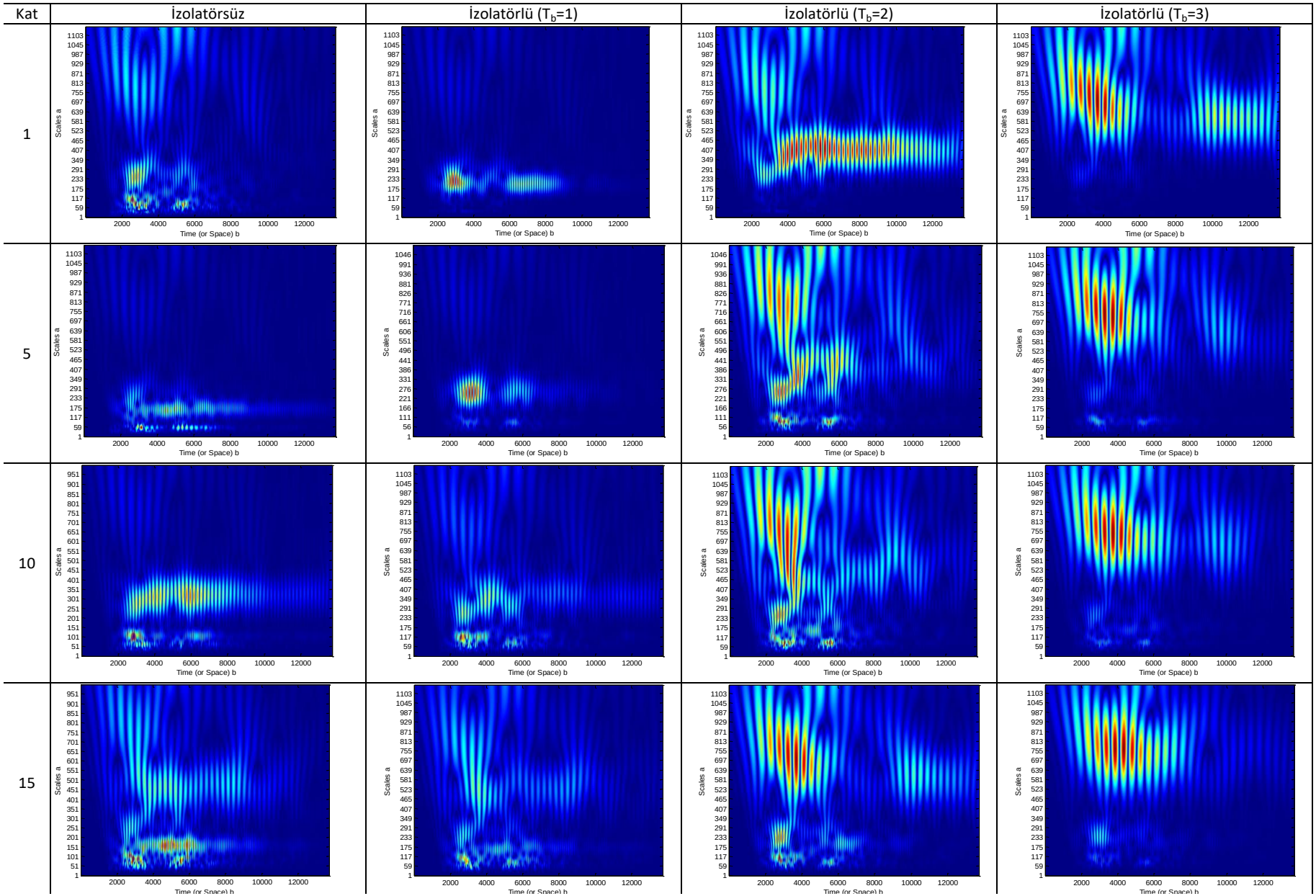

Şekil 3. Düzce depremi altında en üst kat yer değiştirme tepkilerinin dalgacık dönüşümleri

KAYNAKLAR

Arı N, Özen S, Çolak Ö H (2008). Dalgacık Teorisi, Palme Yayıncılık,Ankara.

Chopra AK (2015), Earthquake Dynamics of Base-Isolated Buildings, Dynamics of Structures 4th ed., Prentice Hall, California.

Di Sarno L, Chioccarelli E, Cosenza E (2011). Seismic response analysis of an irregular base isolated building, *Bulletin of Earthquake Engineering* **(9)**: 1673–1702 (İngilizce)

Federal Emergency Management Agency (FEMA) (1997). NEHRP guidelines for the seismic rehabilitation of buildings, Rep. No. 273/274, Building Seismic Safety Council, Washington D.C.

Muthukumar S, DesRoches R (2006). A Hertz Contact Model with Non-linear damping for Pounding Simulation, *Earthquake Engineering & Structural Dynamics* **(35)**: 811-828 (İngilizce)

Türkiye Bina Deprem Yönetmeliği (TBDY) (2019). Ankara, Türkiye.

Türkiye Deprem Tehlike Haritaları, https://tdth.afad.gov.tr/TDTH/main.xhtml

HASTANE BİNALARINDA SİSMİK İZOLASYON SİSTEMLERİNİN KULLANIM KARARININ BİNA ÜRETİM SÜRECİNE ETKİLERİ

Bakkaloğlu E.[1], Taş E.[2]

[1] *Y.Mimar, Elif Bakkaloğlu, İstanbul Teknik Üniversitesi, Mimarlık Anabilim Dalı, Proje ve Yapım Yönetimi Y.L. Programı, İstanbul,*
[2] *Prof. Dr„Elçin Taş , İstanbul Teknik Üniversitesi, Mimarlık Anabilim Dalı, Proje ve Yapım Yönetimi Y.L. Programı, İstanbul,*

ÖZET:

Dünya'da depremlerden yıkılan binaların neden olduğu kayıplar gün geçtikçe artmaktayken ekonomik kayıpların ve evsiz kalan insanların yanı sıra can kayıpları her geçen gün yükselmektedir. Bilindiği üzere ülkemizin de büyük bir kısmı deprem bölgesindedir. Önemli ticaret ağları ve finans merkezleri bu deprem bölgelerinde yer almaktadır. 1.derece fay hattı üzerinde olan ülkemizde de depreme karşı alınan önlemler hızla gelişmektedir. Kalkınma ve gelişme politikası olarak birçok bölge kendi projesini geliştirirken bütün binalarda depreme karşı önlemler alınması hedeflenmektedir. Özellikle depremlerde kesintisiz hizmet vermesi gereken kamu binalarında sismik yalıtım ayrı bir önem kazanmaktadır. Örneğin İstanbul'da afet hazırlık projesi kapsamında hastane binaları gibi birçok kamu binası depreme karşı yalıtımlı hale getirilmektedir. Bu bağlamda çalışmada öncelikle depremden yıkılan binaların neden olduğu kayıpları azaltmak için alınan bölgesel önlemler incelenmiş olup, sismik izolasyonun gerekliliği ve türleri incelenmiştir. Çalışmada daha sonra sismik izolasyon yöntemlerinin Dünya'da ve Türkiye'deki örnekleri incelenmiş ve karşılaştırılmıştır. Özellikle hastane binalarında sismik izolatör kullanımı barındırdığı pahalı ekipmanlar ve sunduğu hizmetin deprem anında da devam etmesi için ayrı bir önem taşımaktadır. Depreme karşı hazırlanan stratejiler yönetmeliklerle de desteklenmekte, 2013 yılında yayınlanan genelge ile 100 yataklı ve üzeri hastane binalarında sismik izolatör kullanımı zorunlu hale getirilmektedir. Bu çalışmada, sismik izolatör kullanım kararı verilen hastane binalarının projelerinde sismik izolatör kullanım kararının verilmesinin bina üretim sürecinin alt evrelerine olan etkisi, izlenmesi gereken adımlar, bu süreçlerde karşılaşılan problemler ve bu problemlerin çözümüne ilişkin alınması gereken önerilerinin ortaya konulması amaçlanmaktadır. Bu çalışma da söz konusu hedefe İstanbul'da sismik izolatör kullanılarak yapımı tamamlanmış/tamamlanmakta olan 5 adet büyük ölçekli hastane binasının bina üretim süreçleri incelenerek ve uzmanlarından görüş alınarak ulaşılacaktır.

ANAHTAR KELİMELER: Deprem, Hastane binaları, Sismik izolatör, Bina Üretim Süreci.

IN THE HOSPITAL PROJECTS SEISMIC ISOLATOR USE, THE IMPACT OF THE DECISION TO USE SEISMIC ISOLATORS ON THE BUILDING PRODUCTION PROCESS

ABSTRACT:

The use of seismic isolation plays an important role in the buildings needed to provide uninterrupted service, especially in hospital buildings. In Istanbul, many public buildings such as hospitals are made insulated against depression. In Turkey, In this context, firstly, the regional measures taken to reduce the losses caused by earthquake-prone buildings have been examined and the necessity and types of seismic isolation have been investigated. In particular, the use of seismic isolators in hospital buildings is of special importance for expensive equipment and service provided during the earthquake. In this study, the seismic isolation in the world

and after examining the samples are compared in Turkey. Deciding of using seismic isolation in a building is closely related with sub-phases of building construction which are enterprise/design/contract/construction/usage. There is a difference between taking the seismic isolator decision to use the building production process in the intervention phase or later in the use phase, and the building production process is affected by this decision difference. In this study, In the hospital projects in which seismic isolator use decision, the impact of the decision to use seismic isolators on the sub-phases of the building production process, the problems encountered in this process and suggestions for solutions to these problems. The aim will be reached by reviewing the building production processes of 5 large scale hospital buildings completed/completed using seismic isolators in Istanbul and by consulting experts working in these projects. Seismic isolators should be used and disseminated not only in hospital buildings but also in all other important buildings. But nowadays seismic isolators use studies in Turkey are usually about to the hospital buildings. Despite the fact that the use of seismic isolators is in our country is becoming more widespread lately than other countries, today our country has reached to the point where the biggest seismic isolator building of our country, especially the health sector and construction sector, is made. The impact of building seismic isolator use decision on the building production process during the intervention phase and during the use phase was evaluated within the scope of hospital samples. As a result, the issues to be considered in the seismic isolator building process are listed step by step in terms of creating a guiding resource for the architecture. Finally, seismic isolators are listed step by step in terms of establishing a guiding resource for the building process.

KEYWORDS: Earthquake, Hospital buildings, Seismic isolator, Building Production Process.

1. GİRİŞ

Her geçen gün Dünya'nın çeşitli yerlerinde birçok insan depreme karşı dayanıksız yapılar nedeniyle hayatını kaybetmektedir. Deprem sonucunda ortaya çıkan kayıplar insanlar üzerinde ciddi sosyal, ekonomik ve kültürel açıdan olumsuz etkiler bırakmaktadır. Ancak doğru yapılaşmayla bunun önüne geçilebileceği gibi önce deprem, depremin etkileri ve depreme karşı alınması gereken önlemler doğru tanımlanmalıdır. Bilindiği üzere ülkemiz büyük çoğunluğu deprem bölgesinde olan bir ülkedir. Bu nedenle çalışmada depremde yıkılan binaların sebep olduğu can kayıplarını azalması için depreme karşı dayanıklı binaların yapımında sismik izolatör kullanım kararının bina üretim sürecine etkilerinin tespit edilmesi hedeflenmiştir.
Dünya'nın farklı yerlerinde son 100 yılda meydana gelen birçok depremde farklı ülkelerden yüz binlerce kişi hayatını kaybetmiş, yüz binlerce insan da evsiz kalmıştır. Depremin en yaygın olduğu ülkelerden ABD, Japonya ve İtalya gibi ülkelerin kayıpları azaltmak için izlediği politikalar, oluşturdukları programlar ve kuruluşlar bulunmaktadır. Japonya'da gelişen inşaat teknolojisi sayesinde yıkılan bina sayısının az olması dolayısı ile ölen insan sayısının az olması ve ülke ekonomisine getirdiği kazanç sismik koruma yöntemlerinin önemini açıkça ortaya koymuştur (Fujia, 1997).

2. HASTANE BİNALARINDA SİSMİK İZOLASYON SİSTEMLERİNİN KULLANIM KARARI

Depremden sonra ilk kullanılacak binalardan biri olan hastane binalarında sismik riskin azaltılması göz önünde bulundurulması gereken en önemli hususlardan biridir.
Hastane binalarında kesintisiz kullanım ihtiyacı; deprem sonrasında hastane binalarının kullanılamaması, toplumsal sağlık açığının artması anlamına gelmektedir. Depremde hastane binalarının yıkılmasıyla can ve mal kayıpları yaşanacak, deprem sonrasında alınması gereken sağlık hizmetinde aksamalar meydana gelecektir. Bu sebeple deprem anında kesintisiz hizmet vermesi gereken hastane binalarında ancak sismik önlemlerin alınmasıyla can ve mal kayıplarını önüne geçilebilmektedir.
Sağlık Bakanlığı'nın yayınladığı genelge ile gelen kullanım zorunluluğu; Türkiye'de sismik izolatörlerin kullanımı yönetmelik ve şartnamelerle de desteklenmekte 2013 yılında yayınlanan 'Sağlıkta Dönüşüm Projesi Kapsamında Yapılacak Sağlık Tesisleri İçin Proje Aşamasında Uyulması Gereken Hususlar 'konulu genelgede

bulunan '1. ve 2. deprem bölgelerinde 100 yatak ve üzeri hastanelerin taşıyıcı sistemleri sismik izolatörlü olarak projelendirilecektir. 'maddesi uyarınca ile 100 yataklı ve üzeri hastane binalarında sismik izolatör kullanımı zorunlu hale getirilmiştir.

Yapısal olmayan elemanlar; Eşya/İşlev Kayıpları; Yapısal olmayan elemanlar; olarak değerlendirilen ekipman ve malzemelerin korunmasıyla ilgili risk değerlendirmesi yapıldığında ise yaşam kayıpları, mal kayıpları ve işlev kaybının yaşandığı gözlemlenmektedir. İşlev kayıpları konusunda depremden sonra ekipmanların zarar görmesi işlevin aksamasına neden olmaktadır. Yapısal olmayan elemanlardan dolayı hem pahalı hem de insan sağlığını etkileyen unsurlar hastane binalarında sismik önlem almanın önemini daha da artırmaktadır (FEMA, 2010).

Veysel Doğan sismik izolasyonun depremden hemen sonra da işlevsel olduğunu Van depremi örneğinde açıklamıştır. Van depreminde hastanenin yıkılmamasına karşın içindeki cihazların hasar görmesi nedeniyle hastanenin çalışamadığı gözlemlenmiştir. Sismik izolasyon deprem şiddetini 10 kat azalttığı için binadakilerin depremi çok hafif hissettiğini ve bu teknolojinin hastane okul gibi binalarda mutlaka kullanılması gerektiğini ifade eden Doğan maliyetin yeni yapılan binalarda %3-10 arasında artırdığını mevcut binalarda ise biraz daha fazla artırdığını eklemiştir (Deprem İzolasyon Derneği, 2017). Yalnızca hastane binalarında değil tüm büyük ölçekli ve önemli binalarda depreme karşı önlem alınması gerekirken günümüzde hastane binalarında yapılan deprem önleme çalışmalarını hız kazanmıştır.

3. HASTANE BİNALARINDA SİSMİK İZOLASYON KULLANIM KARARININ BİNA ÜRETİM SÜRECİ BOYUNCA ALINAN KARARLARA ETKİLERİ

Sismik izolatör kullanım kararının bina üretim süreci ve alt aşamalarında alınan kararlara olan etkileri Türkiye'deki 5 farklı hastane projesi kapsamında incelenmiştir. 5 hastane projesinin 4'ü yeniden yapım projesi olmakla birlikte 1'i güçlendirme projesidir. Çalışma kapsamında ele alınan hastanelerin biri Dünya'nın en büyük sismik izolatörlü binası olma özelliği taşımaktadır. Bu bağlamda farklı ölçeklerde ve büyüklüklerde hastaneler ele alınmış olup sismik izolatör kullanım kararının sürecin başında girişim &fizibilite aşamasında alınmasıyla kullanım aşamasında alınmasındaki farklılığın oluşturduğu etkileri incelenecektir.

Çalışmanın bu kısmında İstanbul'da Okmeydanı Eğitim ve Araştırma Hastanesi, Göztepe Eğitim ve Araştırma Hastanesi, İkitelli Entegre Sağlık Tesisi, Kartal Eğitim ve Araştırma Hastanesi ve Marmara Üniversitesi Başıbüyük Eğitim ve Araştırma Hastanesi'nde sismik izolatör kullanım kararının bina üretim sisteminin alt aşamalarına etkileri incelenmiştir.

3.1. Hastanelerde sismik izolasyon örnekleri kapsamında sismik izolatör kullanım kararının bina üretim sürecine etkilerinin incelenmesi

Çalışmada problem tespit edilirken sismik izolatör kullanım kararının mimari ve yapısal unsurları nasıl etkilediğine dair bir araştırma yapılmıştır. Türkiye Sağlık Bakanlığı'nın getirdiği genelgeye ve ulusal-uluslararası yönetmeliklere bağlı olarak mimari ve yapısal unsurların nasıl değiştiği incelenmiş, sismik izolatör kullanım kararında bina üretim sürecinin nasıl değerlendirildiğini incelemek için 44 soruluk soru grubu oluşturulmuştur. Bu sorular 3 grupta toplanmış olup, birinci grupta demografik sorularla (6) anket uygulanan kişiler hakkında bilgi edinilmesi amaçlanmıştır. İkinci grupta projesel sorular (34) ile sismik izolatör kullanım kararının bina üretim sürecinin girişim, planlama, tasarım, yapım ve kullanım aşamalarına etkisinin tespit edilmesi amaçlanmıştır. Üçüncü grup olan mülakat sorularında ise sismik izolatör kullanım kararı verilen binaların üretim süreçlerinde karşılaşılan sorunların tespiti ve çözüm önerileri sunulmasına ilişkin katılımcılara 4 soru sorulmuştur. Çalışma yapılırken konuyla ilgili sismik izolatör kullanım kararında etkili olan mal sahibi temsilcileri ve tasarım yapım aşamasında rol alan aktörlerle konunun dağılmasını önlemek adına ucu açık yarı yapılandırılmış ve yüzyüze görüşülmüştür. Bina üretim sürecinin sismik izolasyon kullanım kararında rol alan ve uygulanmasının gerekli olduğunu düşünen kişiler görev aldıkları projelerde, teknik ofis mühendisleri, müdürleri ve dizayn ofis müdürü, proje müdürü veya deprem mühendisi ünvanlarıyla üst düzey karar verici olarak rol almaktadırlar.

Şekil 3.Değerlendirilen projeler

Okmeydanı Eğitim ve Araştırma Hastanesi; İstanbul'un merkezinde yer aldığından mevcut hastane işlerken devam edilen inşaat yapım süreci 2 faz halinde yapılmaktadır. Yeniden yapımı tamamlandığında 1089 yataklı olacak hastane binası 250.400 m^2 kapalı inşaat alanı sahiptir. 506 adet 3'lü sarkaç sistem izolatörün kullanıldığı binada izolatörler temel üstü olan 3.bodrum katta yer almaktadır. Arazi eğimli olması bu hastane binasını değerlerinden ayıran en önemli unsurların başında gelir. İzolatörlerin bulunduğu kat otopark olarak kullanılmaktadır.

Şekil 4.Okmeydanı Eğitim ve Araştırma Hastanesi Cephesi

Göztepe Eğitim ve Araştırma Hastanesi; Yapımına devam edilen ve açıldığında 1000 yatak kapasitesine sahip hastane 257.696 m^2 kapalı inşaat alanına sahiptir. 503 adet 3'lü sarkaç sistem tipinde izolatörlere sahip olan binada izolatörler temel üstü kotta yer almaktadır. Proje müellifi ve yüklenici firmaların aynı olması, bina üretim süreçlerinin paralel gitmesi nedenleriyle bu hastane projesi Okmeydanı Hastane binası ile benzerlik göstermektedir.

Şekil 5.Göztepe Eğitim ve Araştırma Hastanesi Cephesi

İkitelli Entegre Sağlık Tesisi; Yapımına devam edilen diğer bir hastane binası olan 2682 yataklı hastaneler kompleksi 1.000.000 m^2 inşaat alanına sahiptir. 1000 adet 3'lü sarkaç sistem kullanılmış olup proje tamamlandığında 'Dünya'nın En Büyük Sismik İzolatörlü Binası' ünvanına sahip olması beklenmektedir. Bina formunun sade ve kare olması sismik izolatörün bina formuna etkisinin bir göstergesi olarak görülmektedir.

Şekil 6.İkitelli Entegre Sağlık Tesisi

Kartal Prof. Dr. Lütfi Kırdar Eğitim ve Araştırma Hastanesi; Kullanıma açılmış olan bu hastane binası 920 yataklı olup 323.000 kapalı inşaat alanına sahiptir. Hastane binası 855 adet 3'lü sarkaç sistem izolatöre sahip olup izolatörler temel üstü kotta konumlandırılmıştır. İzolatörlerin bulunduğu bu kat izolatörlerin bakım onarımı dışında kullanılmamaktadır.

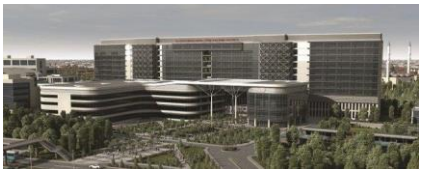

Şekil 7. *Kartal Prof. Dr. Lütfi Kırdar Eğitim ve Araştırma Hastanesi*

Marmara Başıbüyük Eğitim ve Araştırma Hastanesi; Bu hastane binasını diğer projelerden ayıran en temel nokta sismik izolatör kullanım kararının bina üretim sürecinin girişim aşamasında değil, kullanım aşamasında alınmasıdır. Diğer projelerde girişim aşamasında bu karar alındığından bina üretim süreci bu projeden farklı ilerlemiştir. Bu hastane binasında güçlendirme projesi kapsamında izolatörler sonradan mevcut binaya entegre edilmiştir.750 yataklı bu hastane binası yeniden kullanıma açılmış olup 112.440 m^2 kapalı inşaat alanına sahiptir. Güçlendirme projesinde 362 adet kurşun çekirdekli, 326 adet tekli sarkaç sistem izolatör kullanılmış olup izolatörler zemin altı katta kullanılmıştır. İzolatör katı poliklinik, doktor odası gibi günlük kullanıma uygun işlevlerle değerlendirilmektedir.

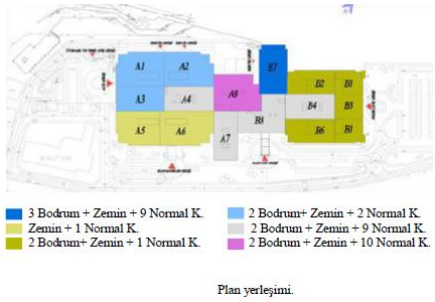

Şekil 8. Marmara Başıbüyük Eğitim ve Araştırma Hastanesi

3.2. Hastane binalarında sismik izolasyon örnekleri kapsamında sismik izolatör kullanım kararının bina üretim sürecinde alınan kararlara etkilerinin incelenmesi

Bina üretim sistemi bina ihtiyacının doğması, ardından bina üretim sisteminin gerçekleşmesi ve binanın meydana gelmesiyle üç ana evreden oluşmaktadır. Şekil 9'da da görüldüğü gibi bina üretim süreci girişim & fizibilite, planlama, tasarım, yapım (uygulama) ve kullanım olmak üzere beş ana alt başlıktan meydana gelmektedir. Ancak sismik izolatörlü bir bina üretim sürecinde tasarım önemli bir karardır ve bina üretim sürecinin tüm aşamaları etkiler. Bu nedenle bu hastane binalarında sismik izolatör kullanım kararının bina üretim sürecini ve alınan kararlar üzerindeki etkileri aşağıda belirtilmektedir.

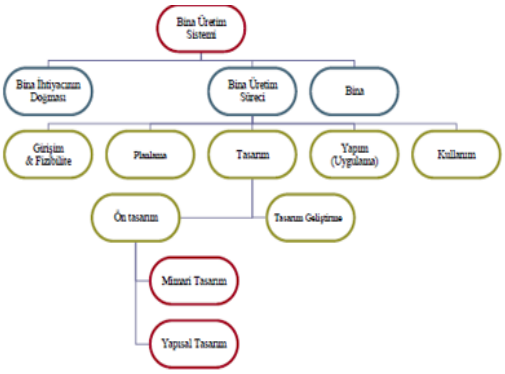

Şekil 9. Bina üretim sistemi aşamaları

3.2.1 Sismik izolatör kullanım kararının 'Girişim&Fizibilite'aşamasına etkisi

1.derece deprem bölgesinde 100 ve üzeri yataklı hastane binalarında sismik izolatör kullanımı girişim aşamasında yönetmeliklerce zorunlu kılındığı için tercihe bağlı bırakılmamıştır. Anket uygulanan uzmanlarca görüşüldüğü üzere 2013'ten sonra yapılan 4 hastane binasında da kullanımı zorunlu olduğu için sismik izolatör kullanım kararı tasarım aşamasından önce alınmıştır. 1 projede yapımı tamamlanmış ve kullanılmakta olan hastane projesinde güçlendirme amaçlı kullanılmıştır. Bina üretim sürecinin ilk aşaması olan girişim aşamasında bu kararın alınması bina üretim sürecinin daha sağlıklı ilerlemesine katkı sağlamıştır.

3.2.2 Sismik izolatör kullanım kararının 'Planlama' aşamasına etkisi

Çalışma kapsamında incelemeye alınan hastane binası projelerinden sorumlu kişiler projelerin 4'ünde planlamanın etkilendiği belirtilmiş olup genel fikir sismik izolatör kullanım kararı sebebiyle ortaya çıkan ilave imalatların bu aşamada öngörülmesi gerektiği yönündedir. Dolayısıyla sismik izolatör kullanım kararının planlama aşamasını sismik izolatör kullanım kararının binanın mimari ve yapısal tasarımını etkileyecek unsurlarının öngürülüp planlaması şeklinde etkiler. İncelenen projelerde planlama aşamasının doğru bir şekilde ilerlemesi için de mimar ve mühendislerin iş birliği içinde çalışmasıyla bu ilave imalatlar iş programına katılmıştır. Bunun sebebi sismik izolatör kullanımı sadece başlı başına bir imalat olmamasıdır. Sismik izolatör kullanım kararının gerektirdiği diğer mimari-statik ve elektromekanik imalatlar bu aşamalarda öngörülmüş bu sayede proje süresi bütün projelerde doğru tahmin edilmeye çalışılmıştır.

3.2.3 Sismik izolatör kullanım kararının 'Tasarım' aşamasına etkisi

Sismik izolatör kullanım kararının en çok etkili olduğu bina üretim süreci tasarım aşamasıdır. Sismik izolatör kullanım kararı alınan bir binada gerek statik tasarım gerekse mimari tasarım binanın formunu yerleşimini etkilendiğinden ve bina üretim sürecinin süre ve maliyet açısından en büyük paydaşlarından biridir.

Sismik izolatör kullanılan hastane projelerinde bina formu uniform, simetrik ve düz (kare, dikdörtgen planlı) olarak seçilmiştir. Marmara Üniversitesi Başıbüyük Hastanesi güçlendirme projesi olduğu için tasarım aşamasında sismik izolatörlü bina tasarımına dikkat edilmemekle birlikte bina formuna genel olarak bakıldığında kareye yakın bir form olduğu belirtilmektedir.

Çalışmaya katılan diğer inşaat projeleri incelendiğinde İkitelli hastane planının dikdörtgen formlu olduğu, diğer hastane binalarının kare formlu olmasa da simetrik formlarda olduğu gözlemlenmiştir. İzolatörün kullanıldığı kat kararına göre ilave bodrum kat gerekebilir ve önerilmektedir. Çalışmaya katılan hastanelerin projelerinde de izolatörler temel üstü kotunda ilave bir bodrum katla tasarlanmıştır. Ancak sadece güçlendirme projesi olan Marmara Üni. Başıbüyük Hastanesinde farklı bodrum kat sayıları belirtilmiş ve izolatörler bodrum katına yerleştirilmiştir. Bunun nedeni de yanyana bulunan bitişik binaların topografyadan dolayı farklı sayıda bodrum katların bulunmasıdır.

İzolatör için yangın dayanımı ihtiyacı gerekebilir. Kullanılan izolatör tipi ve binada yerleştirilen katın kullanımına göre değişmektedir. Çalışmadaki projelerde sismik izolatörlerin yerleştirildiği kat kullanılmıyorsa izolatörler için yangın dayanımı alınmamakla birlikte ilgili katta yangın söndürme sistemi planlanmaktadır.

Şayet ilgili kat kullanılıyor ise kattaki mevcut yangın söndürme sisteminin yanısıra sismik izolatörler için ayrıca bir koruyucu önlem alınması planlanmaktadır. Yapımı tamamlanan Marmara Başıbüyük Hastane binasında bu önlem sismik izolatörlerin 120 dk yangına dayanıklı alçıpan levhalarla kapatılmasıyla alınmıştır.
Statik tasarım:
Çalışmaya katılan güçlendirme projesi hariç diğer 4 hastane projesinde kolon kesitlerinin normal binaya oranla daha küçük olduğu ifade edilmiştir. Ancak güçlendirme projesinde tasarım esnasında sismik izolatör etkisi hesaba katılmadığı için bina kolonları izolatörsüz bina boyutunda kalmıştır. Bu nedenle sismik izolatör kullanım kararının sürecin başında alınması kolon imalatından kaynaklı (demir beton vb.) maliyet düşürülmektedir. Perde ihtiyacı minimumdadır. Ancak çalışmaya katılan hastane projeleri incelendiğinde geleneksel anlayış olan perde kullanımının terkedilemediği yine de büyük oranda azaltıldığı görülmüştür. Sismik izolatör özellikleri belirlenirken sismik tehlike analizi yapılması, performans hedefleri doğrultusunda performans hesabı yapılması, doğrusal olmayan analiz, prototip üretimi ve testleri 5 hastane projesinde de yapılmıştır. Dilatasyon sadece Okmeydanı ve Göztepe Hastanelerinde bulunmakla birlikte diğer hastane binalarında da yapılmamış, güçlendirme projesi olan Başıbüyük hastanesinde de mevcuttaki dilatasyon döşemenin dikilmesiyle kaldırılmıştır.

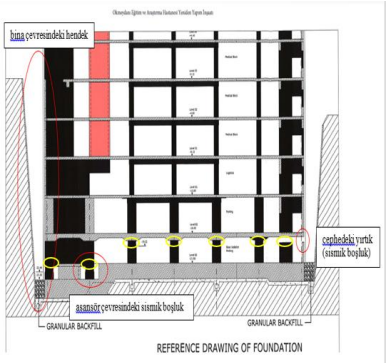

Şekil 10.Sismik izolatör kullanılan Okmeydanı EAH kesiti

3.2.4 Sismik izolatör kullanım kararının 'Yapım' aşamasına etkisi
Sismik izolatör kullanım kararının etkilediği bina üretim süreçlerinden bir diğeri yapım aşamasıdır. Çözülmesi gereken ilave sismik detayların (bina cephesindeki yırtık, bina çevresindeki hendeğin kapatılması, izolatörlerin kapatılması vb.) bulunması ve mimari tasarım aşamasında gözardı edilen birleşim detayları sismik önlemlerin alınması yapım aşamasında karşılaşılan en büyük problemlerdendir. Gerek bina çevresinde bırakılan boşluk, gerekse bina girişlerinde olan detayların yanısıra asansör ve yangın merdivenleriyle ilgili başka birleşim detayları da ortaya çıkabilmektedir. İncelenen hastane binası örneklerinde her hastane binasında farklı detaylarla karşılaşılmış olup sismik detaylar gereken kısımlar aşağıda sıralanmıştır.
- Bina çevresindeki deplasman mesafesini sağlayan hendek gereksinimi
- Hendeğin etrefindaki iksa sistemi (1 hastane binasında forekazık, 1 hastane binasında toprakarme (reinforced earth) sistem ve 3 hastane binasında da çivili beton ankraj sistem kullanılmıştır.)
- Asansör ve basınçlandırılmış yangın merdivenlerindeki sismik detaylar (Okmeydanı ve Göztepe)
- Bina girişlerindeki sismik köprüler (5 hastane binasında de kullanılmıştır.)
- Elektromekanik tesisatların sismik önlemleri (5 hastane binası projesinde ele alınmıştır.)
- Alt yapı tesisatlarının binaya girişindeki esnek bağlantıları (5 hastane binası projesinde de bulunmaktadır.)
- İzolatör katına inen asansör çevresindeki sismik köprü detayları (Okmeydanı, Göztepe ve Başıbüyük)
- İzolatör katına inen basınçlandırılmış yangın merdiveni ve asansörlerin çevresindeki sismik yırtıkta alınması gereken sızdırmazlık önlemi (Okmeydanı ve Göztepe)
- Asma tavan ve taşıyıcı olmayan unsurlarda alınması gereken önlemler (4 hastane binasında da değerlendirilmiş olup güçlendirme projesi olan Başıbüyük hastane binasında asma tavanlarda bir değişiklik yapılmamıştır.)

(a)

(b)

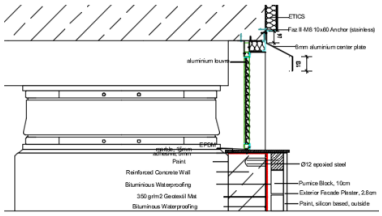

(c)

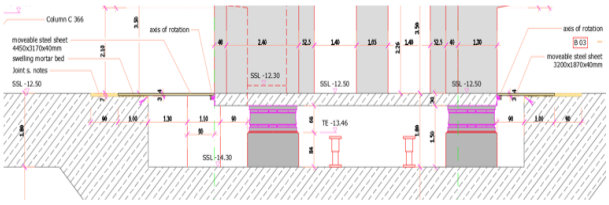

(d)

Şekil 10. (a) İzolatör üstü temel imalatı, (b) Okmeydanı EAH izolatör montaj anından bir görüntü, (c) Cephedeki yırtığın kapatılması, (d) Asansör-zemin birleşimindeki sismik köprü gereksinimi

3.2.5 Sismik izolatör kullanım kararının 'Kullanım' aşamasına etkisi

Periyodik bakım gerektiren izolatörlerle ilgili ayrı bir bakım ve onarım sözleşmesi üretici firmayla yapılmaktadır. Henüz uzun süre kullanılan bir hastane binası olmadığı için bu konu hakkında çok da detaylı bir bilgiye rastlanamamıştır. Ancak izolatör üretici firmayla yapılan görüşmede Başıbüyük hastane binasındaki sismik izolatörlerin garanti süresinin yaklaşık 3-5 yıl olduğu kullanım aşamasında da görsel kontrollerin yapılacağı (korozyon kontrolü, dış koruyucusunun kontrolü vb.) ifade edilmiş olup talep edildiği takdirde sertlik kontrolü yapılabileceği ifade edilmiştir.

Genel olarak projeler incelendiğinde bu sektörde tecrübesi olan firmaların uygulama projesini çizdiği projede karşılaşılan problemlerin en aza indirildiği ancak yine de dikkat edilmesi gereken birçok ilave detayı olduğu gözlemlenmiştir (İkitelli Entegre Sağlık Kampüsü). Buna karşılık bulunduğu merkezi konum sebebiyle yerleşimi etkilenen Okmeydanı ve Göztepe hastane binalarının da farklı sismik detaylar bulundurması farklı çözüm önerilerinin bulunması anlamına gelmektedir. Güçlendirme çalışması olarak kullanım aşamasında sismik izolatör kullanım kararı alınan Marmara Hastane binasının inşaatında bina üretim süreci süre ve maliyet açısından artış göstermiş olup, ileri teknoloji kullanımı açısından diğer hastane binalarının önüne geçmektedir.

Bina üretim sürecinin girişim ve fizibilite aşamasında sismik izolatör kullanım kararının alınması en uygun yöntemdir. Çünkü bu aşamada alınan kararlar diğer süreç adımlarını yakından ilgilendirir. Ayrıca tasarım evresindeki statik-mimari disiplinlerin yakın işbirliği içinde olmasının gerekli olmasıdır. Tasarım aşamasında çözülecek bütün problemler yapım aşamasının sorunsuz geçmesine, yapım süresinin kısalmasına, maliyetin düşmesine ve kalitenin artmasına neden olacaktır. Eğer bir binada sismik izolatör kullanılacaksa, bu kararın bina üretim sürecinin en erken evrelerde alınması, bina üretim sürecinin daha etkin yönetilmesine, süreci etkileyen unsurların önceden fark edilmesine, alternatiflerin belirlenmesine, çözüm arayışlarına gidilmesine yol açacaktır. Söz konusu binaların daha kısa sürede, daha düşük maliyette ve daha iyi bir kalitede üretilebilmesine olanak sağlayacaktır.

4. SONUÇLAR

Ülkemizin bir deprem ülkesi olması nedeniyle üretiminde bu unsurun mutlaka göz önüne alınması gerekmektedir. Bu nedenle sadece proje bazında değil ulusal düzeyde, sektörel düzeyde ve firmasal düzeyde çalışmalar yapılmalıdır.

Ulusal düzeyde; taslak deprem yönetmeliği bir an önce yürürlüğe koyulmalıdır. Sismik izolatör kullanımına uygun olmayan uygulamaların önlenmesi için sismik izolatör kullanılan binaların yapımı kontrol eden bağımsız bir kurum kurulmalıdır. Yeni yönetmeliklerle birlikte bu konuda profesyonel eğitimler gerçekleştirilmelidir.
Yine konuyla ilgili farkındalık çalışmaları yapılmalı ve mimar/mühendislerin konuyla ilgili bilgi sahibi olması sağlanmalıdır. Eğitim programlarında konuyla ilgili dersler konulmalıdır. Deprem izolasyonlu bina projeleri için tasarım gözetim ve kontrol hizmeti verecek bilgi ve deneyime sahip uzmanlar yetiştirilmelidir.
Sektörel düzeyde; sismik izolatör firmalar bilinçlendirilmelidir. Tüm sismik izolasyonlu yapıların envanteri çıkarılmalı ve yerinde kontrol edilerek sertifikalandırılmalıdır. Daha ekonomik ve efektif mimari planlar ortaya konulmalıdır. Üretim ve prototip testlerini yapmak için yeterli kapasiteye sahip bağımsız laboratuvarlar kurulmalı ve işletilmelidir. Sismik izolatör uygulamalarıyla ilgili firmalara bilgi verilmeli, tanıtımlar yapılmalı, konferanslar düzenlenmelidir. Mimarlar ve Mühendisler Odaları konuyla ilgili eğitimler veren programlar hazırlamalıdır.
Firma düzeyinde; inşaat firmaları çalışan mimar ve mühendislerini konuyla ilgili eğitmeli, bilgi eksikliğinin önüne geçmelidir. Sismik izolatör firmaları hangi tip izolatörlerin nerelerde nasıl kullanılacağına ilişkin eğitimler verecek çalışmalar ve sertifika programları düzenlemelidir.
Çalışmada incelenen hastane binalarında sismik izolatör kullanımının bina üretim sürecine etkileri incelendiğinde çeşitli öneriler sunulmuştur.
1)Girişim & Fizibilite aşamasında dikkat edilmesi gereken temel konu kararın bu aşamada verilmesidir. Sismik izolatör kullanım kararının bina üretim sürecinin girişim aşamasında verilmesiyle, bu kararın üretim sürecinin sonraki aşamalarında verilmesine göre süre ve maliyetten kazanç sağlanmış olur. Bu durum bina kalitesini de etkiler.
2) Planlama aşamasında kayda değer konuların başında yurtdışından getirilen izolatörlerin tedarik edilmesi, testlerinin yapılması, imalat ve montaj aşamalarının iyi planlanması gelmektedir. Yurtdışından getirildiği için iş programında ve planlama aşamasında kilit önem taşıyan bu konunun irdelenmesi gerekmektedir. Diğer bir konu da sismik izolatörlü binanın getirdiği ilave statik-mimari ve elektromekanik gereksinimlerin tespit edilip planlamanın doğru yapılmasıdır. Tüm bunlar mimar ve mühendislerin yardımlaşma içinde çalışarak çözülmesiyle mümkündür.
3)Tasarım aşamasında bina formu, yerleşimi ve strüktürü sismik izolatör kullanım kararından etkilenmektedir. Bu nedenle bina maliyeti ve süresi etkilenmektedir. Yine tasarım aşamasında danışmanların sürece katkıda bulunması büyük önem taşımaktadır. Sismik izolasyon, yangın, cephe, medikal gibi konulardaki danışmanlar ve uzmanların kararları koordineli bir şekilde projede belirtilmelidir. Sismik izolatörlü bina tasarımında izolatörlerin konumlandırılması, izolatör kullanım kararının mimariye, cepheye ve medikal yerleşime etkisi, yangın önlemlerinin gereksinimi gibi bilgiler danışmanlardan beklenmektedir. Danışmanlardan gelen bilgiler bu aşamada iş birliği içinde çözümlenmelidir. Bu kararların organize edilmesi ve kararların birbirini etkilememesi için tasarım aşamasına çok fazla önem verilmelidir.
Ayrıca yapısal olmayan elemanlar (Medikal ekipmanlar, elektromekanik ve mimari bileşenler) için sismik önlemler alınmalıdır. Kolon kesitleri narinleşmektedir. Bu sayede imalat kolaylaştırılmakta ve tasarım fonksiyonelliği artırılmaktadır. Ortaya çıkan normal binadan farklı olan detaylar imalatı zorlaştırmaktadır. Yer değiştirmeleri engellemeyecek detayların oluşturulması gerekmektedir. Bunlarla ilgili detaylar yine bu aşamada çözümlenmelidir.
4) Uygulama aşamasında kullanılacak izolatör tipi belirlenirken; efektif, olması ve ileri teknoloji olmasına dikkat edilmelidir, bulunulan ortamın özelliklerine (sıcaklık farkının fazla olup olmadığına) ve binanın yüksekliğine dikkat edilmelidir. Yapının üzerine oturduğu Zemin özelliklerine ve asarım gerekliliklerine dikkat edilmelidir. Teknik bilgilere, işveren talebine, deplasman sınırlamasının sağlanması ve ekonomik olmasına dikkat edilmelidir. Hendek duvarının yüzeyi püskürtme betonla veya toprakarme (reinforced earth) ile yapılabilmektedir. Sismik izolasyonlu binalarda dilatasyon önerilmemekte, dilatasyona gerek duyulmamaktadır. Ancak sismik izolatörlü binalarda da dilatasyona rastalanabilmekte, bu dilatasyonlarda farklı sismik detaylar çözülmektedir. Taşıyıcı olmayan elemanlarda (asma tavan, elektromekanik tesisatlarda, medical ekipman ve cihazlarda) sismik önlem alınmalıdır.
5)Kullanım aşamasında dikkat edilecek hususların en önemlisi bina ömrü boyunca sismik izolatörlerin bakım ve kontrolünün sürekli yapılması, ihmal edilmemesinin önemini belirtmek gerekir. Girişim ve fizibilite aşamasında

bu karar alınırsa bina üretim aşamalarında binadan beklenen performansın sorunsuz karşılanması mümkün olabilir. Bina üretim sürecinin kullanım aşamasında sismik izolatör kullanım kararı alınması güçlendirme projeleri örneklerinde görülmektedir. Bina kullanım aşamasında sismik izolatör kullanım kararı alınması durumunda bina üretim sürecinde üst yapı maliyeti artacak ve güçlendirme projesi süresince bina kullanılmayacağından toplam yapım aşaması da uzamış olacaktır. Bu nedenle daha etkin bir bina üretim süreci için sismik izolatör kullanım kararı girişim&fizibilite aşamasında alınmalıdır.

KAYNAKLAR

Dergi makaleleri için:

Şahin, İ., & Kılınç, T. (2016). Türkiye'de 1980-2014 Yılları Arasında Görülen Depremlerin Ekonomik Etkileri. *Siirt Üniversitesi İktisadi ve İdari Bilimler Fakültesi İktisadi Yenilik Dergisi,* 4(1), 35-37.

Konferans bildirileri için:

Masi, A., Santarsiero, G., & Chiauzzi, L. (2014). *Development of a seismic risk mitigation methodology for public buildings applied to the hospitals of Basilicata region (Southern Italy).* Soil Dynamics and Earthquake Engineering, 65, 30-42.

Kitaplar ve teknik raporlar için:

Deprem İzolasyon Derneği. (2017). 10. Yıl almanak.

FEMA. (2010). The Federal Emergency Management.Earthquake-Resistant Design Concepts. An Introduction to the NEHRP Recommended Seismic Provisions for New Buildings and Other Structures.

Fujita, T. (1997) Demonstration of Effectiveness of Seismic İsolation in the Hanshin-Awaji Earthquake and Progress of Aplication of Base- Isolated Buildings, INCEDE report, Tokyo, Japan.

EFFECT OF MASONRY INFILL PANELS AND RC SHEAR WALLS ON THE SEISMIC PERFORMANCE OF RC BARE FRAMES

Bechtoula H.[1], Aknouche H.[2] and Airouche A.[3]

[1]. *Dr., Technical Department, National Center of Applied Research in Earthquake Engineering CGS, Algiers*
[2]. *Dr., Technical Department, National Center of Applied Research in Earthquake Engineering CGS, Algiers*
[3]. *Dr., Technical Department, National Center of Applied Research in Earthquake Engineering CGS, Algiers*
Email: bechhakim@gmail.com

ABSTRACT:

To investigate the effect of masonry infill panels and RC shear walls on the seismic performance of RC bare frames, four reinforced concrete frame specimens were designed and constructed at CGS laboratory representing a half scale (1/2) of an existing RC frame building located at the east of Algiers. The first specimen represents a bare frame tested under a monotonic loading, pushover. The second specimen was a bare frame tested under a cyclic loading. Whereas, specimen 3 and specimen 4 were, respectively, frames with a full masonry panel and RC shear wall tested under a cyclic loading. The experimental results showed that, for the bare frames damage was localized at the extremities of the columns for a height equal half of the column depth. Strength was considerably increased by inserting a full masonry panel or a RC wall to the bare frame. The strength ratios were, respectively, 2.5 and 5. However, the presence of the masonry panel and the RC shear wall decreased the ductility of the bare frame. Analysis of the experimental data showed that, stiffness degradation of the bare frame was less pronounced than that observed for the frame with infill masonry and the frame with RC wall.

KEYWORDS: masonry infill panel, seismic performance, strength, stiffness, ductility

1. INTRODUCTION

Unreinforced masonry infill panels are used as partitions in RC frames and typically considered as non-structural elements in the Algerian seismic code, RPA99/2003 (MHUV 2003). The Algerian seismic design code, as many other codes, neglects the effect of masonry panels and therefore, the structure is designed as a bare frame. However, observations from recent earthquakes, Boumerdes 2003 (Masanori and Kheir-Eddine 2004) have shown that under seismic excitation, the structural interaction between columns and infill walls can significantly affect the structural behavior and alter the load resisting mechanism and failure pattern of the RC frame (Brokken and Bertero 1981, Pinto et al. 2000, Tsung-Chih and Shyh-Jian 2015, Teguh 2017, Yasushi et al. 2017). A review of the literature on infilled-frames shows that two different research approaches can be identified, one aiming to strengthen the infill, by various methods in order to improve the resistance and monolithic behavior of the frame and infill (Ali et al. 2015), the other to limit the infill frame interaction by certain provisions or devices in order to reduce infill damage and its detrimental effects to the frame. Reducing the infill strength and stiffness or isolating the infill panel masonry from the column is proposed in many recent research (Preti et al. 2012, Gautam and Solomon 2014, Ozkaynak et al. 2014, Fabio 2015, Jarun et al. 2017, Hanhui 2017, Shabdin et al. 2018, Terry et al. 2018). The main objective of this experimental research was to investigate the seismic performance of reinforced concrete frames with a RC wall and frame infilled with perforated clay brick masonry wall. Four one story-one bay reinforced concrete infilled frames of half scale of an existing building were tested at the National Earthquake Engineering Research Center Laboratory, CGS, Algeria. The experiments were carried out under a combined constant vertical axial load and reversed cyclic lateral loading simulating seismic action. This experimental program was performed in order to evaluate the effect of

the infill masonry wall on the lateral stiffness, strength, ductility and failure mode of the reinforced concrete frames.

2. BEHAVIOR OF RC FRAME WITH MASONRY INFILL

Reinforced concrete frame buildings are the most popular in Algeria, particularly for buildings up to 10 stories. Perforated clay brick masonry infill walls, are often used to separate the interior building area. The exterior panels are executed with two infill walls using hollow clay bricks. For high-rise buildings, more than 15 stories, reinforced concrete shear wall structures are used. In some cases, mixed structures, frames and shear walls, are used. External panels are either executed with masonry infill or with prefabricated reinforced concrete panels.

Figure 1. Collapse of an infill wall of the first story

Figure 2. Collapse of infill walls of higher stories

Masonry infill panel is considered as non-structural components. During the May 21st, 2003 Zemmouri earthquake, reinforced concrete shear wall structures suffered slight to no damage. For the majority of the damaged RC frame buildings, masonry of the first floor broke out and plastic hinges were developed near the columns joints, leading to soft story and in several cases to floor mechanisms. Observed damage to the RC frame buildings after the Zemmouri earthquake can be partly attributed to ignorance of the interaction between the frame and masonry in design practice and partly to the low quality of construction. Example of an out of plane collapse is shown in Figure 1. For some old reinforced concrete buildings, the external masonry wall is continuous from the first story to the last one without any ties, which make it very vulnerable to horizontal shakings (Ousalem and Bechtoula 2003). A case of 15-story reinforced concrete frame building, damaged during the 2003 earthquake, can be seen in Figure 2.

3. PROTOTYPE STRUCTURE

The prototype structure chosen in this study is a typical 4-storey residential, reinforced concrete frame building in urban areas in Algeria, which was designed before the Algerian seismic code, RPA99/2003 (MHUV 2003), according to functionality of the building and seismic Zone III, corresponding to the design peak ground acceleration of 0.15g. The selected building is one among 21 others representing a construction program of 70 apartments located at Zeralda, east of Algiers. The construction started 5 months before the 6.8MW, 2003, Boumerdes Earthquake. The design strengths are 25 MPa for concrete and 400 MPa for longitudinal reinforcement. The model represents the lower part of the real building that was scaled down to one-half scale.

4. TEST SPECIMENS

The experimental program consists of four specimens, one-bay and one-storey RC frame specimens, two bare frames, one with masonry infill wall and one with RC wall. Dimensions and the amount of the steel reinforcements of the RC frame were identical for all specimens. The cross-section of the loading beam and the columns were 400 x 400 mm, and 200 x 200 mm, respectively. Dimensions of the tested frames are shown in Figure 3. The amounts of the steel reinforcement in the columns are summarized in Table 1. Longitudinal reinforcement bars were of type FeE400 with a yield strength, f_y= 400 N/mm2, an ultimate strength f_u= 480 N/mm2 and a Young modulus of E=206957 N/mm2. The yield strength of transversal reinforcement of columns (FeE215) ϕ6 steel bars is 215 MPa, ultimate strength is 330 MPa, and Young's Modulus is 200 GPa. For specimen 4, thickness of the RC wall was 80mm with one single steel reinforcement mesh 1T8@85 (0.74%) in the vertical direction and 1T8@150 (0.42%) in the horizontal direction. The four specimens were constructed at the CGS laboratory.

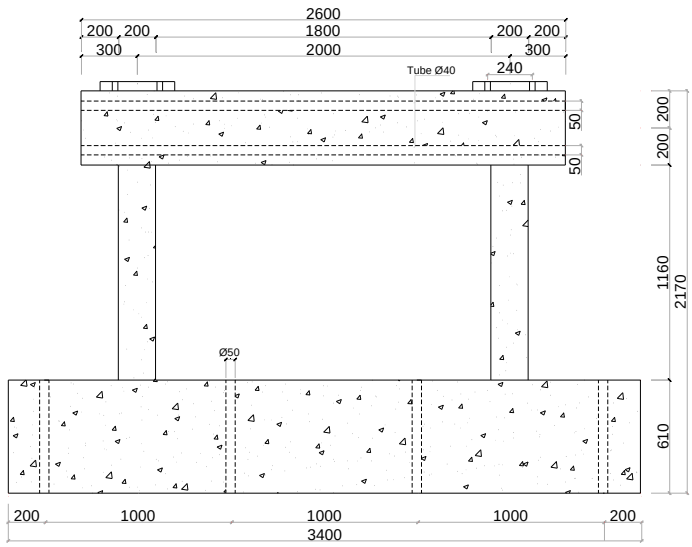

Figure 3. Dimensions of the frames

Ordinary workmanship was intentionally employed in specimen construction. Figure 4 shows the steel arrangement for the foundations and the columns. A clay brick with an approximate size of 300 x 200 x 100 mm in length, height and width, respectively, was used in the real building. The scaled bricks see Figure 5, were obtained by cutting bricks of 300 x 200 x 50 mm, to get two small pieces with an approximate size of 150 x 100 x 50 mm. Figure 6 (a) and (b) show the state of specimen 3 and specimen 4 after setting the masonry panel and the RC wall to the frames. The test variables of this research program are summarized in Table 2.

Table 1. Steel reinforcement in columns

Column	Reinforcement	As (cm^2)	Ratio %
Longitudinal reinforcement	8T8	4.02	1.00
Transversal reinforcement Critical Zone L=380mm	4ϕ6@35mm	1.70	1.62
Transversal reinforcement Non-Critical Zone L=400mm	4ϕ6@50mm	1.70	1.13

Table 2. Test variables

Specimen	Type	Loading
1	Bare frame	Pushover
2	Bare frame	Reversed cyclic
3	Frame with masonry panel	Reversed cyclic
4	Frame with RC wall	Reversed cyclic

Figure 4. Steel arrangement

Figure 5. Full and scaled size brick

(a) With infill masonry panel

(b) With a RC wall

Figure 6. RC bare frame with a full infill masonry panel and RC wall

5. TEST SETUP

Reaction wall, strong floor, and the loading frames were used to carry out this testing program at C.G.S laboratory, as illustrated in Figure 7. Specimens were tested under combined constant axial load and reversed cyclic lateral loading simulating seismic action. The vertical loads, simulating the loading from the upper four stories, were applied to the columns by means of two MTS servo-hydraulic actuators of 500 kN capacity. The lateral load was applied to specimens through the loading beam (see Figure 6) which is the top beam of the specimen, using one MTS-Servo hydraulic actuator of 500 kN capacity. Drift angle, defined as the ratio of lateral displacement to column height, was used to control the incremental loading. As illustrated in Figure 8, two cycles were applied for each prescribed drift. The loading path and the loading rate were set as shown in Table 3. Specimens were instrumented with thirteen (13) linear variable displacement transducer LVDTs to measure displacements at different locations of the specimens as illustrated in Figure 9. Eight (08) strain gauges were set on the reinforcements of the west column, two (02) strain gages on the stirrups (external and internal hoops) and

two (02) strain gages on the vertical bars (external and internal bars). The strain gauges were set at two (02) different levels located at 65 mm from the top and the bottom of the west column. During the whole test process, displacement and steel strains were recorded using MTS, FlexTest for LVDT's and DynaticWave for strain gauge.

Figure 7. Test setup

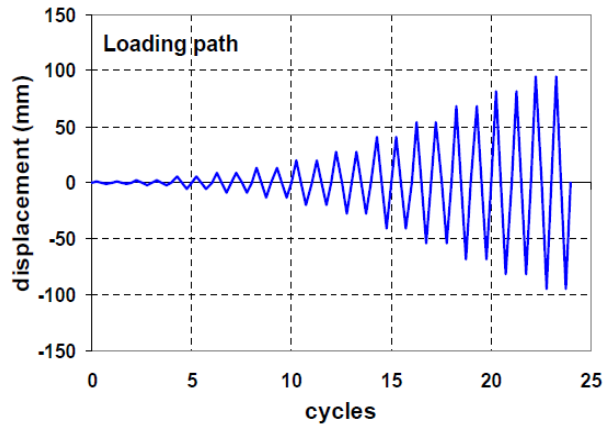

Figure 8. Reversed cycling loading pattern

Table 3. Drift angle

Rd	Drift (%)	Displacement (mm)	Loading Rate for 1mm
1/1000	0.1	1.36	10 Sec
1/500	0.2	2.72	
1/250	0.4	5.44	
1/150	0.67	9.112	
1/100	1	13.6	
1/67	1.5	20.4	5 Sec
1/50	2	27.2	
1/33	3	40.8	
1/25	4	54.4	

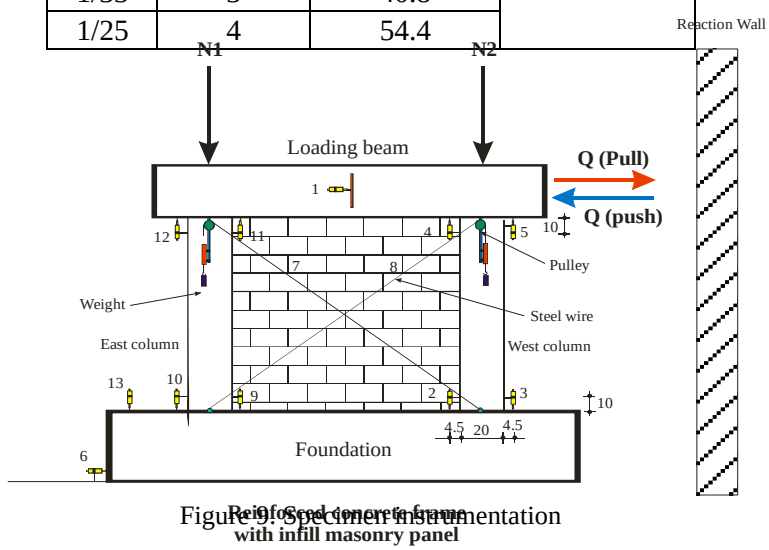

Figure 9. Specimen instrumentation

6. EXPERIMENTAL RESULTS

6.1. Load-drift relationships

As an example, Figure 10 shows le experimental load-drift relationships for specimens 1 and 2. From Figure 10(a) some fluctuation can be seen on the load-drift curve. These fluctuations are due to the difficulty to control the vertical load applied to the columns around 2% drift. We should note that, during the test, the actuators (verticals and horizontals) were set to the desired loading path using the automatically control, force and displacement control, respectively. Figure 11 illustrates the envelope curves and the normalized envelope curves, of the first cycles, of the four specimens. Specimen 1 and specimen 2 show a smooth degradation after reaching the peak load, hence, a large ductility compared to specimens 3 and 4. A big drop was observed in the peak load between the first and the second loading cycles in the push side for specimen 3 and 4 as illustrated in Figure 12 (a) and (b), respectively. This drop was 35% for specimen 3, due mainly to the brittle material (brick masonry) and 17% for specimen 4. For the other side, less than 10% drop was observed as shown in Table 4.

Table 5 shows a comparison between the four specimens in terms of peak loads and the corresponding drifts. For specimen 4, frame with RC wall, the peak load was increased to 6.14 times in the push side and 4.96 times in the pull side, while compared to the peak load reached for the bare frame, specimen 1. These values were, respectively, 2.55 and 2.62 for specimen 3 with an infill brick masonry wall.

For the bare frames (specimens 1 and 2), damage was localized at the extremities of the columns for a height equal half of the column depth. Yielding of the longitudinal reinforcements was observed for the 4 specimens. However, transversal reinforcement did not yield, except for specimen 4.

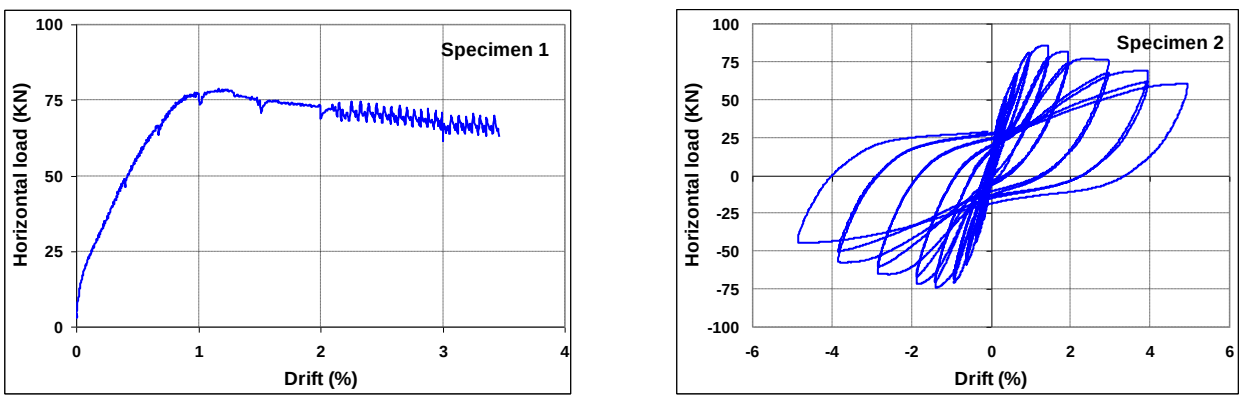

(a) Specimen 1 (b) specimen 2

Figure 10. Load-drift relationships

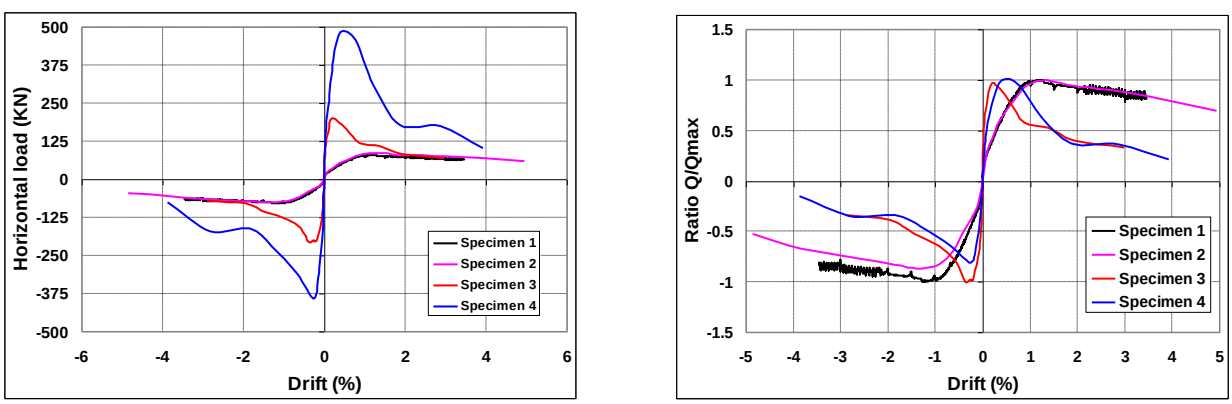

(a) Normal (b) Normalized

Figure 11. Envelope curves

At low drifts, a big difference was observes in the shape of the hysteresis loops between specimens 2, 3 and 4, as illustrated in Figure 13(a). However, at 3% drift, see Figure 13 (b) the envelope curve of specimen 3 matches quite well that of specimen 2. This is due to the damage of the infill masonry wall. In the same manner, at 3% drift the envelope curve of specimen 4 matches that of specimens 3 and 2 between a drift of ± 1.2%. For that region there is no contact between the RC wall and the frame. Beyond that drift, the gap between the wall and the column starts closing and the horizontal load starts increasing. This state, opening and closing of gaps, is illustrated in Figure 14.

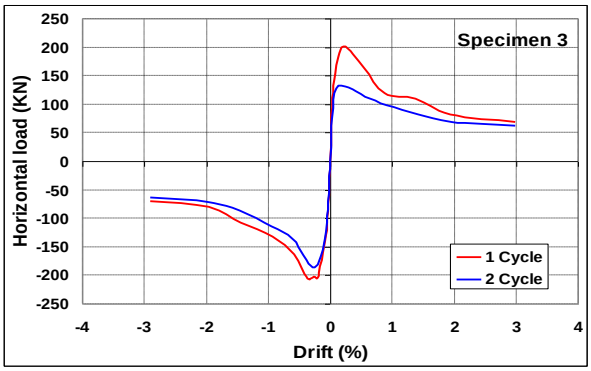

(a) Specimen 3

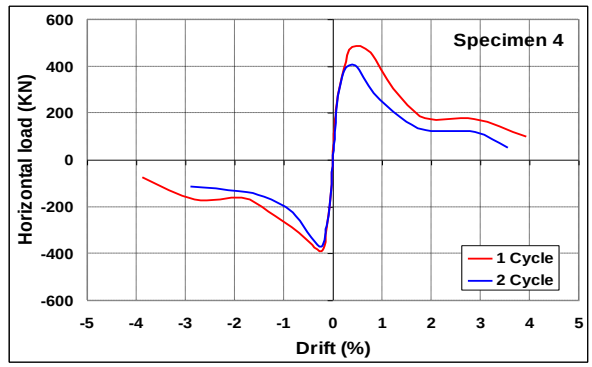

(b) specimen 43

Figure 12. Comparison between the envelope curves of the first and the second cycles

Table 4. Peak loads ratios between the first and the second cycles

Specimen	Cycle	Peak load (KN)		Ratio 2nd/1st	
		Push	Pull	Push	Pull
1	Pushover	78.66			
2	1st	85.60	-74.37	0.90	0.94
	2nd	77.27	-70.09		
3	1st	200.67	-206.36	**0.65**	0.91
	2nd	129.58	-187.02		
4	1st	482.80	-390.11	**0.83**	0.95
	2nd	402.31	-370.02		

Table 5. Comparison between the four specimens

Specimen	Direction	Peak load (KN)	Drift at peak(%)	For the same specimen		Between specimens and specimen 1	
				Ratio (+)/(-) (load)	Ratio (+)/(-) (drift)	Ratio (load)	Ratio (drift)
1	(+) Push	**78.66**	**1.17**			1.00	1.00
2	(+) Push	85.60	1.31	1.15	0.95	1.09	1.12
	(-) Pull	74.37	1.39			0.95	1.19
3	(+) Push	200.67	0.21	0.97	0.57	**2.55**	0.18
	(-) Pull	206.36	0.37			**2.62**	0.31
4	(+) Push	482.80	0.40	1.24	1.69	**6.14**	0.34
	(-) Pull	390.11	0.24			**4.96**	0.20

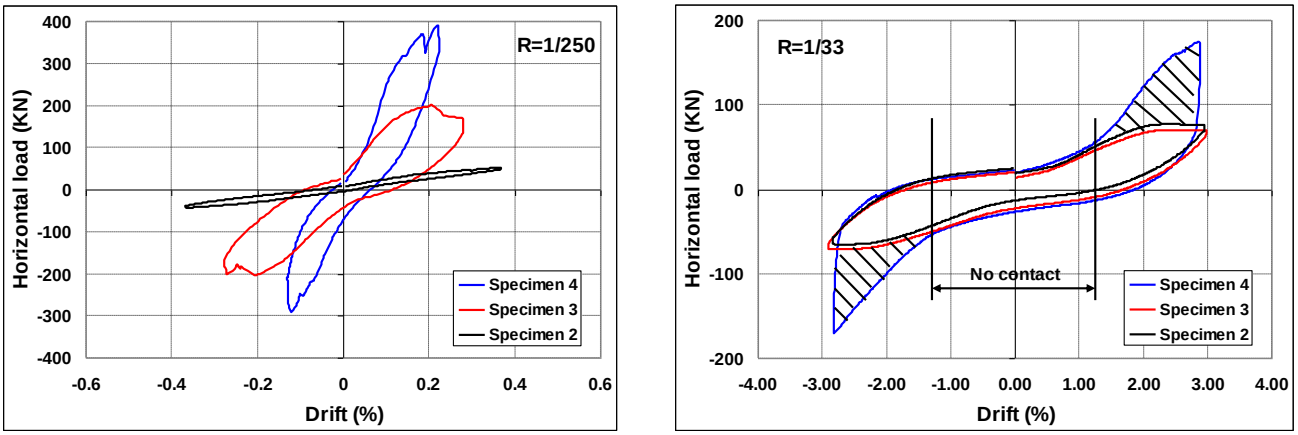

(a) Loops at a drift of 1/250 (b) Loops at a drift of 1/33

Figure 13. Comparison of the hysteresis loop shape's at the same drift

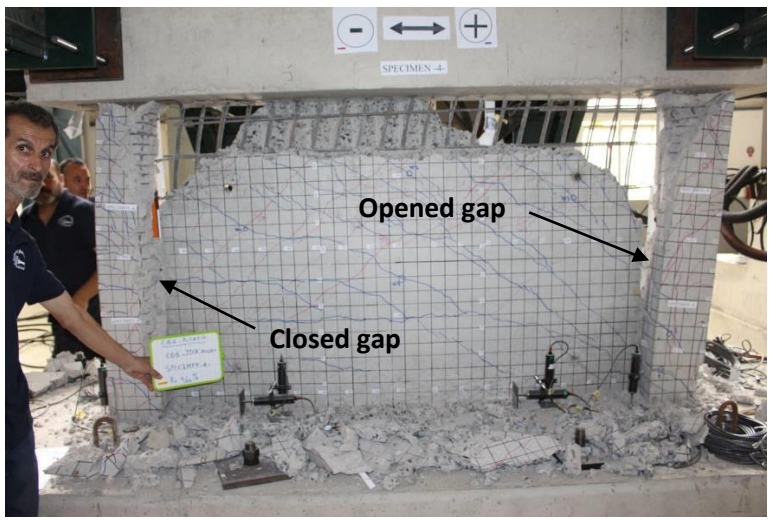

Figure 14. Damage to specimen 4 at 4% drift, opened and closed gap

6.2. Stiffness degradation

From Figure 10 it can be seen that specimen 2 demonstrates a fat loops compared to specimens 3 and 4. In the same time, it can be seen from Figure 11 (a) and (b) that the stiffness degradation of specimen 2 is less pronounced than that observed for specimens 3 and 4. To strengthen these remarks, stiffness degradation along the entire loading process was computed at each drift for each specimen, and compared to the initial stiffness K0. The obtained result is illustrated in Figure 15. As an example, at 1% drift le ratios (K/K0) were 0.31, 0.04 and 0.16 for specimens 2, 3 and 4, respectively.

6.3. Variation of the equivalent viscous damping

Variation of the equivalent viscous damping factor was computed using the first cycle loops at each of the imposed drift angle. The equivalent viscous damping, Heq, was computed using the following expression:

$$H_{eq} = \frac{1}{4\pi}\frac{\Delta_W}{\Delta_e} \tag{1}$$

where: Δ_W is the area enclosed by one cycle hysteresis loop and Δ_e is the equivalent potential energy.

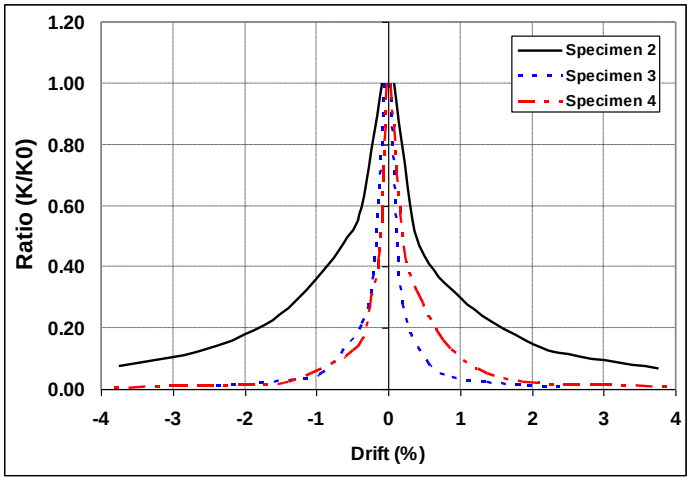

Figure 15. Stiffness degradation

As shown in Figure 16, variation of the equivalent viscous damping was nearly linear for specimen 2. A constant equivalent viscous damping was observed for specimen 3 between 1% and 2% drift. The same remark can be done for specimen 4, for a drift between 1% and 3% drift. Beyond these limits (2% drift for specimen 3 and 3% drift for specimen 4), the 3 specimens show nearly the same slope on the Heq-drift curves. This state corresponding to big drifts and indicates that only frame remains, after collapse of the masonry wall (of specimen 3) and appearance of large gaps between the columns and the RC wall (for specimen 4).

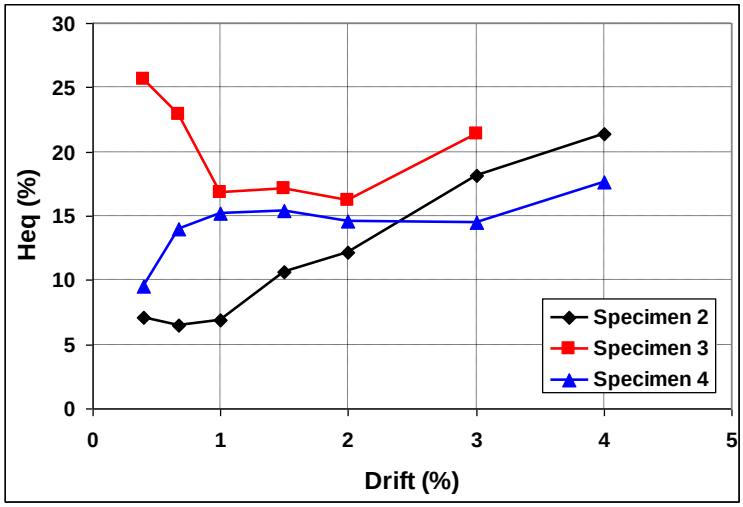

Figure 16. Variation of equivalent viscous damping

7. CONCLUSIONS

The mains results of the testing program can be summarized as follow:

1. For the bare frames (specimens 1 and 2), damage was localized at the extremities of the columns for a height equal half of the column depth.
2. Yielding of the longitudinal reinforcements was observed for the 4 specimens. However, transversal reinforcement did not yield (except for specimen 4).

3. Strength of the original specimen (bare frame) can be increased considerably by inserting a masonry panel or a RC wall.
4. Increasing the strength reduced the ductility of the original specimen.
5. Stiffness degradation of the bare frame (specimen 2) is less pronounced than that observed for the frame with infill masonry (specimens 3) and the frame with RC wall (specimen 4).
6. As for the equivalent viscous damping, Heq, it was observed that beyond 2% drift for specimen 3 and 3% drift for specimen 4, the 2 specimens show nearly the same slope on the Heq-drift curves as the bare frame, specimen 2.

8. ACKNOWLEDGMENTS

This research was financially supported by the National Earthquake Engineering Research Centre, CGS, Algeria and carried out with a Technical Cooperation of the Japan International Cooperation Agency, JICA, Japan.

REFERENCES

Ministère de l'Habitat et de l'Urbanisme, M.H.U.V. et Centre National de Recherche Appliquée en Génie Parasismique, C.G.S. (2003). Règlement Parasismique Algérien, RPA 99 version 2003. Algeria.

Masanori, H. and Kheir-Eddine, R. (2004). Boumerdes Earthquake the 21st May 2003. Japanese Reconnaissance Team, Technical Report, DOI: 10.13140/RG.2.2.36186.34249.

Brokken, S., and Bertero, V.V. (1981), "Studies on effects of infills in seismic resistant RC construction", Report UCB/EERC, 81-12, University of California, Berkeley.

Pinto, A.V., Varum, H. and Molina, J. (2000), "Experimental assessment and retrofit of full-scale models of existing RC frames", Proc. 12th ECEE, London.

Tsung-Chih, C. and Shyh-Jian, H. (2015), "Tests on cyclic behavior of reinforced concrete frames with brick infill" Earthquake Engineering Structural Dynamics, **44:12**, 1939–1958.

Teguh, M. (2017), "Experimental evaluation of masonry infill walls of RC frame building subjected to cyclic loads", Procedia Engineering, SCESCM, 191- 200 Sustainable Civil Engineering Structures and Construction Materials.

Yasushi, S., Yoshiaki, N., Kazuto, M., Devjyoti, P., Polat, G., Baris, B. (2017), "Experimental evaluation of the in-plane behaviour of masonry wall infilled RC frames", Bulletin of Earthquake Engineering, **15:10**, 4245–4267.

Ali M., Behnam M., Mohammad, R.A. (2015). Seismic response of RC frame structures strengthened by reinforced masonry infill panels. *Earthquakes and Structures* **8:6**, 1435-1452.

Preti, M., Bettini, N. and Plizzari, G. (2012). Infill walls with sliding joints to limit infill-Frame seismic interaction: large-scale experimental test. *Journal of Earthquake Engineering*, **16:1**, 125-141.

Goutam, M. and Solomon, T. (2014). Effects of vertical irregularity and thickness of unreinforced masonry infill on the robustness of RC framed buildings. *Earthquake Engineering Structural Dynamics* **43:2**, 205–223.

Ozakaynak, H., Yuksel, E., Yakin, C., Dindar, A.A., Buyukozturk, O. (2015). Masonry infill walls in reinforced concrete frames as a source of structural damping. *Earthquake Engineering Structural Dynamics* **43:7**, 949–968.

Fabio, C. (2015). Seismic behaviour of reinforced concrete frames with different configuration of masonry infill. Master Thesis in civil engineering, University of science and technology, Hong Kong.

Jarun, S., Sutat, L., Arnon W., Panitan, L. (2017). Experimental and analytical evaluation of a low-cost seismic retrofitting method for masonry-infilled non-ductile RC frames. *Earthquakes and Structures* **12:6,** 699-712.

Hanhui, z., Kuang, J.S. and Terry, Y.P. (2017). Low-seismic damage strategies for infilled RC frames: shake-table tests. *Earthquake Engineering Structural Dynamics* **46:14**, 2419–2438.

Shabdin, M., Nader, K.A., Attari, Zargaran, M. (2018). Experimental study on seismic behavior of Un-Reinforced masonry (URM) brick walls strengthened with shotcrete. *Bulletin of Earthquake Engineering* **16:9**, 3931–3956.

Terry, Y.P.Y., Han-hui, Z., Kuang, J.S., Qunxian, H. (2018). Shake table tests on RC frame infilled by slitted masonry panels. *Bulletin of Earthquake Engineering* **16:9**, 4027–4052.

Ousalem, H. and Bechtoula, H. (2003). Report on the Damage Investigation and Post-Seismic Campaign of the 2003 Zemmouri Earthquake in Algeria. The University of Tokyo Department of Architecture 2003 by Earthquake Research Institute, The University of Tokyo C/O Kabeyasawa Laboratory, Division of Disaster Mitigation Science, Tokyo, Japan.